A numerical study of the gravitational instability in protostellar discs

Anthony Mercer

A thesis submitted in partial fulfilment
of the requirements for the degree of
Doctor of Philosophy

Jeremiah Horrocks Institute for Mathematics, Physics and Astronomy
University of Central Lancashire

August 2019

Declaration

Type of Award: Doctor of Philosophy

School: Physical Sciences and Computing

I declare that while registered as a candidate for the research degree, I have not been a registered candidate or enrolled student for another award of the University or other academic or professional institution.

I declare that no material contained in the thesis has been used in any other submission for an academic award and is solely my own work.

No proof-reading service was used in the compilation of this thesis.

Anthony Mercer

August 2019

Abstract

Young protostellar discs may be massive enough that they become unstable and fragment, leading to the formation of planets, brown dwarfs, and low-mass stars. This thesis examines the development of the gravitational instability in discs: how it occurs and whether planets can form through gravitational fragmentation.

I consider the effects of radiative feedback by objects formed through gravitational fragmentation in discs, and compare simulations which consider three cases of radiative feedback: none, continuous, and episodic. I find that when radiative feedback is continuous, only one object forms as its radiative feedback suppresses further fragmentation. However, when radiative feedback is episodic, further fragmentation occurs as the disc cools between episodes. Generally, the stronger the radiative feedback, the fewer objects ultimately form through gravitational fragmentation. Since multiple objects are formed, those of lower mass are ejected due to gravitational interactions. On the other hand, the more massive objects accrete a sufficient amount of gas to eventually become brown dwarfs or low-mass stars. Therefore, disc fragmentation may be a significant source of free-floating planets and companion brown dwarfs.

I study the effects of gravitational instability in protostellar discs around M-dwarfs and determine the minimum disc mass required for fragmentation. Disc-to-star mass ratios of between $q \sim 0.3$ and $q \sim 0.6$ are found to be necessary, and although the metallicity of the disc does not affect this, a high metallicity can inhibit fragmentation altogether. The gravitational fragmentation of protostellar discs around M-dwarfs results in the formation of massive protoplanets: they have initial masses above 5 M_J

and form on wide orbits ($\sim 10-100$ AU from the host star). Therefore, the massive planets on wide orbits observed around M-dwarfs may have formed via gravitational fragmentation, provided that they were attended by relatively massive discs during their early phase of formation.

Contents

List of Tables

List of Figures

Acknowledgements

First and foremost I would like to show my gratitude towards my supervisor Dimitris Stamatellos for the opportunity to make this work a reality, as well as for the exceptional amount of help, guidance and development of ideas. I thank Benjamin MacFarlane and Alex Dunhill for their continued and interesting discussion, criticisms and collaboration. With regard to the implementation of radiative transfer and radiative feedback into GANDALF, I thank Richard Booth and David Hubber for their personal support. Additionally, there have been a great many people at various conferences and workshops who have provided me with not only ideas and insight, but also inspiration, reassurance and motivation. I also appreciate the support from the Science and Technology Funding Council whose funding has kept a roof over my head during the period of this work.

To all of the people who have kept my mind from leaving the realms of sanity. Above all my family who I love dearly: my Mother, the strongest person I will ever know, and my Nan & Grandad, who have made my world a much more wonderful place to live in. To my friends I express the sincerest gratitude: James Orford, a better man among us, and without whom my research years would not have been *lived*; Gary and Lynn Orford for always making me feel welcome; Charles Green and our walks, talks and beers in Arnside and in the Lake District; Nina Schreiner for the myriad of enjoyable memories, her patience for me, and of course, for the time she rescued my lost luggage; Belinda Fischer for our many wonderful Stammtisch sessions and her invaluable help with the German language; and last but not least, my friends I have known since childhood that I have still have the fortune to see on occasion, Mark Atkinson, Conor Jeffers and Tom Nulty. My heartfelt appreciation to you all.

Chapter 1

Introduction

The notion that the planets of our solar system were formed in a disc was first presented in the late 18th century (Laplace 1796). Recently, thanks to the contribution of the Kepler Space Mission (Koch et al. 2010; Borucki et al. 2010a), thousands of planets around other stars have been discovered. These so-called *extra-solar-planets* (henceforth exoplanets) are not only exclusive to single stars, but also orbit binary (Doyle et al. 2011) and even higher multiplicity stellar systems (Wagner et al. 2016). This suggests that planet formation is a highly robust process.

Planets are formed within circumstellar discs, which not only provide the necessary chemical and dynamical environment for planets to form (e.g. Lissauer 1993), but also provide their host protostars with the majority of their final mass through accretion processes. Young circumstellar discs are typically referred to as *protostellar discs* which are accreting rapidly onto the central protostar. After a significant fraction of the mass within the disc has accreted onto the protostar, the long-lived, low-mass disc is where planets have time to form, and is hence referred to as a *protoplanetary disc*. The work presented in this thesis focuses on the former, though theoretical and observational background is presented for circumstellar discs in general.

In this Chapter, I begin with an outline on the formation of young stellar objects. The star formation process itself is important as it sets the initial conditions of the

protostellar disc. The properties of circumstellar discs and their evolution is then discussed, as well as some of the physical processes which occur within these environments.

1.1 Formation of young stellar objects

Young stellar objects (YSOs) form from the collapse of gas in molecular clouds (e.g. Klessen 2011) where local gravitational collapse occurs from density inhomogeneities on much smaller scales than that of the cloud itself. However, clouds are not static entities but are instead turbulent. Turbulence provides an effective pressure and stabilises the cloud. The cloud is also supported by thermal and magnetic pressures and collapse only occurs when gravity dominates over these sources of support.

A feature that has been shown to be ubiquitous to molecular clouds are filaments (e.g. André et al. 2010, 2014). They have typical widths of ~ 0.1 pc, lengths between 1 and 100 pc and possess minimal curvature. Figure 1.1 illustrates the filamentary structure within Taurus B211/B213. The local magnetic field configuration depends on whether the filament is self-gravitating or not (Peretto et al. 2013). Those that are self-gravitating lie perpendicular to the local magnetic field whereas gravitationally unbound filaments lie parallel to the local magnetic field. The flow of material onto the filament ultimately leads to the formation of dense cores via gravitational fragmentation. Until recently, the role of magnetic fields in star formation has not been well constrained (Crutcher & Troland 2000; Curran & Chrysostomou 2007). However, observations obtained from the James Clerk Maxwell Telescope, specifically the B-Fields In Star-Forming Region Observations (BISTRO) survey, have shed light on the importance of magnetic fields in star formation regions (Ward-Thompson et al. 2017; Pattle et al. 2017; Kwon et al. 2018). Figure 1.2 shows the polarisation vectors within the OMC 1 region of the Orion A filament, demonstrating the intricate connection between filamentary structure and magnetic field orientation.

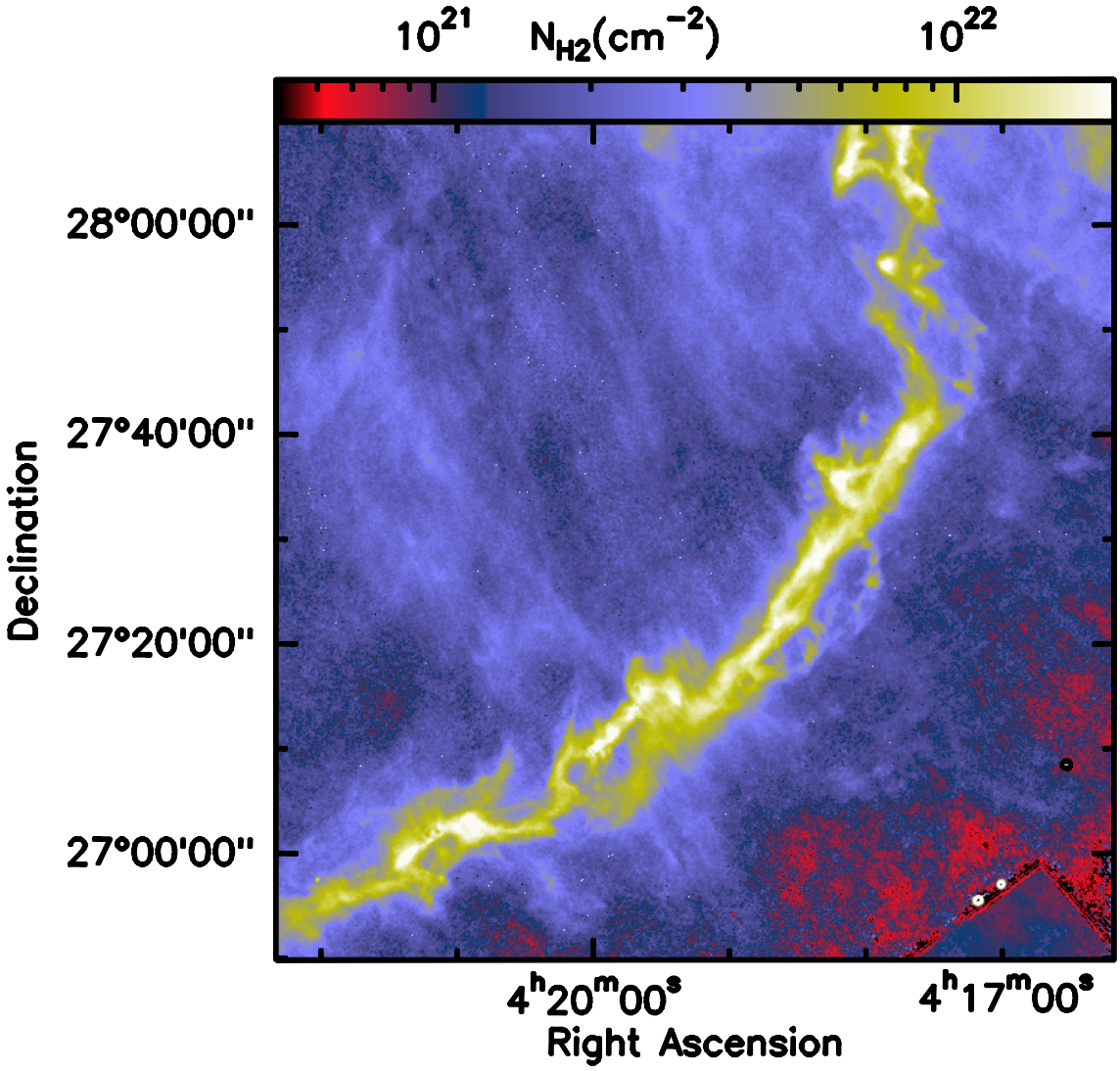

Figure 1.1: A column density map of Taurus B211/B213 showing filamentary structure. This was observed by the Herschel Space Observatory (Palmeirim et al. 2013).

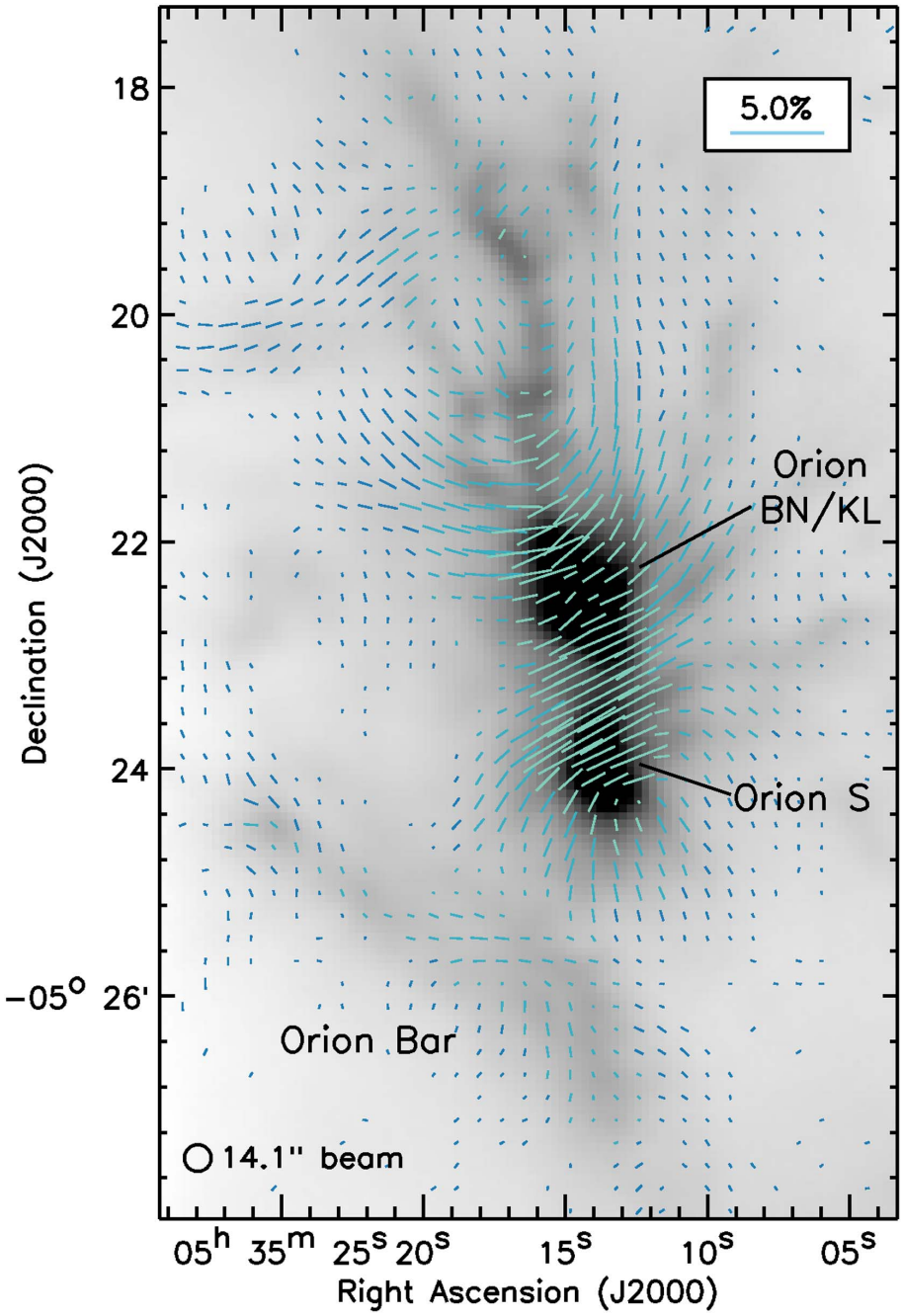

Figure 1.2: Polarisation map of OMC 1 with a SCUBA-2 850 μm continuum emission of Orion A in greyscale. The image demonstrates an observational confirmation of the intricate nature between filamentary structure and magnetic fields within a star forming region. Taken from Pattle et al. (2017).

Observations show that that $\sim$ 70% of all prestellar cores lie on filaments where column densities exceed $N_{\mathrm{H_2}} \gtrsim 7\times10^{21}$ cm^{-2} (e.g. Men'shchikov et al. 2012; Kirk et al. 2013). These are the dense cores that are dominated by gravity such that they will go on to form one or more YSOs. Once collapse occurs, a Class 0 object is formed which is typically undetectable at wavelengths $\lambda < 10$ μm and has a spectral energy distribution akin to a blackbody with $T \leq 30$ K (Andre et al. 1993).

Consequent stages can be classified based on the slope of the infrared region (typically in the range 2 - 14 μm) of the spectral energy distribution of the YSO (Lada 1987; Andre et al. 1987), quantified by the spectral index α where

$$\alpha = \frac{\mathrm{d}\log(\lambda F_\lambda)}{\mathrm{d}\log(\lambda)}. \tag{1.1}$$

As the surrounding envelope accretes onto the disc, emission from the protostellar disc becomes detectable. This is the Class I phase where $\alpha > 0$ and the age of the YSO is a few 10^4 to 10^5 yrs. Emission in this phase is the result of hot dust heated by the protostar and cold dust in the envelope, and may be the epoch in which the gravitational instability could develop within the disc. The envelope is then consequently accreted resulting in the Class II, Classical T-Tauri phase where $-1.5 < \alpha < 0$. Near- and mid-infrared emission is primarily due to emission from the disc itself. Weak-line T-Tauri stars are further evolved and exhibit reduced emission from the disc. The post T-Tauri, Class III phase is characterised by a spectral index $\alpha < 1.5$, where the gaseous disc has dissipated, leaving only a debris disc and planetary or (sub)-stellar companions. The central T-Tauri star then slowly contracts to become a main-sequence star.

1.2 Properties of circumstellar discs

The molecular clouds in which protostars are formed typically have a component of angular momentum (e.g. Imara & Blitz 2011; Tatematsu et al. 2016). Collapsing gas

and dust therefore forms a disc around a young protostar (e.g. Terebey et al. 1984; Attwood et al. 2009), where excess angular momentum may be carried out by bipolar outflows (Bachiller 1996). In this section I discuss the radii, masses and kinematics of circumstellar discs.

1.2.1 Disc radii

The radii of circumstellar discs range from tens of AU around brown dwarfs (Scholz et al. 2006) to 10^4 AU around massive B-type stars (Cesaroni et al. 2007). However, the cool outer regions of circumstellar discs are difficult to observe and thus difficult to constrain spatially. Vicente & Alves (2005) measured outer disc radii in the Trapezium cluster by observing the absorption of the discs against the bright HII background. They determined that 22 of the discs had outer radii between 50 and 194 AU, with an extreme outlier with an outer radius of 612 AU. The Atacama Large Millimetre Array (ALMA) has been key in determining the properties of young discs. Ansdell et al. (2018) utilised ALMA Band 6 (1.33 mm) and determined outer disc radii in the young (1-3 Myr) Lupus star forming region. The 1.33 mm continuum data traces the dust, but observations were also obtained for the ^{12}CO, ^{13}CO and C^{18}O $J = 2-1$ lines, which trace the gas. The authors ubiquitously found that the extent of the dust disc is smaller than the gas disc, probably due to the inward drift of dust. The radial distribution of the dust component of the discs in Lupus ranges from 38 - 334 AU: the gaseous component 68 - 462 AU.

1.2.2 Disc masses

The dynamics of circumstellar discs are governed by the gas content as this constitutes $98-99\%$ of their mass. The small proportion of dust is directly observable via thermal continuum emission. Assuming that the dust opacity within discs is the same as in the interstellar medium, the masses of circumstellar discs can be constrained to

10^{-4} $M_\odot$ $< M_{\rm disc} <$ 10^{-1} $M_\odot$ (Andrews & Williams 2005). This assumption neglects dust evolution whereby dust grains agglomerate and grow in size, reducing the dust opacity in the near-infrared waveband. The range of masses of circumstellar discs may therefore have been underestimated. Young disc masses obtained from position-velocity diagrams may also be underestimated by $\sim$ 20% due to an enhanced radial pressure on the gas (MacFarlane & Stamatellos 2017). This may also lead to dust depletion and a lower dust-to-gas ratio. Bergin et al. (2013) measure the gas mass of TW Hydrae via the fundamental rotational transition of hydrogen deuteride, the emission of which is sensitive to the total mass. They find a disc mass of $M_{\rm disc} = 0.05$ $M_\odot$, typically larger than when using CO as a tracer which yields disc masses in the range 5×10^{-4} $M_\odot$ $< M_{\rm disc} <$ 0.6 $M_\odot$ (Thi et al. 2010; Gorti et al. 2011).

From a 1.33 mm ALMA survey of the discs in the σ Orionis Cluster (Ansdell et al. 2017), the dust mass of the discs was constrained to $\sim$ 2 $M_\oplus$ with only 11 of the 37 discs possessing more than 10 $M_\oplus$. The intermediate age of the sample ($\sim 3-5$ Myr) therefore suggests that after a few Myr of evolution, most of the discs lack sufficient dust to form giant planet cores. The gas mass of discs which had detectable CO was constrained to $\sim$ 3 $M_{\rm J}$. These results suggest that giant planet formation is either a rare phenomenon, or that it begins early in disc evolution. 230 GHz continuum observations of young discs surrounding Class 0 protostars in the Serpens molecular cloud yield disc masses between 0.04 $M_\odot$ and 1.7 $M_\odot$, with a mean value of 0.2 $M_\odot$ (Enoch et al. 2009b, 2011). This supports the idea that the more massive, earlier phase of discs is the one in which gravitational instability may occur (see Section 1.5).

1.2.3 Disc kinematics

Evolved protoplanetary Class II discs have accreted sufficiently onto their accompanying protostar such that they are typically low in mass and are generally thin. The

orbital frequency of gas within the disc is Keplerian such that

$$\Omega_{\rm K}(R) = \sqrt{\frac{GM_\star}{R^3}}, \tag{1.2}$$

where $M_\star$ is the mass of the central protostar and R is the distance from it. The specific angular momentum of gas on a circular orbit at a given radius, $j(R)$, is

$$j(R) = \sqrt{RGM_\star}. \tag{1.3}$$

The requirement for accretion onto the central protostar is that the gas needs to lose angular momentum by some process (see Sections 1.5 and 1.6).

Many protoplanetary discs have been observed to determine their velocity profiles, and they are typically Keplerian (e.g Koerner et al. 1993; Dutrey et al. 1994; Mannings et al. 1997; Duvert et al. 1998; Guilloteau & Dutrey 1998; Simon et al. 2000). However, it is difficult to determine velocity profiles for young embedded protostellar discs (Class 0 and Class I objects) as the disc emission is combined with that of the infalling envelope. Brinch et al. (2007) determine that even at the young embedded stage, a Class I protostellar disc surrounding the protostar L1489 IRS has a Keplerian profile. This was determined using the Sub-Millimetre Array (SMA) observing the HCO^+ $J = 3-2$ line at a resolution of $\sim 1''$. A range of Class I discs have been observed to exhibit Keplerian velocity profiles since (e.g. Lommen et al. 2008; Jørgensen et al. 2009; Lee 2010, 2011; Takakuwa et al. 2012; Yen et al. 2013; Brinch & Jørgensen 2013; Harsono et al. 2014; Chou et al. 2014). In regard to Class 0 objects, Tobin et al. (2013b) observed a Keplerian disc around a very young, 0.3 Myr old protostar L1527 IRS, which is in perhaps the earliest stage of star formation. Indeed, there are multiple systems which exhibit similar properties (e.g Murillo et al. 2013; Codella et al. 2014; Lee et al. 2014; Yen et al. 2015a; Aso et al. 2017). However, there are some systems which show no hint of rotational motion within their envelope (Brinch et al. 2009; Yen

et al. 2013; Maret et al. 2014; Yen et al. 2015b), suggesting that, if they do possess Keplerian discs, they have radii < 10 AU.

1.3 Disc structure

Analytical representations of circumstellar discs are important when developing initial conditions for numerical simulations. In this Section I describe how the density and temperature of circumstellar discs vary radially and vertically. I discuss observational results in comparison to models, and show that the structure of circumstellar discs is subject to variation.

1.3.1 Mass distribution

The distribution of mass within a circumstellar disc is characterised by the surface density Σ, where through the vertical direction of the disc z, is

$$\Sigma(R) = \int_{-\infty}^{+\infty} \rho(R,z)\, \mathrm{d}z. \tag{1.4}$$

R is the radius in the $x-y$ plane and ρ is the density at a given position within the disc. The radial profile of the surface density is typically described by a power law such that $\Sigma(R) \propto R^{-p}$, where the power index p may have a value in the range between 0 and 3/2. From observational inferences of discs in the Taurus-Ariga and Ophiuchus-Scorpius star forming regions (Andrews & Williams 2007), a median index of $p = 1/2$ is determined. Taking an analytical approach, Tsukamoto et al. (2015) assume a steady viscous accretion disc with constant cooling rate and obtain a value of $p = 3/2$. Note that this value also corresponds to the canonical surface density power index of the minimum mass solar nebula (Weidenschilling 1977).

A pure power law truncated at an outer radius of the dust disc may not be compatible with the extended gaseous component (McCaughrean & O'Dell 1996; Piétu et al.

2005; Isella et al. 2007). Instead, an exponentially tapered form of the surface density may be more suitable, of which there is an existing analytical solution for viscous discs (Lynden-Bell & Pringle 1974; Hartmann et al. 1998). It has the form

$$\Sigma(R) = (2-\gamma)\,\frac{M_{\rm disc}}{2\pi R_c^2}\left(\frac{R}{R_c}\right)^{-\gamma}\exp\left[-\left(\frac{R}{R_c}\right)^{2-\gamma}\right], \tag{1.5}$$

where $M_{\rm disc}$ is the total disc mass, γ is a radial viscosity power index (where the kinematic viscosity has the relation $\nu \propto R^{\gamma}$) and R_c is a characteristic radius. The latter is the radius at which the surface density deviates from a power law and instead begins to decline steeply. Hughes et al. (2008) observed four discs in 230 and 345 GHz continuum as well as the CO $J = 3-2$ molecular transition line. They concluded that the tapered exponential surface density profile reproduces both dust and gas emission more closely than a pure power law profile. They also found characteristic radii in the range $R_c = 30-200$ AU and that $R_{\rm out} \approx 2R_c$. Surface density and viscosity power law indices in the ranges $p = 1.0-1.3$ and $\gamma = 0.7-1.1$, respectively, were determined as the best fitting parameters for their continuum models. Andrews et al. (2009, 2010) surveyed the discs in the Ophiuchus star forming region finding characteristic radii in the range $R_c = 14-198$ AU and viscosity power law indices in the range $\gamma = 0.4-1.1$. Additionally, Cieza et al. (2018) find that discs around FU Orionis objects are typically more compact than discs around T-Tauri objects, having characteristic radii of $R_c < 20-40$ AU.

1.3.2 Vertical structure

The vertical structure of a disc depends on the interplay between gravity and the disc thermal pressure. Assuming a disc is azimuthally symmetric and there is no temperature gradient in the vertical direction, vertical hydrostatic equilibrium can be described

by

$$\frac{\mathrm{d}P}{\mathrm{d}z} = -\rho \frac{GM_\star}{R^3} z = -\rho \Omega^2 z. \tag{1.6}$$

P and ρ are the gas pressure and density, respectively, and Ω is the Keplerian frequency at a given radius in the disc. For gas densities up to ~ 0.1 g cm^{-3}, the gas can be assumed to be ideal, thus $P = c_s^2 \rho$, where c_s is the sound speed, defined as

$$c_s = \sqrt{\frac{kT}{\tilde{\mu} m_\mathrm{H}}}. \tag{1.7}$$

T is the temperature, k is the Boltzmann constant, $\tilde{\mu}$ the mean molecular weight, and m_H the mass of the hydrogen atom. Combined with the ideal gas approximation, Equation 1.6 can be written

$$\frac{\mathrm{d}\left(c_s^2 \rho\right)}{\mathrm{d}z} = -\rho \Omega^2 z. \tag{1.8}$$

The temperature has been assumed to be constant vertically at a given radius R, hence one can rearrange to obtain the differential equation

$$\frac{1}{\rho}\frac{\mathrm{d}\rho}{\mathrm{d}z} = -\frac{\Omega^2}{c_s^2} z, \tag{1.9}$$

which has the solution

$$\rho(R,z) = \rho_0 \exp\left(-\frac{z^2}{2H^2}\right). \tag{1.10}$$

The pressure scale height $H = c_s/\Omega$ quantifies the balance between thermal pressure and gravity. Recall the expression for surface density in Equation 1.4, then

$$\rho_0 = \frac{\Sigma}{\int_{-\infty}^{+\infty} \exp\left(\frac{-z^2}{2H^2}\right) \mathrm{d}z} = \frac{\Sigma(R)}{\sqrt{2\pi} H}, \tag{1.11}$$

hence

$$\rho(R,z) = \frac{\Sigma(R)}{\sqrt{2\pi} H} \exp\left(-\frac{z^2}{2H^2}\right). \tag{1.12}$$

1.3.3 Temperature profile

Circumstellar discs can be described as passive, absorbing and re-emitting the radiation from the central protostar, or active, generating heat via viscous dissipation. In the case of a flat, passive disc, the stellar blackbody flux incident on the disc decreases with radius as R^{-3}: a combination of distance from the star R^{-2}, and incidence angle to the disc surface R^{-1}. More specifically, it can be shown (e.g. Armitage 2015) that

$$F_{\rm abs} \propto \sigma T_{\star,\rm eff}^4 \left(\frac{R}{R_\star}\right)^{-3}, \tag{1.13}$$

where σ is the Stefan-Boltzmann constant, $F_{\rm abs}$ is the stellar flux absorbed by the disc, $T_{\star,\rm eff}$ is the effective temperature of the protostar and $R_\star$ is the radius of the protostar. If one assumes that the disc radiates as a blackbody, then the emitted flux is

$$F_{\rm emm} \propto \sigma T_{\rm disc}^4, \tag{1.14}$$

and this can be combined with Equation 1.13 to give

$$T_{\rm disc}(R) \propto T_{\star,\rm eff} \left(\frac{R}{R_\star}\right)^{-3/4}. \tag{1.15}$$

Re-examining the pressure scale height, it is noted that $H \propto T^{1/2}$ and $H \propto R^{-3/2}$ from the sound speed and Keplerian frequency, respectively. Inserting the obtained temperature profile here yields $H \propto R^{-1/4+3/2} \propto R^{5/4}$. The aspect ratio of the disc is then $H/R \propto R^{1/4}$, which increases with radius and so discs are flared. Flared discs receive a greater flux from their central protostar than flat discs, thus $T \propto R^{-3/4}$ is the steepest profile expected for passive discs. In fact, the possibility of flared discs was first presented by Kenyon & Hartmann (1987), who observed that the spectral energy distributions of T-Tauri discs did not match a profile for a flat disc.

Discs which are actively accreting generate heat through viscous dissipation. They

undergo differential rotation, with material moving inward as angular momentum is transferred outward (see Section 1.4.1). It can be shown that half of the gravitational potential energy lost from material moving inward is used to heat the disc. If this energy is radiated away as blackbody radiation between an annulus R and $R + \Delta R$ from both sides of the disc, where mass flows inward at a rate $\dot{M}$, then

$$\frac{1}{2}\frac{GM_\star \dot{M}}{R}\frac{\Delta R}{R} \simeq 4\pi R \Delta R \sigma T_{\rm disc}^4(R). \tag{1.16}$$

This can be rearranged to give

$$T_{\rm disc} \simeq \left(\frac{GM_\star \dot{M}}{8\pi\sigma R^3}\right)^{1/4}, \tag{1.17}$$

or more simply, $T_{\rm disc}(R) \propto R^{-3/4}$. The radial temperature profiles have the same form for both passive and active discs! In the former case, the temperature is regulated by the protostellar effective temperature. In the latter, the temperature is regulated by the accretion rate through the disc.

1.4 Evolution of circumstellar discs

Circumstellar discs evolve subject to an array of processes, including gravitational and magnetorotational instability, viscous accretion, dust accretion and midplane settling, and photoevaporation. Figure 1.3 schematically shows where such processes occur in the disc.

1.4.1 Viscous evolution

As a first order approximation one can assume thin-disc viscous evolution (e.g. see Pringle (1981)). By also making the assumption that the gravitational potential of the system remains constant (and hence $\mathrm{d}\Omega/\mathrm{d}t = 0$), it can be shown (e.g. Frank et al.

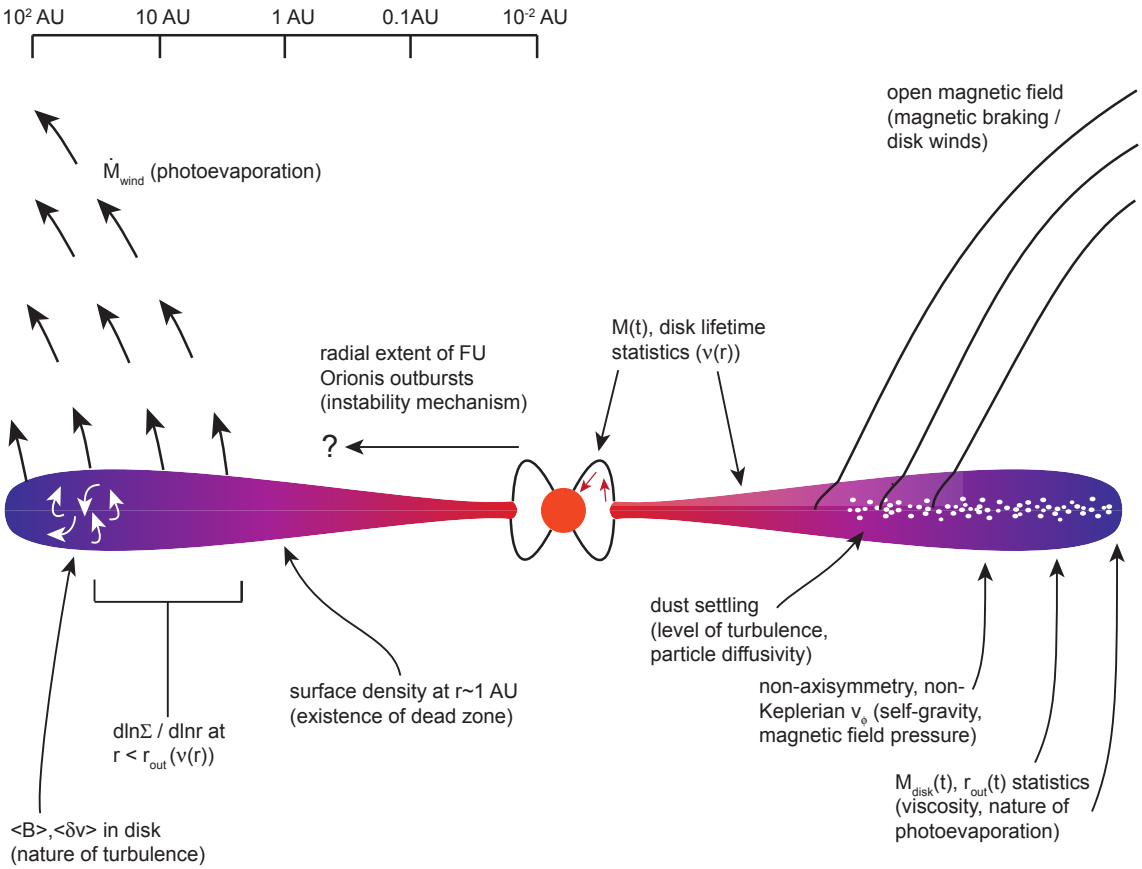

Figure 1.3: Schematic view of a circumstellar disc and the processes that occur within the system. Early on, material is accreted onto the disc from the natal envelope, increasing disc mass and causing instabilities. Later on material is lost due to photoevaporation while dust settles into the midplane. Eventually the gaseous disc dissipates completely. Turbulence exists throughout its evolution providing an effective viscosity. Taken from Armitage (2011).

2002; Armitage 2011) that the surface density evolves as

$$\frac{\partial \Sigma}{\partial t} = \frac{3}{R}\frac{\partial}{\partial R}\left[R^{1/2}\frac{\partial}{\partial R}\left(\nu\Sigma R^{1/2}\right)\right], \tag{1.18}$$

where ν is the kinematic viscosity. From this, a radial velocity can be determined such that

$$v_r = -\frac{3}{\Sigma R^{1/2}}\frac{\partial}{\partial R}\left(\nu\Sigma R^{1/2}\right). \tag{1.19}$$

The material in the inner region migrates inward and accretes onto the central protostar whereas the material in the outer region gains angular momentum resulting in disc expansion.

A typical parameterisation of viscosity is the α-prescription (Shakura & Sunyaev 1973), where viscosity is controlled by a dimensionless parameter α. The viscosity is set to depend on the sound-speed and scale-height of the disc so that

$$\nu = \alpha H c_s. \tag{1.20}$$

Typically, $\alpha = 10^{-4} - 10^{-1}$ estimated from stellar accretion evolution of young stellar objects (Hartmann et al. 1998), or via the fitting of models to single systems (Hueso & Guillot 2005).

1.4.2 Photoevaporation

Protoplanetary discs not only lose their mass through accretion processes (e.g. viscously), but also through magnetic driven jets and winds, as well as photoevaporation from the central protostar and other nearby massive stars. Dissipation by photoevaporation can occur rapidly in comparison to the lifetime of the disc: $\sim 10^5$ yrs (Simon & Prato 1995; Wolk & Walter 1996; Clarke et al. 2001) compared to $5 \times 10^6 - 10^7$ yrs (Strom et al. 1989; Wyatt 2008). Photoevaporation is the process whereby the

surface of a disc is heated by X-ray, EUV, and FUV radiation to a few 10^3 K, at which point the material is stripped away (e.g. Alexander et al. 2014) at subsonic velocity (Owen et al. 2012; Gorti et al. 2015).

Early in the lifetime of a circumstellar disc the mass accretion throughout the disc due to angular momentum transfer is greater than that of mass loss from photoevaporation, which is typically $\sim 10^{-10}$ $M_\odot$ yr^{-1}. Eventually the mass loss due to photoevaporation dominates and gaps form within the disc where material cannot be replenished (e.g. Clarke et al. 2001). Material exterior to a gap cannot flow inward and so a cavity forms around the central star. The subsequent irradiation of the inner rim of the disc then tends to lead to rapid dispersal of the outer disc, on the order of 10^5 yrs Alexander et al. (2006a,b); Haworth et al. (2016b). Similarly, gaps formed from giant planets can yield the same outcome (Rosotti et al. 2013). Figure 1.4 shows this process schematically.

The energy of the incident photons is dependent on the accretion rate onto the central star: at $\dot{M}_\star < 10^{-6}$ $M_\odot$ yr^{-1}, the disc is heated by hard X-ray and far UV photons, and at $\dot{M}_\star < 10^{-9}$ $M_\odot$ yr^{-1} by soft X-ray and extreme UV photons (Gorti et al. 2009). Thus the energy spectrum of emitted stellar radiation varies over time (e.g. Ercolano et al. 2009; Owen et al. 2012), and along with dependencies on disc mass, radius and viscosity as well as stellar mass, can result in photoevaporative mass loss rates of $10^{-11} - 10^{-7}$ $M_\odot$ yr^{-1} for stars with mass $\sim 0.1 - 3$ $M_\odot$.

Similarly, a disc may be irradiated by an external field whose strength is typically quantified by the Habing unit G_0 (Habing 1968) which has a value 1.6×10^{-3} erg s^{-1} cm^{-2} and is a measure of UV flux. Protoplanetary discs in the Orion nebula are subject to an external radiation field of $\sim 5 \times 10^4 - 2 \times 10^7$ G_0 (Störzer & Hollenbach 1999) due to an association of nearby O-stars. These brightly illuminated discs (coined *proplyds*) are well studied and exhibit photoevaporative flows, the observations of which agree well with models (e.g. O'Dell et al. 1993; McCaughrean & O'Dell 1996; Johnstone et al.

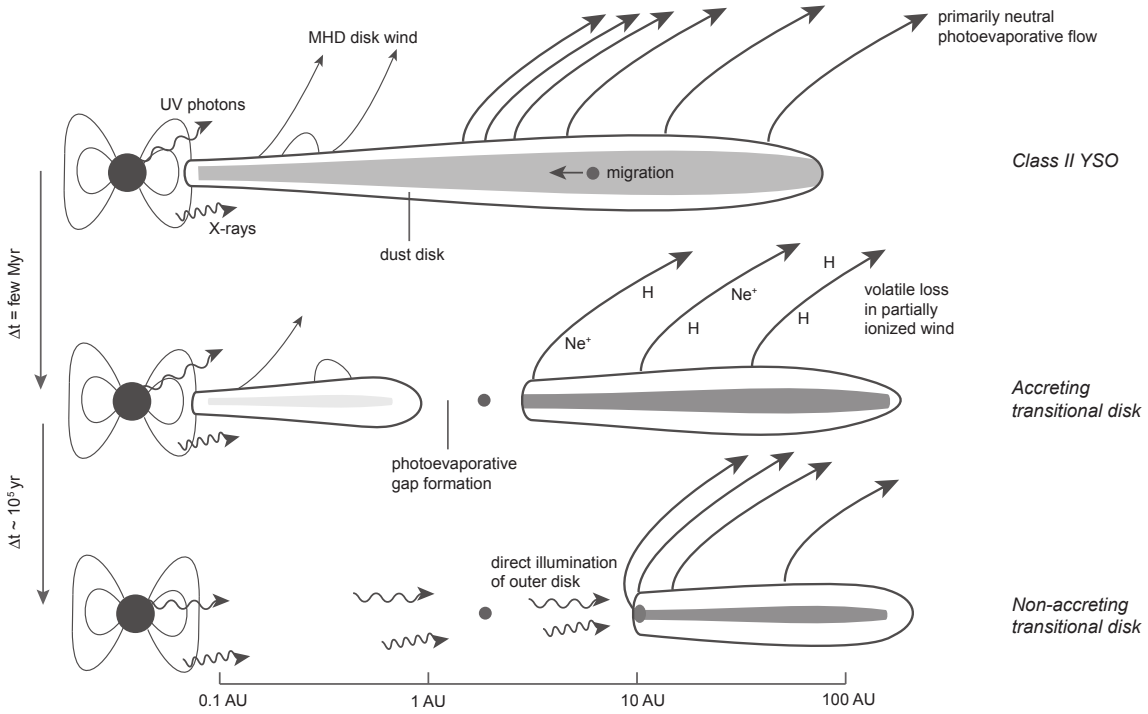

Figure 1.4: A schematic representation of photoevaporation from the central protostar. Early on in the lifetime of a circumstellar disc, active accretion causes material to move inward at a rate where the lost material due to photoevaporation is replenished. Once accretion reduces such that the mass loss rate from photoevaporation becomes dominant, gaps can form thus preventing outer material from drifting inward. As such, a large cavity forms around the central star and radiation incident on the inner rim of the remaining disc causes it to rapidly disperse. Taken from Alexander et al. (2014).

1998; Bally et al. 2000; Mesa-Delgado et al. 2012; Eisner et al. 2016, 2018). However, it may not only be within highly extreme environments that photoevaporative winds can be driven (e.g. Scally & Clarke 2001; Adams et al. 2004; Holden et al. 2011; Haworth et al. 2016a). Theoretical models show that for discs of size $R > 150$ AU, mass loss rates can exceed 10^{-8} $M_\odot$ yr when subject to a ~ 30 G_0 field (Facchini et al. 2016). In fact, observations of proplyds in NGC 1977 have demonstrated that photoevaporation can yield mass loss rates of $\sim 10^{-9} - 10^{-8}$ $M_\odot$ yr^{-1} in ~ 3000 G_0 regions (Kim et al. 2016). Additionally, the protoplanetary disc IM Lup (Cleeves et al. 2016) may exhibit mass loss rates of $\sim 10^{-8}$ $M_\odot$ yr (comparable to the stellar accretion rate) in a very low radiation field of 4 G_0 (Haworth et al. 2017). Although it was typically thought that externally driven photoevaporation only occurred in energetic regions, for example in the vicinity of an O-star association, it may be that it is a much more robust phenomenon. However, this may only apply to discs that are extended enough to receive a sufficient amount of stellar flux, and surround a low-mass protostar such that the disc material is only marginally gravitationally bound.

The formation and evolution of planets may also be affected by photoevaporation. Photoevaporation provides a limit on disc lifetime and also affects planetary orbital properties. Provided a disc has evolved long enough such that a large proportion of its dust content has settled to the midplane, Throop & Bally (2005) suggest that UV radiation can drive gas rich outflows and increase the dust-to-gas mass ratio of the disc, thus enhancing planet formation. Indeed, Gorti et al. (2015) find that dust particles remain in the disc during photoevaporation. Additionally, the rate of planetary migration (discussed in Section 1.4.3) can be inhibited or promoted depending on the radial position of gaps formed by photoevaporation. This could lead to preferential final semi-major axes of planets, and may explain the swathe of detected ~ 1 M_J exoplanets at ~ 1 AU (Alexander & Armitage 2009; Alexander & Pascucci 2012; Ercolano & Rosotti 2015). Wise & Dodson-Robinson (2018) performed 2D simulations, both

with and without photoevaporation, and found only small differences in how giant planets migrate between the two cases. The study however does not cover a wide range of planet masses, formation radii or disc properties.

1.4.3 Disc-planet interaction

Massive planets on short-period orbits (known as hot Jupiters, $P < 10$ days) present a problem for *in-situ* models of planet formation. These planets typically have cores of mass $M_{\rm core} > 10$ $M_\oplus$ (Goldreich et al. 2004; Chiang & Laughlin 2013), and as such, cannot form within the disc lifetime as there is not a sufficient mass reservoir of ice in the inner disc region. Efficient dust growth requires icy grains which are only present outside of the water snow line, typically at a few AU (Kennedy & Kenyon 2008; Martin & Livio 2012, 2013). Furthermore, the formation of a planet through gravitational fragmentation is unlikely to happen at small radii within the disc where the temperature is high (see Section 1.5). As such, it is expected that hot Jupiters form in the cold, outer region of the disc and subsequently migrate inwards to their final orbital radii.

Planetary migration is classified in two main types: type-I is the migration of low-mass planets which do not open a gap in the disc and type-II is the migration of high-mass planets which do carve a gap. Type-I migration does not alter the global disc structure dramatically, but spiral density waves do arise due to the differential velocity shearing. The inner and outer spirals result in Lindblad torques which compete to affect the radial position of the planet. The inner spirals generate a positive torque, increase the planet's angular momentum and cause outward migration. The outer spirals act to cause the opposite effect. Typically, the planet is driven inwards (Ward 1997), though the direction of migration is dependent on disc viscosity, opacity and thermodynamical properties (Paardekooper & Mellema 2006; Duffell & Chiang 2015).

A planet must carve a gap within the disc to undergo type-II migration. The gap

opening criteria are thus: the Hill radius of the planet must exceed the disc scale height of the disc (Ward 1997), and the viscous effects in the disc must not be strong enough to close the gap. The former of these criteria (assuming a circular orbit) can be expressed as

$$R_{\rm Hill} = R_{\rm p}\left(\frac{M_{\rm p}}{3M_\star}\right)^{1/3} \geq H, \tag{1.21}$$

where $R_{\rm p}$ and $M_{\rm p}$ are the planet orbital radius and mass, respectively. This can be rearranged to give a planet-to-star mass ratio q such that

$$q = \frac{M_{\rm p}}{M_\star} \geq 3\left(\frac{H}{R_{\rm p}}\right)^3. \tag{1.22}$$

Given typical values of disc aspect ratio $H/R \approx 0.05$ and stellar mass $M_\star \approx 1\ {\rm M}_\odot$, the minimum planet mass for gap opening is $0.4\ {\rm M}_{\rm J}$. The viscous criterion for gap formation (Lin & Papaloizou 1993) is

$$q \geq \frac{40\nu}{R_{\rm p}^2\Omega_{\rm p}} = \frac{40\alpha c_s H}{R_{\rm p}^2\Omega_{\rm p}}, \tag{1.23}$$

where the right-hand side is obtained using Equation 1.20. This can be simplified further to give

$$M_{\rm p} > 40M_\star\alpha\left(\frac{H}{R_{\rm p}}\right)^2. \tag{1.24}$$

For typical values of disc aspect ratio $H/R \approx 0.05$, stellar mass $M_\star \approx 1\ {\rm M}_\odot$ and $\alpha = 10^{-2}$, the minimum planet mass for keeping a gap open is $1\ {\rm M}_{\rm J}$. However, this ignores the effect of thermal pressure. Crida et al. (2006) performed numerical simulations to determine a consolidated gap opening criterion which has the form

$$\frac{3}{4}\frac{H}{R_{\rm Hill}} + \frac{50}{q{\rm Re}} \lesssim 1, \tag{1.25}$$

where the Reynolds number Re is

$$\mathrm{Re} = \frac{\Omega_\mathrm{p} R_\mathrm{p}^2}{\nu}. \tag{1.26}$$

The depth of a gap is determined by the planetary mass, the disc scale height and the disc viscosity (e.g. Duffell & MacFadyen 2013; Kanagawa et al. 2015b,a) such that

$$\frac{\Sigma_\mathrm{min}}{\Sigma_0} = \frac{1}{1+0.04K}. \tag{1.27}$$

The dimensionless quantity K is defined as

$$K = \left(\frac{M_\mathrm{p}}{M_\star}\right)^2 \left(\frac{H}{R_\mathrm{p}}\right)^{-5} \frac{1}{\alpha}. \tag{1.28}$$

Thus, a higher mass planet opens up a deeper gap. The disc's thermodynamical properties play a key role too, as they control the disc scale height. The migration timescale after the planet has carved a gap is that of the disc viscous timescale (dependent on the stellar mass only). If the planet is massive enough the migration may be slower.

1.5 Gravitational instability

Gravitational instability leads to the formation of spiral features, and possibly the formation of dense clumps within circumstellar discs. The onset of the gravitational instability can be quantified by considering the balance between the disc gravity and the combination between rotational and thermal support. This can be expressed by the Toomre stability criterion Q (Toomre 1964) where

$$Q = \frac{\kappa c_s}{\pi G \Sigma}. \tag{1.29}$$

The rotational support is represented by the epicyclic frequency κ, which can be approximated to the Keplerian frequency Ω. The sound speed, $c_s \propto T^{1/2}$ acts to thermally stabilise the disc. Gravity, represented by the column density Σ, acts to destabilise the disc. In the razor-thin disc approximation a disc may become gravitationally unstable provided $Q < 1$. However, in 3-dimensional discs the critical Toomre value may be $Q < 1.4$ (Durisen et al. 2007), and the disc could fragment provided $Q < 0.6$ (Takahashi et al. 2016).

The Toomre criterion can also be expressed in a context relating to the structure of a circumstellar disc. The mass interior to a radius R within the disc is approximately $\pi R^2 \Sigma$. Recall that the scale-height of the disc can be written $H = c_s/\Omega$, thus the Toomre criterion becomes

$$\frac{M_{\rm in}}{M_\star} \gtrsim \frac{H}{R}. \tag{1.30}$$

If one considers the whole disc such that $R = R_{\rm out}$ and $M_{\rm in} = M_{\rm disc}$, then discs are stable when the disc-to-star mass ratio is small. Thus a disc may only undergo gravitational instability when its mass is comparable to that of the central protostar. This would occur early on in the disc lifetime when the disc is relatively massive. At this stage, the disc is embedded within, and actively accreting from its parent cloud (i.e. in the Class 0 or Class I phase). Observing the gravitational instability may therefore be difficult due to the presence of the surrounding envelope.

The young, 1 Myr old star Elias 2-27, which has a mass of $0.5-0.6$ $M_\odot$ (Luhman & Rieke 1999; Natta et al. 2006), hosts a Class II and relatively massive circumstellar disc, where $M_{\rm disc} = 0.04-0.14$ $M_\odot$ (Andrews et al. 2009; Isella et al. 2009; Ricci et al. 2010). ALMA observations indicate that the system possesses two large-scale spiral arms (Pérez et al. 2016), shown in Figure 1.5. It has recently been considered that the spiral features may exist due to gravitational instability in the disc (Meru et al. 2017; Tomida et al. 2017). Meru et al. (2017) also consider the scenario whereby the spiral arms are driven by a massive companion external to the spirals. The structure of the

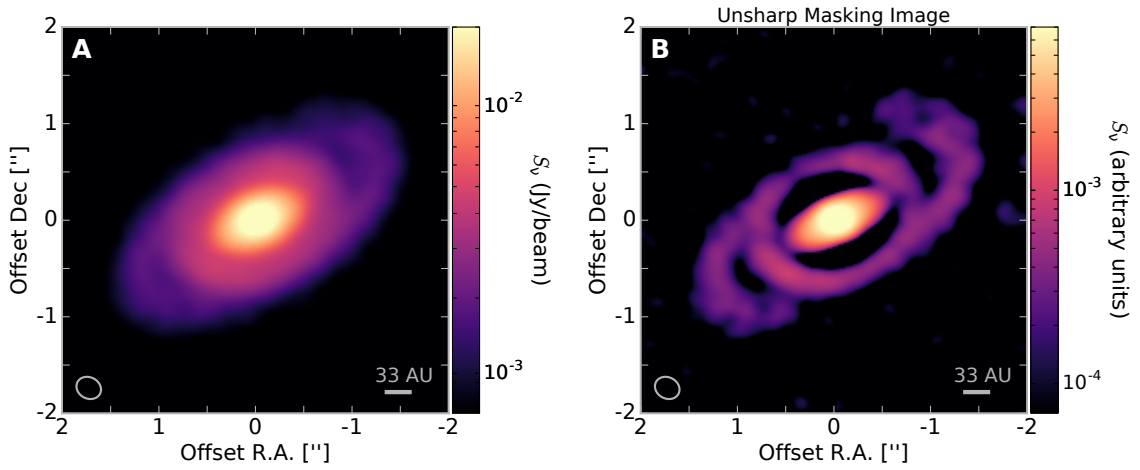

Figure 1.5: Thermal dust emission of the disc surrounding Elias 2-27 observed at 1.33 mm with ALMA. The right hand panel has an increased contrast with an unsharp masking filter applied, highlighting the spiral features of the system. Taken from Pérez et al. (2016).

spirals is analysed by Forgan et al. (2018) who demonstrate that the spirals are best fit with models which consider a constant pitch angle (see Figure 1.6). Importantly, an external companion cannot produce such a fit, so the spirals may well be driven by gravitational instability, and Elias 2-27 could be a circumstellar system exhibiting this phenomenon.

Spiral arms generated by gravitational instability may be a primary driver of angular momentum transfer within protostellar discs (see also Section 1.6). The outward transfer of angular momentum allows the material within the disc to migrate radially inward and ultimately accrete onto the central protostar. A spiral arm may evolve non-linearly and fragment into bound objects. If a region obeys $Q < 1$ and cools efficiently such that $t_{\rm cool} < (0.5-2)t_{\rm orb}$ where $t_{\rm orb}$ is the local orbital period (Gammie 2001; Johnson & Gammie 2003; Rice et al. 2003b, 2005), a dense clump may form and subsequently collapse under gravity. Without efficient cooling, a dense clump may not undergo gravitational collapse due to the large degree of supporting thermal pressure. In the last few years, the validity of this cooling criterion has been scrutinized, and it has been suggested that fragmentation may happen for even slower cooling

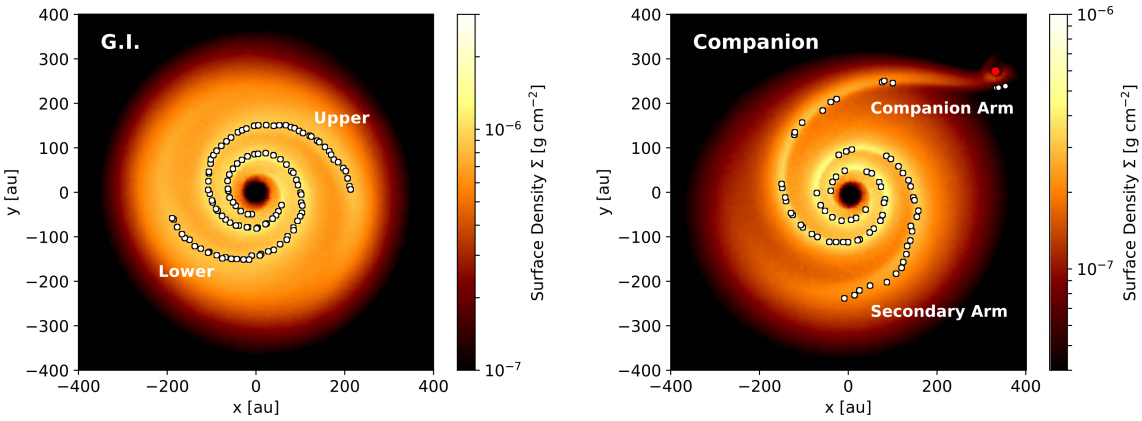

Figure 1.6: Surface density plots of two snapshots from simulations modelling the Elias 2-27 circumstellar disc. Left panel: a simulation where the spiral arms are generated by gravitational instability. Right panel: a simulation where the spiral arms are being excited by an external companion (red point). White points indicate spiral identification. The spirals generated by gravitational instability are best fit to a model with constant pitch angle. Taken from Forgan et al. (2018).

rates (Meru & Bate 2011; Paardekooper et al. 2011; Lodato & Clarke 2011; Rice et al. 2012; Tsukamoto et al. 2015). However, irrespective of the detailed criteria, there has been significant observational evidence that disc fragmentation does occur (Tobin et al. 2013a, 2016; Dupuy et al. 2016).

Object formation through gravitational instability is of great importance: it may be a mechanism for forming massive planets, brown dwarfs and low-mass hydrogen burning stars (e.g. Whitworth & Stamatellos 2006; Stamatellos et al. 2007a; Boley 2009; Stamatellos & Whitworth 2009b; Kratter et al. 2010; Zhu et al. 2012; Lomax et al. 2014; Kratter & Lodato 2016; Vorobyov 2013). Figure 1.7 shows Keck JHK-band combined observations of the HR 8799 system (Marois et al. 2010). With the light from the central star removed, four companions are detected. They orbit at radii of 15, 24, 38 and 68 AU and have masses between 5 and 10 M_J. These planetary companions may have formed via gravitational fragmentation (see Section 1.7.2).

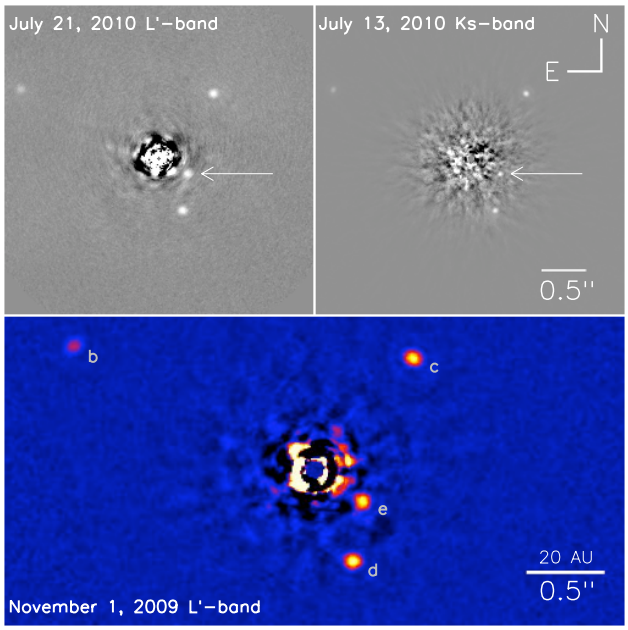

Figure 1.7: Keck image of the HR 8799 planetary system (Marois et al. 2010). The companions b, c, d and e have masses between 5 and 10 M_J and orbit around HD 9799a at 68, 38, 24, and 15 AU, respectively. Gravitational fragmentation may have been the formation mechanism for these objects.

1.6 Magnetorotational instability

The magnetorotational instability (MRI henceforth) was first conceived by Velikhov (1959) and Chandrasekhar (1960). Balbus & Hawley (1991) first presented the relevance of the instability in the context of astrophysical accretion discs. In a typical circumstellar disc, the viscous dissipation timescale considering molecular viscosity alone is very long. Therefore some process must act to transport angular momentum radially outwards more efficiently, allowing material to move inward and accrete onto the central star within the required timeframe. In Section 1.5, I discussed one process to drive accretion, the gravitational instability. However, this requires the fulfillment of the Toomre criterion within a region of the disc. On the other hand, the MRI is activated provided the disc has some degree of ionisation and is threaded by a weak magnetic field.

Consider two particles threaded by the same magnetic field line, separated slightly

in the vertical plane. Shear flow can perturb the particles and put them on slightly different radial orbits such that the inner particle travels at a higher velocity than the outer. The magnetic field line is stretched as they differentially rotate (see Figure 1.8). The magnetic tension acts to restore equilibrium by straightening the field line and as it does so, the inner faster particle transfers some of its angular momentum to the outer particle. Thus the inner particle moves inwards and the outer particle outwards. The evolution is non-linear, but the instability can be suppressed if the magnetic field becomes sufficiently strong.

The MRI can only be onset provided there exists a sufficient level of ionisation at the disc surface due to stellar irradiation and cosmic rays, or deeper within the disc due to radionuclides (Gammie 1996). However, there is a region in the disc midplane where the level of ionisation is expected to be too low; this region is known as the dead-zone. Zhu et al. (2009a) present work which combines the effects of the gravitational instability and the MRI to explain the non-steady accretion onto protostars. They argue that the gravitational instability is active in the outer disc region and transports material efficiently into the inner disc, where it undergoes thermal ionisation and the MRI is onset.

1.7 Planet formation

The detection of thousands of extra-solar planets in recent years has demonstrated that not only is the planet formation process robust, but exoplanets have diverse properties. Ground based telescopes such as ESO-HARPS, Keck and WASP have been paramount in the exoplanet discovery process, with follow-up observations from space based telescopes such as Kepler, Spitzer and the Hubble Space Telescope. This has led to the observations of $> 3,500$ confirmed exoplanets (Schneider et al. 2011). It may be the fundamental formation process of planets itself which gives rise to certain divisions of exoplanet properties.

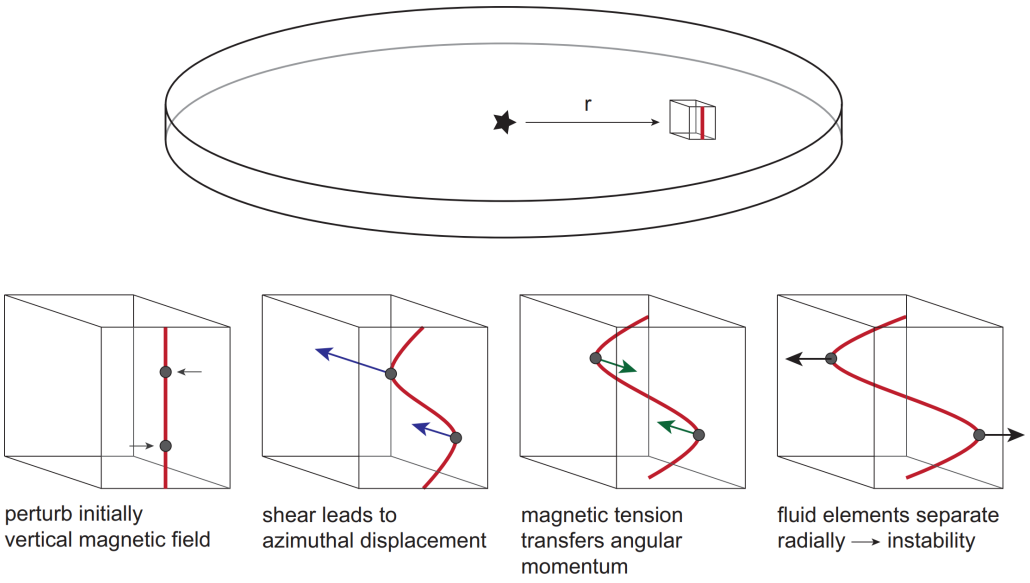

Figure 1.8: Schematic description of the magnetorotational instability where two ionised particles are threaded by the same weak magnetic field line. As the particles move, they stretch the magnetic line threading them. The magnetic field line then responds by straightening due to the restoring magnetic tension. This moves the inner particle inward and the outer particle outward. The net effect is the transfer of angular momentum outward. Taken from Armitage (2015).

1.7.1 Exoplanet detection

Various methods exist for the detection of planets each with their merits and limitations (see Wright & Gaudi (2013) and Fischer et al. (2014) for reviews). Until recently, the main technique of planet detection was Doppler spectroscopy, which measures the radial velocity of stars arising from the gravitational influence induced by the planet. The key issue with this method is that the measured Doppler velocity is dependent on the inclination of the planet. As such, the mass of an orbiting planet will be typically larger than measured: only $M_p \sin i$ can be found where i is the unknown inclination of the planet. There is also a bias toward high-mass planets orbiting close to the central star, as this increases the radial velocity of the star.

The largest number of exoplanets discovered to date have been done so through transits, i.e. the dimming of the star as the planet passes in front of it. The probability of a transit depends on the orientation of the orbit and the photometric detection

depends on the depth of the transit which is typically $[1, 0.1, 0.01]$% for Jupiter-sized, super Earth-sized and Earth-sized planets, respectively. Thus, evermore sensitive instrumentation is required to observe smaller and smaller planets. In order to observe multiple transits, the orbital period must be reasonably small, and so the planet must be close to the central star. The first observations of exoplanetary transits (Henry et al. 2000; Charbonneau et al. 2000) has motivated two decades of results, culminating in the discovery of terrestrial-sized planets (Léger et al. 2009; Batalha et al. 2011); multi-planet transiting systems (Lissauer et al. 2011; Gillon et al. 2016, 2017); and planets with temperatures similar to that of Earth (Deeg et al. 2010; Bonfils et al. 2018).

Figure 1.9 shows the distribution of planetary mass as a function of semi-major axis for confirmed exoplanets. Data were taken from the EU exoplanet archive[1].

1.7.2 Core accretion, gravitational fragmentation, or both?

Planets are formed within circumstellar discs where there exists a sufficient reservoir of gas and dust. There are two theories which aim to explain the formation of planets. The core accretion model (Safronov 1969; Goldreich & Ward 1973; Greenberg et al. 1978; Hayashi et al. 1985; Lissauer 1993) considers the agglomeration of dust and ice grains, which go on to form planetesimals and eventually rocky planets. Once the rocky core is formed, a period of rapid gas accretion (e.g. Pollack et al. 1996) may follow, leading to the formation of a giant gaseous planet. The alternative theory, gravitational fragmentation (Kuiper 1951; Cameron 1978; Boss 1997), involves the collapse of gravitationally unstable regions within protostellar discs. The process is rapid, typically forming massive $\gtrsim 2$ M_J planets, and is the result of the gravitational instability which develops within a disc.

Each theory requires certain conditions. For core accretion to occur, dust agglomeration must be rapid and overcome two barriers. The first of these barriers arises

[1] `exoplanet.eu` Last accessed 03/03/2019.

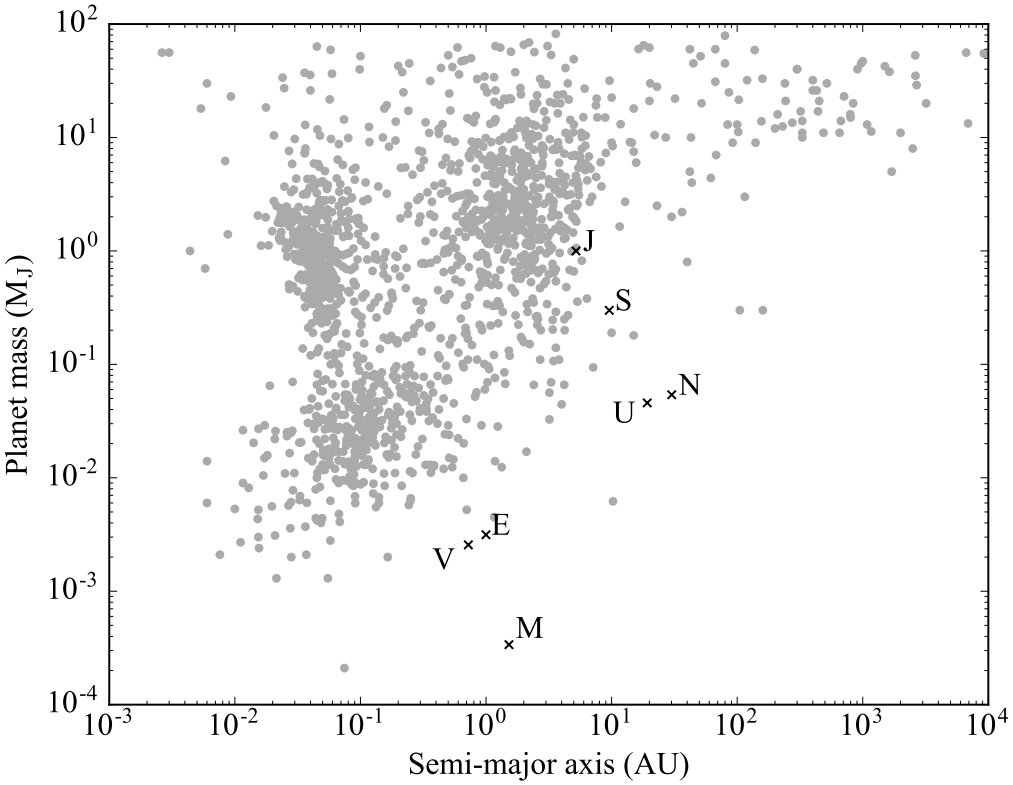

Figure 1.9: Confirmed exoplanet masses as a function of semi-major axis. Planets of the solar system are shown as black crosses. This demonstrates the large range of planetary masses and orbital properties. Data were retrieved from the EU exoplanet archive[1] (Schneider et al. 2011).

from the radial drift of dust (Adachi et al. 1976; Weidenschilling 1977; Laibe 2014). Small dust grains ($\sim$ 1 mm) couple to the gas efficiently, and may be accreted onto the central protostar before having the opportunity to grow. The fragmentation barrier (Blum & Wurm 2008) pertains to larger grains ($\sim$ 10 cm), which, instead of sticking to others during collision, fragment. The trapping of dust, which may be robustly self-induced (Gonzalez et al. 2017), could account not only for asymmetrical features observed within discs (e.g. van der Marel et al. 2013), but could also form ideal regions for rapid grain growth. Consequent planetesimal formation may occur due to further collisions or from gravitational collapse within the dust traps (Johansen et al. 2014; Levison et al. 2015). The planet formation timescale from core accretion is typically a few million years, possibly longer than the disc lifetime itself (Haisch et al. 2001; Cieza et al. 2007). This issue *may* be circumvented by the presence of local pressure maxima (Johansen et al. 2007), or by density perturbations caused by the streaming instability (Youdin & Goodman 2005).

The criteria for gravitational fragmentation are those discussed in Section 1.5, namely a Toomre parameter $Q \lesssim 1$ and efficient cooling. Fragmentation may occur naturally from the rapid cooling of spiral arms in isolated discs or driven by infall accretion from a surrounding cloud (e.g. Kratter et al. 2008). As gravitational instability only occurs in the colder outer disc (e.g. Stamatellos & Whitworth 2008), planets which form via fragmentation are typically super-Jovian, wide-orbit companions. The instability is also only thought to be onset in the early phases of protostellar discs i.e. when there is a large reservoir of gas available for accretion by planets. The inward migration of a planet (see Section 1.4.3) and subsequent accretion increases its mass such that it may become a brown dwarf ($M \gtrsim 13$ M$_\mathrm{J}$) or even a low-mass hydrogen-burning star ($M \gtrsim 80$ M$_\mathrm{J}$) (Stamatellos et al. 2007a; Stamatellos & Whitworth 2009b,a). The protostellar system L1448 IRS3B comprises a central pair of binary protostars (IRS3B-a and IRS3B-b) with a total mass 1 M$_\odot$, as well as a 0.085 M$_\odot$ companion (IRS3B-c).

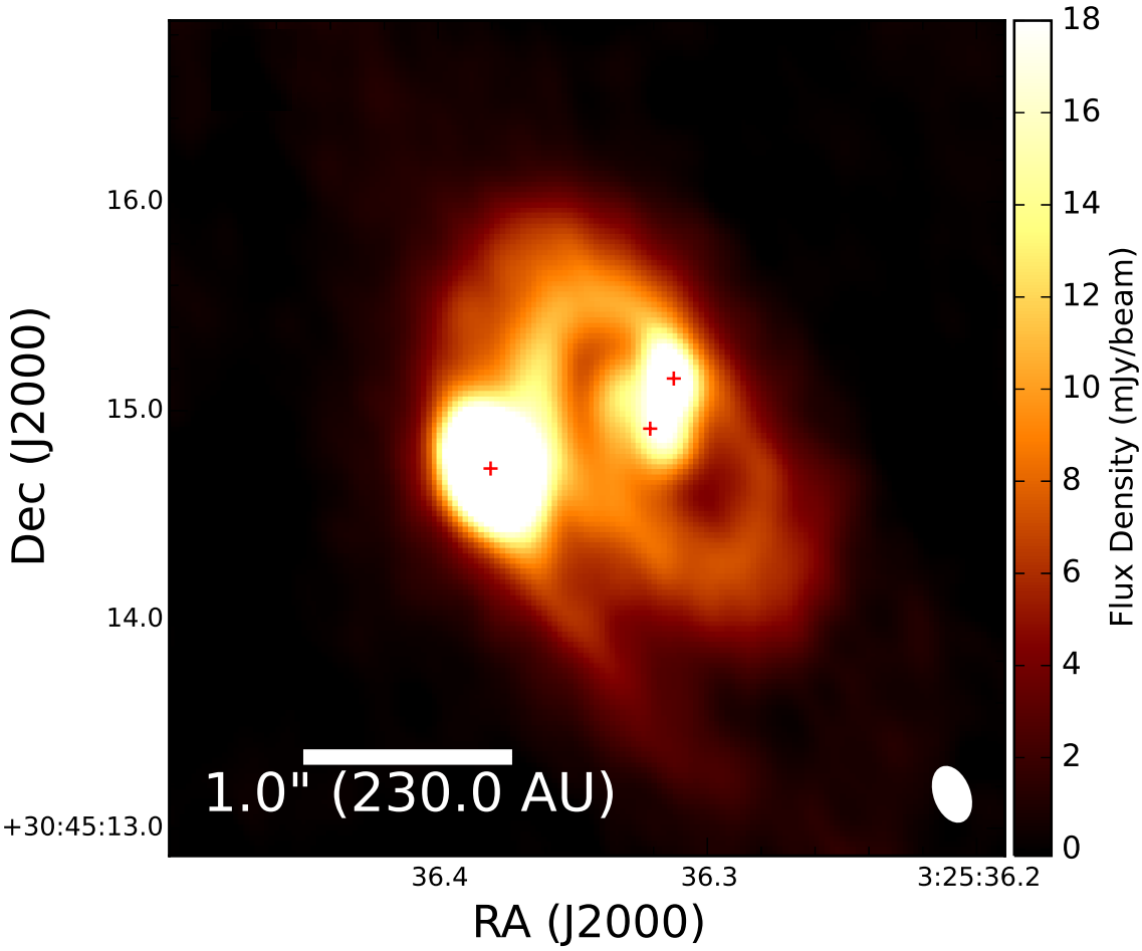

Figure 1.10: ALMA 1.33 mm image of the L1448 IRS3B triple protostellar system (Tobin et al. 2016). The central binary system is represented by the two close-by red crosses and have a combined mass 1 $M_{\odot}$. The third member of the system has a mass 0.085 $M_{\odot}$ and was likely formed through gravitational fragmentation.

The latter may be a candidate of disc fragmentation. Figure 1.10 shows an ALMA 1.33 mm image of the system with IRS3B-c on the left.

The tidal stripping of massive planets formed through gravitational fragmentation could ultimately lead to the formation of Earths and super-Earths (Nayakshin 2015a,b; Nayakshin & Fletcher 2015; Nayakshin 2016). Therefore it may be that both theories discussed in this section contribute to the planetary population.

1.8 Thesis outline

This thesis focuses on the gravitational instability within protostellar discs, the necessary conditions for it to happen and the effects it can have on the evolution of young protostellar systems. Chapter 2 introduces the computational techniques used within this work. I describe the fundamentals of smoothed particle hydrodynamics, explaining its relevance to the studies herein as well as some modern implementations which improve upon the method. Following this, I discuss how thermodynamics is treated, including the radiative feedback from accreting objects and how the thermal properties of a system evolve. A model of episodic accretion is then outlined, which, combined with radiative feedback allows the self-consistent inclusion of thermal effects from accretion outbursts. The chapter ends with a brief introduction to the numerical codes SEREN and GANDALF. The work in Chapter 3 is an investigation into the formation of objects due to disc fragmentation, a consequence of the gravitational instability. Specifically, I determine how the heat generated from accretion onto these objects affects subsequent disc evolution. In Chapter 4 I compare methods of radiative transfer in multiple disc configurations including unstable and fragmented discs. The accuracy of each method is determined and compared to a simple approach with parameterised cooling. As the gravitational instability is sensitive to the thermal properties of a disc, I also discuss the effect of each method on disc stability. Chapter 5 concerns the study of the gravitational fragmentation of discs around M-dwarf stars. I determine the minimum mass for fragmentation for a variety of disc and stellar properties. Additionally, I discuss the properties of the formed clumps/protoplanets formed by fragmentation. The work presented in this thesis is summarised in Chapter 6.

Chapter 2

Computational techniques

2.1 Smoothed particle hydrodynamics

Numerically solving the equations of fluid dynamics for star and planet formation studies requires a technique that can handle a large dynamic range, both spatially and temporally. An inherently adaptive method therefore lends itself ideally to this problem. Smoothed particle hydrodynamics (SPH henceforth), developed independently by Gingold & Monaghan (1977) and Lucy (1977), utilises interpolation points which follow a fluid and probe its properties. These points are generally referred to as SPH particles and each has an associated mass. They are smoothed over a scale length h via a weighting function $W(\boldsymbol{r},h)$ which are referred to as the smoothing length and smoothing function (or smoothing kernel), respectively. This allows the representation of a continuous fluid with a discrete set of particles.

To form the basis of SPH, note that the integral interpolant of a function $f(\boldsymbol{r})$ over a volume V is

$$f(\boldsymbol{r}) = \int_V f(\boldsymbol{r}')W(\boldsymbol{r}-\boldsymbol{r}',h)\,\mathrm{d}V, \tag{2.1}$$

where the smoothing function is normalised so that

$$\int_V W(\boldsymbol{r}-\boldsymbol{r}',h)\,\mathrm{d}V = 1. \tag{2.2}$$

In the limit $h \to 0$ the smoothing function becomes the Dirac delta function. Equation 2.1 can be discretised given a set of particles by replacing the volume element with particle mass and density to give the value of property f at the location of particle i,

$$f(\boldsymbol{r}_i) \approx \sum_{j=1}^{N} f(\boldsymbol{r}_j)\frac{m_j}{\rho_j} W\left(\left|\boldsymbol{r}_i-\boldsymbol{r}_j\right|,h\right), \tag{2.3}$$

where the sum is over neighbouring particles j. The density estimate, and also the continuity equation for SPH, is obtained by substituting $f(\boldsymbol{r})$ with density $\rho(\boldsymbol{r})$. Hence

$$\rho_i = \sum_{j=1}^{N} m_j W(\boldsymbol{r}_{ij},h), \tag{2.4}$$

which has the spatial derivative

$$\frac{\partial \rho_i}{\partial \boldsymbol{r}_i} = \sum_{j=1}^{N} m_j \nabla_i W(\boldsymbol{r}_{ij},h). \tag{2.5}$$

The substitutions $\boldsymbol{r}_{ij} = \boldsymbol{r}_i - \boldsymbol{r}_j$ and $\nabla_i = \partial/\partial \boldsymbol{r}_i$ have been made for convenience. The SPH fluid equations can be derived from the Euler-Lagrange equations which guarantee the conservation of momentum, angular momentum, and energy. This can be achieved using the SPH form of the continuity equation stated above, as well as the first law of thermodynamics. Doing so yields the basic forms of the SPH momentum equation

$$\frac{\mathrm{d}\boldsymbol{v}_i}{\mathrm{d}t} = -\sum_{j=1}^{N} m_j \left(\frac{P_i}{\rho_i^2}+\frac{P_j}{\rho_j^2}\right)\nabla_i W(\boldsymbol{r}_{ij},h), \tag{2.6}$$

and energy equation

$$\frac{\mathrm{d}u_i}{\mathrm{d}t} = \frac{P_i}{\rho_i^2} \sum_{j=1}^{N} m_j \boldsymbol{v}_{ij} \cdot \nabla W(\boldsymbol{r}_{ij}, h). \tag{2.7}$$

The formulation of these equations requires a constant smoothing length h and assumes that there is no dissipation. Gravity is also not taken into account in the momentum equation. These points are revisited in later sections, whilst the final equations are summarised in Section 2.1.8.

The benefits of the Langrangian nature of SPH over Eulerian grid techniques are realised when considering diverse systems. Computational expense is reduced in low density regions where there are few particles. In high density regions, the resolution is necessarily increased as particles follow the fluid. Grid-based approaches instead require continuous adaptive refinement to resolve dense regions.

2.1.1 Smoothing function

The summation across N particles results in $\mathcal{O}(N^2)$ computational cost and so particle properties are calculated based on a much smaller set of neighbour particles N_{neigh}, attained by truncating the smoothing function (typically at some multiple of h). The smoothing function that is adopted for the work presented in this text is the M_4 cubic B-spline kernel (Schoenberg 1946) truncated at $2h$. It has the functional form

$$W(\boldsymbol{r}_{ij}, h) = \frac{\sigma}{h^d} \begin{cases} \frac{1}{4}(2-q)^3 - (1-q)^3, & 0 \leq q < 1; \\ \frac{1}{4}(2-q)^3, & 1 \leq q < 2; \\ 0, & q \geq 2, \end{cases} \tag{2.8}$$

where $q = \boldsymbol{r}_{ij}/h$. Thus, particles outside $2h$ are not considered. The dimensionality of the system is denoted d and σ is a normalisation constant where $\sigma = [2/3, 7/10\pi, 1/\pi]$ in $[1, 2, 3]$ dimensions, respectively. The benefits of this kernel are thus: it is symmetric hence gives a good density estimate, it is twice continuously differentiable, and itself

and its gradient are computationally inexpensive to calculate. Increasing the number of neighbours indeed yields a more accurate density estimate but at the cost of computational expense, and more importantly can lead to the pairing instability when using B-spline kernels. The pairing instability is the result of the negative maximum in the spatial derivative of B-spline kernels, where for the M_4 kernel, mutual forces between particles tend to zero when placed closer than $\sim (2/3)q$ apart. This leads to the particles essentially forming a pair. The number of neighbours at which this occurs is greater than $55-58$ (Dehnen & Aly 2012; Price 2012). A family of kernels which incorporate all desirable properties that do not instigate the pairing instability are the Wendland kernels (Wendland 1995). With a low number of neighbours, the density estimate is inaccurate compared to B-spline kernels and so a large number of neighbours is necessary.

2.1.2 ∇h conservative scheme

A constant smoothing length is not suitable within systems which have large density ranges. Consider a particle which has a small smoothing length due to being within a dense region, that moves into a low density region. Its smoothing length is still small and thus neighbours may not be captured within its smoothing kernel. A similar issue exists for the opposite effect, wherein a particle may have many neighbours thus wasting computational time. By assigning a variable smoothing length to each particle, spatial resolution can be increased considerably (Hernquist & Katz 1989; Benz 1990). Typically one sets the smoothing length to a function of density such that

$$h_i = \eta \left(\frac{m_i}{\rho_i} \right)^{1/d}. \tag{2.9}$$

Here, d represents the number of dimensions and η controls the mean number of neighbours, which depends on the dimensionality. In 3-dimensional space the smoothing length of a particle is

$$h_i = \left(\frac{3 N_{\text{neigh}} m_i}{32 \pi \rho_i} \right)^{1/3}. \tag{2.10}$$

Due to the interdependence of ρ and h (see Equation 2.4), an iterative procedure (e.g. Newton-Raphson) is employed until a chosen convergence criterion is met. The temporal variability of the smoothing length can be found by taking the time derivative of Equation 2.9 to obtain

$$\frac{\mathrm{d}h_i}{\mathrm{d}t} = -\frac{h_i}{\rho_i d} \frac{\mathrm{d}\rho_i}{\mathrm{d}t}. \tag{2.11}$$

To calculate this fully, one can take the Lagrangian time derivative of Equation 2.4 and get

$$\frac{\mathrm{d}\rho_i}{\mathrm{d}t} = \frac{1}{\Omega_i} \sum_{j=1}^{N} m_j \boldsymbol{v}_{ij} \cdot \nabla_i W\left(\boldsymbol{r}_{ij}, h_i\right). \tag{2.12}$$

Ω_i is a dimensionless parameter that corrects for any spatial variability in h which, when included, conserves energy and entropy (Nelson & Papaloizou 1993, 1994; Serna et al. 1996). This factor has the form

$$\Omega_i = 1 - \frac{\partial h_i}{\partial \rho_i} \sum_{j=1}^{N} m_j \frac{\partial W_{ij}}{\partial h_i}(\boldsymbol{r}_{ij}, h_i). \tag{2.13}$$

The resulting momentum and energy equations with the correction term taken self-consistently into consideration can be shown (Springel & Hernquist 2002) to be

$$\frac{\mathrm{d}\boldsymbol{v}_i}{\mathrm{d}t} = -\sum_{j=1}^{N} m_j \left(\frac{P_i}{\Omega_i \rho_i^2} \nabla_i W(\boldsymbol{r}_{ij}, h_i) + \frac{P_j}{\Omega_j \rho_j^2} \nabla_i W(\boldsymbol{r}_{ij}, h_j) \right), \tag{2.14}$$

$$\frac{\mathrm{d}u_i}{\mathrm{d}t} = \frac{P_i}{\Omega_i \rho_i^2} \sum_{j=1}^{N} m_j \boldsymbol{v}_{ij} \cdot \nabla W(\boldsymbol{r}_{ij}, h), \tag{2.15}$$

respectively, which are the forms used within the ∇h-SPH scheme.

2.1.3 Self-gravity

Self-gravity can be included into SPH using the consistent methods of smoothing across particle neighbours, but which also yields an exact form outside of the smoothing kernel. Gravitational softening is used to avoid unphysically large accelerations when SPH particles get close to each other. It has been shown (e.g. Dyer & Ip 1993; Dehnen 2001) that gravitational softening via a smoothing function rather than a softening length is a better choice. This also allows it to be implemented into SPH trivially.

As the density is a continuous property, it can be related to the continuous gravitational potential via Poisson's equation $\nabla^2\Phi = 4\pi G\rho$. Price & Monaghan (2007) derive the SPH momentum equation via the Lagrangian taking into account self-gravity and introduce two new smoothing functions akin to the density smoothing function $W(\boldsymbol{r},h)$. These are the force smoothing function ϕ, and the potential smoothing function ϕ'. When the density smoothing function is an M_4 cubic-spline kernel, these quantities have the forms

$$\phi_{ij}(\boldsymbol{r}_i-\boldsymbol{r}_j,h_i)=\frac{1}{h_i}\begin{cases}\frac{2}{3}q^2-\frac{3}{10}q^4+\frac{1}{10}q^5-\frac{7}{5}, & 0\le q<1;\\ \frac{4}{3}q^2-q^3+\frac{3}{10}q^4-\frac{1}{30}q^5-\frac{8}{5}+\frac{1}{15}q, & 1\le q<2;\\ -q^{-1}, & q\ge 2.\end{cases} \tag{2.16}$$

and

$$\phi'_{ij}(\boldsymbol{r}_i-\boldsymbol{r}_j,h_i)=\frac{1}{h_i^2}\begin{cases}\frac{4}{3}q-\frac{6}{5}q^3+\frac{1}{2}q^4, & 0\le q<1;\\ \frac{8}{3}q-3q^2+\frac{6}{5}q^3-\frac{1}{6}q^4-\frac{1}{15}q^{-2}, & 1\le q<2;\\ q^{-2}, & q\ge 2.\end{cases} \tag{2.17}$$

where $q=\boldsymbol{r}_{ij}/h$. Outside of $2h$, the potential has the form $1/r$ and the force $1/r^2$ i.e. there is no smoothing and the quantities are exact. The form for the gravitational acceleration of a particle i, accounting for adaptive smoothing lengths (see Section

2.1.2) is

$$\left.\frac{\mathrm{d}\boldsymbol{v}_i}{\mathrm{d}t}\right|_{\mathrm{grav}} = -G\sum_{j=1}^{N} m_j \frac{\phi'\left(\boldsymbol{r}_{ij}, h_i\right) + \phi'\left(\boldsymbol{r}_{ij}, h_j\right)}{2}\hat{\boldsymbol{r}}_{ij} - \frac{G}{2}\sum_{j=1}^{N} m_j \left[\frac{\zeta_i}{\Omega_i}\nabla_i W\left(\boldsymbol{r}_{ij}, h_i\right) + \frac{\zeta_j}{\Omega_j}\nabla_i W\left(\boldsymbol{r}_{ij}, h_j\right)\right]. \tag{2.18}$$

ζ accounts for the spatial variability in h, a term similar to Ω which is given in Equation 2.13. It has the form

$$\zeta_i = \frac{\partial h_i}{\partial \rho_i}\sum_{j=1}^{N} m_j \frac{\partial \phi_{ij}}{\partial h_i}(\boldsymbol{r}_{ij}, h_i). \tag{2.19}$$

The gravitational acceleration can be added to the SPH momentum equation to account for gravitational influence from other particles. Similarly, the gravitational potential of a particle is

$$\Phi_i = G\sum_{j=1}^{N} m_j \frac{\phi\left(\boldsymbol{r}_{ij}, h_i\right) + \phi\left(\boldsymbol{r}_{ij}, h_j\right)}{2}. \tag{2.20}$$

As the quantities are derived from the Lagrangian, momentum and energy are conserved.

2.1.4 Artificial viscosity

Artificial viscosity is used within SPH simulations to capture shocks. Within these regions, SPH particles may inter-penetrate and can incorrectly represent the conversion of kinetic energy to heat. As such, artificial viscosity modifies the acceleration and heating/cooling rate of a particle such that

$$\left.\frac{\mathrm{d}\boldsymbol{v}_i}{\mathrm{d}t}\right|_{\mathrm{visc}} = -\sum_{j=1}^{N} m_j \Pi_{ij}\nabla_i W(\boldsymbol{r}_{ij}, h_i), \tag{2.21}$$

and

$$\left.\frac{\mathrm{d}u_i}{\mathrm{d}t}\right|_{\mathrm{visc}} = \sum_{j=1}^{N} m_j \Pi_{ij}\boldsymbol{v}_{ij}\cdot\nabla_i W(\boldsymbol{r}_{ij}, h_i). \tag{2.22}$$

The artificial viscosity term Π_{ij} (Monaghan & Gingold 1983) is given as

$$\Pi_{ij} = \frac{-\alpha \bar{c}_{s,ij} \mu_{ij} + \beta \mu_{ij}^2}{\bar{\rho}_{ij}}, \tag{2.23}$$

where α and β are dimensionless viscosity parameters, $\bar{\rho}_{ij} = \frac{1}{2}(\rho_i + \rho_j)$, c_s is the isothermal sound speed and $\bar{c}_{s,ij} = \frac{1}{2}(c_{s,i} + c_{s,j})$. The term μ_{ij} can be expanded such that

$$\mu_{ij} = \begin{cases} \frac{h_i \boldsymbol{v}_{ij} \cdot \boldsymbol{r}_{ij}}{|\boldsymbol{r}_{ij}|}, & \text{if } \boldsymbol{v}_i \cdot \boldsymbol{r}_{ij} < 0; \\ 0, & \text{otherwise.} \end{cases} \tag{2.24}$$

A small factor ϵ^2 may be added to the $\left|\boldsymbol{r}_{ij}\right|^2$ term to prevent singularities at very small particle distances. Note that artificial viscosity only applies to converging flows, it does not affect receeding flows.

2.1.4.1 Time-dependent artificial viscosity

Morris & Monaghan (1997) developed a method whereby artificial viscosity adapts to the convergence of the flow. Each particle is assigned a viscosity parameter α_i and the α and β terms in Equation 2.23 are replaced with α_i and $2\alpha_i$, respectively. The viscosity parameter for each particle is allowed to change over time (Monaghan 1997) such that

$$\frac{\mathrm{d}\alpha_i}{\mathrm{d}t} = \frac{\alpha_{\min} + \alpha_i}{\tau_i} - S_i. \tag{2.25}$$

The viscosity α_i falls to a minimum value $\alpha_{\min}$ within an e-folding time of τ_i provided the source term $S_i = 0$. This term is represented as

$$S_i = \max[-(\nabla \cdot \boldsymbol{v})_i, 0](\alpha_{\max} - \alpha_i). \tag{2.26}$$

The first term on the right hand side of the equation ensures that: when a particle enters a shock ($\nabla \cdot \boldsymbol{v} < 0$), the viscosity parameter increases to $\alpha_{\max}$; when a particle

leaves a shock ($\nabla \cdot \boldsymbol{v} > 0$), the viscosity parameter decreases to $\alpha_{\rm min}$. The second term on the right hand side of the equation constrains the upper limit of α_i. The e-folding time is described by

$$\tau_i = \frac{h_i}{2\ell c_{s,i}}, \tag{2.27}$$

where ℓ is selected to make τ_i equal to a single sound-crossing time for the smoothing kernel of the particle. Typically, $\ell = 0.1 - 0.2$. Rosswog et al. (2000) proposed to multiply the source function in Equation 2.25 by a factor of $(\alpha_{\rm max} - \alpha_i)$. This prevents α_i from exceeding the maximum viscosity and also increases the rate of change of α_i when it is small. Price (2004) show that this latter point results in a better treatment of shocks.

2.1.4.2 The Balsara switch

Within protostellar discs where shear flows are important, the artificial viscosity may provide non-physical amounts of shear viscosity. To prevent this phenomenon from occurring, the viscosity parameters in Equation 2.23, or the source function in Equation 2.26, may be multiplied by a factor $f_{ij} = \frac{1}{2}(f_i + f_j)$ (Balsara 1995). For a particle i, this factor has the form

$$f_i = \frac{|\nabla \cdot \boldsymbol{v}_i|}{|\nabla \cdot \boldsymbol{v}_i| + |\nabla \times \boldsymbol{v}_i| + \sigma}, \tag{2.28}$$

where $\sigma = 10^{-3}\ c_{s,i}/h_i$. Within shocks, $f_i \rightarrow 1$ as $|\nabla \cdot \boldsymbol{v}_i| \gg |\nabla \times \boldsymbol{v}_i|$ (compression) and within shear flows, $f_i \rightarrow 0$ as $|\nabla \cdot \boldsymbol{v}_i| \ll |\nabla \times \boldsymbol{v}_i|$ (vorticity). The Balsara switch does not remove shear viscosity completely, it only reduces it.

2.1.4.3 The Cullen & Dehnen (2010) inviscid treatment

The previously discussed methods improve the treatment of viscosity but still result in small amounts of unwanted shear viscosity. Cullen & Dehnen (2010) developed a

novel prescription which differentiates shocks from convergent flows, removing viscosity completely except within shock regions. The metric used to achieve this, and to differentiate between pre- and post-shock regions is the time derivative of the velocity divergence, $\dot{\nabla} \cdot \boldsymbol{v}$. If one considers the time derivative of the continuity equation such that

$$-\dot{\nabla} \cdot \boldsymbol{v} = \frac{\mathrm{d}^2 \ln \rho}{\mathrm{d}t^2}, \tag{2.29}$$

then it is clear that $\dot{\nabla} \cdot \boldsymbol{v} < 0$ represents an increase in flow convergence, typical for pre-shock regions. Similarly, $\dot{\nabla} \cdot \boldsymbol{v} > 0$ for the post-shock region. Thus, only negative values need be considered: the shock indicator, analogous to the source function in Equation 2.26, is

$$A_i = \xi_i \max[-(\dot{\nabla} \cdot \boldsymbol{v})_i, 0]. \tag{2.30}$$

ξ is a limiter which acts to prevent false detections of compressive flows, where $\xi \to 0$ when the shear is greater than the convergence of the flow and no shock is present. Provided the shear flow is not too strong, the limiter may be approximated to the Balsara factor (Equation 2.28). A more detailed description is given in §3.3 of Cullen & Dehnen (2010).

The artificial viscosity of a particle is set to a local value

$$\alpha_{\mathrm{loc},i} = \frac{h_i A_i}{v_{\mathrm{sig},i}^2 + h_i^2 A_i}, \tag{2.31}$$

where the signal velocity $v_{\mathrm{sig},i}$ is the velocity at which two sound waves travel toward each other. It has the value

$$v_{\mathrm{sig},i} = \max_j \left(c_{s,i} + c_{s,j} - \beta \min\left(0, \boldsymbol{v}_{ij} \cdot \hat{\boldsymbol{x}}_{ij}\right)\right), \tag{2.32}$$

where $\beta = 2\alpha$ as in the standard α-prescription. When a particle passes through the maximum flow of convergence within a shock, the values of A_i and $\alpha_{\mathrm{loc},i}$ return to

zero: the signal velocity is approximately equal to the sound speed here as the flows are now diverging. The artificial viscosity evolves over time whenever $\alpha_i > \alpha_{\mathrm{loc},i}$ such that

$$\frac{\mathrm{d}\alpha_i}{\mathrm{d}t} = \frac{(\alpha_{\mathrm{loc},i} - \alpha_i)}{\tau_i}, \tag{2.33}$$

where the timescale is the same as that in Equation 2.27.

2.1.5 Time integration

In order to temporally evolve the properties of the fluid an integration scheme must be chosen. Those commonly adopted are the Leapfrog (or Verlet-Störmer) and Runge-Kutta methods.

The Leapfrog method is a second-order integrator where a particle's position and velocity are updated based on the previous half-timestep. It is time-reversible, conserves both angular momentum and energy provided timesteps are constant, and can be implemented via two different approaches. The kick-drift-kick scheme obtains the next position and velocity after a timestep Δt via

$$\boldsymbol{x}_{n+1} = \boldsymbol{x}_n + \boldsymbol{v}_n \Delta t + \frac{1}{2}\boldsymbol{a}_n \Delta t^2, \tag{2.34}$$

$$\boldsymbol{v}_{n+1} = \boldsymbol{v}_n + \frac{1}{2}(\boldsymbol{a}_n + \boldsymbol{a}_{n+1})\Delta t. \tag{2.35}$$

The acceleration need only be calculated once per timestep as the next acceleration becomes the current in the subsequent timestep. Similarly, in the drift-kick-drift scheme where positions and velocities are shifted by half of a timestep, integration is obtained such that

$$\boldsymbol{x}_{n+\frac{1}{2}} = \boldsymbol{x}_n + \frac{1}{2}\boldsymbol{v}_n \Delta t, \tag{2.36}$$

$$\boldsymbol{v}_{n+\frac{1}{2}} = \boldsymbol{v}_n + \frac{1}{2}\boldsymbol{a}_{n-\frac{1}{2}} \Delta t, \tag{2.37}$$

$$\boldsymbol{v}_{n+1} = \boldsymbol{v}_n + \boldsymbol{a}_{n+\frac{1}{2}} \Delta t, \tag{2.38}$$

$$\boldsymbol{x}_{n+1} = \boldsymbol{x}_n + \frac{1}{2} (\boldsymbol{v}_n + \boldsymbol{v}_{n+1}) \Delta t. \tag{2.39}$$

Again, the acceleration is only calculated once per timestep but this time in the middle of the timestep. Note that this scheme requires an extra step of calculations: a 'drift' is performed to find the half-timestep values, the acceleration is calculated, and then another 'drift' is performed using the updated acceleration in order to obtain the new values.

The Runge-Kutta method comes in many flavours, though for brevity, I outline only the 2nd and 4th order techniques here. The second order Runge-Kutta approximation (also called the improved Euler method or Heun's method) calculates the value of $\boldsymbol{x}$ at the next timestep via

$$\boldsymbol{x}_{n+1} = \frac{1}{2} (\boldsymbol{k}_1 + \boldsymbol{k}_2) \Delta t, \tag{2.40}$$

with coefficients

$$\boldsymbol{k}_1 = f(t_n, \boldsymbol{x}_n), \tag{2.41}$$

$$\boldsymbol{k}_2 = f(t_{n+1}, \boldsymbol{x}_n + \boldsymbol{k}_1 \Delta t), \tag{2.42}$$

where each is a slope estimation. The 4th order method instead uses four coefficients with different weightings such that

$$\boldsymbol{x}_{n+1} = \boldsymbol{x}_n + \frac{1}{6} \left(\boldsymbol{k}_1 + 2\boldsymbol{k}_2 + 2\boldsymbol{k}_3 + \boldsymbol{k}_4 \right) \Delta t, \tag{2.43}$$

$$\boldsymbol{k}_1 = f\left(t_n, \boldsymbol{x}_n\right), \tag{2.44}$$

$$\boldsymbol{k}_2 = f\left(t_{n+\frac{1}{2}}, \boldsymbol{x}_n + \frac{1}{2}\boldsymbol{k}_1 \Delta t\right), \tag{2.45}$$

$$\boldsymbol{k}_3 = f\left(t_{n+\frac{1}{2}}, \boldsymbol{x}_n + \frac{1}{2}\boldsymbol{k}_2 \Delta t\right), \tag{2.46}$$

$$\boldsymbol{k}_4 = f\left(t_{n+1}, \boldsymbol{x}_n + \boldsymbol{k}_3 \Delta t\right). \tag{2.47}$$

The Runge-Kutta method can be extended to even higher orders to obtain a more accurate approximation but at the cost of computational efficiency. It should be noted that it does not share the time-reversible properties of the Leapfrog method.

2.1.6 Choosing a timestep Δt

Given any explicit numerical integration scheme, one needs to assure that information is not propagated too rapidly within a timestep. In the case of grid-codes information should be constrained to a single cell within a timestep; for SPH, the information should be constrained to a single smoothing length of a particle. This is achieved via the Courant-Friedrichs-Lewy (CFL) condition (Courant et al. 1928).

For SPH schemes the timestep for a particle i can be calculated using the CFL condition where

$$\Delta t_i = C_{\mathrm{CFL}} \frac{h_i}{v_{\mathrm{sig},i}}. \tag{2.48}$$

The Courant number C_{CFL} acts as a timestep multiplier and is almost always less than unity, typically ~ 0.2. The signal velocity $v_{\mathrm{sig},i}$ is the speed at which information is propagated and is given in Equation 2.32. Additionally, when self-gravity is included within a simulation, a particles timestep can be constrained to

$$\Delta t_i = C_{\mathrm{grav}} \frac{h_i}{\sqrt{\boldsymbol{a}_i}}, \tag{2.49}$$

where typically $C_{\mathrm{grav}} \sim 0.5$ is the gravitational acceleration timestep condition.

Furthermore, particles can be grouped into hierarchical timestep levels based on the current maximum timestep Δt_{max}. This is typically achieved by assigning timesteps to some power-of-two fraction of the maximum timestep (e.g. Hernquist & Katz 1989; Springel 2005; Hubber et al. 2011; Hubber et al. 2018) such that

$$\Delta t_l = \frac{\Delta t_{\mathrm{max}}}{2^l}, \tag{2.50}$$

for timestep levels $l = [0, 1, 2, ..., l_{\max}]$. Particles can move to higher levels of the hierarchy as this is necessarily calculated, but moving to lower levels requires synchronisation of that level. Only when a timestep is performed on the lowest level can the maximum timestep be recalculated. The hierarchical timestepping technique reduces the number of kinetic integrations and spatial partitioning recalculations resulting in a faster computational runtime.

2.1.7 Sink particles

Particles within high density regions of SPH simulations are subject to short timesteps which slows down the temporal evolution of a simulation significantly. A solution to this problem are sink particles (Bate et al. 1995) which replace the high density collection of particles, conserving mass and momentum. The resulting sink particle no longer interacts with the rest of the computational domain hydrodynamically, only gravitationally.

A sink particle is used within a simulation provided an SPH particle exceeds a user-defined density $\rho_{\rm sink}$ and does not have another sink within its smoothing length. Other criteria can be used in conjunction, for example the particle must have the minimum gravitational potential within its neighbour list (Federrath et al. 2010), and have a negative velocity and acceleration divergence (ensures condensation is not affected by shear or tidal forces, respectively). A suitable choice for the sink creation density is 10^{-9} g cm^{-3}. If gas reaches this density it is likely that it is already part of a dense clump which will heat to ~ 2000 K (such that molecular hydrogen dissociates) and continue to collapse.

A sink may accrete other particles provided a particle crosses the sink radius (which can be fixed or a multiple of h), and if the mutual kinetic plus gravitational energy of the sink and particle is negative. The accretion of a single or set of particles i is instantaneous (i.e. occurs within a single simulation time-step), and the following

sink properties (mass, position, velocity and angular momentum) are updated

$$m_s' = m_s + \sum_i m_i, \tag{2.51}$$

$$\boldsymbol{r}_s' = \frac{1}{m_s'}\left(m_s \boldsymbol{r}_s + \sum_i m_i \boldsymbol{r}_i\right), \tag{2.52}$$

$$\boldsymbol{v}_s' = \frac{1}{m_s'}\left(m_s \boldsymbol{v}_s + \sum_i m_i \boldsymbol{v}_i\right), \tag{2.53}$$

$$\boldsymbol{L}_s' = \boldsymbol{L}_s + m_s\left(\boldsymbol{r}_s - \boldsymbol{r}_s'\right) \times \left(\boldsymbol{v}_s - \boldsymbol{v}_s'\right) + \sum_i m_i\left(\boldsymbol{r}_i - \boldsymbol{r}_s'\right) \times \left(\boldsymbol{v}_i - \boldsymbol{v}_s'\right). \tag{2.54}$$

The last of these equations can result in an artificial removal of angular momentum from a simulation. Hubber et al. (2013) have developed a method which solves this issue by allowing feedback of angular momentum to the material nearby a sink particle.

2.1.8 Summary of basic equations

The basic SPH equations can be summarised as thus: the continuity equation

$$\rho_i = \sum_{j=1}^{N} m_j W(\boldsymbol{r}_{ij}, h); \qquad h_i = \left(\frac{3N_{\text{neigh}} m_i}{32\pi\rho_i}\right)^{1/3}; \tag{2.55}$$

the momentum equation

$$\frac{\mathrm{d}\boldsymbol{v}_i}{\mathrm{d}t} = -\sum_{j=1}^{N} m_j \left\{ \frac{P_i}{\Omega_i \rho_i^2} \nabla_i W(\boldsymbol{r}_{ij}, h_i) + \frac{P_j}{\Omega_j \rho_j^2} \nabla_i W(\boldsymbol{r}_{ij}, h_j) + \Pi_{ij} \right\} + \left.\frac{\mathrm{d}\boldsymbol{v}_i}{\mathrm{d}t}\right|_{\text{grav}}, \tag{2.56}$$

with gravitational contribution

$$\begin{aligned} \left.\frac{\mathrm{d}\boldsymbol{v}_i}{\mathrm{d}t}\right|_{\text{grav}} &= -G \sum_{j=1}^{N} m_j \frac{\phi'\left(\boldsymbol{r}_{ij}, h_i\right) + \phi'\left(\boldsymbol{r}_{ij}, h_j\right)}{2} \hat{\boldsymbol{r}}_{ij} \\ &\quad - \frac{G}{2} \sum_{j=1}^{N} m_j \left[\frac{\zeta_i}{\Omega_i} \nabla_i W\left(\boldsymbol{r}_{ij}, h_i\right) + \frac{\zeta_j}{\Omega_j} \nabla_i W\left(\boldsymbol{r}_{ij}, h_j\right) \right]; \end{aligned} \tag{2.57}$$

the energy equation

$$\frac{\mathrm{d}u_i}{\mathrm{d}t} = \sum_{j=1}^{N} m_j \left\{ \frac{P_i}{\Omega_i \rho_i^2} \boldsymbol{v}_{ij} \cdot \nabla_i W(\boldsymbol{r}_{ij}, h_i) + \frac{P_j}{\Omega_j \rho_j^2} \boldsymbol{v}_{ij} \cdot \nabla_i W(\boldsymbol{r}_{ij}, h_j) + \Pi_{ij} \right\}; \tag{2.58}$$

where the viscosity terms are

$$\Pi_{ij} = \frac{-\alpha \bar{c}_{s,ij} \mu_{ij} + \beta \mu_{ij}^2}{\bar{\rho}_{ij}}; \qquad \mu_{ij} = \begin{cases} \frac{h_i \boldsymbol{v}_{ij} \cdot \boldsymbol{r}_{ij}}{|\boldsymbol{r}_{ij}|}, & \text{if } \boldsymbol{v}_i \cdot \boldsymbol{r}_{ij} < 0 \\ 0, & \text{otherwise} \end{cases}; \tag{2.59}$$

and the correction terms are

$$\Omega_i = 1 - \frac{\partial h_i}{\partial \rho_i} \sum_{j=1}^{N} m_j \frac{\partial W_{ij}}{\partial h_i}(\boldsymbol{r}_{ij}, h_i); \qquad \zeta_i = \frac{\partial h_i}{\partial \rho_i} \sum_{j=1}^{N} m_j \frac{\partial \phi_{ij}}{\partial h_i}(\boldsymbol{r}_{ij}, h_i). \tag{2.60}$$

2.2 Radiative transfer in SPH

A radiative term can be added to the SPH energy equation which captures time-dependent radiation transport. Calculating this term is computationally expensive (e.g. Harries 2015; Harries et al. 2017) and so an estimate is made using underlying assumptions. The Stamatellos et al. (2007b) method estimates the column density through which cooling/heating happens, and along with the local opacity, are used to estimate an optical depth for each particle. This can be used to determine the heating and cooling of the particle and incorporates effects from ice melting, dust sublimation, bound-free, free-free and electron scattering interactions. The equation of state used and the effect of each assumed constituent are described in detail in §3 of Stamatellos et al. (2007b). The opacities are based on the Bell & Lin (1994) parameterisation where

$$\kappa(\rho, T) = \kappa_0 \rho^a T^b. \tag{2.61}$$

κ_0, a and b are constants which depend on the species which contribute to opacity at a given density and temperature.

The radiative heating/cooling rate of a particle i is set to

$$\left.\frac{\mathrm{d}u_i}{\mathrm{d}t}\right|_{\mathrm{rad}} = \frac{4\sigma_{\mathrm{SB}}\left(T_{\mathrm{BGR}}^4 - T_i^4\right)}{\bar{\Sigma}_i^2 \bar{\kappa}_{\mathrm{R}}(\rho_i, T_i) + \kappa_{\mathrm{P}}^{-1}(\rho_i, T_i)}, \tag{2.62}$$

where σ_{SB} is the Stefan-Boltzmann constant, T_{BGR} is the pseudo-background temperature below which particles cannot cool radiatively, $\bar{\Sigma}_i$ is mass-weighted mean column density of the particle, and $\bar{\kappa}_{\mathrm{R}}$ and κ_{P} are the pseudo-mean Rosseland- and Planck-mean opacities, respectively (see Stamatellos et al. (2007b)). They are assumed to be equal. Note that whilst particles cannot cool radiatively below T_{BGR}, they can cool due to the expansion of the gas to a minimum of 5 K. The mass-weighted mean column

density for a particle is calculated as

$$\bar{\Sigma}_i = \zeta \left(\frac{\psi_i \rho_i}{4\pi G} \right)^{1/2}, \tag{2.63}$$

where $\zeta = 0.368$ is a dimensionless constant with a weak dependence on polytropic index $n = 1.5$ (see §2.4 of Stamatellos et al. (2007b) for details). The use of a particle's gravitational potential ψ_i here relies on an approximate spherical configuration. Lombardi et al. (2015) proposed a different metric for the mean-weighted column density which instead uses the pressure scale height of a particle such that

$$\bar{\Sigma}_i = \zeta' \frac{P_i}{\left| \boldsymbol{a}_{h,i} \right|}. \tag{2.64}$$

ζ' is a dimensionless quantity on the order of unity. P_i is the pressure of a particle, and $\boldsymbol{a}_{h,i}$ is the hydrodynamical acceleration of a particle which does not include gravitational or viscous influence. It is related to the pressure gradient such that

$$\boldsymbol{a}_{h,i} = \frac{-\nabla P_i}{\rho_i}. \tag{2.65}$$

Figure 2.1 compares the estimated column density against the calculated value for both methods. It demonstrates that the Lombardi et al. (2015) method estimates the column density more accurately within a protostellar disc, specifically at the surface.

Once $\bar{\Sigma}$ has been calculated the necessary pseudo-mean opacities must be found in order to calculate the heating/cooling rate of Equation 3.2. The method describing this calculation is given in detail in §2.2 of Stamatellos et al. (2007b). The requirement for on-the-fly calculation is averted via the use of an opacity look-up table. Using the density and temperature of a given particle, specific internal energy, mean-molecular mass, mass-weighted optical depth, Rosseland- and Planck-mean optical depths, ratio

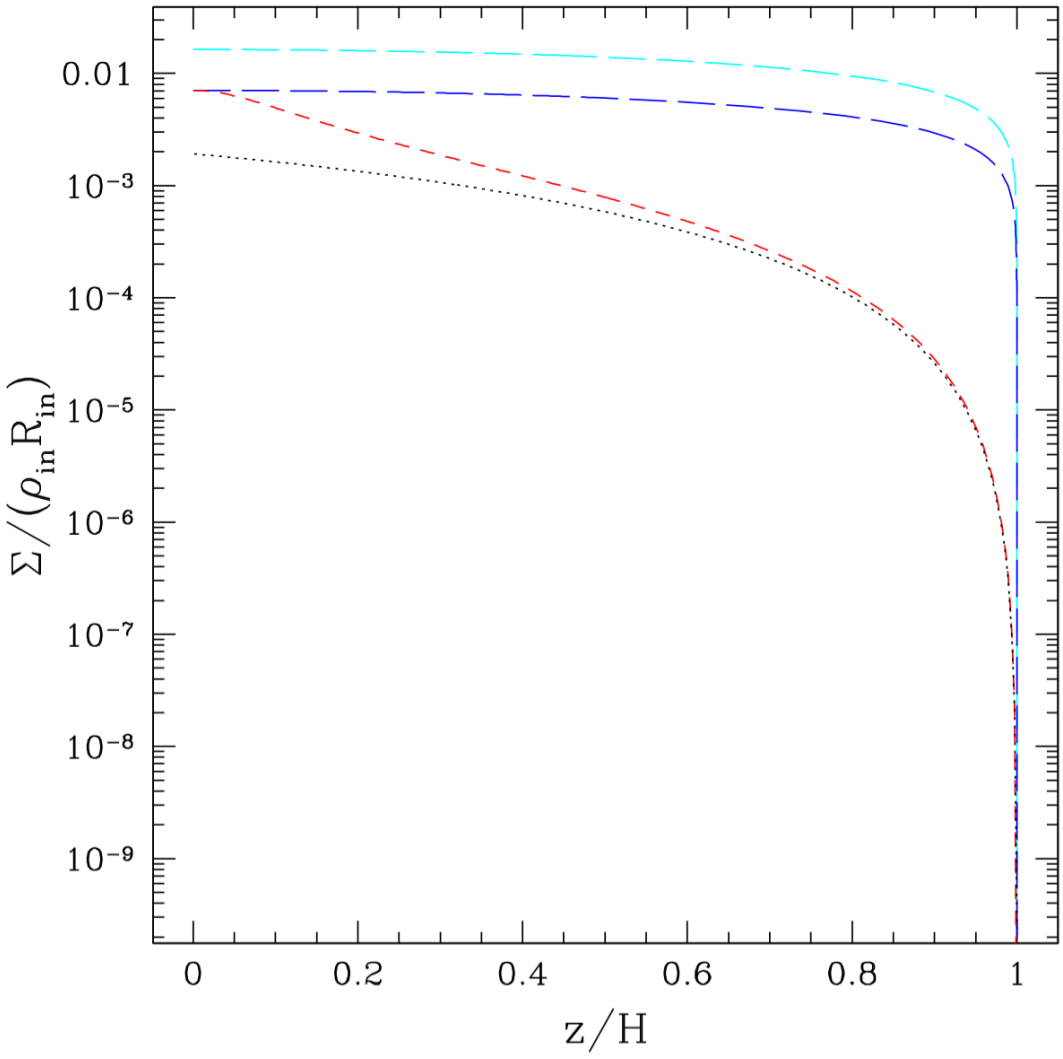

Figure 2.1: Actual column density (black dotted line) as a function of disc height in a protostellar disc. The red dashed line shows the column density estimation using the Lombardi et al. (2015) pressure scale-height method. Both dashed blue lines are estimations using the gravitational potential metric of Stamatellos et al. (2007b). The dashed cyan line includes the gravitational potential from the central star. The pressure scale-height provides a greater accuracy for column density estimation, especially at the surface of the disc. Taken from Lombardi et al. (2015).

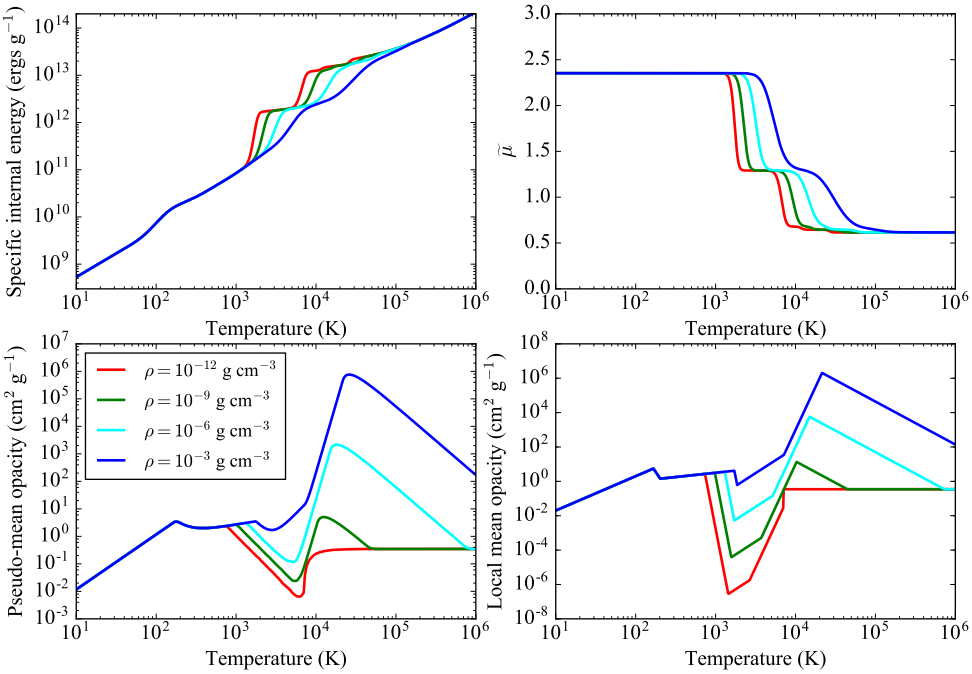

Figure 2.2: Quantities as a function of temperature for a variety of densities. Top left: the specific internal energy; top right: the mean molecular weight; lower left: the pseudo-mean opacity; lower right: the local mean opacity. All of these quantities can be accessed via the look-up table using the density and temperature of a particle. This removes the need for on-the-fly calculation.

of specific heat capacities, and the first adiabatic index can be found efficiently. Figure 2.2 illustrates the variation of specific internal energy, mean molecular mass, the pseudo-mean opacity and local mean opacity as a function of temperature. I also plot isopycnic curves at densities $\rho = \left[10^{-12}, 10^{-9}, 10^{-6}, 10^{-3}\right]$ g cm^{-3}. Some notable features are: the excitation of the rotational degrees of freedom of hydrogen at 80−100 K (see the specific internal energy panel); the dissociation between 1000 and 2000 K and ionisation of hydrogen between 5000 and 10,000 K which modifies the specific internal energy and the mean molecular weight of the gas; the opacity gap between 1000 and 3000 K.

2.2.1 Equation of state

The adopted equation of state accomodates variable adiabatic index and mean molecular weight, and so captures the state changes of the gas e.g. ionisation. Ideal gas is assumed which is reasonable up to densities ~ 0.03 g cm^{-3}. Hence the temperature of the gas is given by

$$T = \frac{(\gamma - 1)\,\widetilde{\mu} m_{\rm H} u}{k}, \tag{2.66}$$

where $m_{\rm H}$ is the mass of hydrogen and $\widetilde{\mu}$ is the mean molecular weight. This relation is shown in the upper left panel of Figure 2.2. The pressure of the gas is

$$P = (\gamma - 1)\,\rho u, \tag{2.67}$$

and its entropy is

$$s = (\gamma - 1)\,\rho^{1-\gamma} u. \tag{2.68}$$

Finally, the sound speed of the gas can be calculated via

$$c_s = \sqrt{\Gamma_1 (\gamma - 1)\, u}, \tag{2.69}$$

where Γ_1 is the first adiabatic exponent of the gas and is given by

$$\Gamma_1 = \left(\frac{\partial \ln P}{\partial \ln \rho}\right)_s = \frac{{\rm d}T}{{\rm d}u} \frac{(\gamma - 1)u}{T} \chi_{\rm T}^2 + \chi_\rho. \tag{2.70}$$

The values $\chi_{\rm T}$ and χ_ρ are the temperature and density exponents defined by

$$\chi_{\rm T} = \left(\frac{\partial \ln P}{\partial \ln T}\right)_\rho = 1 - \frac{\partial \ln \widetilde{\mu}}{\partial \ln T}, \tag{2.71}$$

and

$$\chi_\rho = \left(\frac{\partial \ln P}{\partial \ln \rho}\right)_{\rm T} = 1 - \frac{\partial \ln \widetilde{\mu}}{\partial \ln \rho}, \tag{2.72}$$

respectively. The subscripts of the differential quantities denote that they are calculated at a constant value of that subscript.

Both γ and Γ_1 are dependent on the density and temperature, and therefore vary from particle to particle. For a given ρ and u one can calculate Γ_1 through Equation 2.70. The ratio of specific heats γ can be found by considering the ratio of specific heats at constant pressure and volume such that

$$\gamma = \frac{C_{\rm P}}{C_{\rm V}}. \tag{2.73}$$

These quantities are

$$C_{\rm P} = \frac{{\rm d}u}{{\rm d}T} + \frac{R_\star}{\widetilde{\mu}}, \tag{2.74}$$

and

$$C_{\rm V} = \frac{{\rm d}u}{{\rm d}T}. \tag{2.75}$$

Here, $R_\star = k/m_{\rm H}$ in cgs units. Using these two quantities one arrives at

$$\gamma = 1 - \frac{R_\star}{\widetilde{\mu}} \frac{{\rm d}T}{{\rm d}u}. \tag{2.76}$$

Figures 2.3 and 2.4 show the variation of γ and Γ_1 as a function of temperature, respectively. I show the relationship for densities of $\rho = \left[10^{-12}, 10^{-9}, 10^{-6}, 10^{-3}\right]$g cm^{-3}. The densities are chosen such that a comparison of Γ_1 can be made to figure 1 of D'Angelo & Bodenheimer (2013).

2.3 Radiative feedback

The background temperature $T_{\rm BGR}$ in Equation 3.2 is a limit below which particles cannot cool radiatively. This can be set based on the contribution of radiating objects, and is referred to as radiative feedback. Sinks that represent stars, brown dwarfs and

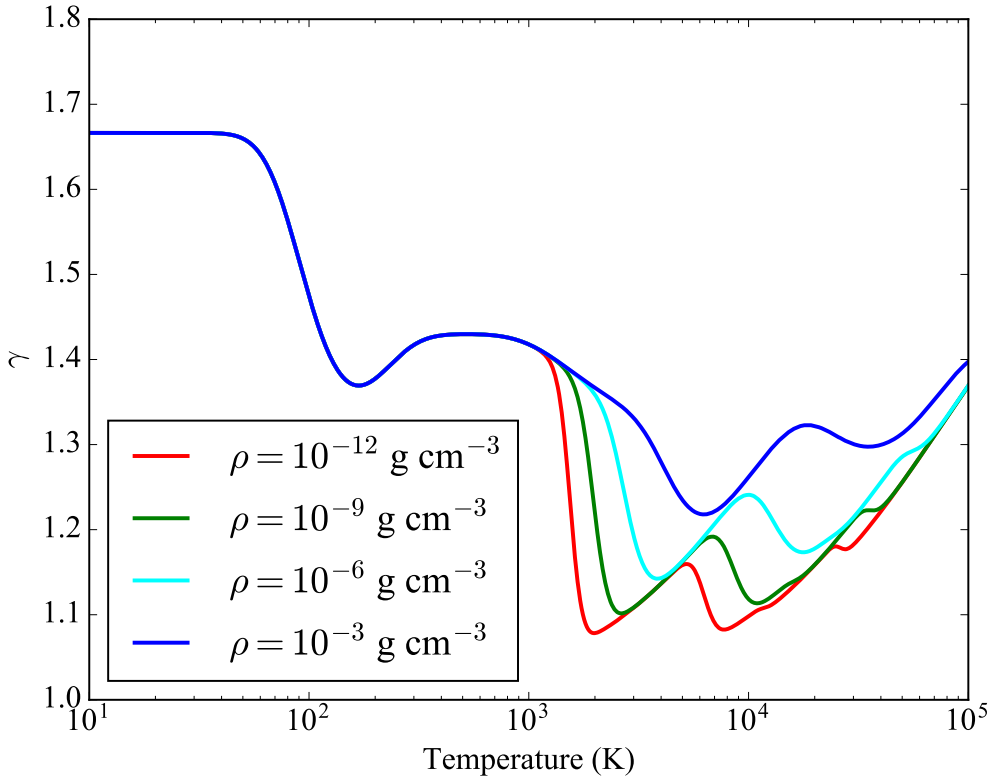

Figure 2.3: The relationship between the ratio of heat capacities with temperature for a variety of densities in units of g cm^{-3}. The values of γ are found via Equation 2.76.

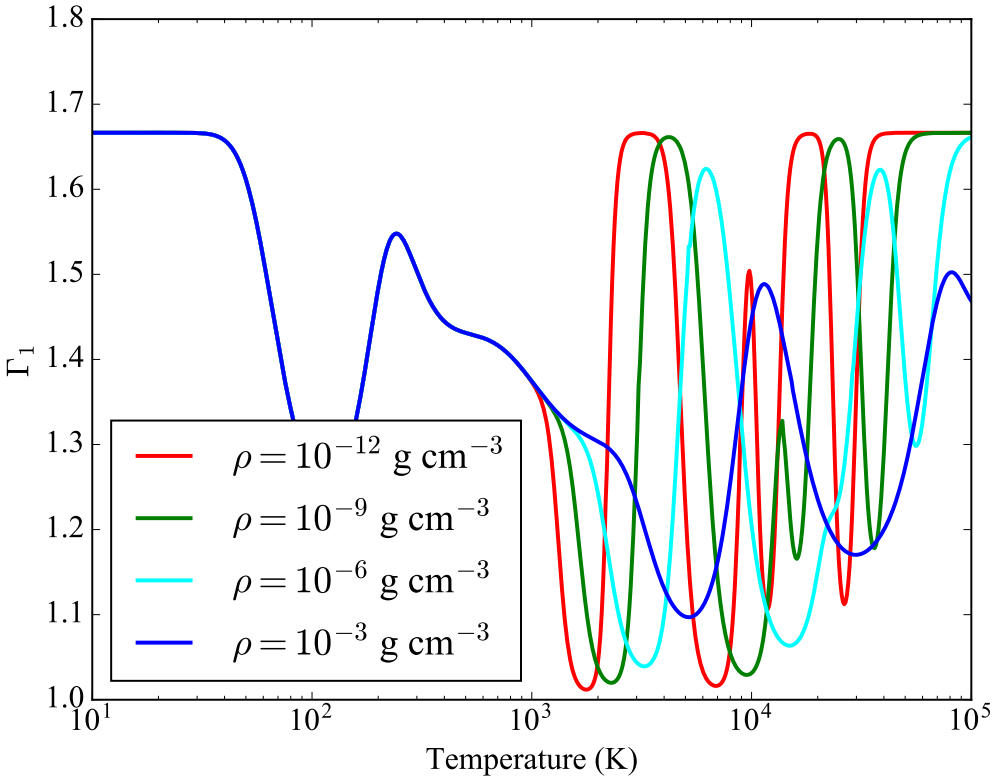

Figure 2.4: The relationship between the first adiabatic index with temperature for a variety of densities in units of g cm^{-3}. The densities are chosen to directly compare with figure 1 of D'Angelo & Bodenheimer (2013). The values of Γ_1 are found via Equation 2.70.

planets in SPH simulations of protostellar systems interact both gravitationally and radiatively with the disc. In the optically thin limit, the temperature that the dust/gas will attain at a distance $|\boldsymbol{r} - \boldsymbol{r}_n|$ from a radiative object n is

$$T_n(\boldsymbol{r}) = \left(\frac{L_n}{16\pi\sigma_{\rm SB}} \right)^{1/4} (|\boldsymbol{r} - \boldsymbol{r}_n|)^{-1/2} \, . \tag{2.77}$$

In the optically thick limit, considering a geometrically thin, passive disc (e.g. Kenyon & Hartmann 1987) the temperature is

$$T_n(\boldsymbol{r}) = \left(\frac{L_n R_n}{4\pi\sigma_{\rm SB}} \right)^{1/4} (|\boldsymbol{r} - \boldsymbol{r}_n|)^{-3/4} \, . \tag{2.78}$$

Therefore, the temperature drops faster with the distance from the radiative object in the optically thick case ($q = 3/4$ vs $q = 1/2$, respectively). However, in the case of a flared disc the temperature drop is less steep, approaching the $q = 1/2$ value. This is because a flared disc intercepts a higher fraction of the star's radiation (e.g. Kenyon & Hartmann 1987; Chiang & Goldreich 1997). This lower value for q is also consistent with disc observations (e.g. Andrews et al. 2009).

Customarily, the optically thin case is used in analytic and computational studies of protostellar disc evolution (e.g. Matzner & Levin 2005; Kratter & Matzner 2006; Stamatellos et al. 2007b; Offner et al. 2009; Stamatellos & Whitworth 2009; Stamatellos et al. 2011b; Zhu et al. 2012; Lomax et al. 2014; Vorobyov & Basu 2015; Dong et al. 2016; Kratter & Lodato 2016), albeit with a scaled down stellar luminosity (by a factor of ~ 0.1) so as to match detailed radiative transfer calculations (see Matzner & Levin 2005). In either case, the temperature at a given distance from a radiative source depends on the luminosity of the source. The luminosity of young stellar and substellar objects is mostly due to accretion of material onto their surfaces. In the work presented here I consider 3 types of radiative feedback, as described in the following sections.

2.3.1 Fixed radiative feedback

This method is used when modelling protostellar discs. I assume that the radiative feedback from the central protostar sets a minimum temperature $T_{\rm BGR}$ below which the gas cannot cool radiatively. This is set to

$$T^{\star}_{\rm BGR}(R) = \left[T_0^4 \left(\frac{R^2 + R_0^2}{\rm AU^2} \right)^{-2q} + T_{\infty}^4 \right]^{1/4}. \tag{2.79}$$

R is the distance from the star on the disc midplane, $R_0 = 0.25$ AU is a smoothing radius which prevents non-physical values when $R \rightarrow 0$, q defines the steepness of the temperature profile, and T_0 is the temperature at a distance of 1 AU from the central star. Heating from a background radiative field is included where $T_{\infty} = 10$ K. In this method, no heating is considered from accreting objects that form through gravitational fragmentation.

2.3.2 Continuous radiative feedback

The heating due to accretion from objects that form through gravitational fragmentation within a simulation (represented by sink particles) provide a pseudo-background temperature set to

$$T^4_{\rm BGR}(\boldsymbol{r}) = (10 \text{ K})^4 + \sum_n \left(\frac{L_n}{16\pi\sigma_{\rm SB} |\boldsymbol{r} - \boldsymbol{r}_n|^2} \right), \tag{2.80}$$

where L_n and $\boldsymbol{r}_n$ are the luminosity and position of a radiative object n (Stamatellos et al. 2011b; Stamatellos et al. 2012; Stamatellos 2015). The above also includes the contribution to heating from a background radiative field. The luminosity of an object n is set to

$$L_n = L_{\rm NB} + \frac{f G M_n \dot{M}_n}{R_{\rm acc}}. \tag{2.81}$$

The first term on the right hand side of the equation describes the luminosity of the object from nuclear burning which is set equal to $(M_n/\ \mathrm{M}_\odot)^3\ \mathrm{L}_\odot$ for stellar objects ($M > 0.08\ \mathrm{M}_\odot$) and 0 for substellar objects. The second term represents the accretion luminosity. $f = 0.75$ is the fraction of accretion energy that is radiated away at the photosphere of the object (Offner et al. 2010). R_{acc} is the accretion radius, set to $R_{\mathrm{acc}} = 3\ \mathrm{R}_\odot$ (Palla & Stahler 1993).

2.3.3 Episodic radiative feedback

Mass accretion onto young stars increases their luminosity due to gravitational energy being converted into heat on the accretion shock around the surface of a star. The accretion is typically considered to be continuous (Krumholz 2006; Bate 2009; Offner et al. 2009; Krumholz & Burkert 2010). However, consider a star which has just evolved out of the Class 0 phase, which will ultimately have a mass of 1 $\mathrm{M}_\odot$. It has an age of $\sim 10^5$ yr and has accumulated half of its final mass. This yields a mean mass accretion rate of $\sim 5 \times 10^{-6}\ \mathrm{M}_\odot\ \mathrm{yr}^{-1}$ and a mean luminosity of $\sim 25\ \mathrm{L}_\odot$. Observational studies show that solar-like protostars have much lower luminosities (e.g. Kenyon et al. 1990; Evans et al. 2009; Enoch et al. 2009a). This is the so called *luminosity problem*. It may be circumvented if accretion onto protostars is not continuous, but rather episodic, happening in short bursts (e.g. Dunham et al. 2010; Dunham & Vorobyov 2012; Audard et al. 2014).

FU Ori objects provide evidence of episodic accretion. These objects exhibit sudden luminosity increases on the order of ~ 5 mag and estimated accretion rates of $> 10^{-4}\ \mathrm{M}_\odot\ \mathrm{yr}^{-1}$ which last from a few tens of years to a few centuries (Herbig 1977; Hartmann & Kenyon 1996; Greene et al. 2008; Peneva et al. 2010; Green et al. 2011).

Episodic accretion maybe due to gravitational instabilities (Vorobyov & Basu 2005; Machida et al. 2011; Vorobyov & Basu 2015; Liu et al. 2016), thermal instabilities in the inner disc region (Hartmann & Kenyon 1985; Lin et al. 1985; Bell & Lin 1994), or

due to gravitational interactions in a binary system (Bonnell & Bastien 1992; Forgan & Rice 2010). It has also been suggested that they may be due to the combined effect of gravitational instabilities operating in the outer disc region transferring matter inwards and the magnetorotational instability (MRI) operating episodically in the inner disc region delivering matter onto the young protostar (Armitage et al. 2001; Zhu et al. 2007, 2009a,b, 2010).

The episodic accretion model that is adopted within this work is described in detail in Stamatellos et al. (2011b) and Stamatellos et al. (2012). Gravitational instabilities cannot develop within the inner regions of a protostellar disc ($\sim$ a few AU) due to high temperatures. Therefore, there is no mechanism to transport angular momentum outwards for the gas to accrete onto the object. Mass accumulates in the inner disc region which leads to an increase in density and temperature. When the temperature is sufficiently high to ionise the gas, the magnetorotational instability (MRI, see Section 1.6) is activated, and gas starts flowing onto the object. As with gravitational instability, angular momentum is transported outwards and matter flows inward. When the mass in the inner accretion disc is depleted, the MRI ceases and mass once again begins to accumulate within the inner disc region. The accretion of gas provides an effective luminosity via Equation 2.81 and consequently a pseudo-background temperature constribution via Equation 2.80.

As the hydrodynamic simulations do not have the resolution to capture the details of the inner accretion disc around each bound object, Stamatellos et al. (2011b) developed a sub-grid model to capture the effect of MRI utilising the time-dependent episodic accretion model ascribed to Zhu et al. (2010). Each object that forms through gravitational fragmentation is represented by a sink particle and is notionally split into two components, the *object* and the *inner accretion disc* (IAD). The total mass of the sink is

$$M_{\rm sink} = M_{\star} + M_{\rm IAD}, \tag{2.82}$$

where $M_\star$ is the mass of the object and $M_{\rm IAD}$ is the mass of its inner accretion disc. The accretion rate onto the object, $\dot{M}_\star$, is assumed to have two components: a small continuous accretion $\dot{M}_{\rm CON}$, and the accretion due to the MRI, $\dot{M}_{\rm MRI}$. The total accretion rate is therefore

$$\dot{M}_\star = \dot{M}_{\rm CON} + \dot{M}_{\rm MRI}. \tag{2.83}$$

The material only couples to the magnetic field when it becomes sufficiently ionised. The temperature at which this occurs is set to $T_{\rm MRI} \sim 1400$ K. Zhu et al. (2010) estimate that the accretion rate during an episode and the duration of an episode are

$$\dot{M}_{\rm MRI} \sim 5 \times 10^{-4}\ {\rm M}_\odot\ {\rm yr}^{-1} \left(\frac{\alpha_{\rm MRI}}{0.1}\right), \tag{2.84}$$

and

$$\Delta t_{\rm MRI} \sim 0.25\ {\rm kyr} \left(\frac{\alpha_{\rm MRI}}{0.1}\right)^{-1} \left(\frac{M_\star}{0.2\ {\rm M}_\odot}\right)^{2/3} \left(\frac{\dot{M}_{\rm IAD}}{10^{-5}\ {\rm M}_\odot\ {\rm yr}^{-1}}\right)^{1/9}, \tag{2.85}$$

respectively. $\dot{M}_{\rm IAD}$ is the mass accretion rate which flows onto the inner accretion disc, i.e. the accretion rate onto the sink. $\alpha_{\rm MRI}$ is the MRI viscosity α-prescription parameter (Shakura & Sunyaev 1973). The MRI is assumed to occur when sufficient mass has been accumulated within the inner accretion disc such that

$$M_{\rm IAD} > M_{\rm MRI} \sim \dot{M}_{\rm MRI} \Delta t_{\rm MRI}. \tag{2.86}$$

Substituting in Equations 2.84 and 2.85 yields

$$M_{\rm IAD} > 0.13\ {\rm M}_\odot \left(\frac{M_\star}{0.2\ {\rm M}_\odot}\right)^{2/3} \left(\frac{\dot{M}_{\rm IAD}}{10^{-5}\ {\rm M}_\odot\ {\rm yr}^{-1}}\right)^{1/9}. \tag{2.87}$$

Observations of FU Orionis stars (see e.g. Hartmann & Kenyon 1996), show that the accretion rate during an outburst episode drops exponentially. The accretion rate onto

the central object is therefore set to

$$\dot{M}_{\rm MRI} = 1.58 \frac{M_{\rm MRI}}{\Delta t_{\rm MRI}} \exp\left\{-\frac{t-t_0}{\Delta t_{\rm MRI}}\right\}, \qquad t_0 < t < t_0 + \Delta t_{\rm MRI}. \tag{2.88}$$

t_0 and $t_0 + \Delta t_{\rm MRI}$ are the temporal bounds of the accretion episode and the factor of $1.58 = e/(e-1)$ is included to allow all of the mass in the IAD to be accreted onto the object within $\Delta t_{\rm MRI}$. The accumulation of mass into the inner accretion disc occurs on a timescale

$$\Delta t_{\rm ACC} \sim \frac{M_{\rm MRI}}{\dot{M}_{\rm IAD}}. \tag{2.89}$$

Using Equation 2.87 gives

$$\Delta t_{\rm ACC} \simeq 13 \text{ kyr} \left(\frac{M_\star}{0.2 \text{ M}_\odot}\right)^{2/3} \left(\frac{\dot{M}_{\rm IAD}}{10^{-5} \text{ M}_\odot \text{yr}^{-1}}\right)^{-8/9}. \tag{2.90}$$

Comparing this with Equation 2.85 shows that the period when mass is being accumulated into the inner accretion disc is much longer than the accretion episodes.

The free variables in this model are $\dot{M}_{\rm CON}$ and $\alpha_{\rm MRI}$. Increasing $\alpha_{\rm MRI}$ yields shorter but more intense accretion episodes. Note that Equations 2.87 and 2.90 are independent of $\alpha_{\rm MRI}$. The uncertainty on $\alpha_{\rm MRI}$, which lies in the range $0.01 - 0.4$ (King et al. 2007), is therefore not reflected in the mass accreted in an episode nor the time interval between successive episodes.

2.4 Numerical codes

The simulations ran in this work are performed using two hydrodynamical codes, SEREN (Hubber et al. 2011), used within Chapter 3, and GANDALF (Hubber et al. 2018), used within Chapters 4 and 5. The features chosen when using SEREN are listed as thus: full 3-dimensional ∇h SPH; kernel-softened gravity; time-dependent artificial viscosity with the Balsara switch; a 2nd order Runge-Kutta integration scheme with

hierarchical timesteps; sink particles; approximate radiative transfer via the Stamatellos et al. (2007b) method; continuous and episodic radiative feedback [1].

GANDALF (the Graphical Astrophysics code for N-body Dynamics And Lagrangian Fluids) is the successor to SEREN designed to have better performance and a more accessible codebase for users to implement their own algorithms. Nearest neighbours and gravitational forces are calculated using a binary k-d tree rather than an octal tree to ensure balancing across compute nodes. The code is also parallelised using a hybrid OpenMP and MPI approach which allows theoretically linear scaling up to 128 cores, though for configurations such as protostellar discs this is not attainable. The features chosen when using GANDALF are: full 3-dimensional ∇h SPH; kernel-softened gravity; time-dependent artificial viscosity with the Cullen & Dehnen (2010) viscosity switch; a Leapfrog kick-drift-kick integration scheme with hierarchical timesteps; sink particles; approximate radiative transfer via either the Stamatellos et al. (2007b) or Lombardi et al. (2015) method (personal contribution).

The features listed are by no means exhaustive and only represent those enabled for the simulations within this work (unless specified otherwise). The codes are publicly available through the online source control service GitHub [2].

[1] Courtesy of Dimitris Stamatellos.

[2] At `https://github.com/dhubber/seren` and `https://github.com/gandalfcode/gandalf/`, respectively.

Chapter 3

The effect of radiative feedback on disc fragmentation

3.1 Introduction

A significant fraction of low-mass stars and brown dwarfs may form by fragmentation in gravitationally unstable discs (Whitworth & Stamatellos 2006; Stamatellos et al. 2007a; Stamatellos & Whitworth 2009b; Kratter et al. 2010; Zhu et al. 2012; Lomax et al. 2014; Kratter & Lodato 2016; Vorobyov 2013). Protostellar discs fragment if two conditions are met. (i) They are gravitationally unstable such that

$$Q \equiv \frac{\kappa c_s}{\pi G \Sigma} < Q_{\rm crit}, \tag{3.1}$$

where Q is the Toomre parameter (Toomre 1964), κ is the epicyclic frequency, c_s is the local sound speed and Σ is the disc surface density. The value of $Q_{\rm crit}$ is on the order of unity and it is dependent on the assumed geometry of the disc and the equation of state used: for a razor-thin disc, $Q_{\rm crit} = 1$; in a 3D disc $Q_{\rm crit} = 1.4$ (see Durisen et al. 2007, and references therein). (ii) They cool sufficiently fast, i.e. $t_{\rm cool} < (0.5-2)t_{\rm orb}$ where $t_{\rm orb}$ is the local orbital period (Gammie 2001; Johnson & Gammie 2003; Rice

et al. 2003b, 2005).

Theoretical work and simulations suggest that the conditions for disc fragmentation are met in the outer disc regions ($> 70-100$ AU) (e.g. Whitworth & Stamatellos 2006; Stamatellos et al. 2011a; Stamatellos & Whitworth 2009, 2008; Boley 2009). Most of the objects formed by disc fragmentation are brown dwarfs, though low-mass stars and planets may also form (Stamatellos & Whitworth 2009b; Zhu et al. 2012; Vorobyov 2013). Fragments that form in gravitationally unstable discs start off with a mass that is determined by the opacity limit for fragmentation, i.e. with a few Jupiter masses (Low & Lynden-Bell 1976; Rees 1976; Boss 1988; Whitworth & Stamatellos 2006; Boley et al. 2010; Forgan & Rice 2011; Rogers & Wadsley 2012). However, they quickly accrete mass to become brown dwarfs or even low-mass stars (Stamatellos & Whitworth 2009b; Kratter et al. 2010; Zhu et al. 2012; Stamatellos 2015). A few of the fragments remain in the planetary-mass regime ($M < 13$ M_J) but these are typically ejected from the disc (Li et al. 2015, 2016) becoming free-floating planets (e.g. Zapatero-Osorio et al. 2000; Kellogg et al. 2016).

These low-mass objects that form by disc fragmentation have properties that are similar to the properties of objects forming from the collapse of isolated low-mass pre-(sub)stellar cloud cores. They are expected to be attended by discs (Stamatellos & Whitworth 2009b; Liu et al. 2015; Sallum et al. 2015), and they may also launch jets perpendicular to the disc axis (Machida et al. 2006; Gressel et al. 2015). Stamatellos & Herczeg (2015) suggest that discs around low-mass objects (brown dwarfs and planets) that form by disc fragmentation are more massive from what would be expected if they were formed in collapsing low-mass pre-(sub)stellar cloud cores, which is consistent with recent observations of brown dwarf discs in Upper Sco OB1 and Ophiuchus (van der Plas et al. 2016).

It is reasonable to assume that low-mass objects that form by disc fragmentation may also exhibit radiative feedback due to accretion of material from their individual

discs onto their surfaces, which for young protostars, is expected to affect the dynamical and thermal evolution of their parent cloud and their discs (Stamatellos et al. 2011b; Stamatellos et al. 2012; Lomax et al. 2014; Guszejnov et al. 2016). The effect of radiative feedback due to accretion onto low-mass objects such as planets and brown dwarfs has been ignored by previous studies of disc fragmentation. Recent simulations of the evolution of giant proto-planets in self-gravitating discs (Stamatellos 2015) have shown that radiative feedback from giant planets may reduce gas accretion and hence suppress their mass growth. The authors found that when radiative feedback is included the fragment's final mass is within the planetary-mass regime (see also Nayakshin & Cha 2013).

The objective of the work presented in this chapter is to examine how radiative feedback (see Section 2.3) from objects that form by disc fragmentation influences the properties of these objects and whether subsequent fragmentation in the disc is affected. More specifically, I investigate whether radiative feedback from objects forming in the disc (hereafter referred to as *secondary objects*) suppresses their mass growth, increasing the possibility that these objects will end up as planets rather than brown dwarfs or more massive objects, in contrast with what previous studies suggest (e.g. Stamatellos & Whitworth 2009b; Kratter et al. 2010).

I construct numerical experiments to examine three different cases of radiative feedback from secondary objects. In Section 3.2, I provide the computational framework of this work and in Section 3.3 I discuss the initial conditions of the simulations. I present the results of the effect of radiative feedback on the evolution of discs and on the properties of the objects form by disc fragmentation in Section 3.4. The results are summarised in Section 3.5.

3.2 Numerical method

The smoothed particle hydrodynamics (SPH) code SEREN (Hubber et al. 2011) is used to simulate gravitationally unstable protostellar discs which are represented by a large number of SPH particles. To avoid small timesteps at a density of $\rho_{\rm sink} = 10^{-9}$ g cm^{-3}, a particle is replaced by a sink (Bate et al. 1995) that represents a bound object (star, brown dwarf or planet, depending on its mass). Sinks interact with the rest of the disc both gravitationally and radiatively (in the cases where radiative feedback is included). Gas particles which pass within $R_{\rm sink} = 1$ AU and are gravitationally bound to a sink are accreted onto it.

The heating and cooling of gas is performed using the radiative transfer method described in Section 2.2 using the gravitational potential (Stamatellos et al. 2007b) to estimate the column density from any given particle to the disc surface. The radiative heating/cooling rate of a particle i is

$$\frac{{\rm d}u_i}{{\rm d}t} = \frac{4\sigma_{\rm SB}\left(T_{\rm BGR}^4 - T_i^4\right)}{\bar{\Sigma}_i^2 \bar{\kappa}_{\rm R}\left(\rho_i, T_i\right) + \kappa_{\rm P}^{-1}\left(\rho_i, T_i\right)}, \tag{3.2}$$

where $\sigma_{\rm SB}$ is the Stefan-Boltzmann constant, $T_{\rm BGR}$ is the pseudo-background temperature below which particles cannot cool radiatively, $\bar{\Sigma}_i$ is mass-weighted mean column density of the particle, and $\bar{\kappa}_{\rm R}$ and $\kappa_{\rm P}$ are the pseudo-mean Rosseland and Planck opacities, respectively.

Once most of the gas in the disc has dissipated (accreted onto the central star and onto the secondary objects formed in the disc; $t = 10$ kyr), an N-body integrator with a 4th-order Hermite integration scheme (Makino & Aarseth 1992) is utilised to follow the evolution of the objects present at the end of each hydrodynamic simulation up to 200 kyr. A strict timestep criterion is used so that energy is conserved to better than one part in 10^8 (Hubber & Whitworth 2005). This allows the ultimate fate of these objects to be determined. It is noted that at this phase, gravitational and dissipative

interactions due to gas within the disc are ignored.

In the simulations presented here, a time-independent contribution from the central star in the optically thick regime (see Section 2.3.1) is assumed as it is part of the initial conditions and does not form self-consistently in the simulations. Therefore the accretion rate onto it may not be properly determined. Additionally, by choosing a relatively steep temperature profile the role of the central star in stabilising the disc is minimised, and focus is put on the radiative effect from the secondary objects forming in the disc. A time-dependent contribution in the optically thin regime from the secondary objects that form self-consistently in the simulations is assumed. It should be noted that these contributions only account for disc heating due to radiation released on the surfaces of bound objects; energy release in the disc midplane due to accretion is taken into account self-consistently within the hydrodynamic simulation. This approach ignores the case in which the density of the gas within the Hill radius of a secondary object is high, shielding the rest of the disc from the effect of heating. However, such a phase would be short-lived as gas is accreted onto the secondary object.

Three cases of radiative feedback from secondary objects forming in the disc by fragmentation are considered: (i) no radiative feedback, (ii) continuous radiative feedback, and (iii) episodic radiative feedback. In the case of no radiative feedback, objects accrete gas but the accretion energy deposited on their surfaces is not fed back into the disc. In the continuous radiative feedback case (see Section 2.3.2), gas accretes onto the object releasing energy that is fed back into the disc through the pseudo-background temperature set by Equations 2.80 - 2.81. In the episodic radiative feedback case, mass accretes in periodic bursts resulting in episodic energy release. The adopted model is discussed in Section 2.3.3.

3.3 Initial conditions

I study the evolution of a 0.3 $M_\odot$ gravitationally unstable protostellar disc around a 0.7 $M_\odot$ star using smoothed particle hydrodynamics (Gingold & Monaghan 1977; Lucy 1977, see Section 2.1 for details). The surface density and temperature profiles of the disc are set to $\Sigma \propto R^{-p}$ and $T \propto R^{-q}$, respectively. The surface density power index p is thought to lie between 1 and 3/2 from semi-analytical studies of cloud collapse and disc creation (Lin & Pringle 1990; Tsukamoto et al. 2015). The temperature power index q has been observed to lie in the range from 0.35 to 0.8 from studies of pre-main sequence stars (Andrews et al. 2009). Here, values of $p = 1$ and a relatively high $q = 0.75$ are adopted. This is to minimise the role of the central star in stabilising the disc and thus focus on the radiative effect from the secondary objects forming in the disc.

The disc extends from an inner radius $R_{\rm in} = 1$ AU to an outer radius $R_{\rm out} = 100$ AU. The surface density profile is set to

$$\Sigma(R) = \Sigma_0 \left(\frac{R_0^2}{R_0^2 + R^2} \right)^{1/2}, \tag{3.3}$$

where $\Sigma_0 = 1.7 \times 10^4$ g cm^{-2} is the surface density at $R = 0$. The initial disc temperature profile is set using Equation 2.79, i.e. initially $T(R) = T^\star_{\rm BGR}(R)$. $N = 10^6$ SPH particles are used to represent the disc which are distributed using random numbers between $R_{\rm in}$ and $R_{\rm out}$ so as to reproduce the disc density profile. Table 3.1 lists all the values for the aforementioned parameters.

The disc is initially massive enough that it is gravitationally unstable ($Q < 1$) beyond ~ 30 AU (see Figure 3.1). Such a profile is chosen to ensure that the disc will fragment so as to study the effect of radiative feedback from secondary objects on subsequent fragmentation. The initial Toomre parameter reaches very low values at the outer edge of the disc which is unrealistic: when a disc forms around a young

protostar its mass increases by in-falling material from the protostellar envelope. This progressively reduces Q to just below ~ 1 and the disc may then fragment (e.g. Stamatellos et al. 2011b). In the simulations that are presented here, the initial low Q value results in high effective viscosity so that the disc attains a nearly uniform $Q \sim 1$ (see Figure 3.1, red & green lines) within a few outer orbital periods. This is similar to what it would be expected for a disc forming in a collapsing cloud.

The gravitational acceleration for every particle is calculated using a spatial octal-tree (Barnes & Hut 1986). The velocity of a particle i in the $x-y$ plane are set using $v_{xy,i} = \sqrt{R_i \left| g_{xy,i} \right|}$, where R_i and $g_{xy,i}$ are the radius and the gravitational acceleration of the particle on the disc midplane, respectively. No initial motions perpendicular to the disc midplane are assumed.

The number of SPH particles used to represent the disc $\left(10^6\right)$ ensures that gravitational fragmentation can be properly resolved. The minimum resolvable mass for a 0.3 $M_\odot$ disc comprising 10^6 particles is 3.14×10^{-4} M_J. Bate & Burkert (1997) argue that the Jeans mass must be resolved by $2 \times N_{\rm neigh}$ and Nelson (2006) conclude that the Toomre mass must be resolved by $6 \times N_{\rm neigh}$. The simulations performed by Stamatellos & Whitworth (2009) with a 0.7 $M_\odot$ disc and 1.5×10^5 particles find a minimum Jeans mass of ~ 2 M_J and a minimum Toomre mass of ~ 2.5 M_J. If one takes 2 M_J as a lower resolution limit, then this corresponds to $\sim 128 \times N_{\rm neigh}$ i.e. the disc is sufficiently resolved. The vertical structure of this disc is also adequately resolved since ~ 7 times more particles are used than the simulations of Stamatellos & Whitworth (2009) where the disc scale-height is resolved by a factor of more than $3-5$ smoothing lengths. The scale-height of the initial disc here is resolved such that $h/H = [0.90, 0.17, 0.12]$ at radii $R = [1, 50, 100]$ AU, respectively.

Table 3.1: The initial disc parameters. The disc is gravitationally unstable, as determined by the Toomre criterion.

Disc Parameter	Value
N	10^6
$M_{\rm disc}$	0.3 $M_\odot$
$M_\star$	0.7 $M_\odot$
$R_{\rm in}$	1 AU
$R_{\rm out}$	100 AU
R_0	0.25 AU
T_0	250 K
T_∞	10 K
p	1
q	0.75

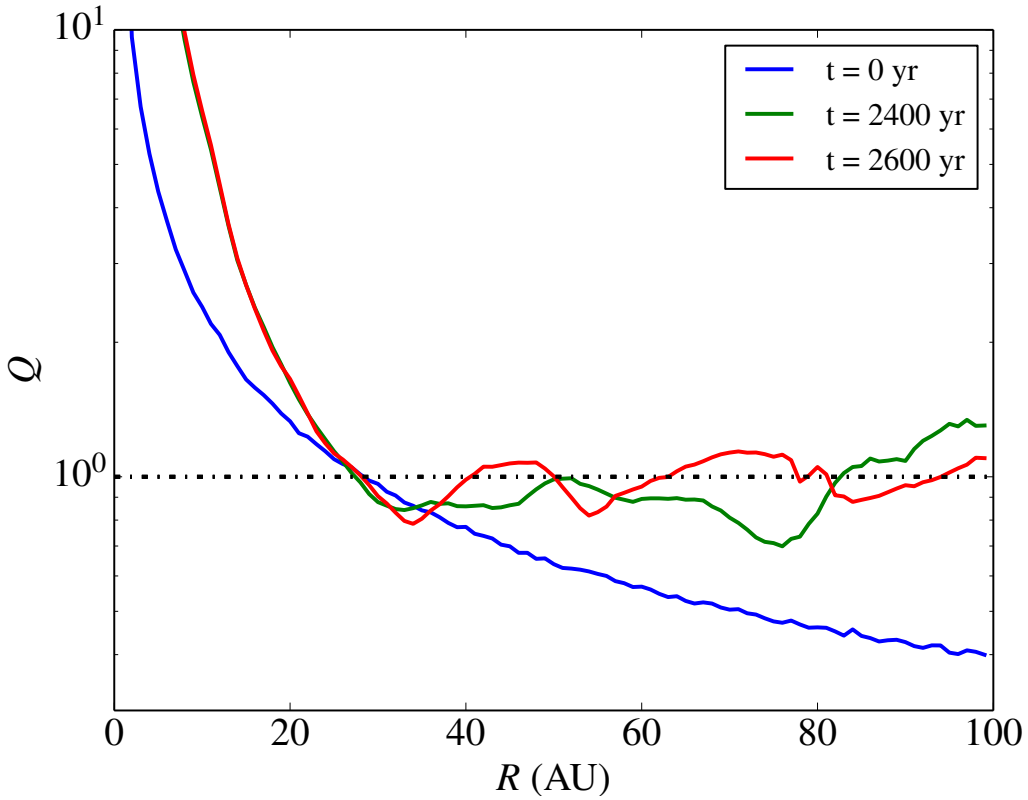

Figure 3.1: Azimuthally-averaged Toomre parameter Q for a disc with the initial conditions listed in Table 3.1, and at later times (as marked on the graph), before the disc fragments.

3.4 Disc fragmentation and the effect of radiative feedback

The disc is gravitationally unstable, thus spiral arms form and the disc fragments to form secondary objects in all 5 cases (see Table 3.2). The only difference between the 5 simulations is the way the radiative feedback from these secondary objects is treated: (i) for simulation "NRF" there is no radiative feedback from secondary objects, (ii) for simulation "CRF", the radiative feedback from secondary objects is continuous, (iii) for simulations "ERF001", "ERF01", "ERF03" the radiative feedback is episodic. The difference between the last three simulations is the value of the viscosity parameter due to the MRI (see Section 2.3.3), which determines the intensity and the duration of the outburst (ERF001: $\alpha_{\rm MRI} = 0.01$; ERF01: $\alpha_{\rm MRI} = 0.1$; ERF03 $\alpha_{\rm MRI} = 0.3$). The disc surface density and the disc midplane temperature of the 5 runs are shown in Figures 3.2-3.6. In all five simulations the discs evolve identically and at 2.7 kyr an object forms due to gravitational fragmentation. From this point on, the simulations differ as this object provides different radiative feedback in each run. In the NRF run, 7 secondary objects from by disc fragmentation, whereas in the CRF run only 1 secondary object forms. In the ERF runs, 3-4 secondary objects form, i.e. somewhere in between the two previous cases, similar to what previous studies have found (Stamatellos et al. 2011b; Stamatellos et al. 2012; Lomax et al. 2014, 2015). The properties of the objects formed in each run are listed in Table 3.2. In the next subsections I discuss each of the simulations in detail.

3.4.1 No radiative feedback (NRF)

Figure 3.2 shows the evolution of the surface density and midplane temperature for the disc where no radiative feedback is provided from secondary objects that form in the disc. Spiral arms develop and the disc fragments to form 7 secondary objects

Table 3.2: The properties of objects formed by gravitational fragmentation in the simulations with no radiative feedback from secondary objects (NRF), with continuous radiative feedback (CRF), and with episodic radiative feedback (ERF001, ERF01, ERF03). N_o is the total number of secondary objects formed, t_i is the formation time of an object, M_i its initial mass, and M_f its final masses (i.e. at the end of the hydrodynamical simulation; $t = 10$ kyr). $M_{\rm MAX}$ is the maximum possible mass it can attain by accreting mass from the disc (see discussion in the text), $\langle \dot{M} \rangle$ is the mean accretion rate, $\dot{M}_f$ is the accretion rate onto the object at 10 kyr, R_i is the distance from the star when it forms, R_f is its final distance from the star, and $\Delta R = R_f - R_i$ is its radial migration within 10 kyr. S denotes the central star, LMS secondary low-mass stars, BD brown dwarfs and P planets. In the final column I mark whether the object is bound to its host star at the end of the N-body simulation (200 kyr). B and E denote bound and ejected, respectively.

Run ID	$\alpha_{\rm MRI}$	N_o	t_i (kyr)	M_i (M_J)	M_f (M_J)	$M_{\rm MAX}$ (M_J)	$\langle \dot{M} \rangle$ (10^{-7} $M_\odot yr^{-1}$)	$\dot{M}_f$ (10^{-7} $M_\odot yr^{-1}$)	R_i (AU)	R_f (AU)	ΔR (AU)	Type	Bound
NRF	-	7	0.0	733	773	774	37.7	5.29	0	0	0	S	-
			2.7	2	97	99	124	14.7	77	105	28	LMS	B
			4.3	4	48	53	75.0	27.3	65	25	-40	BD	E
			5.5	2	13	13	22.0	2.83	160	144	-16	P/BD	E
			5.9	2	4	4	4.63	0.02	270	570	300	P	E
			6.0	2	66	67	154	4.57	103	15	-88	BD	B
			7.1	1	4	4	7.78	3.19	191	169	-22	P	E
			7.5	1	3	3	6.33	0.34	103	235	132	P	E
CRF	-	1	0.0	733	772	826	36.8	31.9	0	0	0	S	-
			2.7	2	79	191	100	66.6	77	68	-9	BD/LMS	B
ERF001	0.01	4	0.0	733	772	811	37.2	33.0	0	0	0	S	-
			2.7	2	87	127	111	35.0	77	76	-1	LMS	B
			5.4	3	32	42	60.5	8.54	93	178	85	BD	B
			8.2	2	8	32	31.0	20.7	166	97	-69	P	E
			9.8	2	3	5	51.0	2.01	119	104	-15	P	E
ERF01	0.1	3	0.0	733	771	805	37.3	25.2	0	0	0	S	-
			2.7	2	91	124	117	24.3	77	64	-13	LMS	B
			6.3	3	13	63	26.9	36.4	85	123	38	P/BD	E
			7.9	2	9	25	31.4	11.9	137	129	-8	P	E
ERF03	0.3	4	0.0	733	771	782	44.3	33.6	0	0	0	S	-
			2.7	2	105	116	135	31.2	77	40	-37	LMS	B
			5.5	2	66	73	138	18.5	106	14	-92	BD	B
			6.0	2	17	24	34.9	29.5	87	142	55	BD	E
			6.0	3	16	16	72.0	0.0	96	300	204	BD	E

(see Table 3.2). Fragmentation occurs outside 65 AU where the disc is gravitationally unstable and cools fast enough (e.g. Rice et al. 2003a, 2005; Stamatellos et al. 2007a, 2011a). After 10 kyr, the first of these objects has accreted a sufficient amount of gas to become a low-mass hydrogen-burning star ($M = 97$ M_J). Two brown dwarfs are formed (with masses 48 and 66 M_J) and orbit within 25 AU of the central star (at 25 and 15 AU, respectively). Three of the objects formed remain in the planetary-mass regime. These form at a late stage and at large orbital radii, thus having less time to accrete gas from the disc. One of these planets undergoes a net radial outward migration of 300 AU between its formation at 5.9 kyr and the end of the hydrodynamical simulation (10 kyr). These objects are bound to the central star by the end of the hydrodynamic simulation. However, a few of them are loosely bound at large radii ($R > 150$ AU for 3 of them), and therefore destined to be ejected from the system. Indeed, at the end of the N-body calculation (at 200 kyr), all but two of these objects are ejected from the system, becoming free-floating planets and brown dwarfs (see also Stamatellos & Whitworth 2009b; Li et al. 2015, 2016; Vorobyov 2016).

3.4.2 Continuous radiative feedback (CRF)

Figure 3.3 shows the evolution of the disc surface density and disc midplane temperature for the simulation with continuous radiative feedback from secondary objects that form in the disc. The disc fragments but only one secondary object forms. Continuous radiative feedback from this object heats and stabilises the disc; therefore, no further fragmentation occurs. The object carves out a gap within the disc and migrates inwards 9 AU by the end of the hydrodynamical simulation (i.e. within 7.3 kyr since its formation). At this point it has accreted enough gas to become a high-mass brown dwarf and is close to overcoming the hydrogen-burning mass limit. As there is still plenty of gas within the disc, the ultimate fate of this system is a binary comprising a solar-type and a low-mass secondary star.

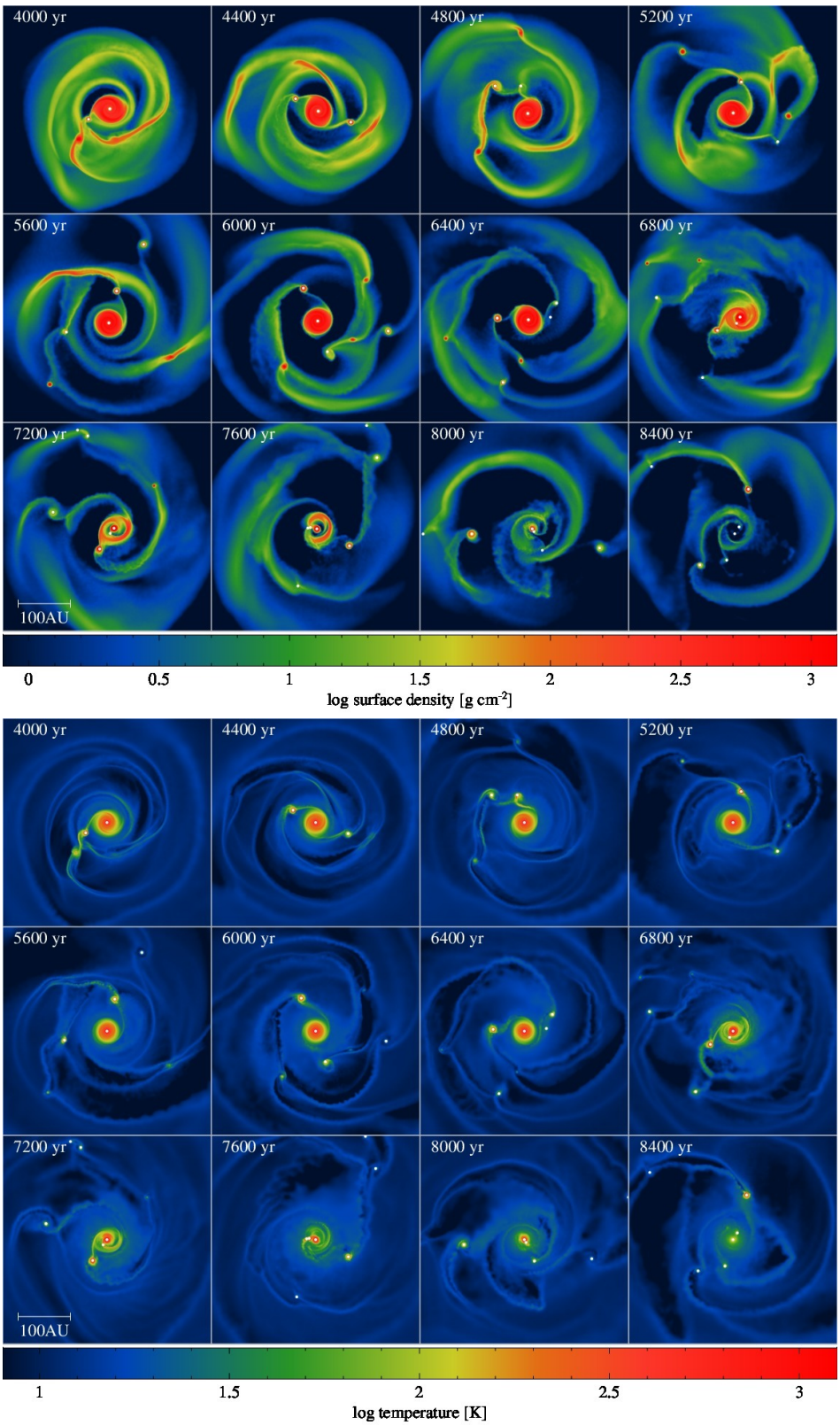

Figure 3.2: Disc evolution without any radiative feedback from secondary objects (NRF run). The top snapshots show the disc surface density and the bottom snapshots show the disc mid-plane temperature (at times as marked on each graph). 7 objects form by gravitational fragmentation due to the disc cooling fast enough in its outer regions. Most of the objects formed are brown dwarfs and planets. Planets are ultimately ejected from the system.

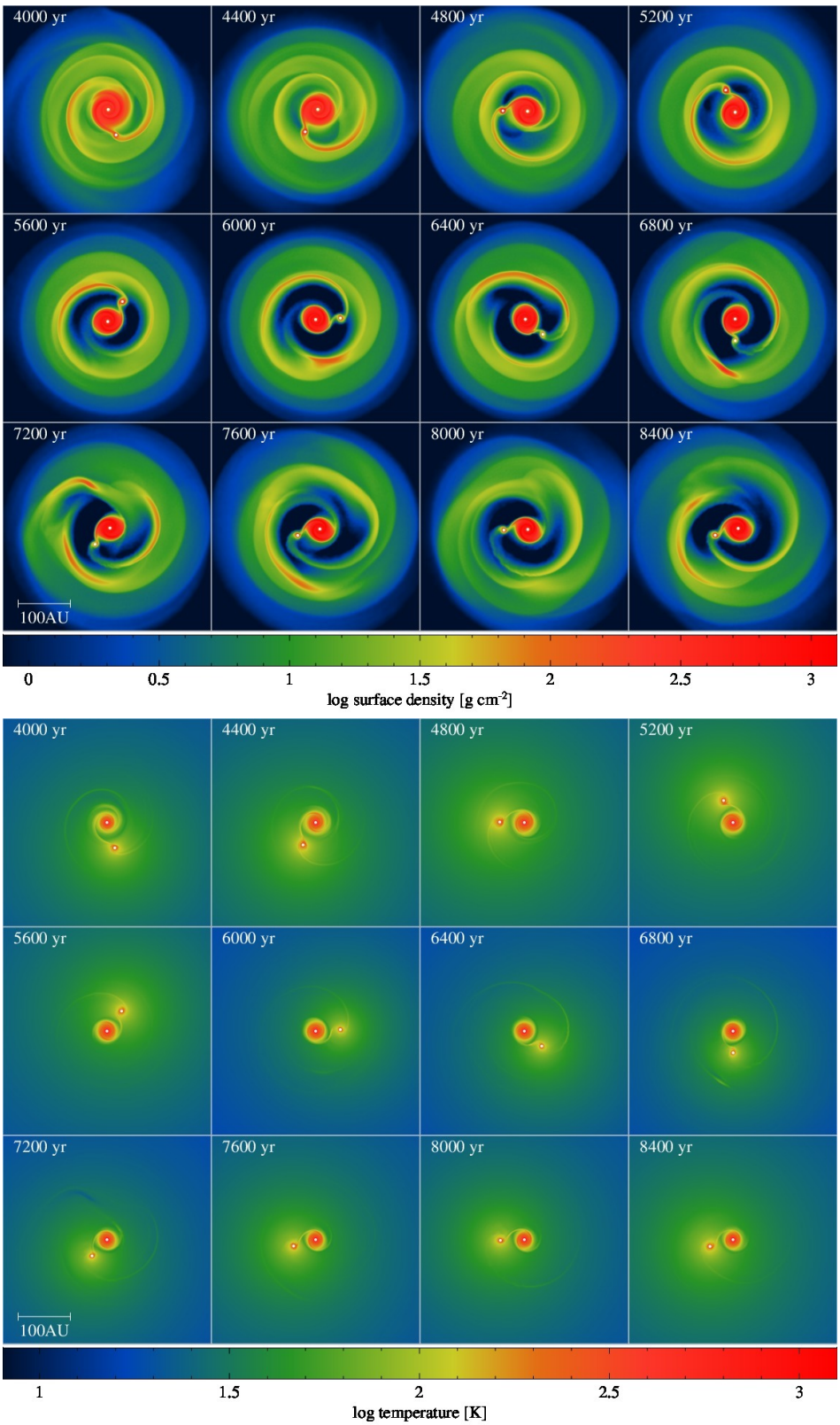

Figure 3.3: Disc evolution with continuous radiative feedback from secondary objects (CRF run). The disc fragments but only one object forms that ends up as a low-mass star. Radiative feedback from this object suppresses further fragmentation. The object forms on a wide orbit (68 AU) and migrates inwards only by 9 AU within 7.3 kyr.

3.4.3 Episodic radiative feedback (ERF)

Figures 3.4, 3.5 and 3.6 show the surface density and disc midplane temperature evolution for the simulations with episodic radiative feedback from secondary objects forming in the disc, in three different cases: $\alpha_{\rm MRI} = 0.01, 0.1, 0.3$, respectively. The disc fragments as in the previous cases; the radiative feedback from secondary objects is now episodic due to episodic accretion. During the accretion/outburst episodes, the mass that has accumulated in the inner disc region of a secondary object flows onto the object, resulting in an increase of its accretion luminosity that affects a large portion of the disc around the central star. This is evident by the sudden increase in the temperature (e.g. in Figures 3.4 and 3.5). The increase of the temperature in the disc is three- to four-fold (see Figure 3.7b), which is enough to stabilise the disc during the outburst. However, in all three cases, when the outburst stops the disc becomes unstable and fragments.

The number of secondary objects formed is similar in all three cases (3-4 objects). Therefore, fewer objects form than in the non-radiative feedback case and more objects than the continuous radiative feedback case (Stamatellos et al. 2011b; Stamatellos et al. 2012; Lomax et al. 2014, 2015).

The frequency and duration (see Table 3.3) of the accretion/feedback outbursts are important for the gravitational stability of the disc. The total duration of episodic outbursts drops from $\sim 18\%$ to $\sim 0.8\%$ of the simulated disc lifetime (10 kyr), as the viscosity parameter $\alpha_{\rm MRI}$ is increased from 0.01 to 0.3. A larger $\alpha_{\rm MRI}$ results in stronger but shorter outbursts. The number of secondary objects forming in the disc does not strongly depend on $\alpha_{\rm MRI}$, which indicates that for suppressing disc fragmentation the total duration of episodic outbursts must be longer.

I find that the average mass of secondary objects at the end of the hydrodynamical simulation (10 kyr) increases with $\alpha_{\rm MRI}$; the average masses are 33, 38 & 51 M_J for $\alpha_{\rm MRI} = 0.01$, 0.1, and 0.3, respectively. In all cases, the two lowest mass objects are

Table 3.3: The duration of episodic accretion events from each secondary object in the simulations which consider episodic radiative feedback.

Run ID	$\alpha_{\rm MRI}$	Sink #	Episodes	Duration (yr)
ERF001	0.01	2	3	1170
		3	2	487
		4	1	90
		5	0	0
		All	6	1747
ERF01	0.1	2	3	108
		3	1	10
		4	1	9
		All	5	128
ERF03	0.3	2	3	46
		3	2	22
		4	1	4
		5	2	9
		All	6	81

ultimately ejected from the system. For $\alpha_{\rm MRI} = 0.01$, the two lowest mass objects are planets. For $\alpha_{\rm MRI} = 0.1$, the two lowest mass objects consist of a planet and a brown dwarf. And finally, for $\alpha_{\rm MRI} = 0.3$, the two lowest mass objects are brown dwarfs. The estimated maximum mass that all of all these objects will eventually attain (see next section) is above the deuterium-burning limit, except for one object in the $\alpha_{\rm MRI} = 0.01$ run.

I also find that subsequent formation of secondary objects happens on a more rapid timescale for greater values of $\alpha_{\rm MRI}$. Radiative feedback episodes are shorter for a higher $\alpha_{\rm MRI}$: the disc cools fast after an episode ends, becoming gravitationally unstable and fragments again within a shorter time.

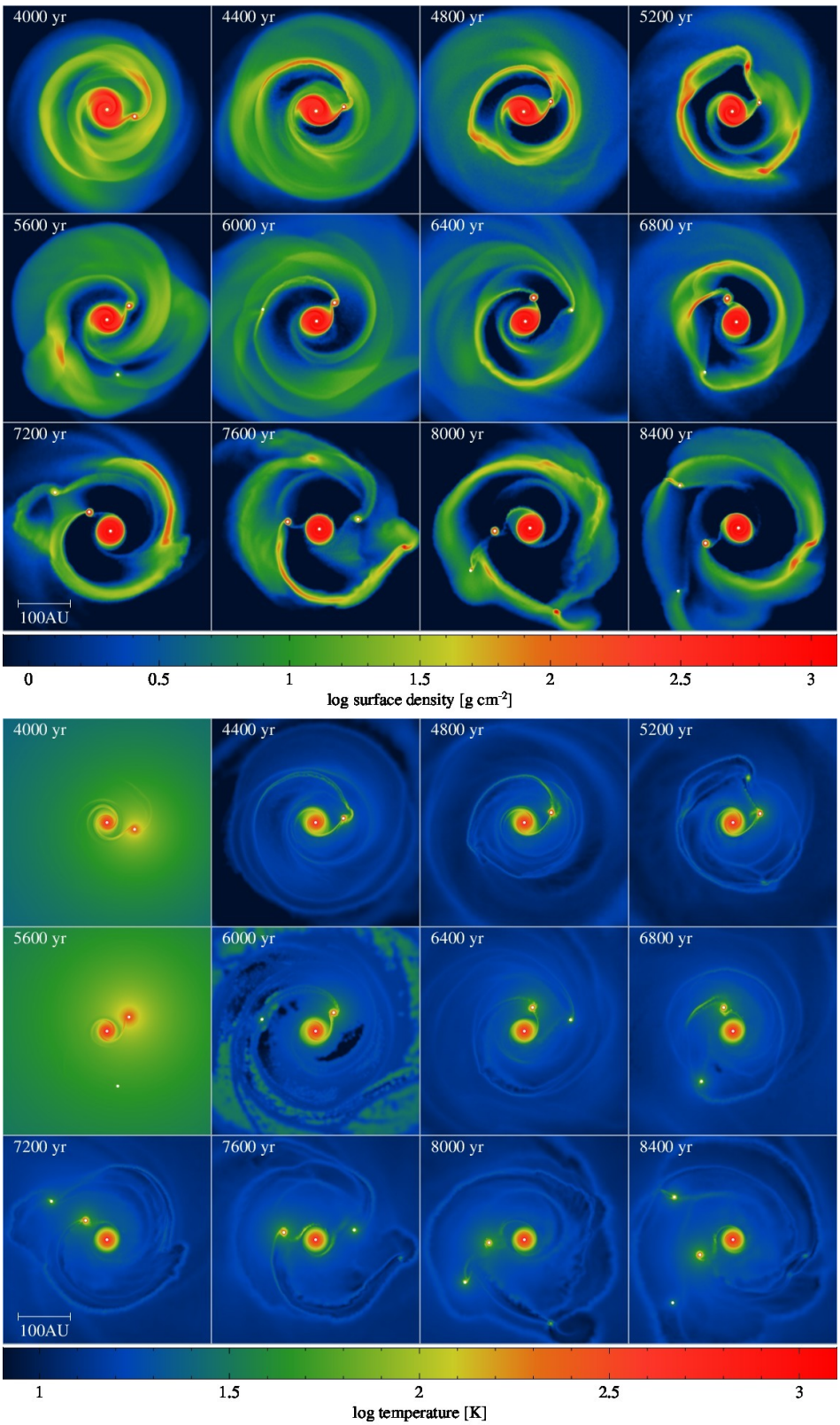

Figure 3.4: Disc evolution with episodic radiative feedback from secondary objects and a viscosity parameter $\alpha_{\rm MRI} = 0.01$ (ERF001 run). The disc fragments and 4 objects form as the disc is cool enough to be gravitationally unstable between accretion episodes.

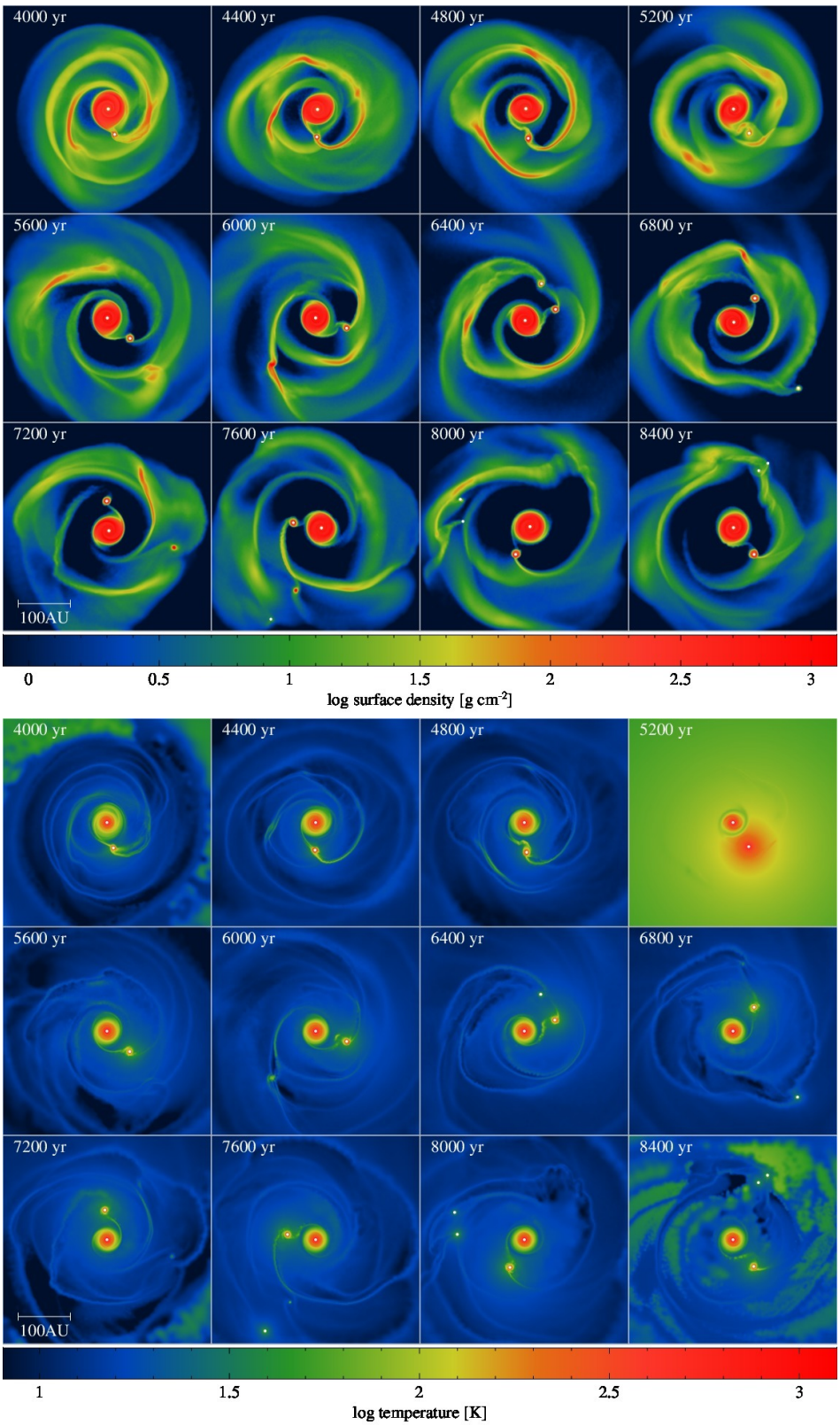

Figure 3.5: Disc evolution with episodic radiative feedback from secondary objects and a viscosity parameter $\alpha_{\rm MRI} = 0.1$ (ERF01 run). The disc fragments and 3 objects form. Two of these objects are planets, as in the ERF001 run.

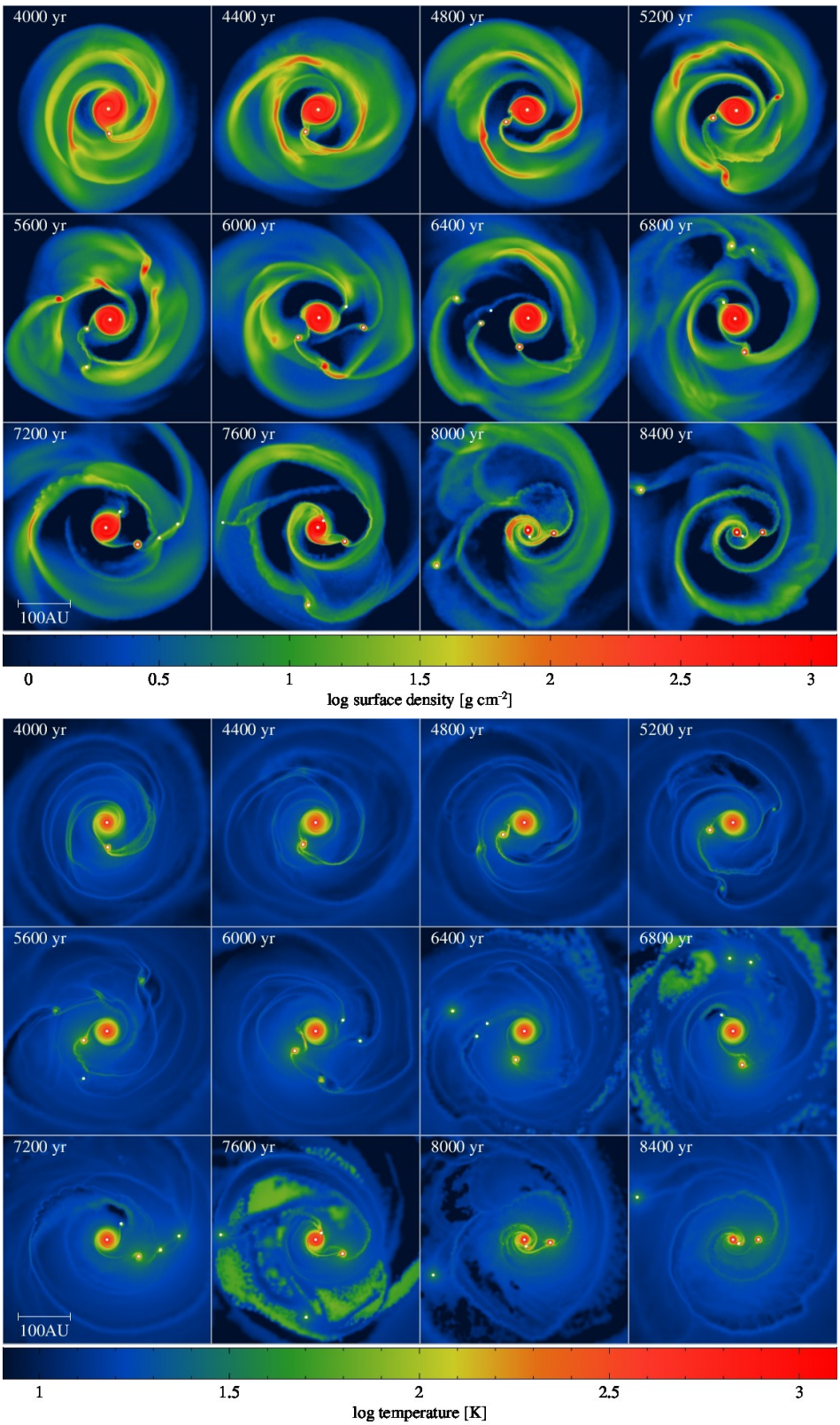

Figure 3.6: Disc evolution with episodic radiative feedback from secondary objects and a viscosity parameter $\alpha_{\rm MRI} = 0.3$ (ERF03 run). The disc fragments and 4 objects form. One object migrates inwards significantly such that it accretes a large amount of gas while in a close orbit to the central star. The two lowest mass objects are ultimately ejected from the system.

3.4.4 Comparison of simulations

Table 3.2 lists information pertaining to the secondary objects that form in the disc simulations: the number of objects formed in each simulation; their initial and final masses (i.e. at the end of the hydrodynamical simulation, $t = 10$ kyr) and an estimate of the maximum mass they can ultimately attain (considering that they will still be evolving in a gaseous disc); the gas accretion rate onto them; their formation and final radius; their type; and whether they are still bound to the central star at the end of the N-body simulation (200 kyr).

The maximum mass, $M^i_{\rm MAX}$, that an object i can attain is calculated as follows. It is assumed that each object will continue to accrete at its accretion rate $\left(\dot{M}^i_f\right)$ at the end of the hydrodynamic simulation (which is likely an overestimate as generally the accretion rate decreases, unless there is some kind of violent interaction within the disc). Therefore, the maximum mass that an object i can attain is

$$M^i_{\rm MAX} = M^i_f + \dot{M}^i_f \; t_{acc}, \tag{3.4}$$

where M^i_f is the mass of an object i at $t = 10$ kyr, and t_{acc} is the time for which it will keep on accreting gas. I also assume that only a fraction $\xi = 0.9$ of all the gas from the disc could eventually accrete either onto the central star or onto the secondary objects, therefore

$$\xi M_{\rm disc} = \sum_{sec} M^i_f + \sum_{all} \dot{M}^i_f t_{acc} \tag{3.5}$$

where the first sum on the right hand side is over the secondary objects and the second sum is over all objects to include gas accreting onto the central star. I assume that the accretion time t_{acc} is the same for all objects within each simulation, therefore it is calculated such that

$$t_{acc} = \frac{\xi M_{\rm disc} - \sum_{sec} M^i_f}{\sum_{all} \dot{M}^i_f}. \tag{3.6}$$

The maximum estimated mass for an object i can then be calculated using Equation 3.4.

Radiative feedback from secondary objects affects the entire disc as these secondary objects are high accretors (at their initial stages of their formation). For a short time they may even outshine the central star (see Figure 3.8). The assumed pseudo-background temperature profile provided by each secondary object (see Equation 2.80) influences the temperature at a given location in the disc and may affect disc fragmentation (Stamatellos et al. 2011a) but probably not significantly. If one adopts a pseudo-background temperature profile with $q = 3/4$ instead of $q = 1/2$, then the disc temperature at a distance 50 AU from a radiative object will be a factor of ~ 5 smaller, and the Toomre parameter Q (see Figure 3.7a) a factor of ~ 2 smaller, bringing it (for the CRF and ERF runs), close to the critical value for fragmentation ($Q \approx 1$; see e.g. Durisen et al. 2007). However, this is the maximum expected effect. Even in the case of $q = 3/4$ (which is an upper limit for q) the disc temperature is expected to be higher than the minimum "background" value due to energy dissipation within the disc as it is gravitationally unstable.

With regard to the episodic radiative feedback runs, the number of secondary object does not vary much for a different MRI viscosity parameter $\alpha_{\rm MRI}$. 4 objects form when $\alpha_{\rm MRI} = 0.01$; 3 objects form when $\alpha_{\rm MRI} = 0.1$; 4 objects form when $\alpha_{\rm MRI} = 0.3$. More secondary objects result in more radiative feedback episodes and a hotter disc for longer periods of time. Thus this provides sustained stability against gravitational fragmentation. The duration of episodic outbursts affects the stability of the disc. For a smaller $\alpha_{\rm MRI}$, episodes are longer and provide longer periods of stability. The opposite is true for a larger $\alpha_{\rm MRI}$. This is shown in Table 3.3. However, it is evident that episodic feedback from only 1 or 2 secondary objects cannot suppress further disc fragmentation, in contrast with the continuous feedback case, where the presence of just one secondary object suppresses fragmentation.

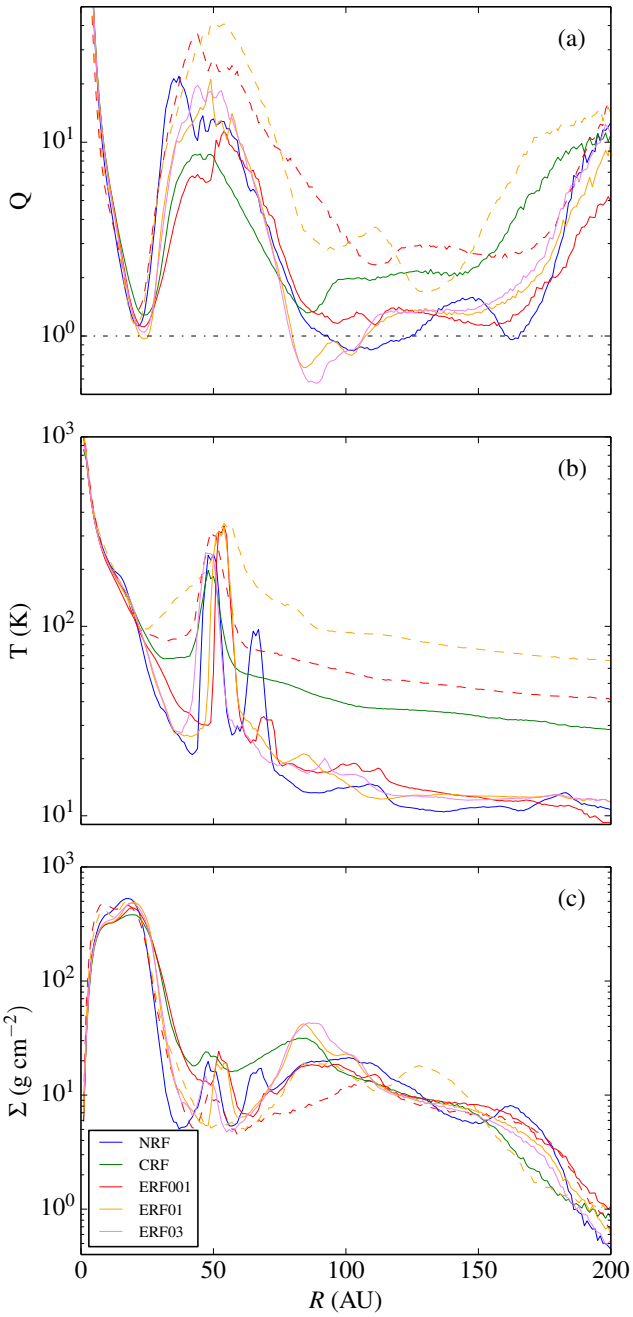

Figure 3.7: (a) Azimuthally-averaged Toomre parameter Q, (b) disc midplane temperature, and (c) disc surface density for all simulations at $t = 4.4$ kyr. The coloured dashed lines correspond to times when outburst episodes are happening: $t = 5.6$ kyr and $t = 5.2$ kyr for the simulations ERF001 and ERF01, respectively. The disc inner region is gravitationally stable due to the high temperature, whereas the disc is unstable outside ~ 70 AU. The temperature peaks between 50 and 100 AU correspond to regions close to secondary objects.

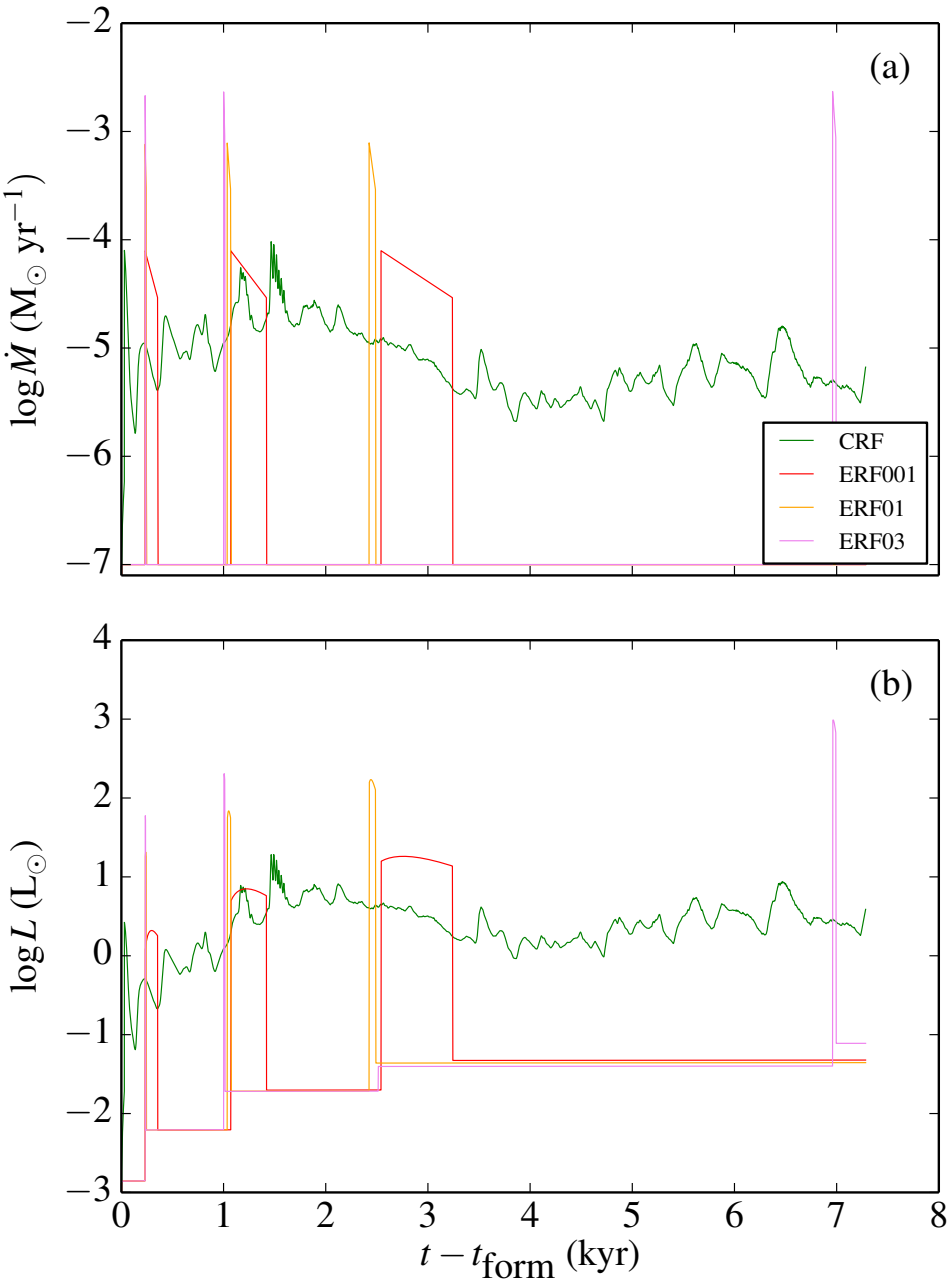

Figure 3.8: (a) Mass accretion rates onto and (b) accretion luminosities of the first secondary object that forms in each of the simulations where radiative feedback is considered. Time is given with respect to the formation time of each object. At their initial stages of their formation, secondary objects are high accretors and they may even outshine the central star. In the case where radiative feedback is episodic this only happens for a short time and therefore would be difficult to observe. In the case of continuous radiative feedback (which is probably not realistic) secondary objects may outshine the central star for longer.

Observations of episodic outbursts from secondary objects do not require high-sensitivity; during these outbursts their luminosity increases from a few $L_\odot$ to tens of $L_\odot$ (see Figure 3.8). In the case of $\alpha_{\rm MRI} = 0.01$, where the outburst events are mild and long, 18% of the initial 10 kyr of the disc's lifetime correspond to the outburst phase. On the other hand, when $\alpha_{\rm MRI} = 0.3$, where the events are short and intense, this percentage drops down to just 0.8% (see Table 3.3). However, episodic accretion events are expected to be relatively more frequent only during the initial stages of disc evolution, i.e. within a few kyr after the disc's formation, while the newly formed secondary objects are vigorously accreting gas from the disc. Therefore, such outbursts from secondary objects at the initial stages of disc evolution should not significantly influence the observed number of outbursting sources. Scholz et al. (2013) observed a sample of $\sim$ 4000 YSOs over a period of 5 years and they found $1-4$ possible outbursting sources indicating that outbursts happens at intervals of $(5-50)$ kyr; this is roughly consistent with the models presented here after the initial $\sim$ 4 kyr during the disc's evolution (see Figure 3.8).

Figure 3.7 shows a comparison between radially-averaged Toomre parameter, temperature and surface density for a representative snapshot from each simulation exhibiting strong spiral features ($t = 4.4$ kyr). Within the inner $\sim$ 25 AU, the disc is stable due to heating from the central star. The peaks in surface density and temperature around $\sim$ 50 AU correspond to regions around secondary objects. The discs are unstable or close to being unstable outside $\sim$ 80 AU in all cases apart from the CRF run and the ERF runs (during episodic outbursts).

In all simulations disc fragmentation occurs beyond radii $\sim$ 65 AU (see Figure 3.9a), where the disc is gravitationally unstable and can cool fast enough (e.g. Stamatellos & Whitworth 2009b). The initial mass of a fragment is a few M_J, as set by the opacity limit for fragmentation (Low & Lynden-Bell 1976; Rees 1976). The masses of the secondary objects at the end of the hydrodynamical simulations are shown in Figure 3.10.

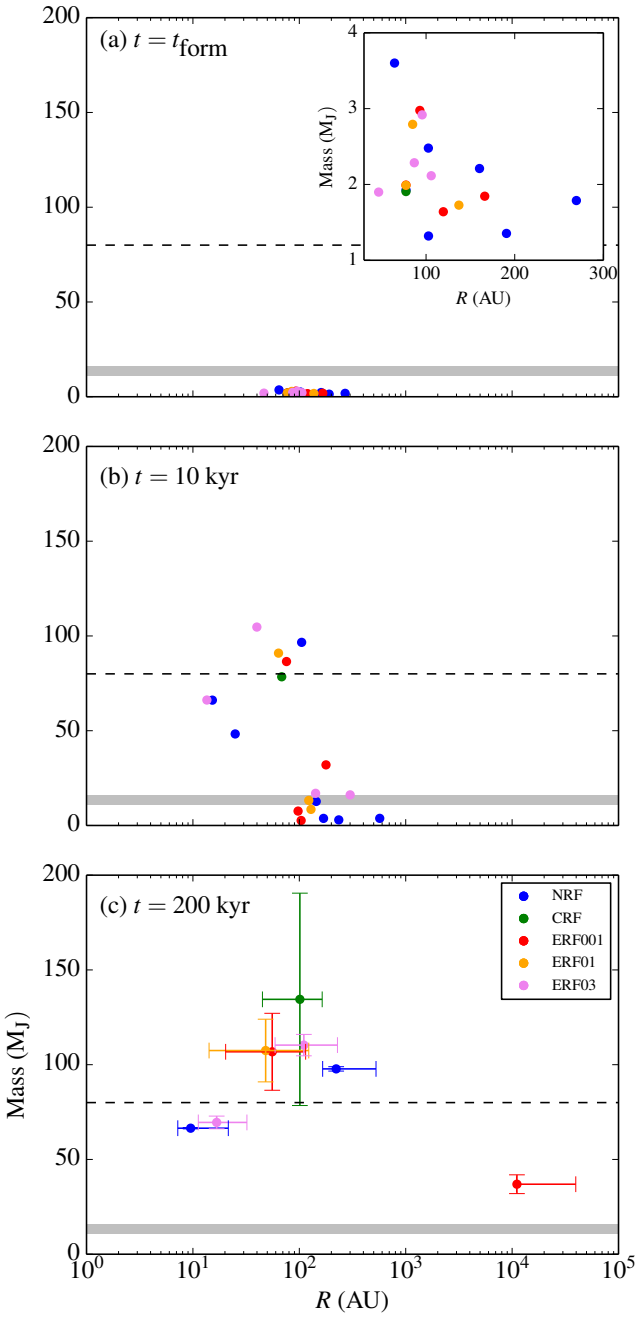

Figure 3.9: Mass-radius plots of the secondary objects formed by disc fragmentation in all 5 simulations. (a) Mass and radius at formation. A zoomed inset panel is shown for clarity. (b) Mass and radius at the end of the hydrodynamical simulation (10 kyr). (c) Mass and and semi-major axis at the end of the N-body simulation (200 kyr). The upper mass limits correspond to the maximum mass that the object may attain (see text for details), whereas the lower mass limits corresponds to the mass of the object at the end of the hydrodynamical simulation. The horizontal bars in this panel represent the periastron and apastron of the secondary object's orbit around the central star. The dashed line represents the hydrogen burning limit, and the grey band the deuterium burning limit ($\sim 11-16$ M_J; Spiegel et al. 2011).

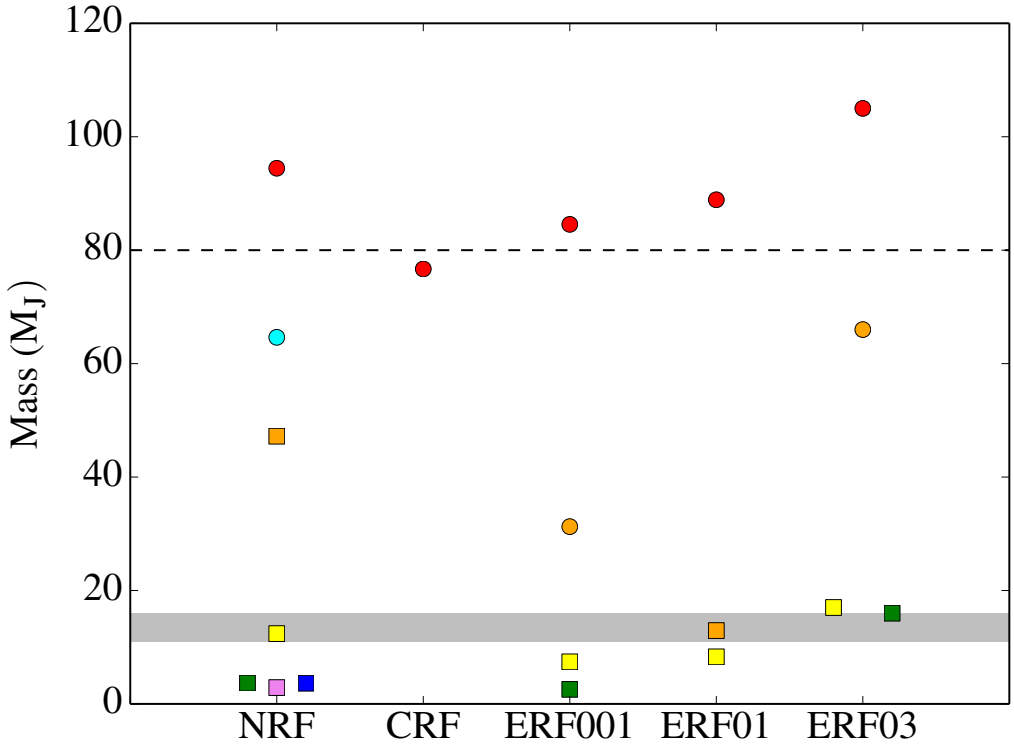

Figure 3.10: The masses of the secondary objects at the end of the hydrodynamic simulations (10 kyr). Colour denotes the order in which each secondary object formed; from earliest to latest: red, orange, yellow, green, cyan, blue, violet. Circles and squares correspond to objects that are ultimately bound or ejected (at 200 kyr), respectively. The lower points in the NRF and ERF003 simulations are separated for clarity. The dashed line represents the hydrogen burning limit (~ 80 M_J). The grey band represents the deuterium burning limit.

The first object that forms in each simulation generally migrates inwards and accretes enough mass to become a low-mass star; this object remains ultimately bound to the central star. All secondary objects increase in mass as they accrete gas from the disc. However, roughly half of the objects formed in each simulation (excluding continuous radiative feedback) remain as planets by the end of the hydrodynamical simulation as shown in Figure 3.10.

In the continuous radiative feedback simulation (CRF) the mass growth of the secondary object is mildly suppressed (Figures 3.11a,3.12a) due to an increased outward

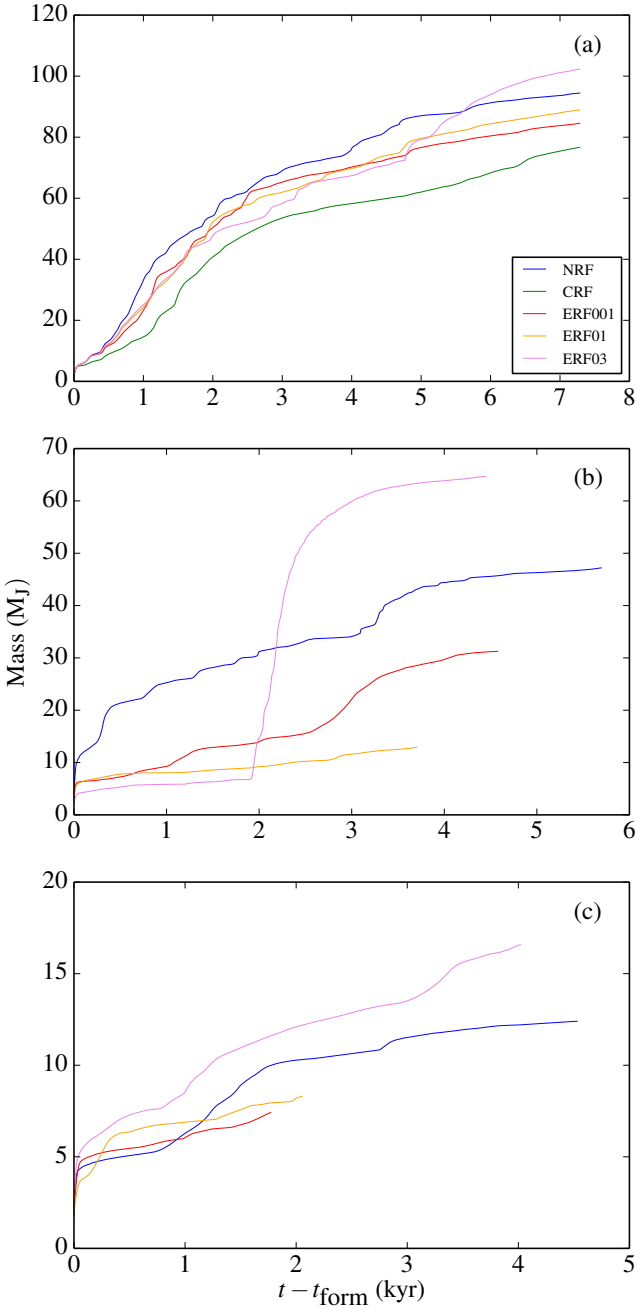

Figure 3.11: The mass evolution of the first 3 secondary objects that form in each of the 5 simulations (for the simulations with episodic radiative feedback the mass refers to the sink mass, i.e. both the object and the inner accretion disc). Time is given with respect to the formation time of each object. The second object in the ERF03 run (b) undergoes a rapid increase in mass as it migrates into a dense region around the central star.

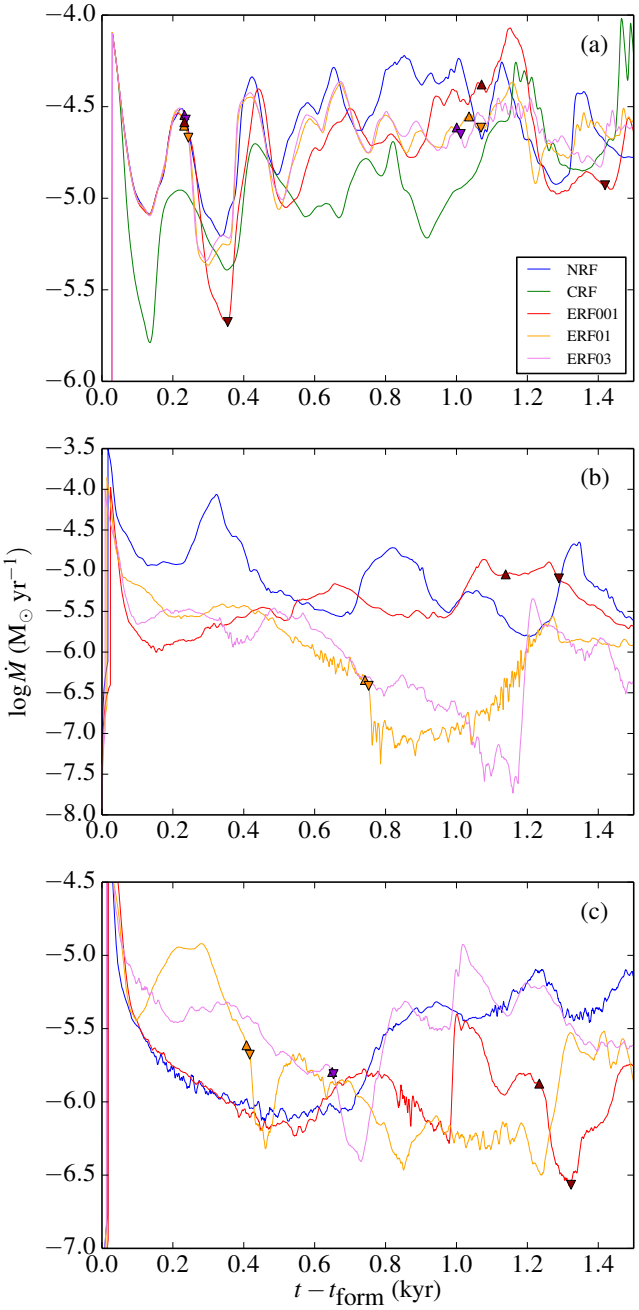

Figure 3.12: Mass accretion rates onto the first 3 secondary object that form in each of the 5 simulations (for the simulations with episodic radiative feedback the accretion rates onto the sinks are plotted). Time is given with respect to the formation time of each object. Upward pointing triangles represent the beginning of accretion episodes in the ERF runs. These are followed by corresponding downward pointing triangles denoting the end of episodes.

thermal pressure, so that the final mass of the object is within the brown dwarf regime. Secondary objects that form at later times tend to have lower masses (Figure 3.10).

Episodic feedback also mildly suppresses the mass growth of the first secondary object that forms (Figure 3.11a). Its effect is more pronounced for the second secondary object (Figure 3.11b). However, the mass growth of each object also depends on where the object forms in the disc and how it interacts both with other objects and with the spiral structure of the disc. Therefore, the mass growth of an object can be rather erratic, e.g. for the second object at around 2 kyr (Figure 3.11b). Specifically, this object migrates into the high density region surrounding the central star where it rapidly accretes a large amount of gas (see Figure 3.6, 7.2-8 kyr). The effect of episodic accretion is to suppress mass accretion during/after the outburst (e.g. Figure 3.12a compare NRF and ERF runs after the first outburst; also seen in Figures 3.12b, c). However, the accretion rate is restored to its previous value within $200-400$ yr. Ultimately, there is no strong anti-correlation between the mass that an object and the number and duration of the episodic outbursts it undergoes.

I find a population of planetary-mass objects on wide orbits ($100-800$ AU) around the central star. However, these objects are loosely bound to the central star and could be liberated into the field becoming free-floating planets. The evolution of these systems is followed using N-body simulations. Indeed I find that all planetary-mass objects are ejected from the discs (Figure 3.10c); what is left behind is a central star with a low-mass star or brown dwarf companion. Consequently, it is unlikely that the observed wide-orbit giant planets (Kraus et al. 2008, 2014; Marois et al. 2008; Faherty et al. 2009; Ireland et al. 2011; Kuzuhara et al. 2011, 2013; Aller et al. 2013; Bailey et al. 2014; Rameau et al. 2013; Naud et al. 2014; Galicher et al. 2014; Macintosh et al. 2015) may form by disc fragmentation, unless somehow the mass growth of secondary objects forming in the disc is suppressed. On the other hand disc fragmentation may readily produce free-floating planets and brown dwarfs (Stamatellos & Whitworth

2009b; Hao et al. 2013; Li et al. 2015; Vorobyov 2016).

Note however that in order to follow the long term evolution of the system, the effect of the gas has been ignored once the hydrodynamical simulation has evolved for 10 kyr. The effect of gas is to stabilise the system. Therefore it is possible that some of these planets may remain bound to the central star. However, they should co-exist with a higher mass object (e.g. a low-mass star or a brown dwarf) and they may accrete enough mass to become brown dwarfs.

3.4.5 Caveats of sink particles

Sink particles are used in the simulations to prevent large running times. In dense regions, time-steps become very short and without sinks the simulation effectively stalls.

In the presented simulations, a sink particle is created when the density exceeds 10^{-9} g cm^{-3}. It is therefore assumed that if a proto-fragment reaches this density it will continue to contract to heat to $\sim$ 2000 K such that molecular hydrogen dissociates to initiate the second collapse. The proto-fragment will ultimately reach stellar densities ($\sim$ 1 g cm^{-3}) to become a bound object. The density threshold used for sink creation is higher than the density required for the formation of the first hydrostatic core ($\sim$ 10^{-13} g cm^{-3}). Therefore, the proto-fragment at this stage contracts on a Kelvin-Helmholtz timescale. The time that it takes a proto-fragment to evolve from the first to second hydrostatic core is $\sim 1-10$ kyr (Stamatellos & Whitworth 2009). Thus, it is possible that some of the proto-fragments may get disrupted e.g. by interactions with spiral arms and/or tidal forces, and dissolve (Stamatellos & Whitworth 2009; Zhu et al. 2012; Tsukamoto et al. 2013).

Another limitation in the use of sink particles relates to their size. It is assumed that the sink radius of secondary objects that form in the disc is 1 AU, which roughly corresponds to the size of the first hydrostatic core during the collapse of a proto-fragment

(Masunaga & Inutsuka 2000; Tomida et al. 2013; Vaytet et al. 2013). The size of the Hill radius of proto-fragments that form in the disc is on the order of a few AU. Therefore, a significant fraction of the accretion disc around a proto-fragment is not resolved. The flow of material from the sink radius to the secondary object is considered to be instantaneous, but in reality there is a time delay. This results in increased accretion onto secondary objects, which in the case of continuous feedback, results in an increased luminosity. As such, the effect of luminosity on disc fragmentation may be overestimated. However, for the episodic accretion runs, a sub-grid model (within a sink radius) is employed based on an α-viscosity prescription that allows gas to flow (episodically) onto the secondary object (see Section 3.4.3). Even in this case, the accretion rate is possibly overestimated, as the inner accretion disc within the sink (< 1 AU) does not exchange angular momentum with the rest of the accretion disc (for an additional discussion of this issue see Hubber et al. 2013). Nevertheless, considering the uncertainties in $\alpha_{\rm MRI}$ (which in effect modulates the accretion of material onto the secondary objects and for which I examine a wide range of values, all of which lead to similar outcomes) I have confidence that the choice of sink size does not qualitatively affect the results of this work regarding the effect of radiative feedback on disc fragmentation.

3.5 Conclusions

I have performed SPH simulations of gravitationally unstable protostellar discs which investigate the effect that radiative feedback from secondary objects formed by fragmentation has on disc evolution. I have considered three cases of radiative feedback from secondary objects: (i) No radiative feedback: where no energy from secondary objects is fed back into the disc. (ii) Continuous radiative feedback: where energy, produced by accretion of material onto the surface of the object is continuously fed

back into the disc. (iii) Episodic radiative feedback: where accretion of gas onto secondary objects is episodic, resulting in episodic radiative feedback. The findings are summarised as follows.

- Radiative feedback from secondary objects that form through gravitational fragmentation stabilises the disc, reducing the likelihood of subsequent fragmentation. When there is no radiative feedback from secondary objects, 7 objects form, compared to a single object forming when radiative feedback is continuous. When radiative feedback happens in episodic outbursts, $3-4$ objects form. This is because the disc cools sufficiently to become gravitationally unstable between the outbursts. All objects in the three different radiative feedback cases that I examine here form at radii > 65 AU, with initial masses of a few M_J.

- The mass growth of secondary objects is mildly suppressed due to their radiative feedback. The mass of the first object that forms within the disc is generally larger when there is no radiative feedback; in the case when radiative feedback is continuous the mass of the first secondary object is the lowest. Episodic radiative feedback tends to reduce the mass accretion rate onto a secondary object during and after an episode outburst. However, the accretion rate is restored to its previous value relatively quickly (within $\sim 200-400$ yr).

- The intensity and the duration of an outburst (which is determined by the effective viscosity due to the magnetorotational instability, $\alpha_{\rm MRI}$) does not affect the number of objects that form within the disc when episodic radiative feedback is considered. The total duration of the radiative feedback outbursts is not long enough to fully suppress disc fragmentation. However, I find that $\alpha_{\rm MRI}$ affects the average mass of the objects formed: lower $\alpha_{\rm MRI}$ results into lower mass secondary objects. Moreover, subsequent fragmentation happens faster for higher $\alpha_{\rm MRI}$, as the first outburst finishes faster. The first object that forms in each case undergoes a larger inward migration for increased values of $\alpha_{\rm MRI}$.

- Regardless of the type of radiative feedback, I find that the first object that forms within the disc remains ultimately bound to the central star. It accretes mass while it generally migrates inwards. Brown dwarfs also form in the simulations and a fraction of them remain bound to the central star. Gravitational fragmentation may therefore provide a method for the formation of intermediate separation, low-mass-ratio binary systems.

- A significant fraction ($\sim$ 40%, dropping to $\sim$ 20% if the estimated final mass is considered) of the secondary objects formed by disc fragmentation are planets, regardless of the type of radiative feedback. However, every planet that forms within the disc is ultimately ejected from the system. I do not find any giant planets that remain on wide-orbits around the central star. Secondary objects that form and remain within the disc accrete enough mass to become brown dwarfs, even in the case where radiative feedback suppresses gas accretion. Thus, gravitational fragmentation may produce free-floating planets and brown dwarfs, but not wide-orbit gas giant planets, unless the mass growth of fragments forming in a young protostellar disc is further suppressed.

Chapter 4

Efficient radiative transfer techniques in hydrodynamic simulations

4.1 Introduction

Full 3-dimensional, wavelength dependent radiative transfer within hydrodynamic simulations is computationally expensive (e.g. Harries 2015; Harries et al. 2017). It is only typically used to post-process snapshots of simulations to produce synthetic observations (e.g. RADMC-3D; Dullemond 2012). However, the inclusion of radiative transfer is important when an accurate treatment of the thermal evolution of the system is needed.

There are various methods which efficiently include approximate radiative transfer in hydrodynamic simulations, each with their underlying simplifying assumptions (Oxley & Woolfson 2003; Whitehouse & Bate 2004; Stamatellos et al. 2007b; Forgan et al. 2009b; Young et al. 2012; Lombardi et al. 2015). There are two main types of approach: (i) using the diffusion approximation (e.g. Whitehouse & Bate 2004; Boley et al. 2006; Commerçon et al. 2011b,a), a method which may still be computationally expensive, or (ii) use a metric to estimate the optical depth for each element of

the fluid and hence the heating/cooling rate (Stamatellos et al. 2007b; Forgan et al. 2009b; Young et al. 2012; Lombardi et al. 2015). Another method that is used in the context of protostellar discs is the β-cooling approximation (e.g. Gammie 2001; Rice et al. 2003b). This method assumes that the temporal evolution of the specific internal energy, u, is inversely proportional to the cooling time such that $\dot{u} = -u/t_{\rm cool}$. The cooling time is set inversely proportional to the Keplerian frequency with a constant β, i.e. $t_{\rm cool}(R) = \beta\Omega^{-1}(R)$, where R is the distance from the central star as measured on the disc midplane. This method over-simplifies the underlying physics but comes at low computational cost.

Stamatellos et al. (2007b) proposed a radiative transfer method which uses the gravitational potential and the density of gas as a metric to estimate the optical depth through which a gas element cools. This is then used to calculate an estimated cooling rate, and, in the optically thick case, reduces to the diffusion approximation. The method works well for roughly spherical systems and results in an increase of computational time by less than $\sim 5\%$. However, Wilkins & Clarke (2012) showed that the cooling rate calculated with the Stamatellos et al. (2007b) method can be systematically underestimated in the optically thick midplane of protostellar discs. Therefore, the Stamatellos et al. (2007b) method may not be suitable to provide accurate cooling rates in non-spherical systems. This method has been combined with flux-limited diffusion to increase accuracy in high-optical depth regions (e.g. Forgan et al. 2009b).

Young et al. (2012) proposed a method, in the context of protostellar discs, that uses the gravitational potential in the z direction only, i.e. out of the disc midplane. From this, they obtain accurate estimates (within a few tens of percent) of column density and optical depths. However, when fragments form due to the gravitational instability in massive discs, the Stamatellos et al. (2007b) gives better estimates of the cooling rates within the dense fragments, which can be assumed to be approximately spherical.

Instead of using the gravitational potential to estimate the optical depth, Lombardi et al. (2015) proposed to use the pressure scale-height. This retains the majority of the characteristics of the original Stamatellos et al. (2007b) method, merely employing a different metric to estimate optical depth. It is shown to provide a much more accurate estimate of cooling rate in spherical polytropes and protostellar discs with specified density and temperature profiles. The reader is directed to Section 2.2 for a detailed comparison of the two methods.

The aim of this chapter is to compare how the above methods (Stamatellos et al. 2007b; Lombardi et al. 2015) behave when applied to actual hydrodynamic simulations. I test the two methods in the context of collapsing clouds and protostellar discs. In the case of the latter, I consider relaxed discs, discs with spiral arms, discs with clumps, and discs with embedded planets which carve gaps. I also examine whether the β-cooling method, which is widely used for protostellar discs, provides a good approximation to the thermal physics. Such tests of different methods are needed as radiative transfer plays a critical role in many cases (e.g. disc fragmentation and gap opening in discs with planets).

Section 4.2 shows the comparison between the aforementioned methods for the collapse of spherically-symmetric cloud. I test the behaviour of both methods for protostellar discs in Section 4.3 and for discs with embedded planets in Section 4.4. A discussion on the performance of the β-cooling approximation is presented in Section 4.5. A comparison to demonstrate the effect on dynamical evolution from the two radiative transfer methods discussed, as well as the β-cooling approximation, is presented in Section 4.6. The results are summarised in Section 4.7.

4.2 Cloud collapse

I utilise the Graphical Astrophysics code for N-body Dynamics and Lagrangian Fluids (GANDALF, Hubber et al. 2018) to perform simulations of a collapsing molecular cloud,

using the Stamatellos et al. (2007b) and Lombardi et al. (2015) methods of estimating optical depths. The cloud is initially static, has a mass of 1.5 $M_\odot$ and is isothermal with a temperature 5 K. The cloud is represented by $N \approx 2 \times 10^6$ SPH particles distributed such that the density profile of the cloud is uniform across its radius $R_{\rm cloud} = 10^4$ AU.

Figure 4.1 shows the evolution of the central density and temperature for the two methods of estimating optical depths. Initially, the cloud collapses almost isothermally and the core temperature increases slowly with increasing density. The core temperature starts to increase rapidly as the cloud becomes optically thick ($\rho \sim 10^{-13}$ g cm^{-3}). At $\sim$ 100 K the rotational degrees of freedom of molecular hydrogen are excited and the temperature increases at a slower rate as the gravitational energy is diverted away from heating the cloud. The increasing temperature leads to increased thermal pressure that is able to slow down the collapse and the first hydrostatic core forms (Larson 1969; Masunaga & Inutsuka 2000; Whitehouse & Bate 2006; Stamatellos et al. 2007b). The first core contracts and heats slowly to $\sim$ 2000 K at which point hydrogen begins to dissociate. This results in the second collapse and the formation of the second hydrostatic core (the protostar).

The Lombardi et al. (2015) method gives similar results regarding the central density and temperature of the cloud with the Stamatellos et al. (2007b) method, which in turn compares very well with the Masunaga & Inutsuka (2000) method, indicating that both methods work reasonably well for spherical geometries. The second collapse in the case of the Stamatellos et al. (2007b) method is delayed by $\sim$ 100 yr, which may arise due to a slight over-estimate in optical depth and thus less efficient cooling, as can be seen from the slightly higher temperatures calculated by this method (see Figure 4.1).

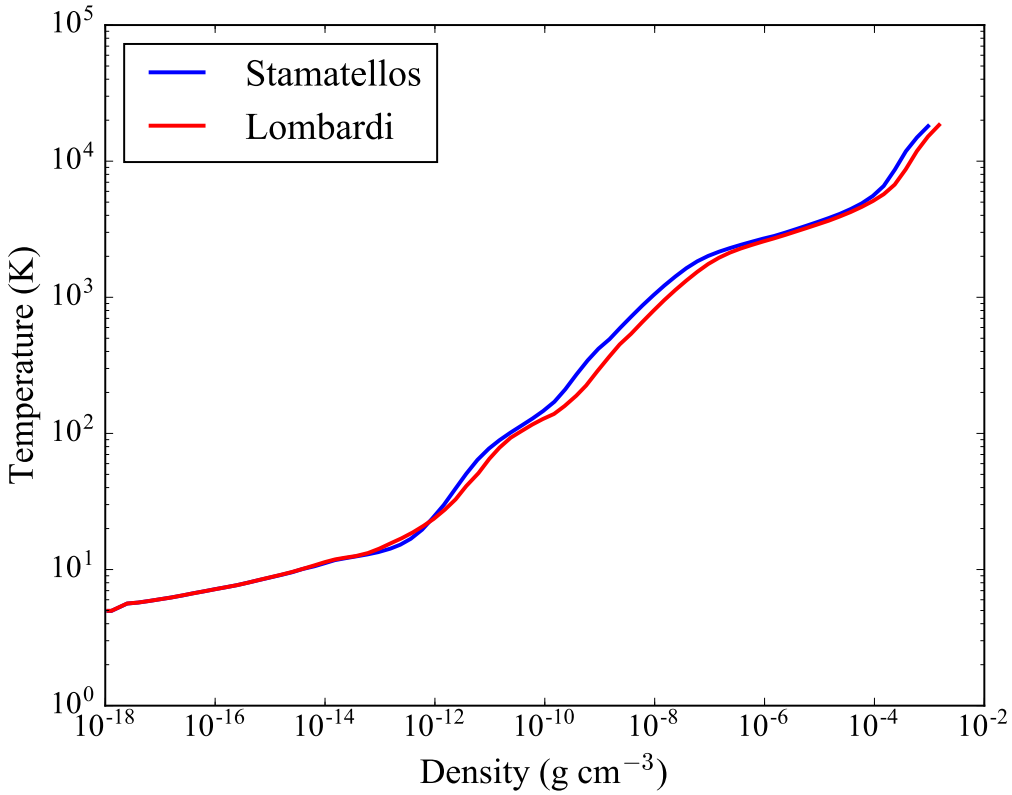

Figure 4.1: The evolution of central temperature as a function of central density for the collapse of an initially isothermal, non-rotating, 1.5 $M_{\odot}$ cloud with a radius of 10^4 AU. The radiative transfer methods of Stamatellos et al. (2007b) and Lombardi et al. (2015) are in good agreement.

4.3 Protostellar discs

Protostellar discs form due to the turbulence and/or initial rotation of their progenitor molecular clouds. Their study is important as they are the birthplace of planets, which can form either through core accretion (e.g. Safronov & Zvjagina 1969; Lissauer 1993), or by gravitational fragmentation of discs (Whitworth & Stamatellos 2006; Stamatellos et al. 2007a; Stamatellos & Whitworth 2009b; Kratter et al. 2010; Zhu et al. 2012). Massive protostellar discs fragment if two conditions are met: (i) They are gravitationally unstable i.e.

$$Q \equiv \frac{\kappa c_s}{\pi G \Sigma} < Q_{\rm crit}, \tag{4.1}$$

where Q is the Toomre parameter (Toomre 1964), κ is the epicyclic frequency, c_s is the local sound speed and Σ is the disc surface density. The value of $Q_{\rm crit}$ is on the order of unity. (ii) They cool sufficiently fast, i.e. $t_{\rm cool} < (0.5-2)t_{\rm orb}$, where $t_{\rm orb}$ is the local orbital period (Gammie 2001; Johnson & Gammie 2003; Rice et al. 2003b, 2005). Both requirements are dependent on the thermal properties of the disc, and so it is important that the cooling rate and the disc temperature are accurately calculated with the employed radiative transfer method.

Here I present comparisons of estimated optical depth and cooling rate obtained via the Stamatellos et al. (2007b) and Lombardi et al. (2015) radiative transfer methods. In Section 4.3.1 I present the comparison methodology. Section 4.3.2 considers a low-mass relaxed disc and Section 4.3.3 considers a high-mass disc which fragments forming spiral arms (Section 4.3.4) and eventually gravitationally bound clumps (Section 4.3.5).

4.3.1 Methodology

The Graphical Astrophysics code for N-body Dynamics and Lagrangian Fluids (GANDALF, Hubber et al. 2018) is utilised to perform simulations of protostellar discs (Section 4.3)

and protostellar discs with embedded planets (Section 4.4). From these simulations, snapshots are selected for which the behaviour of the Stamatellos et al. (2007b) and Lombardi et al. (2015) radiative transfer methods are compared.

The estimated column density for both the gravitational potential and pressure scale-height metrics, $\bar{\Sigma} \equiv \Sigma_{\rm est}$, is found by post-processing a snapshot of the GANDALF hydrodynamic simulation. The corresponding estimated optical depth is $\bar{\tau} \equiv \tau_{\rm est} = \Sigma_{\rm est}\bar{\kappa}_{\rm R}$, where $\bar{\kappa}_{\rm R}$ is the mass-weighted opacity for each method (note that this is slightly different for the two methods, see Lombardi et al. (2015)). The column density and optical depth are calculated for each particle in the simulation. It should be emphasised that the optical depths and cooling rates are calculated for the same snapshots for both methods, i.e. using the same density and temperature disc configurations. Azimuthally-averaged radial profiles of the optical depth and cooling rates at the disc midplane (defined such as $|z| < 0.5$ AU) are constructed. Similarly, profiles vertical to the disc midplane are also constructed.

The actual values of column density and optical depth are calculated by integrating from a given gas element to the disc surface along the z-axis (perpendicular to the disc midplane) such that $\Sigma_{\rm actual} = \int \rho \, {\rm d}z$ and $\tau_{\rm actual} = \int \kappa(\rho, T)\rho \, {\rm d}z$.

The estimated cooling rate per unit mass can then be found via Equation 3.2. This is normalised with respect to $4\sigma_{\rm SB}\left(T^4 - T_{\rm BGR}^4\right)$ such that the quantity

$$\dot{u}_{\rm est} \equiv -\left.\frac{{\rm d}u}{{\rm d}t}\right|_{\rm est} \frac{1}{4\sigma_{\rm SB}\left(T^4 - T_{\rm BGR}^4\right)} = \frac{1}{\bar{\Sigma}^2\bar{\kappa}_{\rm R} + \kappa_{\rm P}^{-1}}, \tag{4.2}$$

represents the estimated cooling-rate per unit mass. This is compared with the actual cooling-rate per unit mass which is calculated using the actual optical depth and column density, hence

$$\dot{u}_{\rm actual} \equiv -\left.\frac{{\rm d}u}{{\rm d}t}\right|_{\rm actual} \frac{1}{4\sigma_{\rm SB}\left(T^4 - T_{\rm BGR}^4\right)} = \frac{1}{\Sigma\left(\tau_{\rm R} + \tau_{\rm P}^{-1}\right)}, \tag{4.3}$$

where $\tau_{\rm R}$ and $\tau_{\rm P}$ are the optical depths calculated using the Rosseland-mean and Planck-mean opacities, respectively (which in many cases are assumed to be the same). It should be noted that the above equation is itself an approximation to the diffusion approximation (Mihalas 1970) in which the radiative flux is

$$F = -\frac{4}{3\kappa_{\rm R}\rho}\nabla\left(\sigma_{\rm SB}T^4\right). \tag{4.4}$$

From this, the cooling rate per unit mass can be obtained

$$\dot{u} = \frac{1}{\rho}\nabla\cdot F \approx \frac{\sigma_{\rm SB}T^4}{\kappa_{\rm R}\Sigma^2} \approx \frac{\sigma_{\rm SB}T^4}{\tau_{\rm R}\Sigma}, \tag{4.5}$$

and has the same form of Equation 4.3 in the optically thick limit.

4.3.2 Relaxed low-mass disc

I simulate a protostellar disc with a mass of 0.01 $\rm M_\odot$ around a 1 $\rm M_\odot$ protostar. $N \approx 2\times10^6$ SPH particles are distributed between radii of 5 and 100 AU such that the initial column density and temperature profiles follow $\Sigma(R) \propto R^{-1}$ and $T(R) \propto R^{-1/2}$, respectively. The temperature at 1 AU from the central star is $T_0 = 250$ K. The disc is heated by an ambient radiation field of 10 K.

A steady-state is reached after a few outer orbital periods, shown in Figure 4.2a. The disc is optically thin, thus both the Stamatellos and Lombardi methods provide accurate cooling rate estimates (see Figure 4.2b). However, the Stamatellos method generally overestimates the optical depth, especially in the inner disc, consequently underestimating the cooling rate. I also take an annulus of the disc between 34 and 36 AU and show the azimuthally-averaged vertical profiles of optical depth and cooling rate (Figure 4.2d, e). The cooling rate from the disc midplane to the surface is accurately estimated as the region is optically thin. In this regime, the optical depth is not important for calculating the cooling rate (see Equation 3.2).

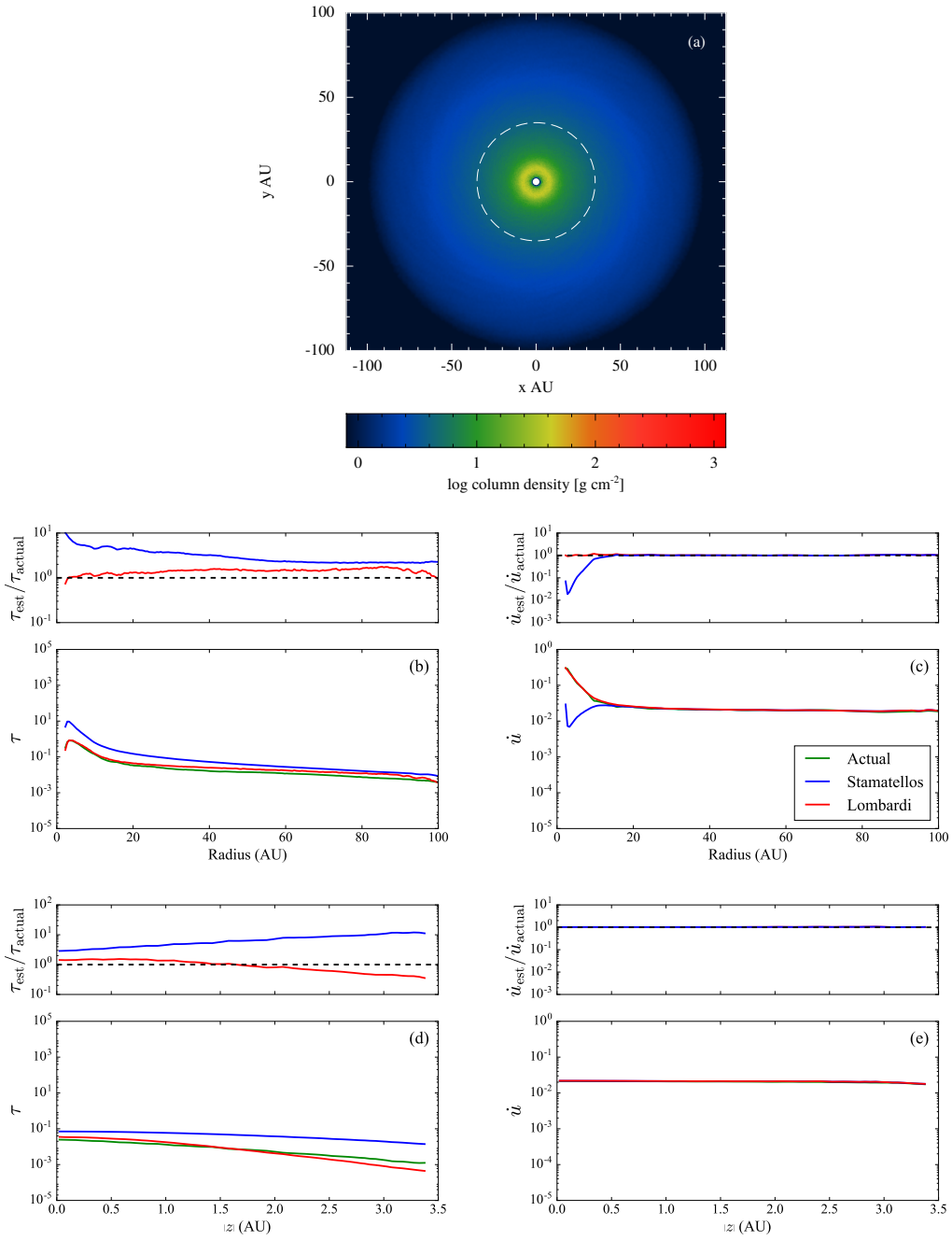

Figure 4.2: A low-mass disc which has evolved for a few outer orbital periods and has reached a steady-state. Panel (a): a column density snapshot where the dashed white line represents the radius at which an analysis perpendicular to the disc midplane is performed. Panels (b) and (c): comparisons of azimuthally-averaged optical depth and cooling rate at the disc midplane ($|z| < 0.5$ AU). Panels (d) and (e): azimuthally-averaged optical depth and cooling rate perpendicular to the disc midplane for a radial annulus of $34 - 36$ AU. The upper plots in panels (b-e) show the ratio between estimated and actual values. The black dashed lines represent equality. The disc is optically thin, and as such, both methods give good estimates of the cooling rate. The Stamatellos method generally overestimates the optical depth at the disc midplane, especially in the inner disc region, consequently underestimating the cooling rate.

4.3.3 High-mass disc

I simulate a massive protostellar disc which develops spiral features, undergoes fragmentation, forming dense, gravitationally-bound clumps. The disc has an initial mass of 0.2 $M_\odot$ and attends a 0.8 $M_\odot$ protostar. $N \approx 2 \times 10^6$ SPH particles are distributed between radii of 5 and 100 AU such that the initial column density and temperature profiles follow $\Sigma(R) \propto R^{-1}$ and $T(R) \propto R^{-1/2}$, respectively. The temperature at 1 AU from the central star is $T_0 = 250$ K. The disc is heated by an ambient radiation field of 10 K.

Figure 4.3a shows the column density of the disc before any significant dynamical evolution occurs. The disc midplane is optically thick (out to a radius of ~ 30 AU), but the optical depth does not drop below $\tau = 0.1$ further out (Figure 4.3b). The Stamatellos method overestimates the optical depth by a factor of a few throughout the disc. The Lombardi method yields a better estimate for both the optical depth and the cooling rate. Similar results are found when considering the vertical profiles of these quantities in a radial annulus between 34 and 36 AU (Figure 4.3d, e).

4.3.4 High-mass disc with spiral arms

After some time, the disc becomes unstable and spiral arms begin to form. This is shown in Figure 4.4a. The optical depth and cooling rate at the disc midplane are well described by the Lombardi method, but are over- and underestimated, respectively, by the Stamatellos method. The cooling rate estimated by the Stamatellos method is in agreement with the actual value when the disc is optically thin (Figure 4.4b). Two cylindrical regions with base radius of 5 AU are considered wherein vertical analyses are performed: one cylinder is inside a spiral arm and and the other outside (see marked regions in Figure 4.4a). Outside the spiral arm, the disc is optically thin and the cooling rate is estimated well by both methods (Figure 4.4e, dashed lines). However, inside the spiral arm where the disc is optically thick, the Stamatellos method

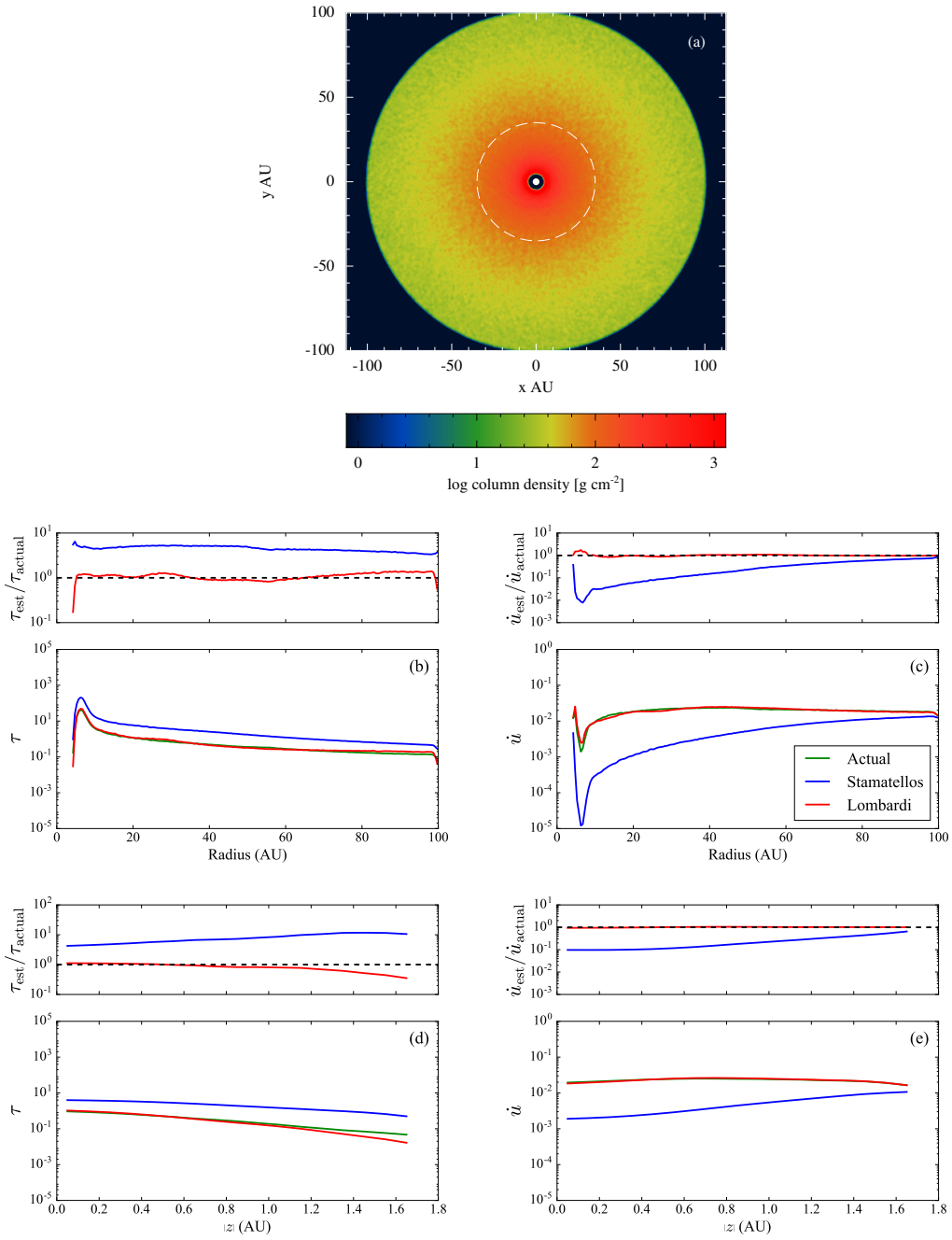

Figure 4.3: A high-mass disc which has not yet undergone significant evolution. Panel (a): a column density snapshot where the dashed white line represents the radius at which an analysis perpendicular to the disc midplane is performed. Panels (b) and (c): comparisons of azimuthally-averaged optical depth and cooling rate at the disc midplane. Panels (d) and (e): azimuthally-averaged optical depth and cooling rate perpendicular to the disc midplane for a radial annulus of $34-36$ AU. The upper plots in panels (b-e) show the ratio between estimated and actual values. The black dashed lines represent equality. The Stamatellos method overestimates the optical depth at the disc midplane by a factor ~ 5 at all disc radii, but the Lombardi method yields a more accurate estimate. This is reflected in the cooling rate. Similar results are found when considering the optical depth and cooling profiles perpendicular to the disc midplane (d-e).

overestimates the optical depth and therefore the cooling rate. The Lombardi method provides more accurate values for both quantities (Figure 4.4e, solid lines).

4.3.5 High-mass disc with clumps

The disc eventually fragments and dense clumps form. The column density snapshot in Figure 4.5a contains four clumps. The central density of the densest clump is $\sim 10^{-6}$ g cm^{-3} and for the least dense clump is $\sim 10^{-10}$ g cm^{-3}. Figure 4.5b shows that both the Stamatellos and Lombardi methods give good estimates of the azimuthally-averaged optical depth at the disc midplane, but it should be noted that an azimuthally-averaged analysis is not ideal for describing this disc, as it is highly non-axisymmetric. Therefore I focus on two of the clumps: the inner, densest clump, and the least dense clump. A cylinder with base radius of 5 AU centered on each of these clumps and a vertical analysis in the direction perpendicular to the disc midplane. Figure 4.5d shows the optical depth comparison. For the least dense clump (dashed lines), the Stamatellos method is accurate in the center of the clump. The Lombardi method overestimates the optical depth by a factor ~ 2. In the center of the densest clump, both methods are inaccurate, but only by a factor of a few. In general - for the disc as a whole as well as the clumps - the Lombardi method estimates the cooling rate well, whilst the Stamatellos method systematically underestimates the cooling rate.

4.4 Protostellar discs with embedded planets

The gravitational interaction between a planet and the surrounding disc may result in the formation of planet-induced gaps (e.g. Goldreich & Tremaine 1980; Lin & Papaloizou 1993; Bryden et al. 1999; Kley & Nelson 2012). Such structures may provide indirect evidence for the presence of planets in discs. The Crida et al. (2006) semi-analytical criterion for gap formation involves the balance between the tidal torque

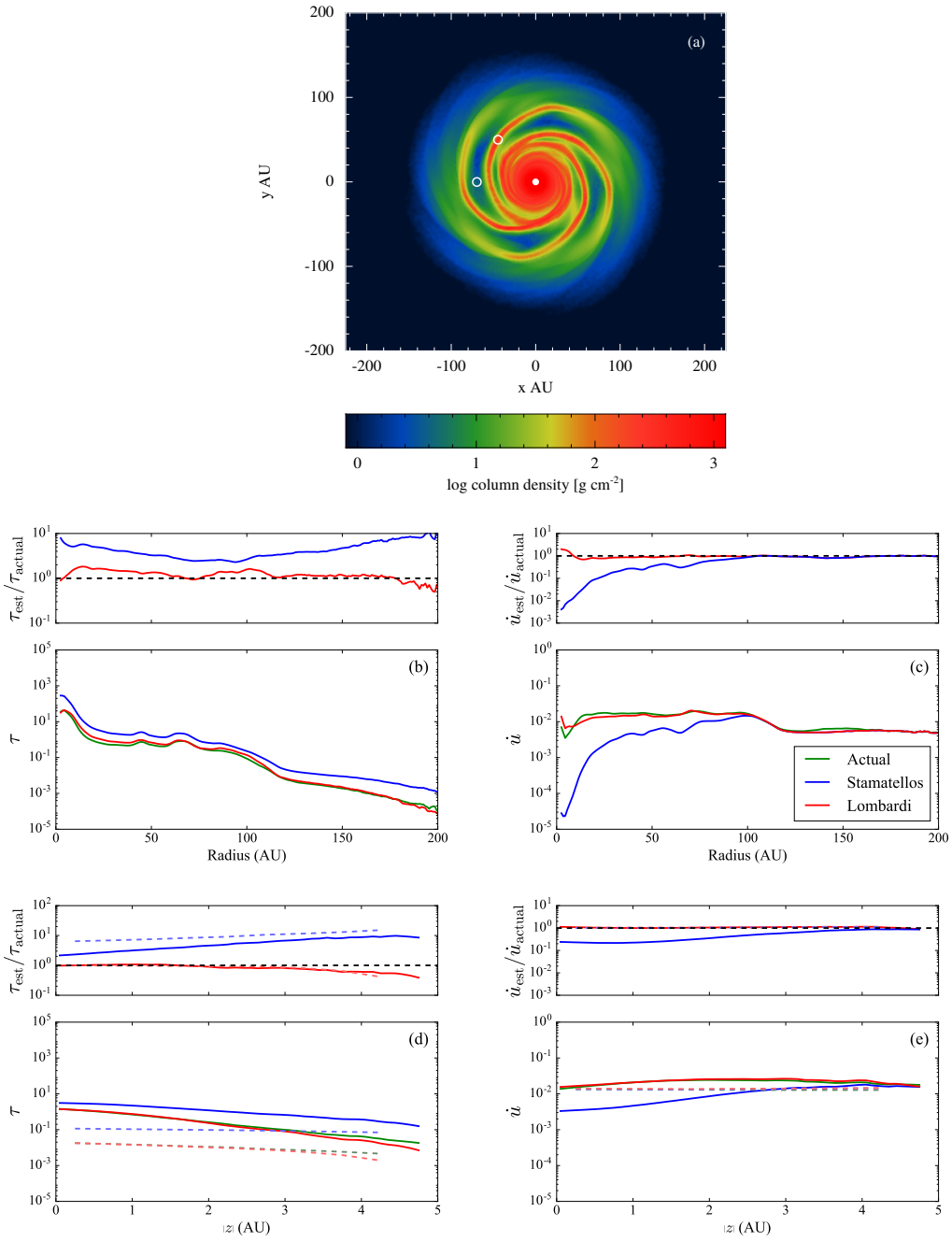

Figure 4.4: A high-mass disc which has evolved to form spiral arms. Panel (a): a column density snapshot. White circles represent cylindrical regions where an analysis perpendicular to the disc midplane is performed. Panels (b) and (c): comparisons of azimuthally-averaged optical depth and cooling rate at the disc midplane. Panels (d) and (e): optical depth and cooling rate comparisons perpendicular to the disc midplane inside (solid lines), and outside (dashed lines) of a spiral arm. The upper plots in panels (b-e) show the ratio between estimated and actual values. The black dashed lines represent equality. The optical depth and cooling rate at the disc midplane are well estimated by the Lombardi method at all disc radii, but are over- and underestimated by the Stamatellos method, respectively. Vertically to the disc midplane, the same result is observed within a spiral arm. However, outside of the spiral arms, where the disc is optically thin, both methods yield a good estimate for the cooling rate.

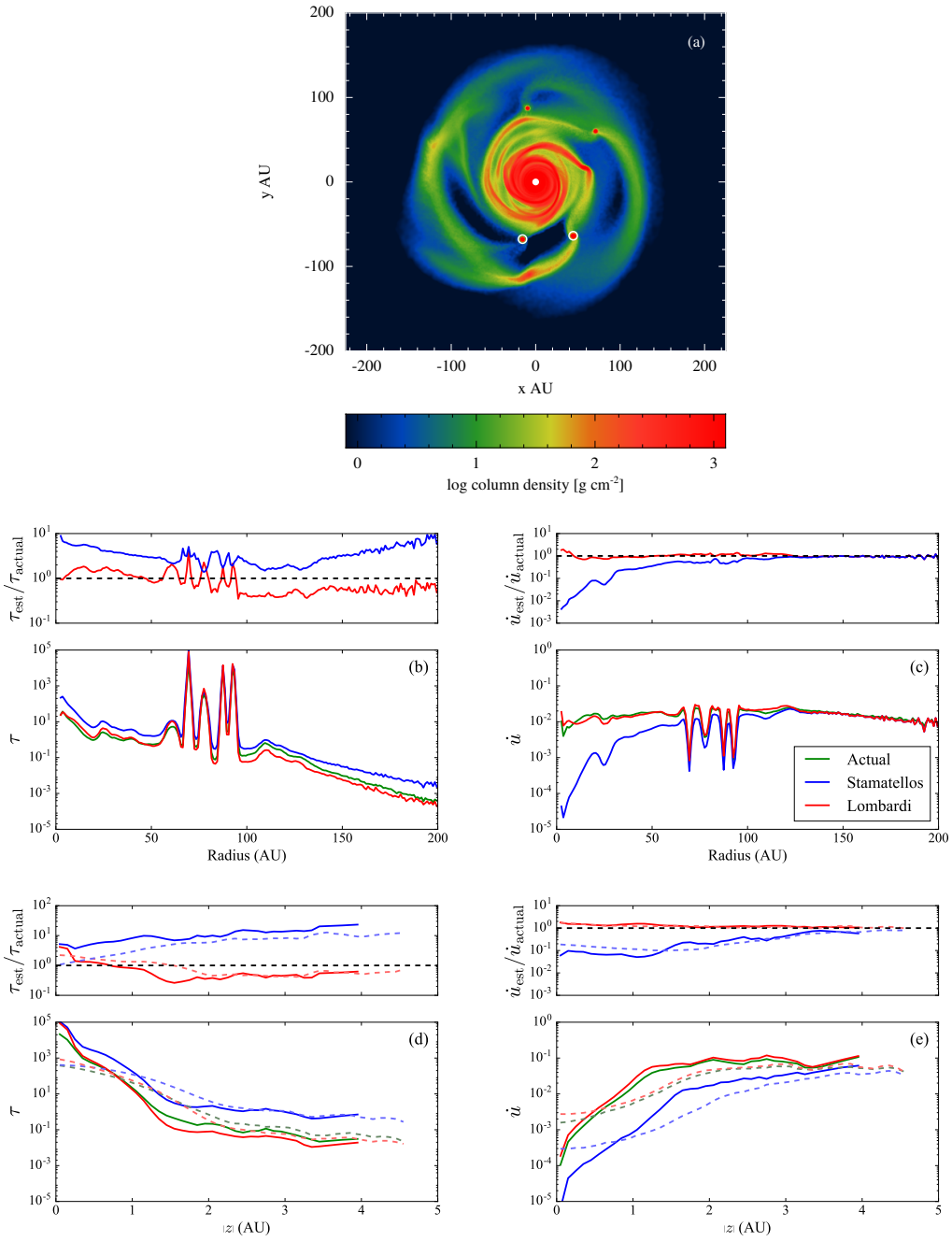

Figure 4.5: A high-mass disc which has evolved to form dense clumps. Panel (a): a column density snapshot. White circles represent regions where vertical analyses are performed. Panels (b) and (c): comparisons of azimuthally-averaged optical depth and cooling rate at the disc midplane. Panels (d) and (e): optical depth and cooling rate comparisons perpendicular to the disc midplane for the densest clump (solid lines), and the least dense clump (dashed lines). The upper plots in panels (b-e) show the ratio between estimated and actual values. The black dashed lines represent equality. The optical depth is generally overestimated by the Stamatellos method. The Lombardi method gives a better estimate, even within the dense clump. The cooling rate is also estimated more accurately.

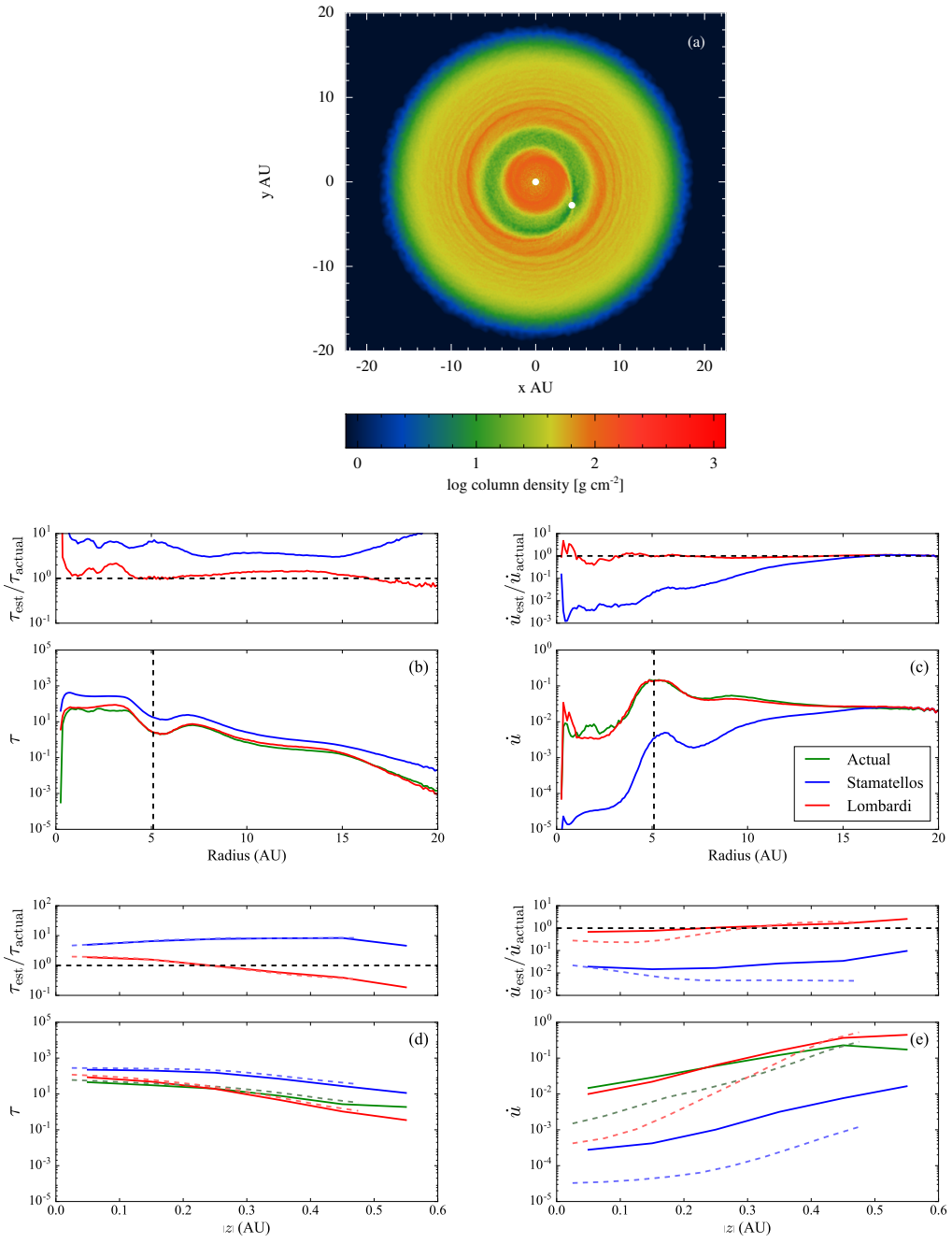

Figure 4.6: A disc which has an embedded 1.4 M_J planet at a radius of 5.1 AU. Panel (a): a column density snapshot. Panels (b) and (c): comparisons of azimuthally-averaged optical depth and cooling rate at the disc midplane. The vertical black dashed lines in panels (b) and (c) represent the location of the planet. Panels (d) and (e): optical depth and cooling rate comparisons perpendicular to the disc midplane between radial annuli of $4-6$ AU (in the gap, solid lines), and $3-4$ AU (interior to the gap, dashed lines). Gas within $R_{\rm HILL} = 0.6$ AU of the planet is excluded when analysing the gap. The upper plots in panels (b-e) show the ratio between estimated and actual values. The black dashed lines represent equality. The Stamatellos method overestimates the optical depth by a factor of 3 or more throughout the disc. The Lombardi method estimates the optical depth within a factor of 2, and it also gives an accurate estimate of the cooling rate, both inside and outside the planet-induced gap.

which opens the gap and the viscous torque which closes the gap. It has been shown that planets with masses down to 10 $M_\oplus$ can open gaps (Duffell & MacFadyen 2012). However, for migrating planets, a gap must form on a rapid enough timescale. Malik et al. (2015) argue that a gap can only form provided the gap opening time is longer than the migration timescale of the planet. The accurate treatment of the radiative transfer in such planet-disc systems is important and may play a significant role when determining the rate and the direction (i.e. inwards or outwards) of migration, and the final mass of the planet (Stamatellos 2015; Benítez-Llambay et al. 2015; Stamatellos & Inutsuka 2018).

Here I examine two cases of protostellar discs with embedded planets: one with an embedded 1.4 M_J planet (§4.4.1) and one with an embedded higher-mass, 11 M_J, planet (§4.4.2). I compare the estimated optical depth and cooling rate obtained via the Stamatellos et al. (2007b) and Lombardi et al. (2015) radiative transfer methods.

4.4.1 Disc with an embedded 1.4 M_J planet

I consider a disc with an initial mass 0.005 $M_\odot$ surrounding a 1 $M_\odot$ protostar. A 1 M_J mass planet is embedded within the disc at a radius of 5.2 AU. The initial disc extends out to 15.6 AU with a surface density profile $\Sigma(R) \propto R^{-1/2}$ (e.g. Bate et al. 2003), temperature profile $T(R) \propto R^{-3/4}$, and is represented by 10^6 SPH particles. The temperature at 1 AU from the central star is $T_0 = 250$ K. The planet migrates slightly inwards (0.1 AU) and increases in mass by accreting gas from the disc. At the snapshot presented here (Figure 4.6a) the planet is at 5.1 AU and has carved out a gap between 4 and 6 AU. Its mass has increased to 1.4 M_J.

The density of the disc is high and as such, the disc is optically thick (Figure 4.6b). The Stamatellos method overestimates the optical depth at the disc midplane throughout the disc by a factor of a few, whilst the Lombardi method provides a better estimate

(accurate within a factor of ~ 2). This is reflected in the estimated cooling rates (Figure 4.6c).

Vertical profiles are shown for radial annuli at the planet gap (4—6 AU; Figure 4.6d, e - solid lines) as well as on a region interior to the gap ($3-4$ AU, Figure 4.6d, e - dashed lines). The gas within the Hill radius ($R_{\rm HILL} = 0.6$ AU) of the planet is excluded when analysing the gap region. Both of these regions are optically thick. Again, the Lombardi method provides a better estimate for the optical depth and cooling rate.

In the gap region, which is important for the evolution of the planet, the Lombardi method is very accurate, whereas the Stamatellos method overestimates the optical depth, and therefore underestimates the cooling rate.

4.4.2 Disc with an embedded 11 M_J planet

I consider a system comprising a star which has an initial mass 1 $M_\odot$, that is attended by a protostellar disc with mass 0.1 $M_\odot$ and initial radius 100 AU. The disc is represented by 10^6 SPH particles, and has initial surface density and temperature profiles $\Sigma(R) \propto R^{-1}$ and $T(R) \propto R^{-3/4}$, respectively (Stamatellos 2015). The temperature at 1 AU from the central star is $T_0 = 250$ K. A planet with an initial mass 1 M_J is embedded in the disc at radius of 50 AU. At the snapshot presented in Figure 4.7a the disc mass has dropped to 0.08 $M_\odot$ and the planet mass has increased to 11 M_J. The planet has migrated inwards and is located at a radial distance of 36 AU. It has carved a gap between ~ 30 and ~ 40 AU.

Figure 4.7b shows that the Lombardi method estimates the optical depth at the midplane of the disc well within the gap, but overestimates it by a factor of a few outside of the gap. The Stamatellos method overestimates the optical depth at all radii: by a factor of ~ 2 outside of the gap and ~ 10 within the gap.

Two radial annuli are considered where vertical analyses are performed. One includes the gap (between 33 and 37 AU, Figure 4.7d, e - solid lines), the other a region

interior to the gap (between 23 and 27 AU, Figure 4.7d, e - dashed lines). The disc is optically thin within the gap. Thus the cooling rate is well estimated by both methods. The gas within the Hill radius of the planet ($R_{\rm HILL} = 8.0$ AU) is excluded when analysing the gap. The region interior to the gap is optically thick. The cooling rate is well estimated at all z by the Lombardi method, but the Stamatellos method underestimates the cooling rate by up to a factor of 10.

4.5 Testing the β-cooling approximation

The β-cooling approximation (e.g. Gammie 2001; Rice et al. 2003b) is a computationally inexpensive technique used when simulating accretion discs. This method assumes that the cooling rate at a given radius R within the disc, is inversely proportional to cooling time such that

$$\dot{u} = \frac{u}{t_{\rm cool}}, \tag{4.6}$$

where the cooling time is

$$t_{\rm cool} = \beta \Omega^{-1}. \tag{4.7}$$

Ω is the Keplerian frequency and β is a dimensionless parameter which is typically assumed to be between 1 and 20. Provided a disc is close to Toomre instability (i.e. $Q \approx 1$), a disc may only be able to fragment if the cooling is sufficiently fast (β on the order of a few). The critical value at which gravitational fragmentation occurs, $\beta_{\rm crit}$, is still debated. Meru & Bate (2011) suggest that the limit may be as high as $\beta_{\rm crit} \approx 30$. More recent studies by Baehr et al. (2017) suggest a value of $\beta_{\rm crit} = 3$.

In this section, I compare the β-cooling approximation with the cooling rates which is obtained from Equation 4.3 (referred to as *actual* cooling). An effective beta, $\beta_{\rm eff}$ is

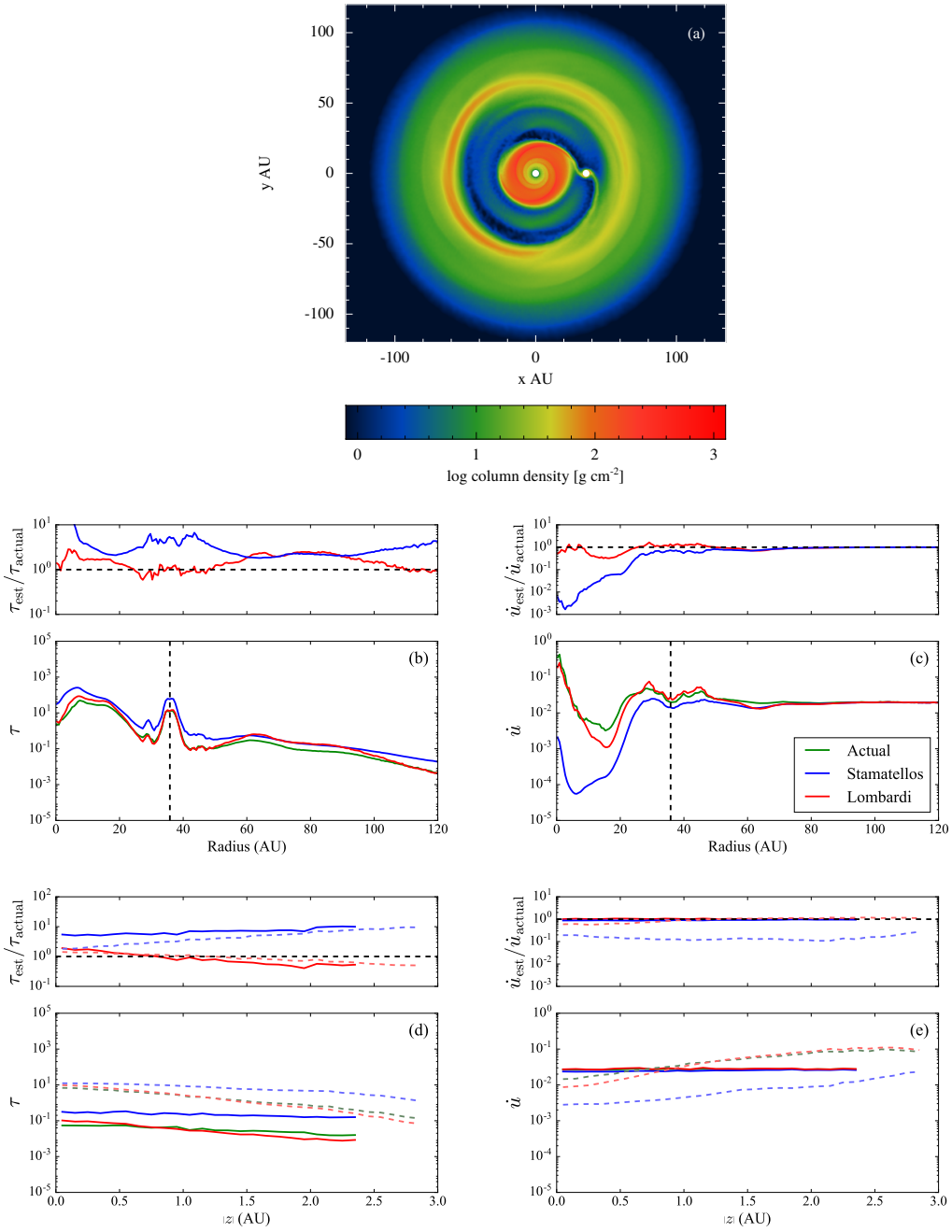

Figure 4.7: A disc which has an embedded 11 M_J planet at a radius of 36 AU. Panel (a): a column density snapshot. Panels (b) and (c): comparisons of azimuthally-averaged optical depth and cooling rate at the disc midplane. The vertical black dashed lines in panels (b) and (c) represent the location of the planet. Panels (d) and (e): optical depth and cooling rate comparisons perpendicular to the disc midplane between radial annuli of $33-37$ AU (inside the gap, solid lines), and $23-27$ AU (outside the gap, dashed lines). Gas within $R_{\rm HILL} = 8.0$ AU of the planet is excluded when analysing the gap. The upper plots in panels (b-e) show the ratio between estimated and actual values. The black dashed lines represent equality. Both methods overestimate the optical depth in the outer disc by a factor of 2 or 3. However, the Lombardi method estimates both the optical depth and the cooling within the gap more accurately than the Stamatellos method. Outside and within the gap, the Lombardi method gives a good estimate for both quantities from the disc midplane to the disc surface. The Stamatellos method estimates the cooling rate well within the gap as this region is optically thin.

calculated in order to determine whether the assumption of a constant β is a reasonable approximation. Therefore, I define $\beta_{\rm eff}$ as

$$\beta_{\rm eff} = \frac{u}{\dot{u}}\Omega. \tag{4.8}$$

where

$$\dot{u} = \frac{4\sigma_{\rm SB}T^4}{\Sigma\left(\tau_{\rm R} + \tau_{\rm P}^{-1}\right)}. \tag{4.9}$$

I emphasise that when calculating u the detailed equation of state used by Stamatellos et al. (2007b) is also used here (see Section 2.2).

I show the $\beta_{\rm eff}$ that is calculated for the snapshots of protostellar discs presented in Sections 4.3 and 4.4. Figure 4.8 shows the azimuthally-averaged $\beta_{\rm eff}$ at the disc midplane; Figure 4.9 shows the value of $\beta_{\rm eff}$ vertically towards the surface of the disc at the given regions; Figure 4.10 shows colour maps of $\beta_{\rm eff}$ at the disc midplane. It is clear that $\beta_{\rm eff}$ varies significantly throughout different regions of each disc, between ~ 0.1 and ~ 200.

For the smooth axis-symmetric disc cases that are examined here (Figures 4.10a, b), $\beta_{\rm eff}$ is high in the inner disc regions ($\beta_{\rm eff} > 20$) but drops down to ~ 3 in the outer regions. For the disc with the spiral arms (Figure 4.10c), the spirals are regions where $\beta_{\rm eff} \sim 1$, hence cooling is efficient. Thus, spiral arms may be prone to gravitational collapse as thermal energy generated by the contraction of a forming gas clump can efficiently escape. The dense, bound clumps in Figure 4.10d cool inefficiently ($\beta_{\rm eff} \sim 200$), due to being extremely optically thick.

Figure 4.10e shows $\beta_{\rm eff}$ for a disc with a 1.4 M_J embedded planet. $\beta_{\rm eff}$ is high in the outer regions but is low within the planet gap. This may be attributed to the associated high and low optical depths, respectively, of these regions. For a disc with an embedded higher-mass 11 M_J planet (Figure 4.10f), the planet induces a high-density spiral wake which cools fast ($\beta_{\rm eff} \sim 1$), whereas the gap region cools slowly

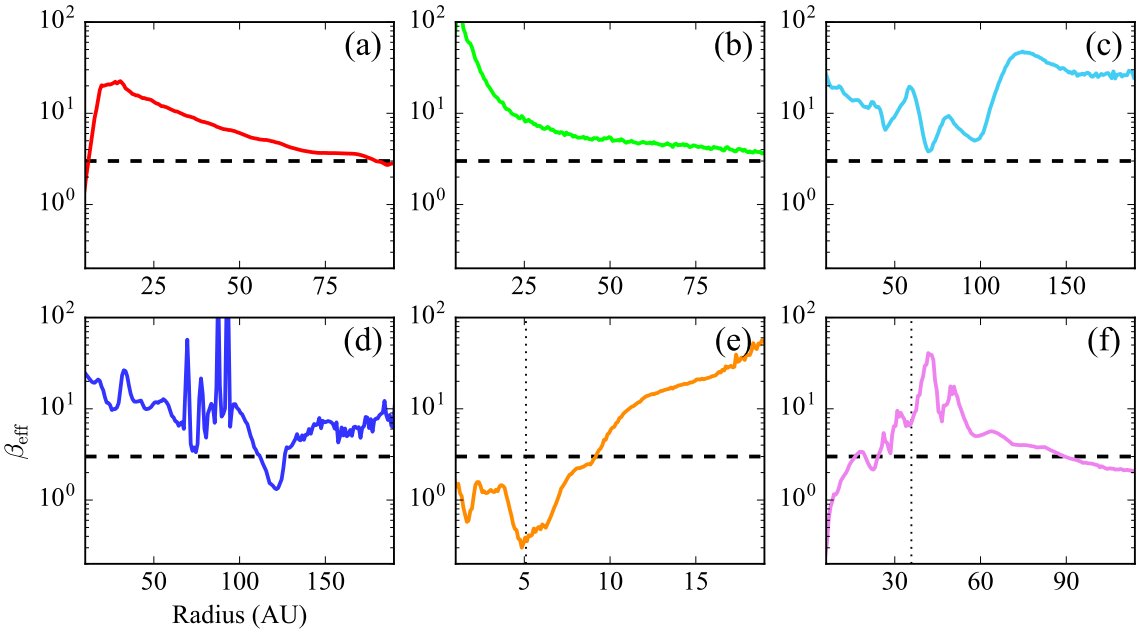

Figure 4.8: Azimuthally-averaged effective β at the disc midplane for the following snapshots: (a) a low-mass relaxed disc; (b) a high-mass disc; (c) a high-mass disc with spirals arms; (d) a high-mass disc with dense clumps; (e) a disc with an embedded 1.4 M_J planet; (f) a disc with an embedded higher-mass 11 M_J planet. Horizontal dashed lines represent $\beta_{\rm eff} = 3$. Vertical dotted lines represent the radii of planets (in the last two cases).

($\beta_{\rm eff} > 50$). The region around the planet has a low $\beta_{\rm eff}$ (< 1) and thus cools more efficiently.

As expected, the regions of the disc cool inefficiently (slowly) when they are optically thin (low-density regions of the disc, e.g in gaps), efficiently (quickly) when they are just optically thick ($\tau \sim 1$, e.g. in spirals induced by gravitational instabilities or planets), and again inefficiently (slowly) when they become extremely optically thick (in clumps/fragments).

I conclude that the actual cooling rate in a protostellar disc varies radially, vertically and with time as the disc evolves. Significant variations are observed within dense clumps which form through gravitational fragmentation. This makes the β-cooling method a rather crude approximation of the disc thermal physics when considering highly dynamical systems.

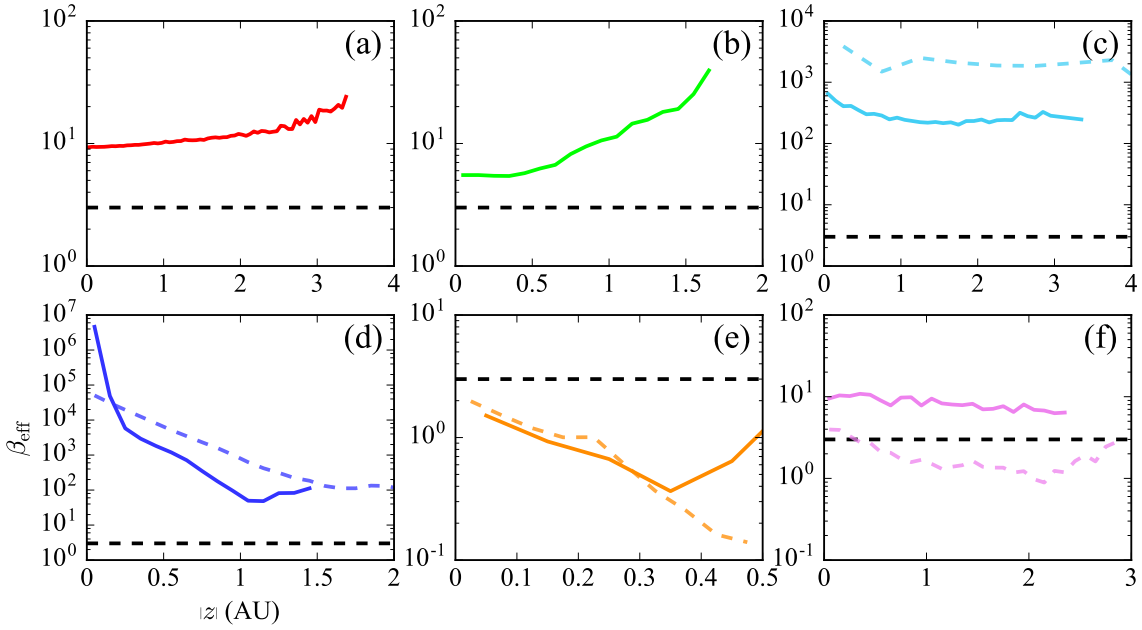

Figure 4.9: Effective β from the disc midplane to the disc surface for the following snapshots: (a) a low-mass relaxed disc (radial annulus $34 < R < 36$ AU); (b) a high-mass relaxed disc (radial annulus $34 < R < 36$ AU); (c) a disc with spirals arms (vertical cylinders with a base with radius of 5 AU regions centered within a spiral arm, solid line, and outside spiral arms, dashed line); (d) a disc with dense clumps (vertical cylinders with a base with radius of 5 AU centered within the densest clump, solid line, and the least dense clump, dashed line); (e) a disc with an embedded 1.4 M_J planet (radial annuli $4 < R < 6$ AU, solid line) and $3 < R < 4$ AU ,dashed line); (f) a disc with an embedded higher-mass 11 M_J planet (radial annuli $33 < R < 37$ AU, solid line) and $23 < R < 27$ AU, dashed line). Horizontal dashed lines represent $\beta_{\rm eff} = 3$.

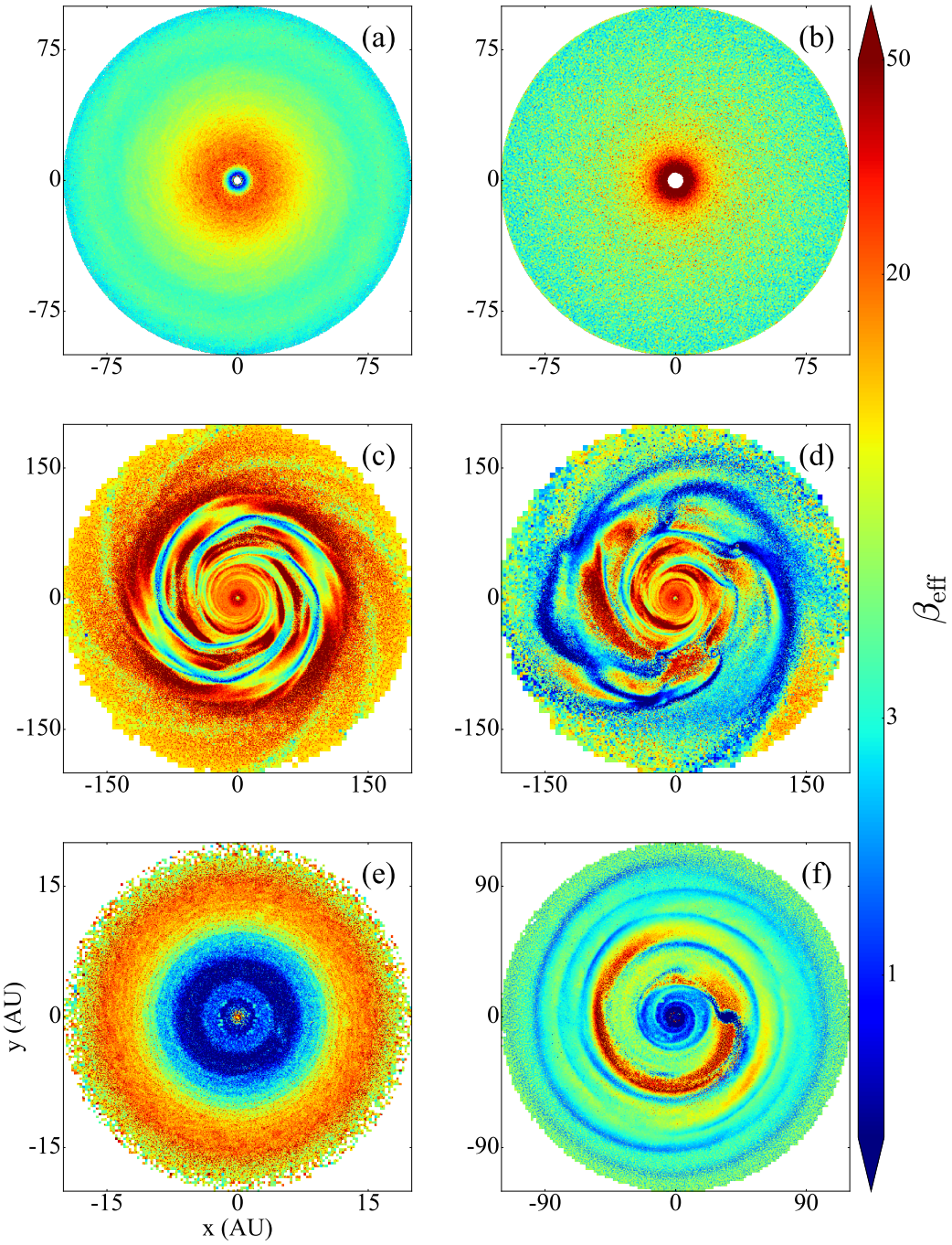

Figure 4.10: Effective β values at the disc midplane for the following snapshots: (a) a low-mass relaxed disc; (b) a high-mass disc; (c) a disc with spirals arms; (d) a disc with dense clumps; (e) a disc with an embedded 1.4 M_J planet; (f) a disc with an embedded higher-mass 11 M_J planet. Regions where $\beta_{\rm eff}$ is lower cool more efficiently. Gravitational instability is typically considered to occur for $\beta < 3$ provided that the Toomre parameter is also on the order of unity. It is clear that β varies across the disc, especially within spiral features and dense clumps. As such, it may not be appropriate to assume that β is constant throughout the disc.

4.6 Dynamical evolution comparison

I perform three simulations to demonstrate the differences that the β-cooling approximation, the Stamatellos et al. (2007b), and the Lombardi et al. (2015) radiative transfer methods exhibit. I consider a 0.8 $M_\odot$ protostar which is attended by a 0.2 $M_\odot$ disc with surface density and temperature profiles $\Sigma(R) \propto R^{-1}$ and $T(R) \propto R^{-1/2}$, respectively. $N \approx 2 \times 10^6$ particles represent the disc, which is heated by a 10 K external radiative field. No heating from the central star is included. I test the β-cooling approximation with a value of $\beta = 3$, a limit at which cooling is efficient enough for gravitational instability to occur (Rice et al. 2003a).

Figure 4.11 shows the three discs after 1.5 kyr of evolution using: (a) the β-cooling approximation; (b) the Stamatellos radiative transfer method; and (c), the Lombardi radiative transfer method. Whilst all three discs become gravitationally unstable, the β-cooling approximation yields a more stable disc than the two radiative transfer methods. Due to a generally higher estimation of the cooling rate, the Lombardi method allows the disc to cool more efficiently and develop stronger spiral arms.

4.7 Discussion

I have compared two approximate (but computationally inexpensive) methods to include radiative transfer in hydrodynamic simulations. These methods use two different metrics to calculate the optical depth through which the gas heats and cools: (i) the Stamatellos et al. (2007b) method uses the gravitational potential and the density, and (ii) the Lombardi et al. (2015) method instead uses the pressure scale-height.

I find that although both methods yield accurate estimates in the case of collapsing clouds, the use of the pressure scale-height metric to estimate optical depths (Lombardi et al. 2015) is more accurate when considering protostellar discs. I summarise the results in Figure 4.12, which illustrates the difference of optical depth estimation

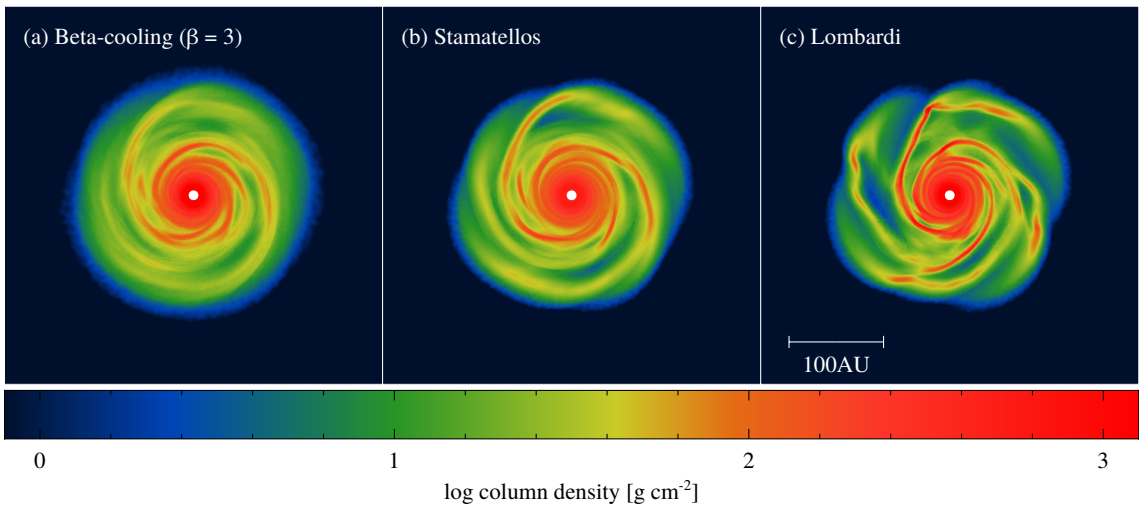

Figure 4.11: Surface density plots of a 0.2 $M_\odot$ disc around a 0.8 $M_\odot$ protostar after 1.5 kyr of evolution. Panel (a): a disc evolved using the β-cooling approximation with $\beta = 3$. Panel (b): a disc evolved using the Stamatellos et al. (2007b) radiative transfer method. Panel (c): a disc evolved using the Lombardi et al. (2015) method. Each disc becomes gravitationally unstable, but it is clear that the Lombardi disc (panel c) is more unstable, demonstrated by the stronger, more detailed spiral arms.

for the cases examined in this chapter for both methods. Using the pressure scale-height as a metric, a more accurate estimate of optical depth (by a factor of 2 or better) and cooling rate is obtained for protostellar discs in a variety of configurations: low-mass and high-mass discs, with or without an embedded planet, as well as gravitationally unstable discs which develop spiral arms and form bound clumps. The Stamatellos et al. (2007b) method may overestimate the optical depth by a factor of 10 in some cases, but the Lombardi et al. (2015) method is generally accurate within a factor of 3. Consequently, the Stamatellos et al. (2007b) method underestimates the cooling rate in optically thick protostellar discs, whereas the Lombardi et al. (2015) method provides better accuracy (although generally it also underestimates the cooling rate). Both methods give accurate estimates in the optically thin regime.

I also compare the cooling rates in hydrodynamic simulations of discs with those of the commonly used β-cooling approximation (e.g. Gammie 2001; Rice et al. 2003b). I find that using a constant value of β for a disc may not be a suitable approximation

as this parameter may vary radially and vertically throughout the disc (between ~ 0.1 and ~ 200 in the cases examined here). It also varies with time as the disc evolves (e.g. when spiral arms and/or gaps form in the disc), but most significantly within dense clumps. The approximate radiative transfer methods discussed previously may be more appropriate to use as, at comparable computational cost, they are adaptive to the changes that happen as the disc evolves (e.g. the formation of spiral arms and clumps). Nevertheless, the β-cooling approximation is a useful parameterisation that facilitates greater control in numerical experiments considering the thermal behaviour of a disc.

Many hydrodynamic simulations of protostellar discs (in the context of e.g. disc evolution, disc fragmentation, disc-planet interactions, planet migration) have used such approximations for the radiative transfer to avoid excessive computational cost (e.g Rice et al. 2003a; Lodato & Rice 2004; Clarke et al. 2007; Lodato et al. 2007; Forgan & Rice 2009; Meru & Bate 2010; Stamatellos & Whitworth 2011; Ilee et al. 2017). Their results need to be seen in the context of the accuracy of the radiative transfer method used.

Studies of disc fragmentation (e.g Stamatellos & Whitworth 2009b; Stamatellos et al. 2011a) that use the Stamatellos et al. (2007b) method may have underestimated disc cooling by a factor of a few, so that their discs are less prone to fragmentation. This would mean that even discs with lower masses than the ones studied by Stamatellos et al. (2011a) may be able to fragment (i.e. a disc with mass less than 0.25 M around a 0.7 M star). However, it should be noted that the uncertainties in the disc opacities could also be up to an order of magnitude, i.e. the uncertainty introduced is similar to that of the Stamatellos et al. (2007b) method.

Disc simulations using the β-cooling approximation also suffer from uncertainties in calculating cooling rates. For discs that start off optically thin, the cooling is inefficient and hence $\beta_{\rm eff}$ is large. $\beta_{\rm eff}$ decreases (i.e. the cooling becomes more efficient)

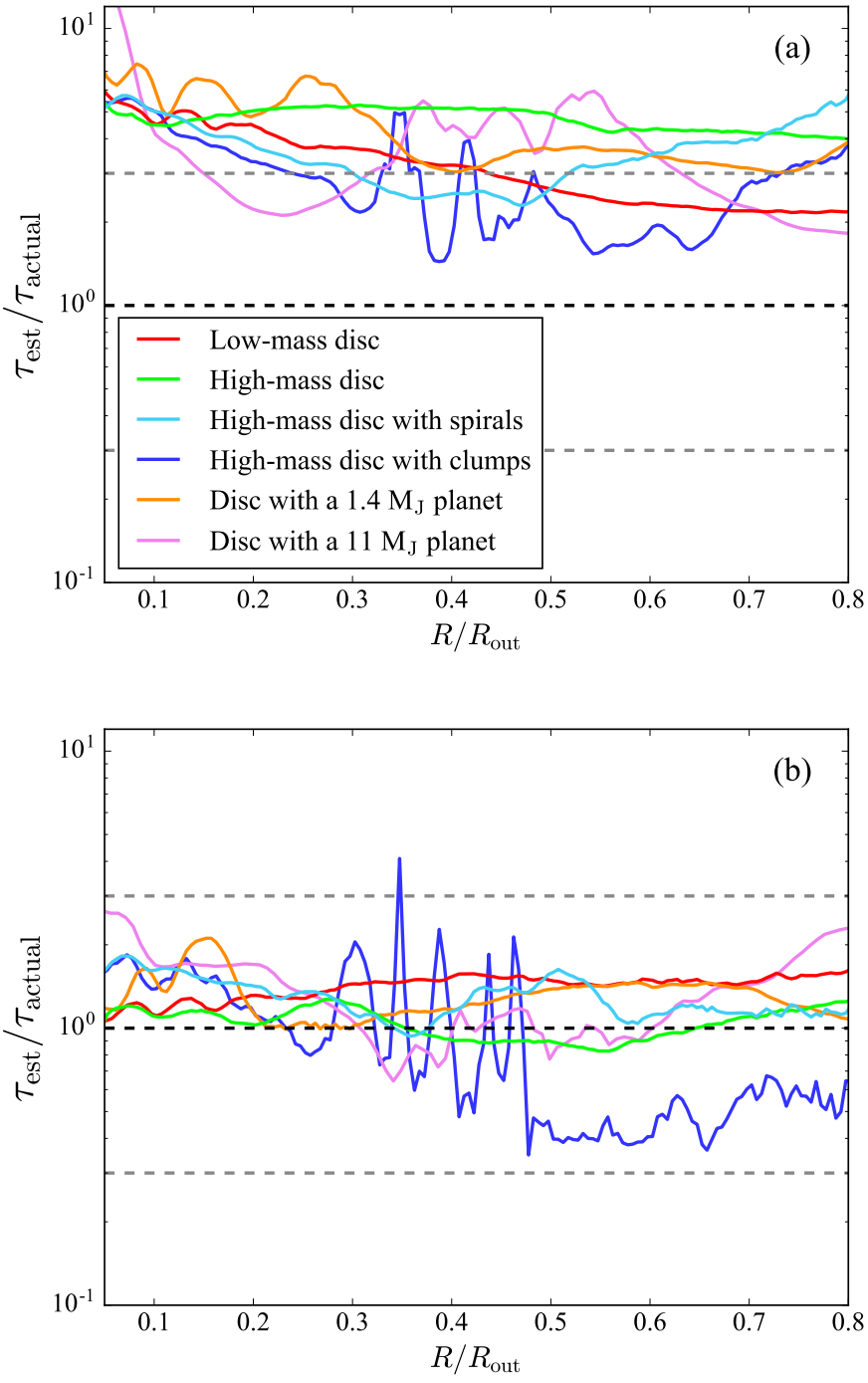

Figure 4.12: The ratio between estimated and actual optical depth for: (a) the Stamatellos et al. (2007b) method; (b) the Lombardi et al. (2015) method. Various disc configurations are shown. Radii have been normalised to the outer radius of each disc. The black dashed lines represent equal values of estimated and actual optical depth. The upper and lower grey dashed lines represent factors of 3 over- and underestimation respectively. The Lombardi et al. (2015) metric of estimating optical depths provides better accuracy in all cases presented. The optical depth is accurate by a factor of less than 3. The Stamatellos et al. (2007b) method is accurate within dense clumps/fragments.

as the density increases in spiral arms and in the region around a planet (i.e. its circumplanetary disc). If the density continues to increase and clumps form, the cooling becomes inefficient due to the high optical depth, and $\beta_{\rm eff}$ increases. The use of a constant β misses this variation of cooling efficiency (both in space and time). Therefore the physics of disc fragmentation may not be captured appropriately. I demonstrate that a disc evolved using the β-cooling approximation, with a value of $\beta = 3$, results in a more stable disc as compared to similar simulations which employ the Stamatellos et al. (2007b) and Lombardi et al. (2015) radiative transfer methods (see Section 4.6).

In the case of planets embedded in discs, it has been suggested that efficient cooling promotes gas accretion (Nayakshin 2017; Stamatellos & Inutsuka 2018) and dust accretion (Humphries & Nayakshin 2018) onto the planet. Therefore, cooling rates may affect the mass growth of planets, their metallicity, and their associated circumplanetary discs. This in turn results in different migration rates, final masses and orbital characteristics for these planets e.g. as seen in Stamatellos (2015) in comparison with Baruteau et al. (2011) (see Stamatellos & Inutsuka 2018).

4.8 Conclusions

Approximate radiative transfer methods are useful due to their computational efficiency, but they should be treated with caution as radiative transfer may, in many cases, fundamentally affect the evolution of an astrophysical system. The Lombardi et al. (2015) method (that uses the pressure scale-height to calculate optical depths) is more accurate than the Stamatellos et al. (2007b) method (that uses the gravitational potential and the gas density as a proxy for optical depths) for disc simulations. Both methods behave accurately for spherical geometries (i.e. collapsing clouds or clumps in discs). When used for modelling protostellar discs, both methods are more accurate than the β-cooling approximation (at similar computational cost), which nevertheless is a good tool for controlled numerical experiments of disc thermodynamics.

Chapter 5

Planet formation around M-dwarfs via gravitational instability

5.1 Introduction

M-dwarf stars are the most common within the galaxy (Chabrier 2003) and so the study of their early evolution is important, especially in the context of planet formation. Each method of planet detection is better suited to a different range of orbital separations: radial velocity and transit techniques are most sensitive to small (< 2 AU) planetary separations (e.g. Borucki et al. 2010b), and direct imaging allows the detection of planets beyond ~ 10 AU (e.g. Kalas et al. 2008; Marois et al. 2010). There exists catalogues for planets around M-dwarfs detected by radial velocity (Bonfils et al. 2013; Reiners et al. 2018a,b) and direct imaging (Bowler et al. 2015), the latter of which predicts an occurrence rate of $\sim 10\%$ for planets of mass $1 - 13$ M_J orbiting between 10 and 100 AU. The circumstellar discs of M-dwarfs early in their lifetime are typically less massive than their higher mass counterparts (Apai 2009; Andrews et al. 2013), yet massive planets (> 0.1 M_J) are still discovered orbiting these stars. Figure 5.1 shows the masses of detected exoplanet and brown dwarfs as a function of

their semi-major axis, taken from the EU exoplanet archive[1] (Schneider et al. 2011). Highlighted in red are those objects > 1 M_J surrounding stars with masses < 0.5 $M_\odot$. These are candidates which may not have formed through core accretion (Safronov & Zvjagina 1969; Goldreich & Ward 1973; Greenberg et al. 1978; Hayashi et al. 1985; Lissauer 1993) as the formation of such massive planets may exceed the lifetime of the disc (Haisch et al. 2001; Cieza et al. 2007).

An alternative theory of planet formation is the gravitational fragmentation of young protostellar discs (Kuiper 1951; Cameron 1978; Boss 1997). The protoplanets initially have characteristic masses of a few M_J (set by the opacity limit for fragmentation) but can rapidly accrete gas, growing massive enough to become brown dwarfs or low-mass hydrogen-burning stars (Stamatellos & Whitworth 2009b; Kratter et al. 2010; Vorobyov 2013; Kratter & Lodato 2016). Those objects that do remain as planets are typically ejected through gravitational interactions with more massive bodies however (Li et al. 2015, 2016, also see Chapter 3). Free-floating planets have indeed been detected using direct imaging (Mróz et al. 2018; Shvartzvald et al. 2019) and it has been suggested that the distribution of planet masses are the same for both bound and free objects (van Elteren et al. 2019).

Disc fragmentation originates from the gravitational instability, which can happen within an accretion disc provided the Toomre criterion (Toomre 1964) is satisfied, where

$$Q \equiv \frac{c_s \kappa}{\pi G \Sigma} < Q_{\rm crit}. \tag{5.1}$$

Rotational and thermal stability are provided through the epicyclic frequency κ and the local sound speed c_s, respectively. Note that within Keplerian discs, the epicyclic frequency is equal to the rotational frequency Ω. Instability is driven by gravity, represented by the column density Σ. The critical value for instability, $Q_{\rm crit}$, is of order unity for razor-thin discs, but studies of 3-dimensional discs show that this value may

[1] `exoplanet.eu` Last accessed 03/03/2019.

be as high as ~ 1.6 (Durisen et al. 2007). The gravitational instability leads to the formation of spiral arms which transfer angular momentum radially outwards. This then results in the inward movement of material and subsequent accretion onto the central body.

A spiral arm can evolve non-linearly and collapse if the cooling rate is sufficiently high: typically on the order $t_{\rm cool} < (0.5-2)t_{\rm orb}$, i.e. within a few orbital periods (Gammie 2001; Johnson & Gammie 2003; Rice et al. 2003b, 2005). Typically the cooling time is parameterised as a fixed factor β of the orbital period. In Chapter 4 I show that a more realistic treatment of thermal evolution yields a large range in β, both radially and vertically throughout the disc.

As M-dwarfs are cooler than their solar-type counterparts, so are their protostellar discs. These discs are therefore less thermally supported which may promote the development of gravitational instability, but on the other hand they are less massive than the discs of solar-type counterparts. Boss (2006) shows that the formation of Jupiter mass bodies is indeed possible via fragmentation of discs around stars with masses 0.1 and 0.5 $M_{\odot}$. These discs are small in extent ($4 < R < 20$ AU) and so the column density remains relatively high. Similarly, Backus & Quinn (2016) perform simulations of discs surrounding a 0.33 $M_{\odot}$ star. They find that only the discs which exhibit a $Q_{\rm crit} \lesssim 0.9$, fragment. The radii of the discs studied are between 0.3 and 30 AU, with masses between 0.01 and 0.08 $M_{\odot}$. Typically, fragments which form due to gravitational instability form at radii > 65 AU, where discs are sufficiently cool (Rafikov 2005; Stamatellos & Whitworth 2009b). Such studies consider solar-type stars which are hotter and more massive than M-dwarfs.

In this chapter, I study the evolution of protostellar discs around M-dwarf stars. The key aim is to find a minimum disc mass for which fragmentation happens. The chapter is laid out as follows. In Section 5.2, I describe the numerical methods employed within the chapter. Section 5.3 outlines the initial conditions of each simulation. In

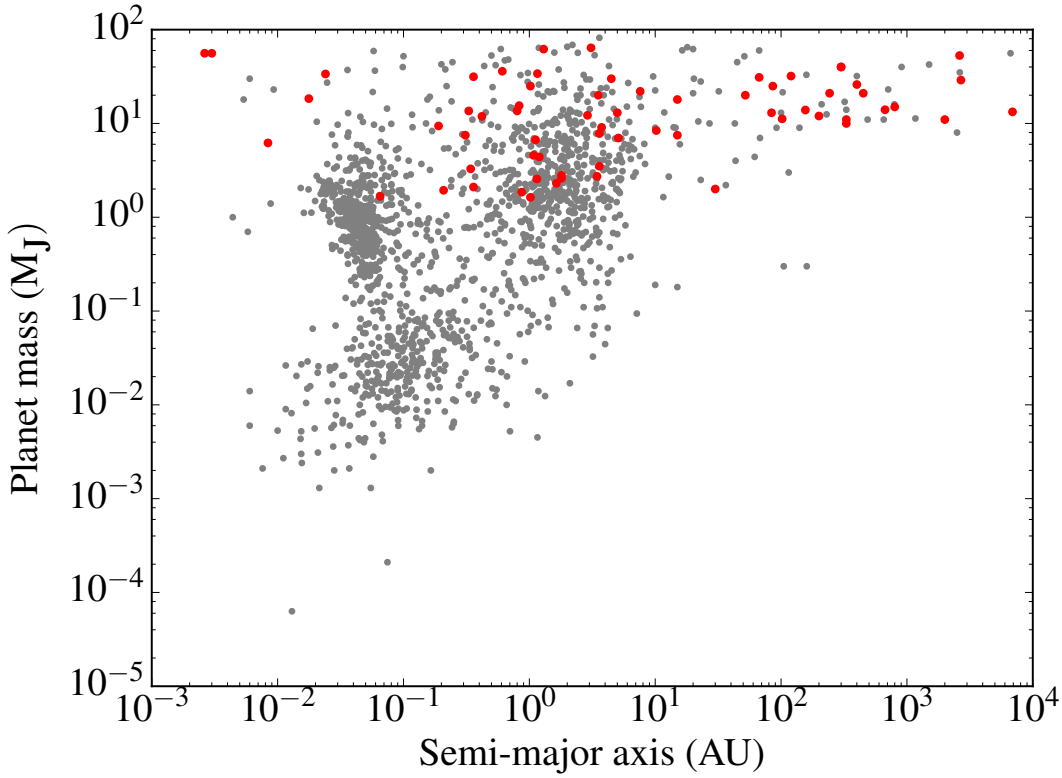

Figure 5.1: Detected exoplanet mass as a function of semi-major axis. In red is the population of planets with masses > 1 M_J around stars with mass < 0.5 $M_\odot$. These massive planets may have formed via gravitational fragmentation within a protostellar disc around an M-dwarf protostar. Data were retrieved from the EU exoplanet archive[1] (Schneider et al. 2011).

Section 5.4 I discuss the fragmentation of discs around M-dwarfs, the mass at which they do so, and how initial conditions and disc metallicity affect this. I investigate the properties of the formed protoplanets in Section 5.5. The work is summarised in Section 5.6.

5.2 Numerical method

I use GANDALF (Hubber et al. 2018) to perform smoothed particle hydrodynamical simulations of protostellar discs using the conservative grad-h SPH scheme (Springel & Hernquist 2002). Artificial viscosity is included to capture shocks where the Cullen

& Dehnen (2010) switch is utilised in order to eliminate unwanted dissipation away from shock regions (see Section 2.1.4.3). The simulations also employ an approximate radiative transfer scheme where the heating/cooling rate is described as

$$\frac{\mathrm{d}u_i}{\mathrm{d}t} = \frac{4\sigma_{\mathrm{SB}}\left(T_{\mathrm{BGR}}^4 - T_i^4\right)}{\bar{\Sigma}_i^2\kappa_{\mathrm{R}}(\rho_i, T_i) + \kappa_{\mathrm{P}}^{-1}(\rho_i, T_i)}. \tag{5.2}$$

σ_{SB} is the Stefan-Boltzmann constant and T_{BGR} is a background temperature which particles cannot radiatively cool below. κ_{R} and κ_{P} are the Rosseland- and Planck-mean opacities respectively, and are assumed to be the same. $\bar{\Sigma}_i$ is the mass-weighted column density. I utilise the Lombardi et al. (2015) method to calculate the column density, which uses the pressure scale-height of the gas $H_{\mathrm{P},i}$ to obtain $\bar{\Sigma}_i \sim \rho_i H_{\mathrm{P}_i}$. The pressure scale-height can be calculated from readily available quantities within a hydrodynamical simulation such that

$$H_{\mathrm{P},i} = \frac{P_i}{\rho_i \left|\boldsymbol{a}_{h,i}\right|}, \tag{5.3}$$

where P_i and ρ_i are the pressure and density of the gas respectively. $\boldsymbol{a}_{h,i}$ is the hydrodynamical acceleration of the gas, which does not consider the gravitational or viscous components. The full form for the Lombardi et al. (2015) column density estimation is therefore

$$\bar{\Sigma}_i = \zeta\rho_i \frac{P_i}{\left|\boldsymbol{a}_{h,i}\right|}. \tag{5.4}$$

$\zeta = 1.014$ is a dimensionless coefficient with a weak dependence on polytropic index. This formulation has been shown to yield a more accurate estimate in the context of protostellar disc as compared to using the gravitational potential to estimate the column density (see Chapter 4). Note that the opacities used within this pressure scale-height method are not the same as in the Stamatellos et al. (2007b) prescription, but are slightly modified (see §2.1 of Lombardi et al. (2015)). The opacities are based on the Bell & Lin (1994) parameterisation such that $\kappa(\rho, T) = \kappa_0\rho^a T^b$, where κ_0, a

and b are constants, set depending on the chemical species contributing to opacity at a given density and temperature. These opacity contributions include ice melting, dust sublimation, bound-free, free-free and electron scattering interactions.

Equation 5.2 allows the calculation of cooling rate smoothly between the optically thin and thick regimes. It must be noted that the optically thick regime reduces to the diffusion approximation (Mihalas 1970). Flux-limited diffusion can be combined with this prescription to increase accuracy in the optically thick limit (e.g. Forgan et al. 2009a).

In order to find a minimum fragmentation mass for a disc, the disc mass is slowly increased at a constant rate, employing a low mass accretion rate (see Zhu et al. (2012)). The method can be conceptually thought as accretion onto the disc from an infalling envelope, where material is distributed across the whole disc instead of just the outer regions. The disc mass accretion rate is set to

$$\dot{M}_{\rm disc} = \frac{\chi M_{\rm disc,0}}{t_{\rm orb}}, \tag{5.5}$$

where $M_{\rm disc,\,0}$ is the initial disc mass and χ is a quantity which regulates the magnitude of accretion. $t_{\rm orb}$ is the orbital period at a radius $R = 100$ AU where

$$t_{\rm orb} = 2\pi\sqrt{\frac{R^3}{GM_\star}}. \tag{5.6}$$

The mass accretion is simply performed by increasing the mass of every particle equally every timestep. This is referred to as *mass loading*. The discs are evolved until they fragment i.e. as when a density of $\rho > 10^{-9}$ g cm^{-3} is attained. The caveat of this method is that higher density regions of the disc i.e. where there are more particles, will be preferentially mass-loaded. For example, spiral arms may receive a higher mass accretion and the collapse of a dense region may be driven artificially.

When a disc has fragmented, its mass is calculated to yield a minimum mass for

fragmentation, denoted $M_{\rm disc}$. I calculate the time of fragmentation t, disc-to-star mass ratio when fragmentation happens q, and the outer radius of the disc $R_{\rm disc}$, which encompasses 95% of the disc mass. The distance between the central star and the formed fragment is denoted $a_{\rm frag}$, and its radius, $r_{\rm frag}$, is defined as the distance at which the surrounding density drops below 10^{-10} g cm^{-3}. The fragment mass $m_{\rm frag}$ is the total mass enclosed within this radius.

5.3 Initial conditions

I construct protostellar systems with different stellar mass, disc radial extent and metallicity. The stellar masses are set to $M_\star = [0.2,\ 0.3,\ 0.4]$ M$_\odot$ exploring a range of masses for M-dwarfs. The disc extents are set to $R_{\rm init} = [60,\ 90,\ 120]$ AU whereas the inner edge is set to 5 AU. The metallicity is varied through the opacities by factors of $z = [0.1, 1, 10]$. The initial disc mass is chosen such that the Toomre parameter has a fixed value at the outer radius of the disc chosen such that $Q_{\rm out} = 10$. This is shown in Figure 5.2 and ensures that the discs are initially gravitationally stable. Each disc is comprised of $N \approx 2 \times 10^6$ SPH particles, and so both the Jeans mass and Toomre mass are well resolved (Bate & Burkert 1997; Nelson 2006). Similarly, the disc vertical structure is adequately resolved (see Chapter 3).

The surface density and temperature profiles of the disc are set to $\Sigma \propto R^{-p}$ and $T \propto R^{-q}$, respectively. The surface density power index p is thought to lie between 1 and 3/2 from semi-analytical studies of cloud collapse and disc creation (Lin & Pringle 1990; Tsukamoto et al. 2015). The temperature power index q has been observed to lie in the range from 0.35 to 0.8 from studies of pre-main sequence stars (Andrews et al. 2009). Here, I adopt $p = 1$ and $q = 0.7$. The surface density profile has the form

$$\Sigma(R) = \Sigma_0 \left(\frac{R_0^2}{R_2 + R_0^2} \right)^{p/2}, \tag{5.7}$$

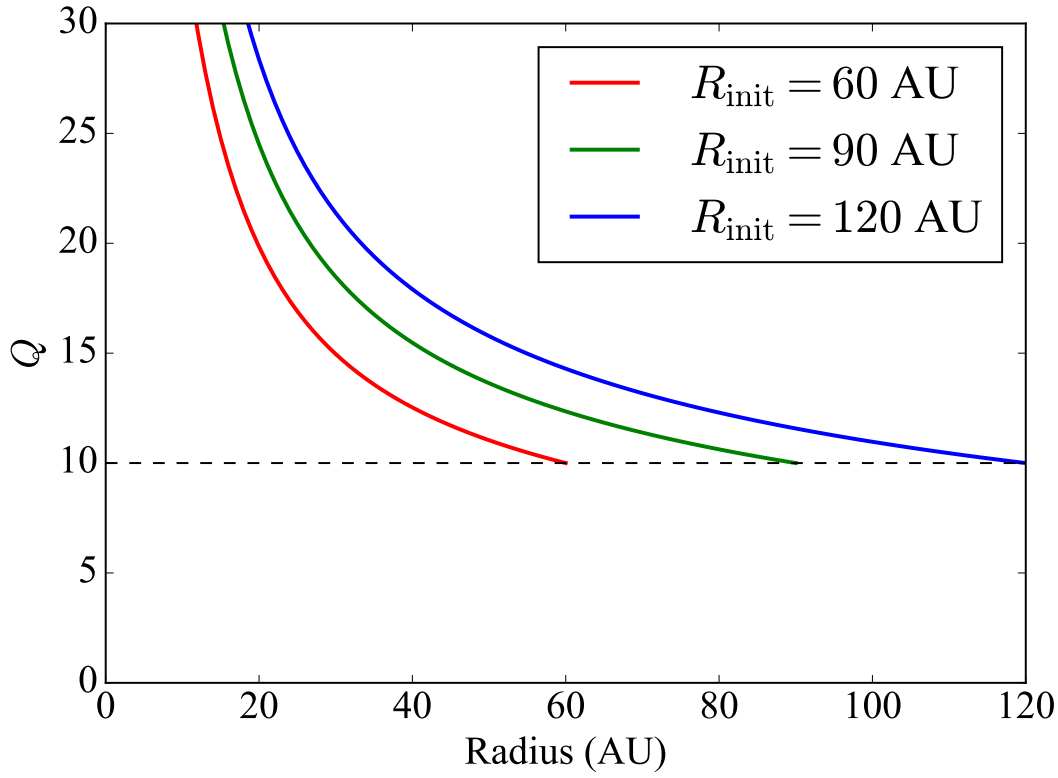

Figure 5.2: Toomre parameter as a function of disc radius for discs with outer radial extents of $R_{\rm init} = [60,\ 90,\ 120]$ AU. The dashed black line represents a value of $Q = 10$, the Toomre value at each disc outer edge. Every disc is initially stable at all radii.

where Σ_0 is the surface density 1 AU away from the star and $R_0 = 0.01$ AU is a smoothing radius to prevent unphysical quantities close to the star. The disc temperature profile is set to

$$T(R) = \left[T_0^2 \left(\frac{R^2 + R_0^2}{\mathrm{AU}^2} \right)^{-2q} + T_\infty^2 \right]^{1/2}. \tag{5.8}$$

Here, $T_0 = 100$ K is the temperature at 1 AU from the star, $T_\infty = 10$ K is the temperature far away from the protostar. This term is used to provide a minimum temperature below which particles cannot radiatively cool, and is equivalent to $T_{\rm BGR}$ in Equation 5.2.

The strategy is to start with a gravitationally stable disc and slowly increase its mass

until it becomes unstable and fragments. However, a relatively low disc accretion rate is used so that accretion is not the key driver of the gravitational instability, contrary to other studies of accretion onto protostellar discs (Hennebelle et al. 2016). The full set of initial conditions for each simulation are listed in Table 5.1.

5.3.1 Mass loading test and convergence

To check the validity of the mass loading method, I perform a simulation where the initial disc mass is set to 0.12 $M_\odot$ and the disc accretion rate to 3×10^{-5} $M_\odot$ yr^{-1} i.e. $\chi \sim 0.5$ (see Equation 5.5). I also perform a set of simulations where the disc masses are fixed, but each with an increased mass: from 0.15 to 0.2 $M_\odot$ in 0.01 $M_\odot$ intervals. Each disc has column density and temperature profiles of $\Sigma \propto R^{-1}$ and $T \propto R^{-0.7}$ respectively, extend from 5 to 90 AU, with a 0.2 $M_\odot$ host star and are comprised of $N \approx 2{\times}10^6$ particles. I find that the disc with a fixed mass of 0.17 $M_\odot$ does not undergo fragmentation whereas the disc with a fixed mass of 0.18 $M_\odot$ does. The disc which includes mass loading fragments at a mass of 0.176 $M_\odot$, consistent with fixed-mass disc simulations.

The number of particles are also varied to determine whether the mass loading simulations have converged. Figure 5.3 shows the mass at which a disc fragments under mass loading with an increasing number of particles. Even for a relatively small number of particles ($N = 128,000$) convergence is achieved. Only negligible differences are seen when the particle number is consequently doubled, up to a maximum of $N \approx 8 \times 10^6$.

Finally, I investigate the effect of the quantity which regulates the amount of mass loading, χ (see Equation 5.5). I choose a disc with initial conditions similar to those of run 4 in Table 5.1, albeit with a disc accretion rate of 2.5×10^{-5} $M_\odot$ yr^{-1}. Figure 5.4 shows disc fragmentation masses where values of $\chi = [0.05, 0.075, 0.1, 0.2, 0.5]$ have been adopted. The corresponding mass accretion rates are $\dot{M}_{\rm disc} = [1.25, 1.88, 2.5, 5, 12.5]\times$

Table 5.1: List of initial conditions for each simulation. Disc masses are set such that the Toomre parameter at the outer radius is $Q = 10$ (i.e. they are initially gravitationally stable). The constant mass accretion rate onto the disc is set from Equation 5.5 where $\chi = 0.1$. Disc metallicity is varied by modifying the opacities by a factor z (see Equation 5.2).

Run	$M_{\star,0}$ ($M_\odot$)	$R_{\rm init}$ (AU)	z	$M_{\rm disc,\,0}$ ($M_\odot$)	$\dot{M}_{\rm disc}$ ($\times 10^{-6}$ $M_\odot$ yr^{-1})
01	0.2	60	1	0.040	1.80
02	0.2	60	0.1	0.040	1.80
03	0.2	60	10	0.040	1.80
04	0.2	90	1	0.050	2.25
05	0.2	90	0.1	0.050	2.25
06	0.2	90	10	0.050	2.25
07	0.2	120	1	0.059	2.63
08	0.2	120	0.1	0.059	2.63
09	0.2	120	10	0.059	2.63
10	0.3	60	1	0.049	2.70
11	0.3	60	0.1	0.049	2.70
12	0.3	60	10	0.049	2.70
13	0.3	90	1	0.062	3.38
14	0.3	90	0.1	0.062	3.38
15	0.3	90	10	0.062	3.38
16	0.3	120	1	0.072	3.95
17	0.3	120	0.1	0.072	3.95
18	0.3	120	10	0.072	3.95
19	0.4	60	1	0.057	3.60
20	0.4	60	0.1	0.057	3.60
21	0.4	60	10	0.057	3.60
22	0.4	90	1	0.071	4.50
23	0.4	90	0.1	0.071	4.50
24	0.4	90	10	0.071	4.50
25	0.4	120	1	0.083	5.26
26	0.4	120	0.1	0.083	5.26
27	0.4	120	10	0.083	5.26

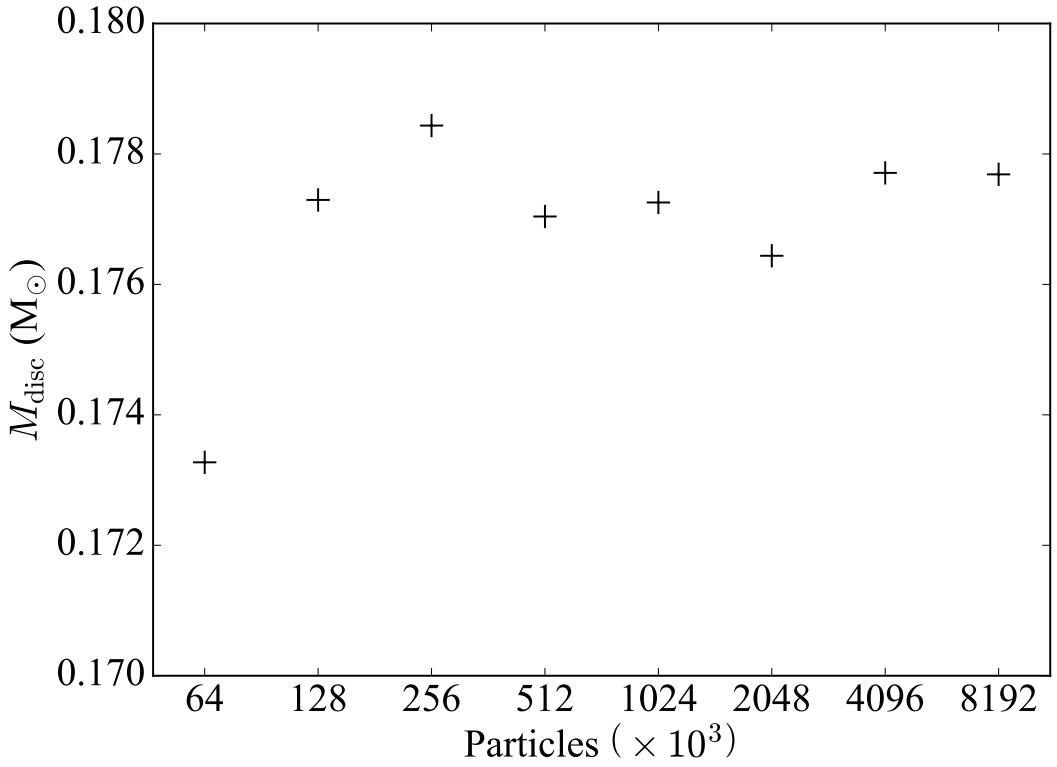

Figure 5.3: Convergence test for the mass loading method described in Section 5.2. I run SPH simulations with an increasing number of particles and compare the disc mass at the point of fragmentation. For $> 128 \times 10^3$ particles, there is little difference in the fragmentation mass of a disc that has undergone mass loading. I therefore conclude that the method is well behaved for $N \approx 2 \times 10^6$, the number of particles used for the simulations presented in this work.

10^{-6} $M_\odot$ yr^{-1}. A low accretion rate onto the disc is preferable so that its evolution is not affected by the mass loading, whereas for computational purposes it would be preferable to have a high accretion rate so that the fragmentation mass is achieved quickly. There is little difference in the computed fragmentation mass for $\chi \leq 0.1$ and so this is the adopted value for the rest of the work presented in this chapter.

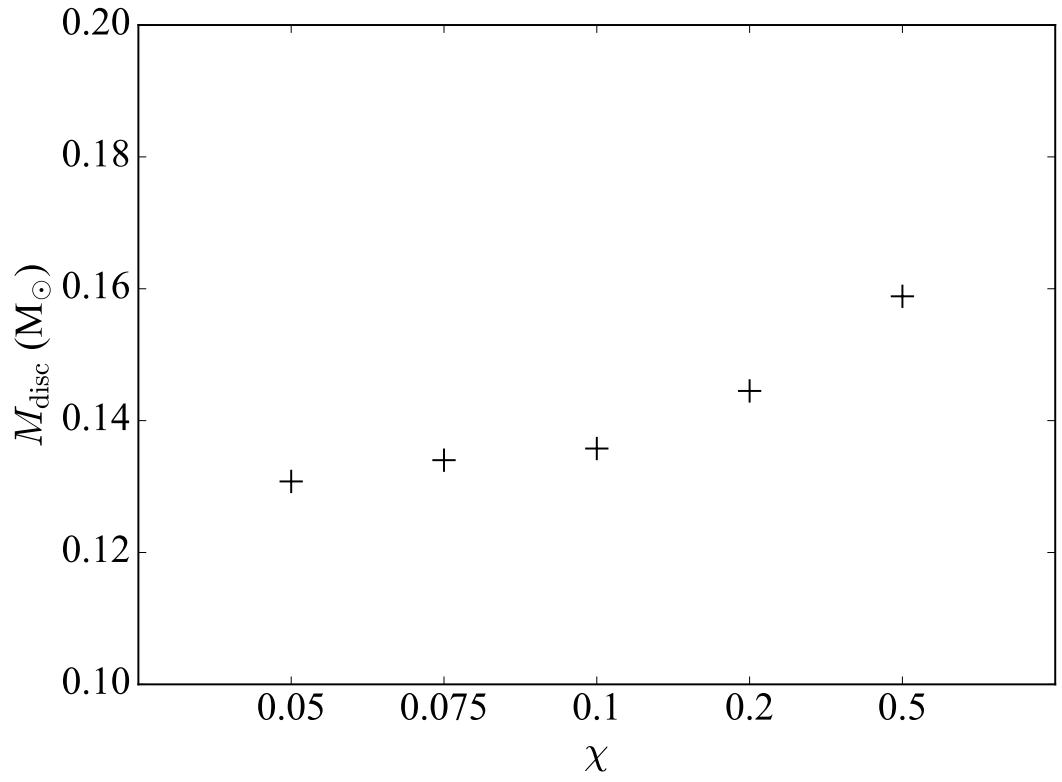

Figure 5.4: A comparison of disc fragmentation mass for different values of the parameter χ which regulates the disc accretion rate (see Equation 5.5). This tests by how much the disc fragmentation mass is affected when it fragments given by the disc accretion rate. The corresponding mass accretion rates for $\chi = [0.05, 0.075, 0.1, 0.2, 0.5]$ are $\dot{M}_{\rm disc} = [1.25, 1.88, 2.5, 5, 12.5] \times 10^{-6}$ M$_\odot$ yr^{-1} respectively. For values of $\chi \leq 0.1$, there is only a small difference in the disc fragmentation mass. As such, a value of $\chi = 0.1$ is adopted for work presented here.

5.4 Fragmentation of M-dwarf discs

I perform a set of 27 simulations, varying initial disc radius and stellar mass, as well as the disc metallicity. Each disc is initially gravitationally stable, but the mass of each disc increases over time. As such, each disc eventually becomes unstable and spiral arms develop. In the majority of cases, continued mass loading causes the spiral arms to evolve non-linearly, and ultimately form gravitationally bound fragments. The results of the disc simulations are presented in Table 5.2. Stated are the stellar mass and the mass of the disc when fragmentation occurs, as well as the corresponding time and the disc-to-star mass ratio. I also define a disc radius as the radius which encompasses 95% of the disc mass. Additionally, the distance to the central star, radius and mass of the formed fragment is given. Figure 5.5 shows column density snapshots of six of the simulations at the time when the density at the center of the fragment is 10^{-9} g cm^{-3}.

The effects of the varied initial conditions are discussed in Section 5.4.1 and different metallicities in Section 5.4.2. In each of these sections, I also discuss why seven of the discs do not fragment. The relationship between disc and stellar accretion rate is examined in Section 5.4.3.

Table 5.2: Results for discs with initial conditions listed in Table 5.1 after 30 kyr of evolution. $M_\star$ and $M_{\rm disc}$ are the masses of the star and disc when the disc fragments. Similarly, t and q are the time at which fragmentation occurs and the disc-to-star mass ratio at fragmentation, respectively, and $R_{\rm disc}$ is the radius of the disc which encompasses 95% of the gas mass. $a_{\rm frag}$ is the distance of the fragment from the host star, $r_{\rm frag}$ is the radius of the fragment and $m_{\rm frag}$ is its mass. Some discs do not fragment within 30 kyr, noted by empty rows.

Run	$M_\star$ ($M_\odot$)	$M_{\rm disc}$ ($M_\odot$)	$\Delta M_{\rm disc}$ (M_J)	t (kyr)	q	$R_{\rm disc}$ (AU)	$a_{\rm frag}$ (AU)	$r_{\rm frag}$ (AU)	$m_{\rm frag}$ (M_J)
01	0.205	0.075	36.6	22.07	0.367	75	49	1.2	2.5
02	0.205	0.077	38.9	23.29	0.378	72	35	1.4	2.3
03	-	-	-	-	-	-	-	-	-
04	0.205	0.104	56.2	25.90	0.508	92	54	1.3	2.9
05	0.205	0.106	58.4	27.02	0.517	96	14	1.3	2.6
06	0.207	0.106	58.1	28.00	0.510	169	32	1.3	3.2
07	0.204	0.124	68.7	26.67	0.608	144	46	1.2	2.3
08	0.205	0.126	70.8	27.60	0.617	128	30	0.9	1.3
09	0.207	0.128	72.2	28.83	0.618	190	54	1.2	2.5
10	0.305	0.094	46.9	18.53	0.308	96	40	1.2	2.3
11	0.305	0.097	50.2	19.60	0.319	68	32	1.1	1.6
12	-	-	-	-	-	-	-	-	-
13	0.305	0.122	63.0	19.19	0.400	89	59	2.1	5.2
14	0.305	0.125	66.3	20.21	0.410	89	28	1.0	1.4
15	-	-	-	-	-	-	-	-	-
16	0.304	0.146	77.8	19.96	0.481	131	55	2.0	4.4
17	0.305	0.150	81.7	21.02	0.492	126	60	1.6	3.1
18	0.307	0.155	86.7	22.67	0.505	159	84	1.7	5.1
19	-	-	-	-	-	-	-	-	-
20	-	-	-	-	-	-	-	-	-
21	-	-	-	-	-	-	-	-	-
22	0.405	0.144	76.2	17.32	0.355	105	57	1.1	2.0
23	0.405	0.140	72.1	16.36	0.346	91	37	1.1	1.7
24	-	-	-	-	-	-	-	-	-
25	0.405	0.165	86.1	16.51	0.409	123	47	1.4	3.2
26	0.405	0.171	91.6	17.59	0.422	130	43	1.0	1.3
27	0.407	0.176	97.4	19.00	0.433	164	116	1.3	3.1

5.4.1 Consequences of initial stellar mass and disc radius

The fragmentation mass is shown as a function of the stellar mass in Figure 5.6, and demonstrates that for a given initial disc radius, the fragmentation mass increases linearly with stellar mass. A more massive central protostar results in a more stable disc as $Q \propto \Omega$ and $\Omega \propto M_{\star}^{1/2}$. The fragmentation mass also increases with respect to initial disc radius, and although the discs expand due to outward angular momentum transport, they all do so by a similar amount by the time they fragment. Consequently, the average surface density of smaller discs is larger for the same disc mass. Hence, smaller discs fragment at a lower mass, as $\Sigma \propto R^{-2}$ and $Q \propto \Sigma^{-1}$.

The discs in runs 19 - 21 do not fragment which may be attributed to a period of rapid disc expansion, a result of strong spiral arm formation and efficient outward transport of angular momentum. This stabilises the discs, which, in this case are more stable than their same radius counterparts as they orbit a more massive central star. To demonstrate the effect of disc expansion, I compare runs 1 - 3 where runs 1 and 2 undergo fragmentation and run 3 instead exhibits disc expansion. Figure 5.7 shows azimuthally-averaged Toomre parameter (a) and ratio between cooling time and orbital period (b). Although in each case the cooling time is small enough to allow for a fragment to condense out, run 3 does not become sufficiently gravitationally unstable. The spiral arms do not evolve non-linearly and instead efficiently distribute angular momentum outward, expanding the disc.

In Figure 5.8 the relationship between the disc mass and disc-to-star mass ratio with the disc radius at the time of fragmentation is presented. Extended discs are typically more massive and need a higher disc-to-star mass ratio to fragment. A larger disc requires more mass than a smaller one to attain the same surface density, but it must also be noted that at larger radii the thermal and rotational support are lower (as the temperature is lower and the disc rotates slower), thus promoting the development

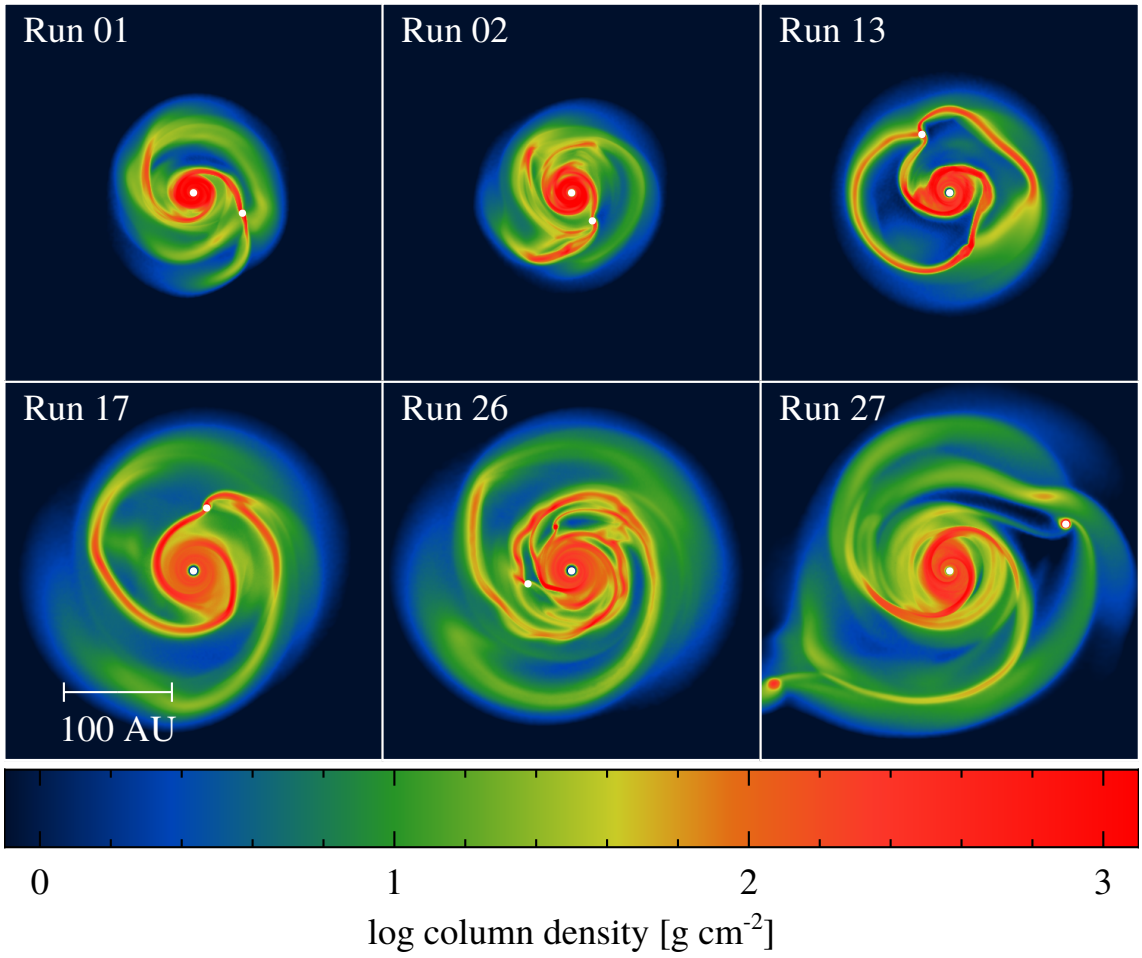

Figure 5.5: Column density snapshots for a selection of discs at the time of fragmentation. This is defined as when a density of 10^{-9} g cm^3 is reached. The fragments are shown by the orbiting white points. The initial conditions for each run can be found in Table 5.1 and final results in Table 5.2.

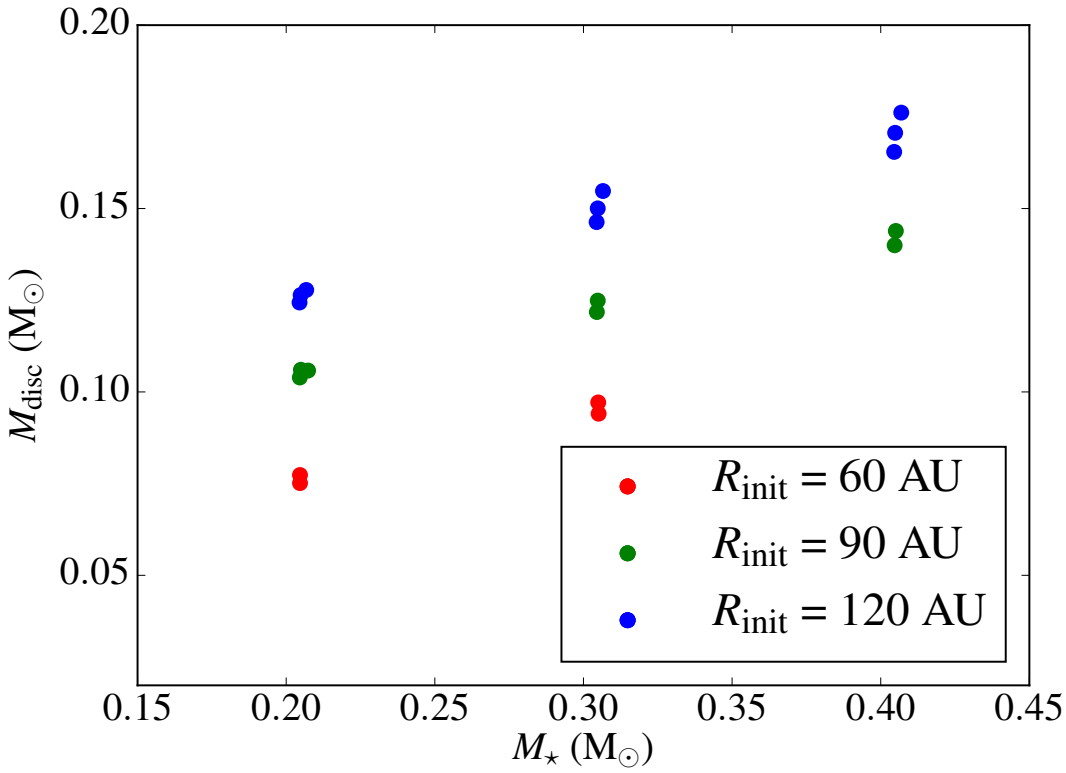

Figure 5.6: The disc mass as a function of stellar mass at the time when the disc fragments. The relationship between the two quantities is linear for a given initial disc radius. Smaller discs fragment at a lower mass as the average disc surface density is larger.

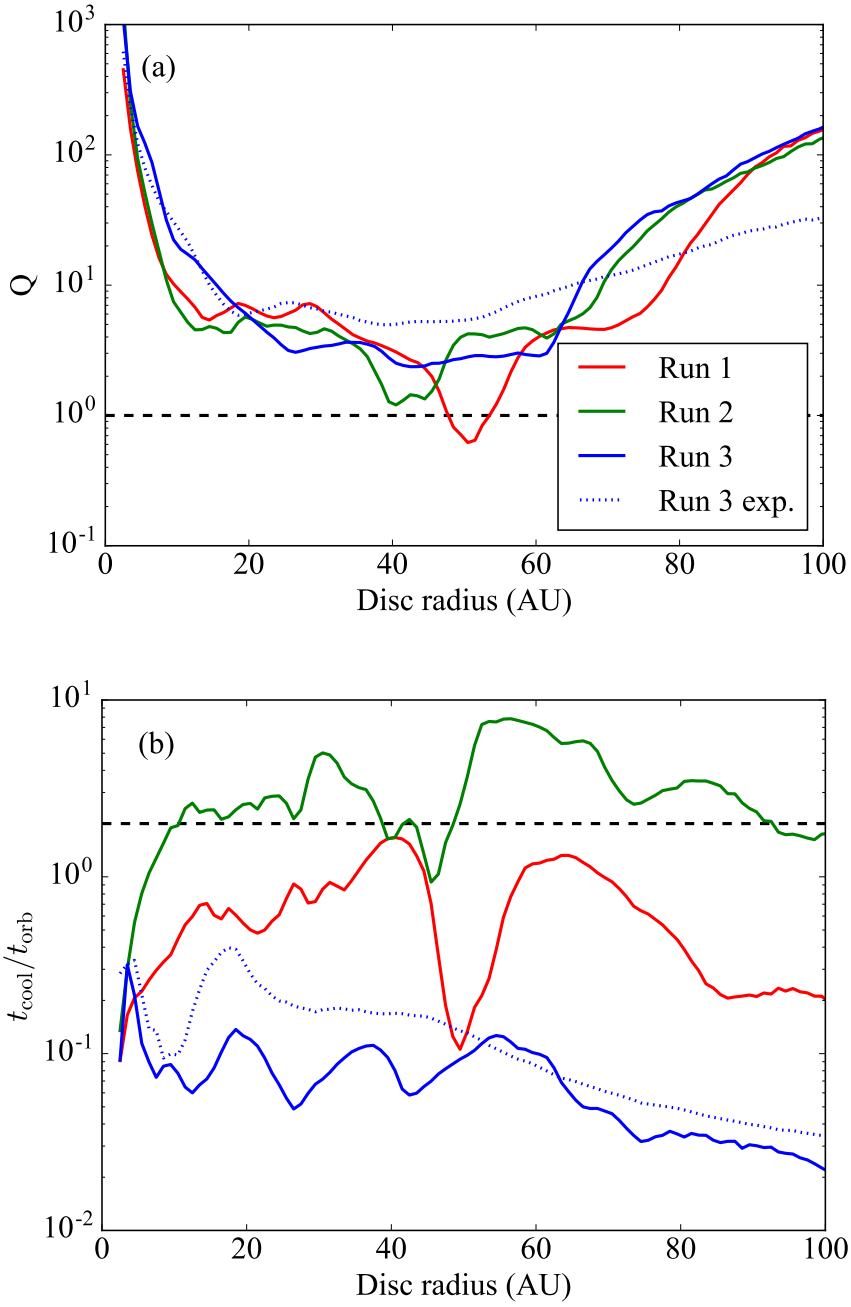

Figure 5.7: Azimuthally-averaged Toomre parameter (a) and ratio between cooling time and orbital period (b) for runs 1 - 3 in red, green and blue respectively. The time at which these quantities are shown are just prior to fragmentation (runs 1 and 2), and just prior to a period of disc expansion (run 3). The dashed blue line shows run 3 after the expansion. Each disc is gravitationally unstable such that spiral arms form, but only in runs 1 and 2 does the Toomre parameter fall below unity such that bound fragments form. In all cases, the cooling time is sufficiently short for a condensed fragment to collapse. The expansion of the disc in run 3 (and characteristic of most runs with an increased metallicity) acts to stabilise it.

of disc instabilities (assuming that the surface density is sufficiently high). The disc-to-star mass ratios required for the fragmentation of discs around M-dwarfs are from $q \sim 0.3$ for smaller discs to $q \sim 0.6$ for more extended discs.

5.4.2 Effect of metallicity

The metallicity of the discs is varied by modifying the opacities used in Equation 5.2 by factors of $z = [0.1, 1, 10]$, and the effect that this has on the fragmentation mass of the disc is determined. Changing the metallicity has little effect on the fragmentation mass. In fact, in all cases, the disc mass increases by a factor ~ 2 before fragmentation occurs. However, the disc evolution is affected by metallicity; from the onset of the gravitational instability, to the collapse of dense fragments.

In Figure 5.9, column density snapshots of runs 1 - 3 (panels a, b and c, respectively) at a time of 22 kyr are presented. Figure 5.9a is shown shortly before fragmentation for the disc with $z = 1$ (solar metallicity). I show that in Figure 5.9b where the metallicity is lower ($z = 0.1$), the disc exhibits weaker, but well defined spiral features. Given that $\tau = \Sigma\kappa$, and the metallicity has been reduced, a greater amount of material is required for the spiral arms to attain $\tau \sim 1$, where cooling is most efficient. As such, the spirals in this case take longer to fragment. Once a sufficient density is reached however, fragmentation happens as cooling is more efficient. In the case of Figure 5.9c, where the metallicity is increased ($z = 10$), the disc does not fragment as the disc cannot cool fast enough. The fragments that do form have masses between ~ 2 and ~ 8 M_J, all above the opacity limit. Although an increased metallicity (and therefore mean molecular mass) reduces the opacity limit (see Whitworth (2018)), no relation is found between metallicity and fragment mass, though it should be noted that the exact definition of fragment mass is important for comparisons with theory.

In general, the metal rich discs fragment at a higher disc-to-star mass ratio (Figure 5.10a) and do so with a larger outer radius (Figure 5.10b). The latter point is probably

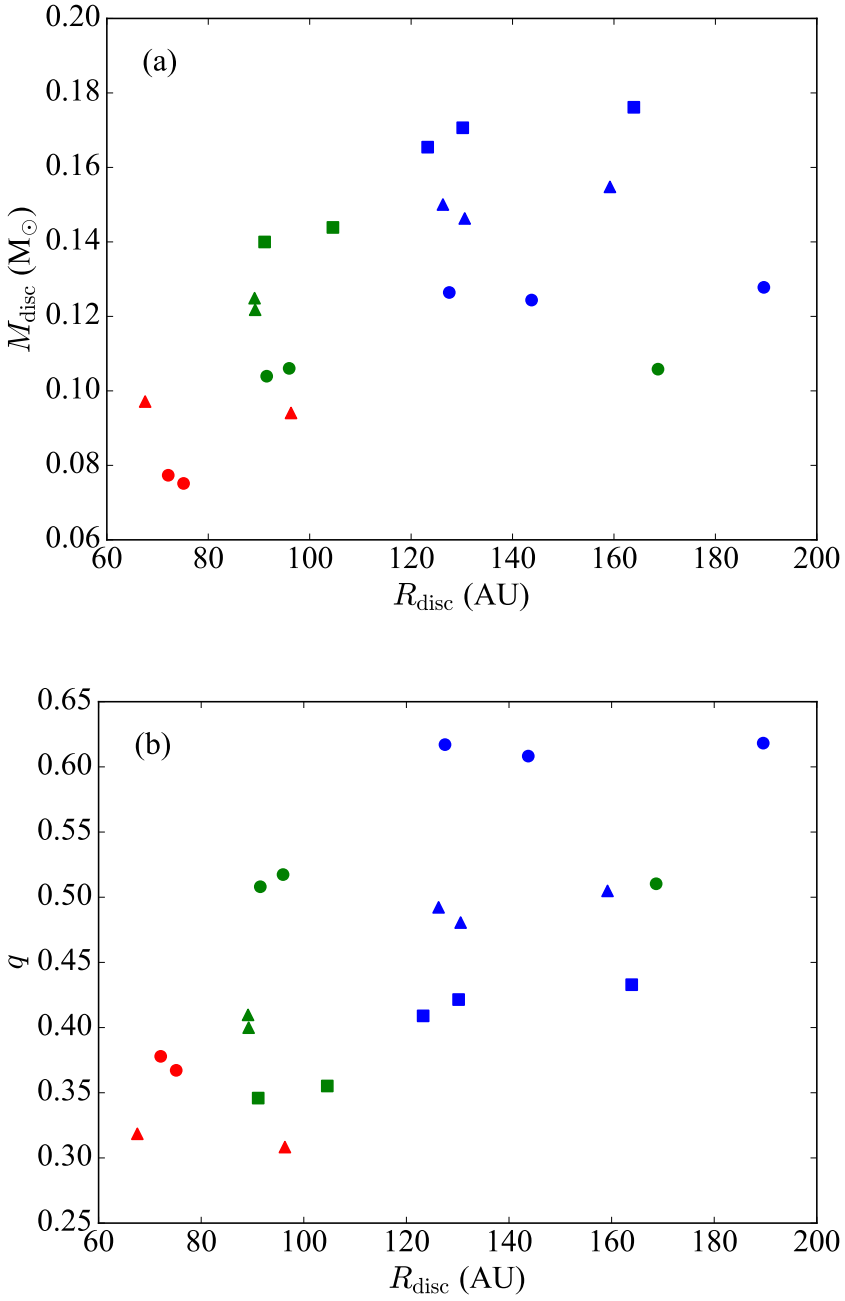

Figure 5.8: (a) The disc mass and (b) disc-to-star mass ratio as a function of disc radius at the time when the disc fragments. The radius is defined as an annulus which encompasses 95% of the disc mass. A higher disc mass is required for fragmention for more extended discs. The same applies to the disc-to-star mass ratio. Initial disc radii of $R_{\rm init} = [60, 90, 120]$ AU are shown by the red, green and blue points, respectively. The initial stellar masses of $M_\star = [0.2, 0.3, 0.4]$ $M_\odot$ are denoted by the circles, triangles and squares, respectively. Discs surrounding more massive stars fragment at a higher mass as they rotate faster. The disc-to-star mass ratio required for fragmentation varies from ~ 0.3 (for small discs) to ~ 0.6 (for more extended discs).

a result of a disc expansion period after spiral arms develop. Discs with initial outer radii $R = [60, 90]$ AU do not fragment for $z = 10$ (apart from run 006). For the discs with metallicities $z = [0.1, 1]$, only small differences in the disc-to-star mass ratio at fragmentation are found.

All of the discs studied reach a point where fragmentation occurs, or the disc undergoes expansion, stabilises and retains spiral arms which provide an efficient mechanism for material to move radially inward. This is characterised by an increase in stellar accretion rate. Typically, it is found that the smaller discs with $z = 10$ do not fragment. This is a combination of inefficient cooling in the spiral arms and a higher rate of disc expansion when the spiral features become strong. Runs 3, 12 and 15 are examples of this. However, an increased stellar mass also provides stability. Combined with the other stabilising factors, this is the reason why runs 19 - 21 as well as 24 do not fragment (see discussion in Section 5.4.1).

5.4.3 Accretion relation

Typically, the mass accretion rate of the central star scales with the disc accretion rate, albeit $\sim$ 3 orders of magnitude smaller. Figure 5.11 shows this relation. The average stellar accretion rate throughout the whole simulation is shown, as well as the beginning and end of each simulation. It is found that the stellar accretion rate is smaller at the start of each simulation and larger at the end when compared to the total average accretion rate. This demonstrates the angular momentum transport provided by the gravitational instability, as the end of the simulations are when the discs are unstable. Prior to the onset of the instability, angular momentum transport outward is inefficient, and material only moves inward slowly.

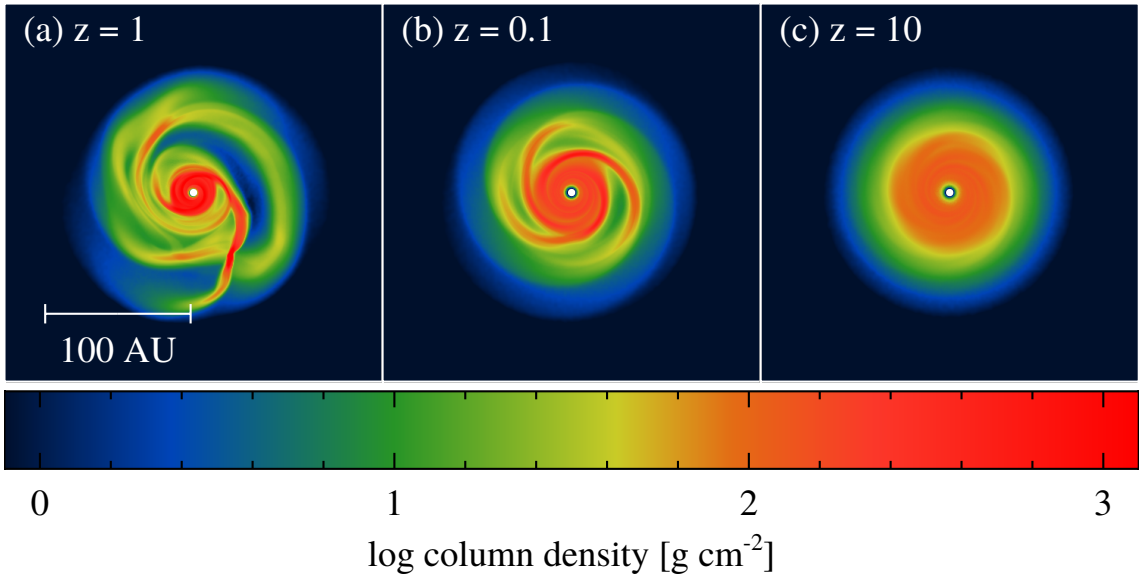

Figure 5.9: Column density snapshots of discs at a time of 22 kyr, specifically for runs 1 - 3 (see Table 5.2). Panel (a) is a disc where $z = 1$ (solar metallicity), and is shown just prior to the formation of a bound fragment. Panel (b) is a disc where the metallicity has been reduced by an order of magnitude with $z = 0.1$. The disc is stable as more material is required in the spiral arms for them to become optically thick. Panel (c) is a disc where the metallicity has been increased by an order of magnitude with $z = 10$. No strong spirals have yet formed as material can be efficiently distributed throughout the disc. Spirals do eventually form, but the disc does not fragment due to inefficient cooling.

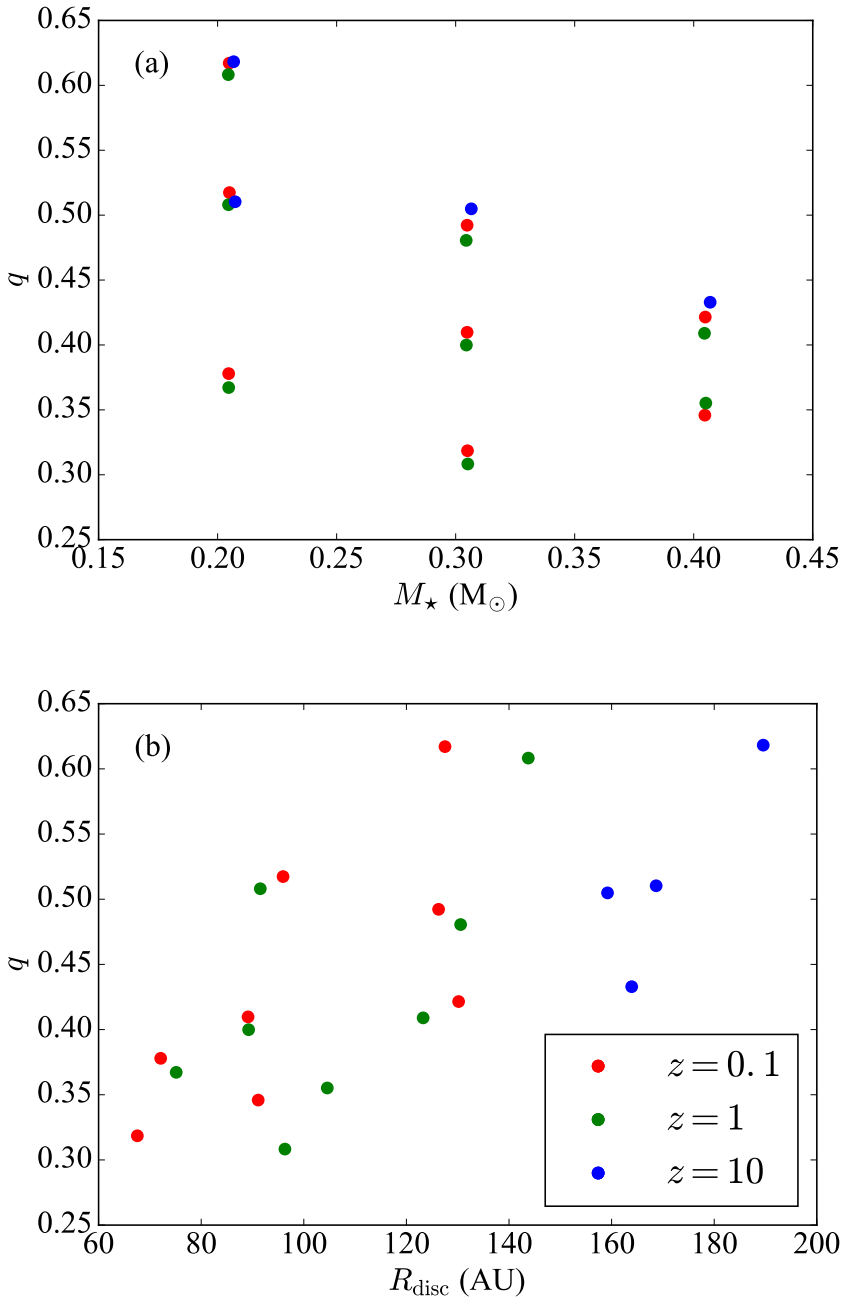

Figure 5.10: The effect of metallicity on M-dwarf disc fragmentation. The disc-to-star mass ratio, q, at the time of disc fragmentation as a function of (a) stellar mass, and (b) disc radius, for metallicities $z = [0.1, 1, 10]$ marked by the red, green and blue points, respectively. Typically, discs with a higher metallicity require a larger q to fragment. Similarly, these discs are larger, suggesting a period of expansion. There exists no significant difference in q for discs with metallicities of $z = [0.1, 1]$. Generally, discs around more massive stars fragment at a lower disc-to-star mass ratio. The required disc-to-star mass ratio for fragmentation increases with disc size.

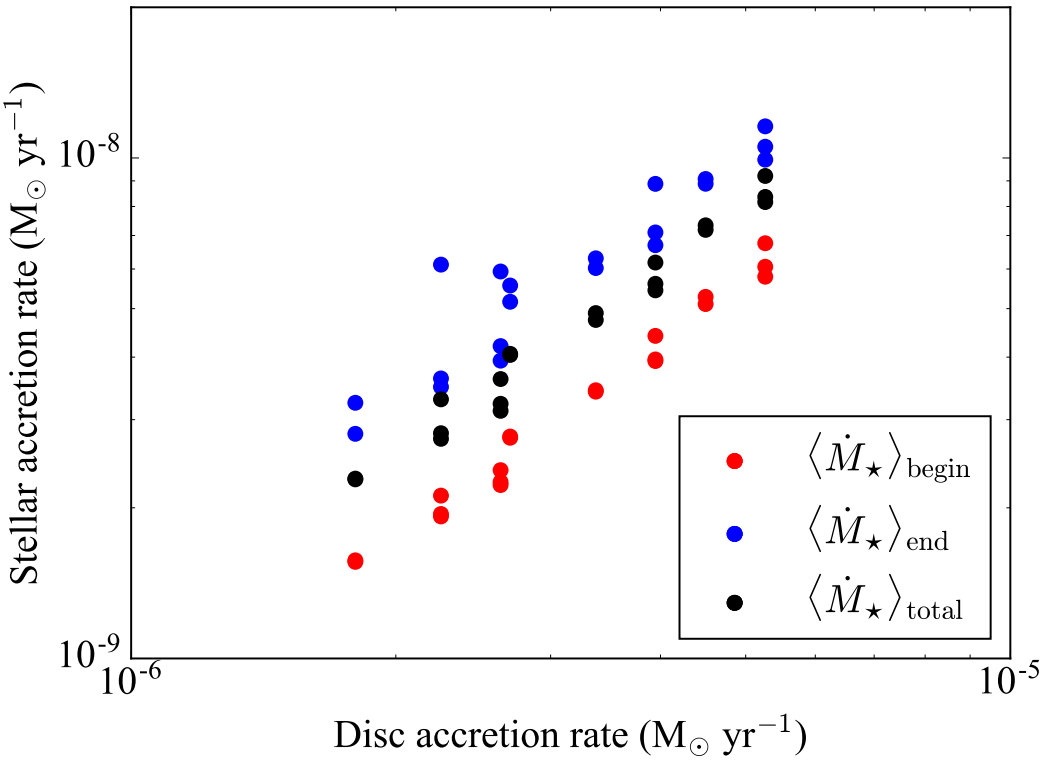

Figure 5.11: The relationship between the mass accretion rate onto the disc (set by Equation 5.5) and the accretion rate onto the central star during the simulation. The black points show the average stellar accretion rate for each simulation. The red and blue points show the average stellar accretion rate during the first and last 10% of the disc evolution period, respectively. Toward the end of the simulations, the discs are gravitationally unstable, providing a means of outward angular momentum transport. As such, material can move inward and accrete onto the central star, hence the observed increase in the stellar accretion rate.

5.5 The properties of planets formed through disc fragmentation

The evolution of discs which undergo fragmentation is continued until a fragment collapses and attains a central density of 10^{-3} g cm^{-3}. These dense objects are referred to as protoplanets. Note that due to the violent interactions with the discs and other fragments, the fragments analysed in the previous section are not necessarily those which correspond with the formed protoplanets here. When a fragment undergoes a second collapse (Larson 1969), I define the boundaries for the corresponding first and second cores as the maxima in the radial/infall velocity profiles.

The protoplanet data are presented in Table 5.3, showing the distance from the central star at which they form, the radii and masses of the first and second cores, and the ratios of rotational-to-gravitational and thermal-to-gravitational energy at the first and second core boundaries. The first core masses are super-Jovian and in some cases, are higher than the brown dwarf mass limit of ~ 13 M$_{\rm J}$. They have radii between 1 and 10 AU, typical of more massive cloud collapse simulations (Larson 1969; Stamatellos et al. 2007b). The second cores are an order of magnitude smaller.

Table 5.3: Properties of protoplanets which attain a central density of 10^{-3} g cm^{-3}. The first and second hydrostatic core boundaries ($R_{\rm fc}$ and $R_{\rm sc}$ respectively) are determined from maxima in the spherically-averaged infall velocity profiles. The first cores have radii between 1 and 10 AU and are super-Jovian in mass, with some breaching the brown dwarf mass limit of ~ 13 M$_{\rm J}$. Runs 14, 16, 18, 23 and 25 do not show evidence for a second core which may be attributed to rotational support.

Run	a (AU)	$R_{\rm fc}$ (AU)	$R_{\rm sc}$ (AU)	$R_{\rm sc}$ (R$_\odot$)	$M_{\rm fc}$ (M$_{\rm J}$)	$M_{\rm sc}$ (M$_{\rm J}$)	$\left\|\frac{E_{\rm rot}}{E_{\rm grav}}\right\|_{\rm fc}$	$\left\|\frac{E_{\rm ther}}{E_{\rm grav}}\right\|_{\rm fc}$	$\left\|\frac{E_{\rm rot}}{E_{\rm grav}}\right\|_{\rm sc}$	$\left\|\frac{E_{\rm ther}}{E_{\rm grav}}\right\|_{\rm sc}$
05	27	3.2	0.03	7.3	9.2	2.6	0.12	0.80	0.07	0.95
06	32	4.5	0.13	28	21	11	0.06	0.92	0.05	0.96
07	27	3.7	0.03	5.8	10	2.8	0.08	0.86	0.05	1.02
08	14	3.2	0.03	5.5	6.0	2.9	0.05	0.90	0.04	1.06
09	105	7.1	0.03	6.1	13	5.0	0.08	0.88	0.06	0.99
11	24	2.3	0.03	5.9	6.9	2.4	0.10	0.84	0.06	0.99
14	18	2.8	-	-	6.1	-	0.10	0.86	-	-
16	63	6.5	-	-	21	-	0.11	0.82	-	-
17	51	4.5	0.04	8.8	11	2.6	0.13	0.78	0.08	0.93
18	72	1.0	-	-	15	-	0.09	0.90	-	-
22	40	3.1	0.03	6.4	9.7	3.5	0.07	0.87	0.04	1.05
23	33	3.2	-	-	8.9	-	0.11	0.82	-	-
25	49	6.2	-	-	16	-	0.11	0.83	-	-
26	46	5.1	0.03	5.5	5.6	1.9	0.07	0.86	0.04	1.00
27	79	8.9	0.04	7.6	17	4.9	0.10	0.86	0.09	0.94

Spherically-averaged radial profiles for the protoplanets are presented in Figure 5.12. Shown are: (a) density; (b) temperature; (c) rotational and (d) radial infall velocity; (e) mass within a given radius; and (f) ratios of the thermal-to-gravitational and rotational-to-gravitational energy. Structurally, the various protoplanets are similar to one another, differing only by mass. The temperature is generally higher within the more massive protoplanets, and as such, the radius at which the thermal energy exceeds the gravitational energy is larger. The rotational velocity is comparable to the infall velocity, but despite this, the ratio between rotational energy and gravitational energy is generally small throughout, between 0.01 and 0.1. The thermal energy is comparable to the gravitational energy, becoming dominant at radii 0.02 - 0.04 AU.

Some of the protoplanets do not show any infall velocity signatures indicative of a second core (runs 14, 16, 18, 23 and 25). Figure 5.13 shows the spherically-averaged radial profiles for the protoplanets in these runs. The protoplanets with and without second cores are structurally similar to each other with regard to density and temperature. Most strikingly however is the difference in infall velocity (Figures 5.12d and 5.13d, respectively). The protoplanets without a second core have an almost zero infall velocity in their inner regions and some even exhibit expansion (i.e. $-v_r < 0$).

Figure 5.14 shows azimuthally-averaged radial profiles of the ratio between rotational to infall velocity. I compare protoplanets which show a clear sign of second core formation with those that do not. The protoplanets with a second core (runs 8 and 11, green and blue lines, respectively) have $v_{\rm rot}/v_r < 10$ in their inner regions, which is relatively low compared to the protoplanets without second cores. In these latter cases (runs 16 and 25, orange and purple lines, respectively), the rotational velocity is a factor of 2 - 4 magnitudes higher than the infall velocity.

The initial mass and semi-major axis of the protoplanets are shown in Figure 5.15, and are compared against known exoplanet data. Although the protoplanets formed through gravitational instability are massive ($5-21$ M_J) on intermediate separation

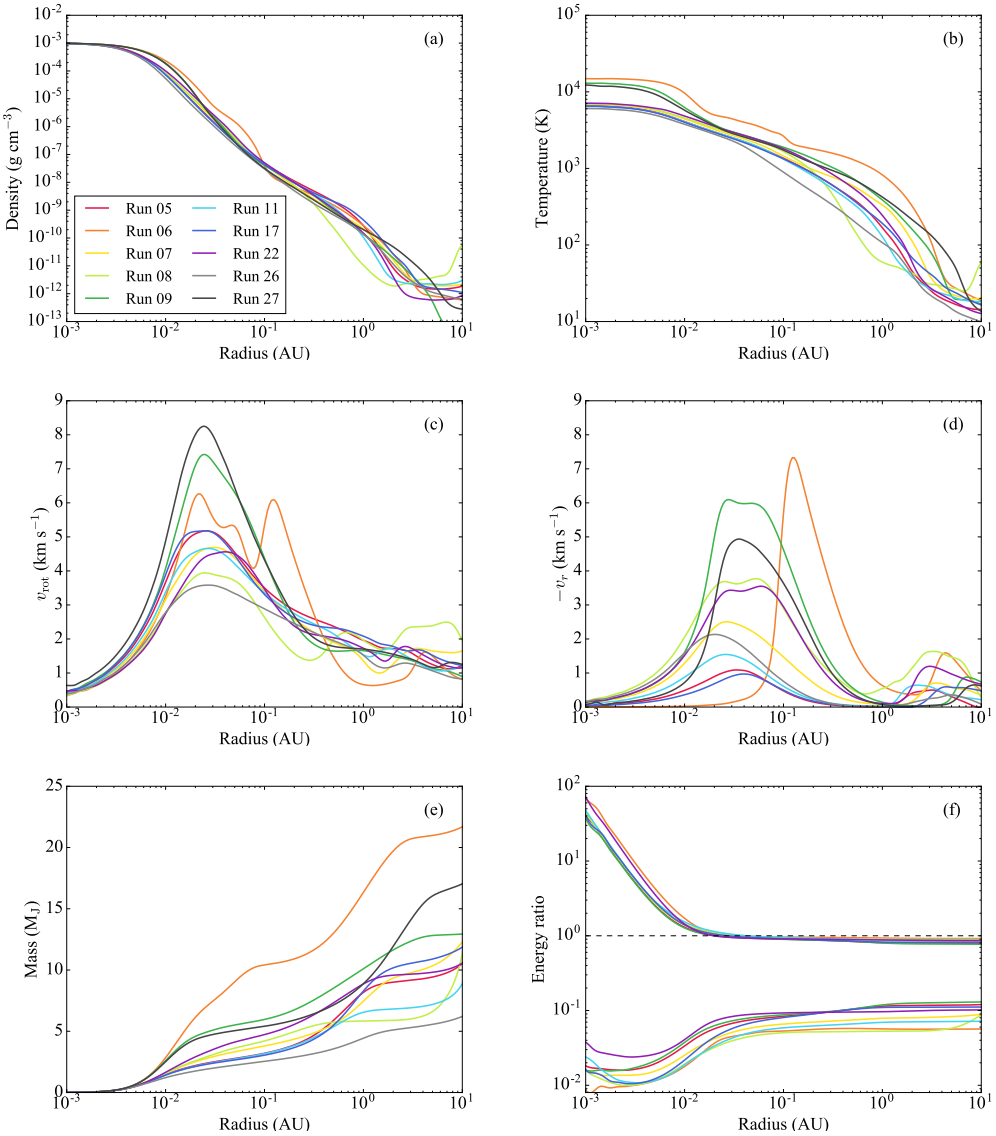

Figure 5.12: Spherically-averaged properties for a set of protoplanets, i.e. fragments which have undergone second collapse and attained a central density of 10^{-3} g cm^{-3}. Panels (a) and (b) show the density and temperature respectively. They do not vary significantly from protoplanet to protoplanet, though the protoplanets in runs 6, 9 and 27 possess denser and hotter central regions due to their high mass. Panels (c) and (d) show rotational and infall velocity, the former of which is significant as the protoplanets reside in a disc. The peaks in infall velocity are indicative of surface boundaries where gas begins to decelerate. The second core boundaries are at $R = 10^{-2}$–10^{-1} AU and the first core boundaries at $R = 1$–10 AU. Panel (e) shows the mass of the protoplanet at a given radius demonstrating that even in low-mass discs, the masses of formed objects are on the order of a few M$_{\rm J}$ or higher. Panel (f) shows the ratio of energies interior to a given radius: $E_{\rm ther}/E_{\rm grav}$ (top lines) and $E_{\rm rot}/E_{\rm grav}$ (bottom lines). The thermal energy only exceeds the gravitational energy within the second core. Rotational energy is generally much lower compared to gravitational energy. The protoplanets are resolved down to $10^{-4} < R < 10^{-3}$ AU.

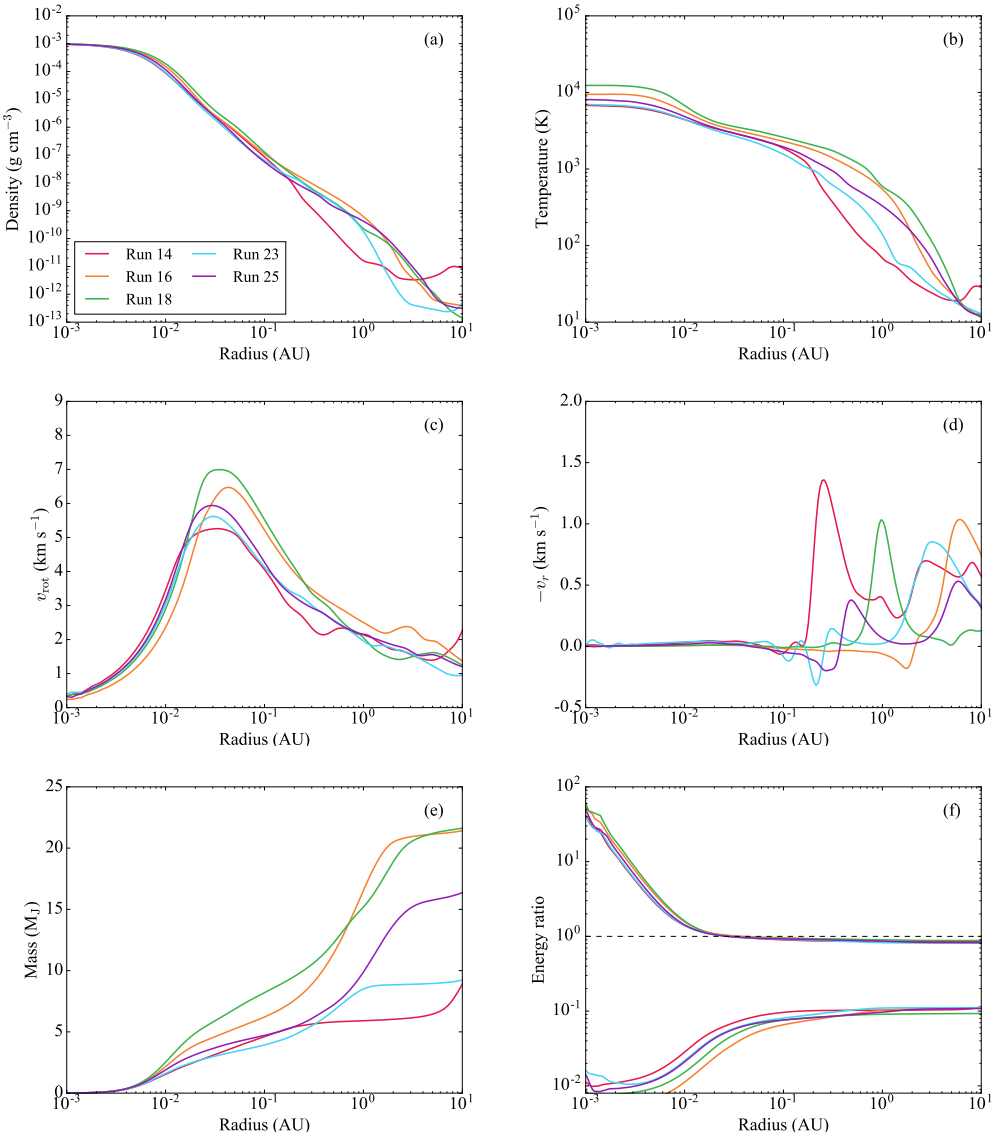

Figure 5.13: Spherically-averaged properties for a set of protoplanets, i.e. fragments that have attained a central density of 10^{-3} g cm^{-3}. These are the protoplanets that do not show any infall velocity signatures indicative of a second core. They are structurally similar to the protoplanets in Figure 5.12, however the infall velocities here are almost zero, and even show that parts of the protoplanet are slowly expanding. The protoplanets are resolved down to $10^{-4} < R < 10^{-3}$ AU.

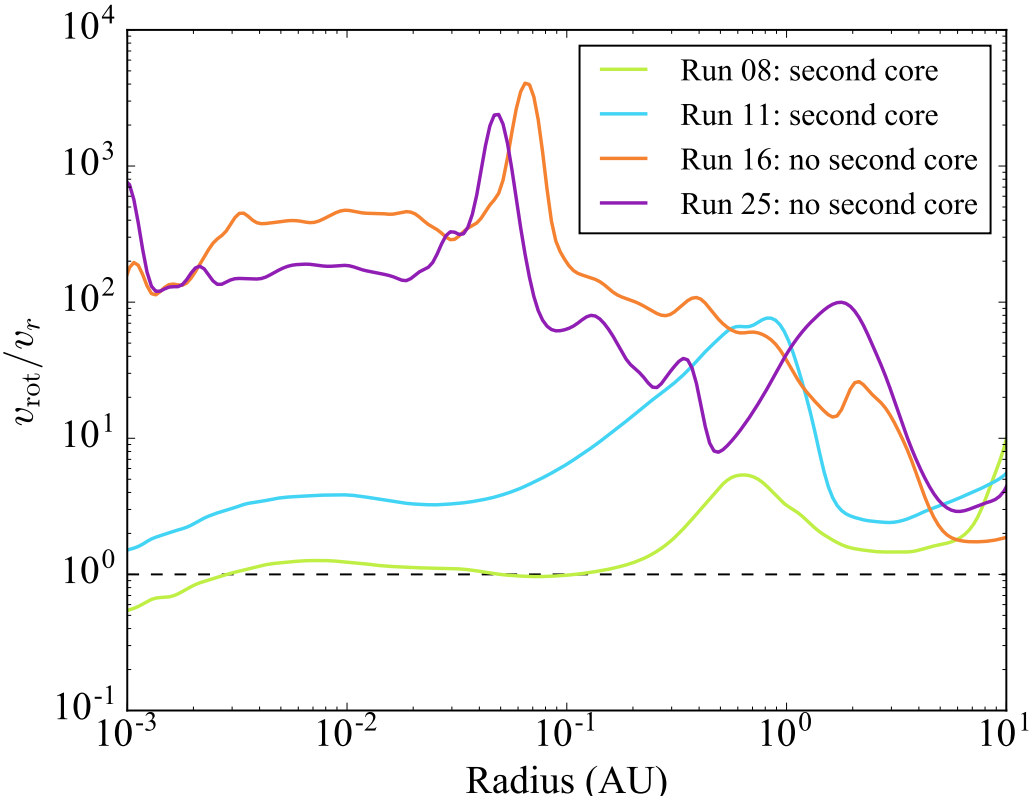

Figure 5.14: Azimuthally-averaged rotational-to-infall velocity for a set of protoplanets with and without any second core signatures as determined from infall velocity peaks. Runs 8 and 11 do possess second cores and exhibit values of $v_{\rm rot}/v_r < 10$ in their inner regions. Runs 16 and 25 do not have second core signatures, and their rotational velocity is on the order 3 magnitudes higher than the infall velocity in their inner regions. It may be that a significant amount of rotational velocity can inhibit the formation of the second core completely.

orbits ($14-105$ AU), these may not be their final properties. Massive planets embedded within a protostellar disc can open up a gap. Prior to gap formation, the planet can migrate inward. This may continue albeit on a shorter timescale after the gap is formed. However, the direction of migration may also change, and the planet can migrate outward. This depends on the mass of the planet, as well as disc thermodynamics, structure and viscosity. Additionally, gravitational interactions with other planets may also affect their orbital configuration.

A massive planet may also accrete material from the disc. This typically results in an overall mass increase, so much so that the planet may become a brown dwarf > 13 M_J or a hydrogen-burning star > 80 M_J. The mass accretion rate of the planet depends on the availability of material of the disc, and can be reduced if the planet provides radiative feedback, heating the neighbouring disc (e.g. Stamatellos & Inutsuka 2018). Alternatively, if a protoplanet formed through gravitational fragmentation undergoes tidal stripping via disruption or migration, then the resulting mass may not only be smaller, but potentially in the terrestrial mass regime (Nayakshin 2010, 2011).

5.6 Conclusions

I have performed a set of 27 SPH simulations of protostellar discs surrounding M-dwarf mass protostars. I varied the initial stellar mass such that $M_\star = [0.2, 0.3, 0.4]$ $M_\odot$ as well as the initial disc radius where $R_{\rm out} = [60, 90, 120]$ AU. Additionally, I investigated the effect of metallicity by adopting values $z = [0.1, 1, 10]$. The discs are initially stable, but their masses are steadily increased through mass loading. As such, they become gravitationally unstable, spiral arms develop, and in the majority of cases, a protoplanet forms via fragmentation within 30 kyr. The density requirement for fragment formation is chosen to be $\rho > 10^{-9}$ g cm^{-3} i.e. a threshold typically reached during gravitational collapse. From the discs that do fragment, I determine a minimum disc mass necessary for fragmentation to occur. The results are summarised as follows.

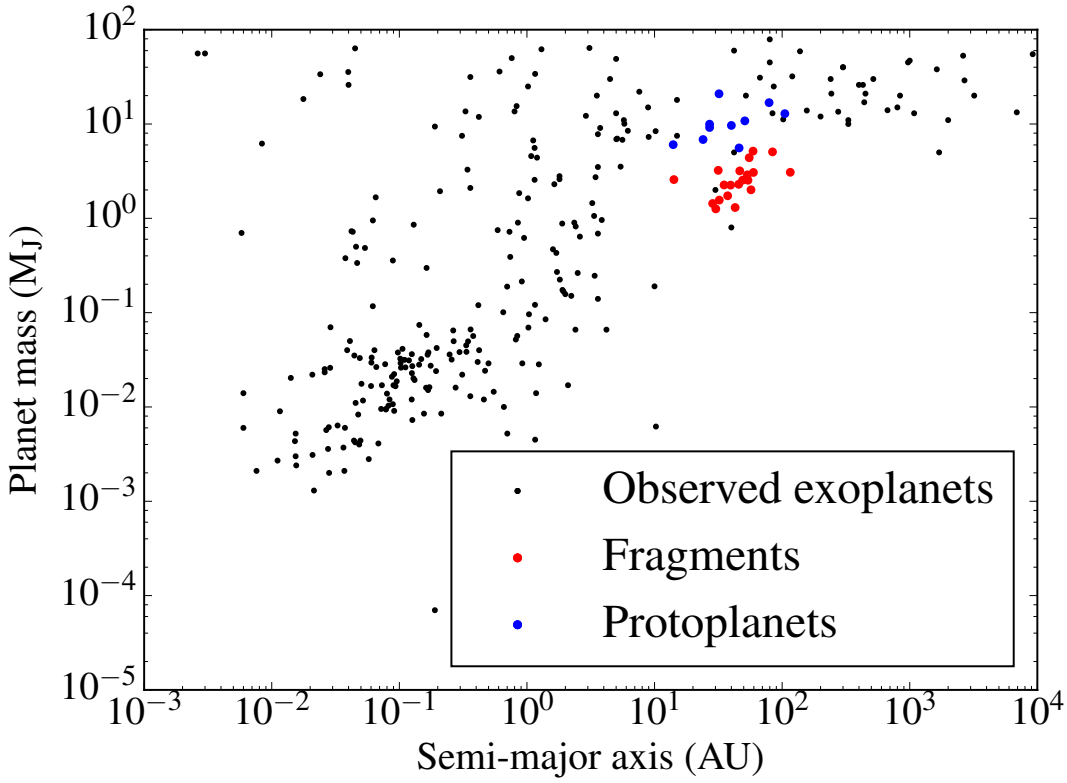

Figure 5.15: The distribution of planet mass as a function of their semi-major axis surrounding M-dwarf stars with masses $M_\star < 0.5$ $M_\odot$. Black points show the current discovered exoplanets. The red and blue points are the data from this work, where semi-major axis represents the distance to the central star. In red are the fragments which form through gravitational instability and have attained a central density of 10^{-9} g cm^3. The blue points are the protoplanets, defined as bound objects which have undergone second collapse and have reached a central density of 10^{-3} g cm^3. As these massive protoplanets are still embedded within their protostellar discs, they may radially migrate inwards or outwards, affecting their final semi-major axis. Similarly, they may undergo mass accretion or tidal stripping, affecting their final mass.

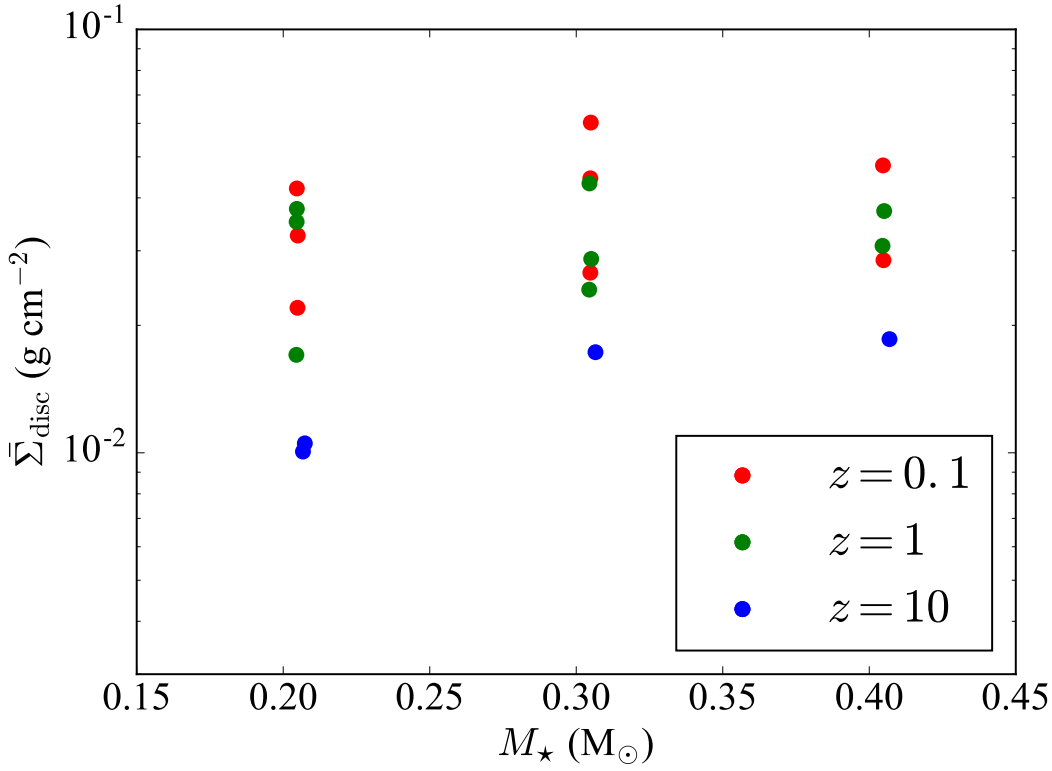

Figure 5.16: The average surface density of the discs at the time they fragment where $\bar{\Sigma}_{\rm disc} = M_{\rm disc}/\pi R^2_{\rm disc}$. A higher average surface density is required for fragmentation when the disc metallicity is lower. The lowest $\bar{\Sigma}$ is attained by metal rich discs around low-mass stars. However, an increased metallicity decreases the cooling rate in dense fragments, and can inhibit gravitational collapse altogether.

- The fragmentation of protostellar discs around M-dwarfs requires a disc-to-star mass ratio of at least $q \sim 0.3$ for smaller discs ($R_{\rm out} = 60$ AU) surrounding stars with masses $0.2 - 0.3$ M$_\odot$. When the stellar mass is increased to 0.4 M$_\odot$, such discs do not fragment. The disc-to-star mass ratio increases to $q \sim [0.4, 0.5, 0.6]$ for larger discs ($R_{\rm out} = 120$ AU) around stars of mass $M_\star = [0.4, 0.3, 0.2]$ M$_\odot$, respectively.

- The mass at which a disc fragments increases with both the size of the disc and the mass of the central star. However, no fragmentation occurs for discs of initial radius $R_{\rm out} = 60$ AU around stars with mass 0.4 M$_\odot$. This is likely a combined effect of rapid disc expansion from the formation of strong spiral features, with the fact that a larger stellar mass provides a greater degree of rotational support. I find that the smallest discs around lower mass stars are most susceptible to gravitational fragmentation, provided no extended period of rapid expansion occurs.

- The disc metallicity does not affect the mass at which discs fragment, but in some cases fragmentation may be suppressed. In the cases where the metallicity is an order of magnitude smaller, spiral arms are longer lived prior to fragment formation. When the metallicity is increased by an order of magnitude, spiral arms take longer to develop, and may not undergo gravitational fragmentation at all. This inhibition of collapse is due to inefficient cooling.

- I have calculated an average column density $\bar{\Sigma}_{\rm disc}$ for the fragmented discs for a variety of stellar masses, shown in Figure 5.16. I find that disc fragmentation requires $0.01 < \bar{\Sigma}_{\rm disc} < 0.1$ g cm^{-2} and that lower metallicity discs require a higher average column density in order to fragment. These are the discs which are generally more compact and can cool more efficiently. Fragmentation occurs at $\bar{\Sigma}_{\rm disc} \sim 0.01$ g cm^{-2} for discs with metallicity $z = 10$.

- Protoplanets that form by gravitational fragmentation around M-dwarfs are initially massive ($5-21$ M_J) on intermediate separation orbits ($14-105$ AU), have similar density and temperature profiles, and possess significant rotational velocity. In some cases this can act to preclude the collapse and formation of a protoplanet. The masses and semi-major axes of the formed planets are compatible with known exoplanets, though it should be noted that processes such as migration and mass accretion can affect these properties.

Chapter 6

Summary

The work presented in this thesis pertains to the gravitational instability of protostellar discs with the objective of determining how it occurs and the implications it has on planet formation. This has been achieved through the use of numerical simulations where novel techniques have been employed in order to capture the physics of the gravitational instability and the formation of planets through gravitational fragmentation. I began with an investigation of the gravitational instability in massive protostellar discs, and how the radiative feedback from objects formed through disc fragmentation affects their evolution and the evolution of the disc. This was followed by a numerical comparison between approximate radiative transfer methods for a variety of disc configurations, including those undergoing gravitational instability and fragmented discs. I finished with a study into the gravitational instability of discs surrounding M-dwarf stars with a focus on the feasability of planet formation. Here I summarise the results from each of these studies, and conclude the thesis with considerations of potential future endeavours.

6.1 The effect of radiative feedback

The gravitational fragmentation of massive protostellar discs can lead to the formation of planets, brown-dwarfs and low-mass stars. I studied the effect of radiative feedback from such formed objects (referred to as secondary objects) using radiative hydrodynamic simulations. I compared the results of simulations without any radiative feedback from secondary objects with those where two types of radiative feedback were considered: continuous and episodic. I found that: (i) continuous radiative feedback stabilises the disc and suppresses further fragmentation, reducing the number of secondary objects formed; (ii) episodic radiative feedback from secondary objects heats and stabilises the disc when the outburst occurs, but shortly after the outburst stops, the disc becomes unstable and fragments again. Fewer secondary objects are formed compared to the case without radiative feedback. I also found that the mass growth of secondary objects is mildly suppressed due to the effect of their radiative feedback. However, their mass growth also depends on where they form in the disc and on their subsequent interactions, such that their final masses are not drastically different from the case without radiative feedback. I found that the masses of secondary objects formed by disc fragmentation range from a few M_J to a few 0.1 $M_\odot$, though planets formed by fragmentation tend to be ejected from the disc. I concluded that planetary-mass objects on wide orbits are unlikely to form by disc fragmentation. Nevertheless, the fragmentation of massive protostellar discs may be a significant source of free-floating planets and companion brown dwarfs.

6.2 Efficient radiative transfer

Radiative transfer is an important component of hydrodynamic simulations as it determines the thermal properties of a physical system. It is especially important in cases where heating and cooling regulate significant processes, such as in the collapse of

molecular clouds, the development of gravitational instabilities in protostellar discs, disc-planet interactions, and planet migration. The computationally inexpensive treatment of radiative transfer in numerical simulations (Stamatellos et al. 2007b) was examined and compared with a novel approach whereby the column density of the gas (through which heating/cooling occurs) was estimated using the pressure scale height instead of the gravitational potential (Lombardi et al. 2015). I found that both methods are accurate for spherical configurations e.g. in collapsing molecular clouds and within clumps that form in protostellar discs. However, the pressure scale-height approach is more accurate in protostellar discs (low and high-mass discs, discs with spiral features, fragmented discs, discs with embedded planets). I also investigated the β-cooling approximation which is commonly used when simulating protostellar discs. This method assumes that the cooling time of the gas is proportional to its orbital period. I demonstrated that the use of a constant β cannot capture the wide range of spatial and temporal variations of cooling in protostellar discs, which may affect the development of gravitational instabilities, planet migration, planet mass growth, and the orbital properties of planets. I emphasised that computationally inexpensive approximate radiative transfer is available within numerical simulations, and can adequately capture the physics of the gravitational instability as well as disc fragmentation.

6.3 Gravitational instability in discs around M-dwarfs

There exists a number of super-Jovian mass exoplanets orbiting M-dwarf stars. These may be prime candidates of planets which formed through the gravitational fragmentation of their natal protostellar disc. Utilising an approximate prescription of radiative transfer (Lombardi et al. 2015), I explored the potential for planet formation via the

gravitational fragmentation of low-mass protostellar discs around M-dwarf stars. I determined the minimum mass required for fragmentation for discs by steadily increasing their masses until they fragmented and a bound object formed. The discs that were considered had radial extents $R = [60, 90, 120]$ AU and metallicities $z = [0.1, 1, 10]$ solar metallicity, each surrounding stars of mass $M_\star = [0.2, 0.3, 0.4]$ $M_\odot$. I found that disc-to-star mass ratios of $q \sim 0.6$ are required for extended discs ($R = 120$ AU) to fragment, and $q \sim 0.3$ for compact discs ($R = 60$ AU) to fragment. However, compact discs surrounding stars of mass 0.4 $M_\odot$ do not fragment due to a high degree of rotational support: they tend to expand rapidly and become gravitationally stable. The mass at which a disc fragments increases with both the initial disc radius and stellar mass. Metallicity does not affect the fragmentation mass of a disc, but it does however affect its evolution: spirals are longer lived when the metallicity is lower, and develop later when the metallicity is higher. Additionally, a high metallicity may inhibit the collapse of dense fragments in spiral arms as thermal support against gravity is significant. Planets form via gravitational fragmentation with masses $5 - 21$ M_J and at distances $14 - 105$ AU from the central star. They all have similar density and temperature profiles, attained after second collapse has occurred, and all possess significant angular velocity. Their masses and orbital radii from the host star agree well with the population of massive exoplanets on wide orbits around M-dwarf stars. However, migration, mass accretion and tidal stripping can affect these properties, and so an evolutionary study of the planets is required to determine their ultimate masses and orbital configurations.

6.4 Future work

The gravitational instability is an important process regarding protostellar discs, not only as a key driver of angular momentum transfer, but may also be a way to form massive wide-orbit or free-floating planets.

This work has focused on massive protostellar discs and discs around Sun-like stars and M-dwarfs. However, I have not considered the gravitational instability of circumbinary discs, where it is expected that the thermal contribution from the secondary star would act to provide additional thermal support. Although there exists studies of the gravitational instability in such systems (see Mayer et al. (2010) for a review), it would be useful to compare the results of simulations where a realistic treatment of radiative transfer is used. Additionally, the feasibility of gravitational fragmentation of circumbinary discs can be determined, and the properties of formed protoplanets can be compared with those that form in similar discs around single stars.

Dense clumps within simulations are typically replaced with sink particles at a relatively early stage (typically when the density reaches 10^{-9} g cm^{-3}), but it would be useful to implement a technique which can track the clump until it undergoes second collapse and a protoplanet is formed. At this point, the temperature profile of the protoplanet can be obtained and included as a thermal contribution after a sink is introduced. This improved method of obtaining realistic temperature profiles may lead to changes in the subsequent evolution of the disc, and in the migration and mass accretion of the protoplanet.

There already exists observations of protostellar discs potentially undergoing gravitational instability (e.g Pérez et al. 2015) and of planets which may have formed via gravitational fragmentation (e.g. Marois et al. 2010; Tobin et al. 2016). With accurate treatments of physical processes and ever increasing computational performance, we can now begin to construct synthetic population models of planets formed through gravitational fragmentation, probing their properties, and following their evolution from collapse to ultimate orbital configuration. Combined with the swathe of recent observations, a statistical comparison would then be able to be made. Although I have demonstrated that planet formation can result from the gravitational fragmentation of protostellar discs, a comparison with current and upcoming observations will be

able to elucidate details regarding its frequency, requirements, and importance in the context of planet formation.

Chapter 7

Appendix

7.1 SPH extras

7.1.1 Momentum equation

The SPH fluid equations can be derived from the Euler-Lagrange equations which guarantees the conservation of momentum, angular momentum, and energy. The Lagrangian of a given system is

$$\mathscr{L} = T - V, \tag{7.1}$$

where T and V are the kinetic and potential energies respectively. For a hydrodynamical system neglecting self-gravity (e.g. Eckart 1960; Salmon 1988; Morrison 1998), the Lagrangian can be written

$$\mathscr{L} = \int_V \left(\frac{1}{2} \rho \boldsymbol{v}^2 - \rho u \right) \mathrm{d}V, \tag{7.2}$$

which in discreet form is

$$\mathscr{L}_i = \sum_{j=1}^{N} m_j \left(\frac{1}{2} \boldsymbol{v}_j^2 - u_j \right). \tag{7.3}$$

The specific internal energy u is a function of both entropy and density (and therefore spatial co-ordinate). The Euler-Lagrange equations guarantee conservation i.e.

$$\frac{\mathrm{d}}{\mathrm{d}t}\left(\frac{\partial \mathscr{L}_i}{\partial \boldsymbol{v}_i}\right) - \frac{\partial \mathscr{L}_i}{\partial \boldsymbol{r}_i} = 0. \tag{7.4}$$

Differentiating Equation 7.3 with respect to $\boldsymbol{v}$ and $\boldsymbol{r}$, noting that $u(\boldsymbol{r})$, yields

$$\frac{\mathrm{d}}{\mathrm{d}t}\left(\frac{\partial \mathscr{L}_i}{\partial \boldsymbol{v}_i}\right) = m_i \frac{\mathrm{d}\boldsymbol{v}_i}{\mathrm{d}t}, \tag{7.5}$$

$$\frac{\partial \mathscr{L}_i}{\partial \boldsymbol{r}_i} = \sum_{j=1}^{N} m_j \frac{\partial u_j}{\partial \rho_j}\bigg|_s \frac{\partial \rho_j}{\partial \boldsymbol{r}_j}. \tag{7.6}$$

Consider the first law of thermodynamics which states that the total energy of a system is conserved i.e.

$$\mathrm{d}U = T\mathrm{d}S - P\mathrm{d}V, \tag{7.7}$$

where the first term on the right hand side represents heat added to the system in terms of temperature T and entropy S. The second term on the right hand side represents work done via expansion and contractions in terms of pressure P and volume V. As the SPH volume estimate is $V = m/\rho$, then $\mathrm{d}V/\mathrm{d}\rho = -m/\rho^2$, and the above can be written as

$$\mathrm{d}u = T\mathrm{d}s + \frac{P}{\rho^2}\mathrm{d}\rho, \tag{7.8}$$

where now, $u = U/m$ is the specific internal energy and $s = S/m$ the specific entropy. Then, at constant entropy

$$\frac{\partial u}{\partial \rho} = \frac{P}{\rho^2}. \tag{7.9}$$

We can put this and Equation 2.5 into Equation 7.6 to get

$$\frac{\partial \mathscr{L}_i}{\partial \boldsymbol{r}_i} = -m_i \sum_{j=1}^{N} m_j \left(\frac{P_i}{\rho_i^2} + \frac{P_j}{\rho_j^2}\right) \nabla_i W\left(\boldsymbol{r}_{ij}, h\right), \tag{7.10}$$

and hence the SPH momentum equation

$$\frac{\mathrm{d}\boldsymbol{v}_i}{\mathrm{d}t} = -\sum_{j=1}^{N} m_j \left(\frac{P_i}{\rho_i^2} + \frac{P_j}{\rho_j^2} \right) \nabla_i W(\boldsymbol{r}_{ij}, h). \tag{7.11}$$

This is only valid for constant smoothing lengths and no dissipation. It is however fully conservative provided the smoothing kernel is symmetric: the summation of the momentum of particle i is equal and opposite to that of particle j.

7.1.2 Energy equation

The SPH energy equation can be found by considering the first law of thermodynamics in the form from Equation 7.8. If entropy is constant then

$$\mathrm{d}u = \frac{P}{\rho^2}\mathrm{d}\rho, \tag{7.12}$$

and the time derivative is

$$\frac{\mathrm{d}u}{\mathrm{d}t} = \frac{P}{\rho^2}\frac{\mathrm{d}\rho}{\mathrm{d}t}. \tag{7.13}$$

Noting that in discreet form

$$\frac{\partial \rho_i}{\partial t} = -\sum_{j=1}^{N} m_j \boldsymbol{v}_{ij} \cdot \nabla_i W(\boldsymbol{r}_{ij}, h), \tag{7.14}$$

then the SPH energy equation is

$$\frac{\mathrm{d}u_i}{\mathrm{d}t} = \frac{P_i}{\rho_i^2} \sum_{j=1}^{N} m_j \boldsymbol{v}_{ij} \cdot \nabla W(\boldsymbol{r}_{ij}, h), \tag{7.15}$$

where $\boldsymbol{v}_{ij} = \boldsymbol{v}_i - \boldsymbol{v}_j$. This assumes no dissipation (i.e. constant entropy) and constant smoothing length.

Bibliography

Adachi, I., Hayashi, C., & Nakazawa, K. 1976, Progress of Theoretical Physics, 56, 1756

Adams, F. C., Hollenbach, D., Laughlin, G., & Gorti, U. 2004, *Astrophys. J.*, 611, 360

Alexander, R., Pascucci, I., Andrews, S., Armitage, P., & Cieza, L. 2014, Protostars and Planets VI, 475

Alexander, R. D. & Armitage, P. J. 2009, *Astrophys. J.*, 704, 989

Alexander, R. D., Clarke, C. J., & Pringle, J. E. 2006a, *Mon. Not. Roy. Astron. Soc.*, 369, 216

Alexander, R. D., Clarke, C. J., & Pringle, J. E. 2006b, *Mon. Not. Roy. Astron. Soc.*, 369, 229

Alexander, R. D. & Pascucci, I. 2012, *Mon. Not. Roy. Astron. Soc.*, 422, L82

Aller, K. M., Kraus, A. L., Liu, M. C., et al. 2013, *Astrophys. J.*, 773, 63

André, P., Di Francesco, J., Ward-Thompson, D., et al. 2014, Protostars and Planets VI, 27

André, P., Men'shchikov, A., Bontemps, S., et al. 2010, *Astron. Astrophys.*, 518, L102

Andre, P., Montmerle, T., & Feigelson, E. D. 1987, *Astron. J.*, 93, 1182

Andre, P., Ward-Thompson, D., & Barsony, M. 1993, *Astrophys. J.*, 406, 122

Andrews, S. M., Rosenfeld, K. A., Kraus, A. L., & Wilner, D. J. 2013, *Astrophys. J.*, 771, 129

Andrews, S. M. & Williams, J. P. 2005, *Astrophys. J.*, 631, 1134

Andrews, S. M. & Williams, J. P. 2007, *Astrophys. J.*, 659, 705, (c) 2007: The American Astronomical Society

Andrews, S. M., Wilner, D. J., Hughes, A. M., Qi, C., & Dullemond, C. P. 2009, *Astrophys. J.*, 700, 1502

Andrews, S. M., Wilner, D. J., Hughes, A. M., Qi, C., & Dullemond, C. P. 2010, eprint arXiv, 1007, 5070, accepted in ApJ, 39 pages, 10 figures

Ansdell, M., Williams, J. P., Manara, C. F., et al. 2017, *Astron. J.*, 153, 240

Ansdell, M., Williams, J. P., Trapman, L., et al. 2018, *Astrophys. J.*, 859, 21

Apai, D. 2009, Earth, 105, 311

Armitage, P. J. 2011, *Ann. Rev. Astron, Astrophys.*, 49, 195

Armitage, P. J. 2015, ArXiv e-prints

Armitage, P. J., Livio, M., & Pringle, J. E. 2001, *Mon. Not. Roy. Astron. Soc.*, 324, 705

Aso, Y., Ohashi, N., Aikawa, Y., et al. 2017, *Astrophys. J.*, 849, 56

Attwood, R. E., Goodwin, S. P., Stamatellos, D., & Whitworth, A. P. 2009, *Astron. Astrophys.*, 495, 201

Audard, M., Ábrahám, P., Dunham, M. M., et al. 2014, Protostars and Planets VI, Eds. H. Beuther, R. Klessen, C. Dullemond, T. Henning, University of Arizona Press, 387

Bachiller, R. 1996, *Ann. Rev. Astron, Astrophys.*, 34, 111

Backus, I. & Quinn, T. 2016, *Mon. Not. Roy. Astron. Soc.*, 463, 2480

Baehr, H., Klahr, H., & Kratter, K. M. 2017, *Astrophys. J.*, 848, 40

Bailey, V., Meshkat, T., Reiter, M., et al. 2014, *Astrophys. J. Letters*, 780, L4

Balbus, S. A. & Hawley, J. F. 1991, *Astrophys. J.*, 376, 214

Bally, J., O'Dell, C. R., & McCaughrean, M. J. 2000, *Astron. J.*, 119, 2919

Balsara, D. S. 1995, Journal of Computational Physics, 121, 357

Barnes, J. & Hut, P. 1986, *Nature*, 324, 446

Baruteau, C., Meru, F., & Paardekooper, S.-J. 2011, *Mon. Not. Roy. Astron. Soc.*, 416, 1971

Batalha, N. M., Borucki, W. J., Bryson, S. T., et al. 2011, *Astrophys. J.*, 729, 27

Bate, M. R. 2009, *Mon. Not. Roy. Astron. Soc.*, 392, 1363

Bate, M. R., Bonnell, I. A., & Price, N. M. 1995, *Mon. Not. Roy. Astron. Soc.*, 277, 362

Bate, M. R. & Burkert, A. 1997, *Mon. Not. Roy. Astron. Soc.*, 288, 1060, (c) 1997 The Royal Astronomical Society

Bate, M. R., Lubow, S. H., Ogilvie, G. I., & Miller, K. A. 2003, *Mon. Not. Roy. Astron. Soc.*, 341, 213

Bell, K. R. & Lin, D. N. C. 1994, *Astrophys. J.*, 427, 987

Benítez-Llambay, P., Masset, F., Koenigsberger, G., & Szulágyi, J. 2015, *Nature*, 520, 63

Benz, W. 1990, in Numerical Modelling of Nonlinear Stellar Pulsations Problems and Prospects, ed. J. R. Buchler, 269

Bergin, E. A., Cleeves, L. I., Gorti, U., et al. 2013, *Nature*, 493, 644

Blum, J. & Wurm, G. 2008, *Ann. Rev. Astron, Astrophys.*, 46, 21

Boley, A. C. 2009, *Astrophys. J. Letters*, 695, L53

Boley, A. C., Hayfield, T., Mayer, L., & Durisen, R. H. 2010, Icarus, 207, 509

Boley, A. C., Mejía, A. C., Durisen, R. H., et al. 2006, *Astrophys. J.*, 651, 517, (c) 2006: The American Astronomical Society

Bonfils, X., Astudillo-Defru, N., Díaz, R., et al. 2018, *Astron. Astrophys.*, 613, A25

Bonfils, X., Delfosse, X., Udry, S., et al. 2013, *Astron. Astrophys.*, 549, A109

Bonnell, I. & Bastien, P. 1992, *Astrophys. J.*, 401, L31

Borucki, W. J., Koch, D., Basri, G., et al. 2010a, Science, 327, 977

Borucki, W. J., Koch, D., Basri, G., et al. 2010b, Science, 327, 977

Boss, A. P. 1988, *Astrophys. J.*, 331, 370

Boss, A. P. 1997, Science, 276, 1836

Boss, A. P. 2006, *Astrophys. J.*, 644, L79

Bowler, B. P., Liu, M. C., Shkolnik, E. L., & Tamura, M. 2015, *Astrophys. J. Supple.*, 216, 7

Brinch, C., Crapsi, A., Jørgensen, J. K., Hogerheijde, M. R., & Hill, T. 2007, *Astron. Astrophys.*, 475, 915

Brinch, C. & Jørgensen, J. K. 2013, *Astron. Astrophys.*, 559, A82

Brinch, C., Jørgensen, J. K., & Hogerheijde, M. R. 2009, *Astron. Astrophys.*, 502, 199

Bryden, G., Chen, X., Lin, D. N. C., Nelson, R. P., & Papaloizou, J. C. B. 1999, *Astrophys. J.*, 514, 344

Cameron, A. G. W. 1978, Moon and Planets, 18, 5

Cesaroni, R., Galli, D., Lodato, G., Walmsley, C. M., & Zhang, Q. 2007, Protostars and Planets V, 197

Chabrier, G. 2003, The Publications of the Astronomical Society of the Pacific, 115, 763

Chandrasekhar, S. 1960, Proceedings of the National Academy of Science, 46, 253

Charbonneau, D., Brown, T. M., Latham, D. W., & Mayor, M. 2000, *Astrophys. J. Letters*, 529, L45

Chiang, E. & Laughlin, G. 2013, *Mon. Not. Roy. Astron. Soc.*, 431, 3444

Chiang, E. I. & Goldreich, P. 1997, *Astrophys. J.*, 490, 368

Chou, T.-L., Takakuwa, S., Yen, H.-W., Ohashi, N., & Ho, P. T. P. 2014, *Astrophys. J.*, 796, 70

Cieza, L., Padgett, D. L., Stapelfeldt, K. R., et al. 2007, *Astrophys. J.*, 667, 308

Cieza, L. A., Ruíz-Rodríguez, D., Perez, S., et al. 2018, *Mon. Not. Roy. Astron. Soc.*, 474, 4347

Clarke, C. J., Gendrin, A., & Sotomayor, M. 2001, *Mon. Not. Roy. Astron. Soc.*, 328, 485

Clarke, C. J., Harper-Clark, E., & Lodato, G. 2007, *Mon. Not. Roy. Astron. Soc.*, 381, 1543

Cleeves, L. I., Öberg, K. I., Wilner, D. J., et al. 2016, *Astrophys. J.*, 832, 110

Codella, C., Cabrit, S., Gueth, F., et al. 2014, *Astron. Astrophys.*, 568, L5

Commerçon, B., Hennebelle, P., & Henning, T. 2011a, *Astrophys. J. Letters*, 742, L9

Commerçon, B., Teyssier, R., Audit, E., Hennebelle, P., & Chabrier, G. 2011b, eprint arXiv, 1102, 1216

Courant, R., Friedrichs, K., & Lewy, H. 1928, Mathematische Annalen, 100, 32

Crida, A., Morbidelli, A., & Masset, F. 2006, , 181, 587

Crutcher, R. M. & Troland, T. H. 2000, *Astrophys. J. Letters*, 537, L139

Cullen, L. & Dehnen, W. 2010, *Mon. Not. Roy. Astron. Soc.*, 408, 669, (c) Journal compilation © 2010 RAS

Curran, R. L. & Chrysostomou, A. 2007, *Mon. Not. Roy. Astron. Soc.*, 382, 699

D'Angelo, G. & Bodenheimer, P. 2013, ArXiv e-prints

Deeg, H. J., Moutou, C., Erikson, A., et al. 2010, *Nature*, 464, 384

Dehnen, W. 2001, *Mon. Not. Roy. Astron. Soc.*, 324, 273

Dehnen, W. & Aly, H. 2012, *Mon. Not. Roy. Astron. Soc.*, 425, 1068

Dong, R., Vorobyov, E., Pavlyuchenkov, Y., Chiang, E., & Liu, H. B. 2016, *Astrophys. J.*, 823, 141

Doyle, L. R., Carter, J. A., Fabrycky, D. C., et al. 2011, Science, 333, 1602

Duffell, P. C. & Chiang, E. 2015, *Astrophys. J.*, 812, 94

Duffell, P. C. & MacFadyen, A. I. 2012, *Astrophys. J.*, 755, 7

Duffell, P. C. & MacFadyen, A. I. 2013, *Astrophys. J.*, 769, 41

Dullemond, C. P. 2012, RADMC-3D: A multi-purpose radiative transfer tool, Astrophysics Source Code Library

Dunham, M. M., Evans, N. J., Terebey, S., Dullemond, C. P., & Young, C. H. 2010, *Astrophys. J.*, 710, 470

Dunham, M. M. & Vorobyov, E. I. 2012, *Astrophys. J.*, 747, 52

Dupuy, T. J., Kratter, K. M., Kraus, A. L., et al. 2016, *Astrophys. J.*, 817, 80

Durisen, R. H., Boss, A. P., Mayer, L., et al. 2007, Protostars and Planets V, 607

Dutrey, A., Guilloteau, S., & Simon, M. 1994, *Astron. Astrophys.*, 286, 149

Duvert, G., Dutrey, A., Guilloteau, S., et al. 1998, *Astron. Astrophys.*, 332, 867

Dyer, C. C. & Ip, P. S. S. 1993, *Astrophys. J.*, 409, 60

Eckart, C. 1960, Physics of Fluids, 3, 421

Eisner, J. A., Arce, H. G., Ballering, N. P., et al. 2018, *Astrophys. J.*, 860, 77

Eisner, J. A., Bally, J. M., Ginsburg, A., & Sheehan, P. D. 2016, ArXiv e-prints

Enoch, M. L., Corder, S., Duchene, G., et al. 2011, eprint arXiv, 1106, 1899, accepted to *Astrophys. J.*Supplements

Enoch, M. L., Corder, S., Dunham, M. M., & Duchêne, G. 2009a, *Astrophys. J.*, 707, 103

Enoch, M. L., Evans, N. J., Sargent, A. I., & Glenn, J. 2009b, *Astrophys. J.*, 692, 973

Ercolano, B., Clarke, C. J., & Drake, J. J. 2009, *Astrophys. J.*, 699, 1639

Ercolano, B. & Rosotti, G. 2015, *Mon. Not. Roy. Astron. Soc.*, 450, 3008

Evans, N. J., Dunham, M. M., Jorgensen, J. K., et al. 2009, *Astrophys. J.*Supplement, 181, 321

Facchini, S., Clarke, C. J., & Bisbas, T. G. 2016, *Mon. Not. Roy. Astron. Soc.*, 457, 3593

Faherty, J. K., Burgasser, A. J., Cruz, K. L., et al. 2009, *Astron. J.*, 137, 1

Federrath, C., Banerjee, R., Clark, P. C., & Klessen, R. S. 2010, eprint arXiv, 1001, 4456, 30 pages, 17 figures, submitted to ApJ

Fischer, D. A., Howard, A. W., Laughlin, G. P., et al. 2014, Protostars and Planets VI, 715

Forgan, D. & Rice, K. 2009, *Mon. Not. Roy. Astron. Soc.*, 400, 2022

Forgan, D. & Rice, K. 2010, *Mon. Not. Roy. Astron. Soc.*, 406, 2549

Forgan, D. & Rice, K. 2011, *Mon. Not. Roy. Astron. Soc.*, 417, 1928

Forgan, D., Rice, K., Stamatellos, D., & Whitworth, A. P. 2009a, COOL STARS, 1094, 377

Forgan, D., Rice, K., Stamatellos, D., & Whitworth, A. P. 2009b, *Mon. Not. Roy. Astron. Soc.*, 394, 882

Forgan, D. H., Ilee, J. D., & Meru, F. 2018, *Astrophys. J. Letters*, 860, L5

Frank, J., King, A., & Raine, D. J. 2002, Accretion Power in Astrophysics: Third Edition, 398

Galicher, R., Rameau, J., Bonnefoy, M., et al. 2014, *Astron. Astrophys.*, 565, L4

Gammie, C. F. 1996, *Astrophys. J.*, 457, 355

Gammie, C. F. 2001, *Astrophys. J.*, 553, 174

Gillon, M., Jehin, E., Lederer, S. M., et al. 2016, *Nature*, 533, 221

Gillon, M., Triaud, A. H. M. J., Demory, B.-O., et al. 2017, *Nature*, 542, 456

Gingold, R. A. & Monaghan, J. J. 1977, *Mon. Not. Roy. Astron. Soc.*, 181, 375

Goldreich, P., Lithwick, Y., & Sari, R. 2004, *Ann. Rev. Astron, Astrophys.*, 42, 549

Goldreich, P. & Tremaine, S. 1980, *Astrophys. J.*, 241, 425

Goldreich, P. & Ward, W. R. 1973, *Astrophys. J.*, 183, 1051

Gonzalez, J.-F., Laibe, G., & Maddison, S. T. 2017, *Mon. Not. Roy. Astron. Soc.*, 467, 1984

Gorti, U., Dullemond, C. P., & Hollenbach, D. 2009, *Astrophys. J.*, 705, 1237

Gorti, U., Hollenbach, D., & Dullemond, C. P. 2015, *Astrophys. J.*, 804, 29

Gorti, U., Hollenbach, D., Najita, J., & Pascucci, I. 2011, *Astrophys. J.*, 735, 90

Green, J. D., Evans, N. J., Kóspál, Á., et al. 2011, eprint arXiv, 1103, 2156

Greenberg, R., Wacker, J. F., Hartmann, W. K., & Chapman, C. R. 1978, , 35, 1

Greene, T. P., Aspin, C., & Reipurth, B. 2008, *Astron. J.*, 135, 1421

Gressel, O., Turner, N. J., Nelson, R. P., & McNally, C. P. 2015, *Astrophys. J.*, 801, 84

Guilloteau, S. & Dutrey, A. 1998, *Astron. Astrophys.*, 339, 467

Guszejnov, D., Krumholz, M. R., & Hopkins, P. F. 2016, *Mon. Not. Roy. Astron. Soc.*, 458, 673

Habing, H. J. 1968, , 19, 421

Haisch, Jr., K. E., Lada, E. A., & Lada, C. J. 2001, *Astrophys. J. Letters*, 553, L153

Hao, W., Kouwenhoven, M. B. N., & Spurzem, R. 2013, *Mon. Not. Roy. Astron. Soc.*, 433, 867

Harries, T. J. 2015, *Mon. Not. Roy. Astron. Soc.*, 448, 3156

Harries, T. J., Douglas, T. A., & Ali, A. 2017, *Mon. Not. Roy. Astron. Soc.*, 471, 4111

Harsono, D., Jørgensen, J. K., van Dishoeck, E. F., et al. 2014, *Astron. Astrophys.*, 562, A77

Hartmann, L., Calvet, N., Gullbring, E., & D'Alessio, P. 1998, *Astrophys. J.*, 495, 385

Hartmann, L. & Kenyon, S. J. 1985, *Astrophys. J.*, 299, 462

Hartmann, L. & Kenyon, S. J. 1996, *Ann. Rev. Astron, Astrophys.*, 34, 207

Haworth, T. J., Boubert, D., Facchini, S., Bisbas, T. G., & Clarke, C. J. 2016a, *Mon. Not. Roy. Astron. Soc.*, 463, 3616

Haworth, T. J., Clarke, C. J., & Owen, J. E. 2016b, *Mon. Not. Roy. Astron. Soc.*, 457, 1905

Haworth, T. J., Facchini, S., Clarke, C. J., & Cleeves, L. I. 2017, *Mon. Not. Roy. Astron. Soc.*, 468, L108

Hayashi, C., Nakazawa, K., & Nakagawa, Y. 1985, in Protostars and Planets II, ed. D. C. Black & M. S. Matthews, 1100–1153

Hennebelle, P., Lesur, G., & Fromang, S. 2016, ArXiv e-prints

Henry, G. W., Marcy, G. W., Butler, R. P., & Vogt, S. S. 2000, *Astrophys. J. Letters*, 529, L41

Herbig, G. H. 1977, *Astrophys. J.*, 217, 693, a&AA ID. AAA020.065.019

Hernquist, L. & Katz, N. 1989, *Astrophys. J. Supple.*, 70, 419

Holden, L., Landis, E., Spitzig, J., & Adams, F. C. 2011, *Pub. Astron. Soc. Pac.*, 123, 14

Hubber, D. A., Batty, C. P., Mcleod, A., & Whitworth, A. P. 2011, *Astron. Astrophys.*, 529, A27

Hubber, D. A., Rosotti, G. P., & Booth, R. A. 2018, *Mon. Not. Roy. Astron. Soc.*, 473, 1603

Hubber, D. A., Walch, S., & Whitworth, A. P. 2013, *Mon. Not. Roy. Astron. Soc.*, 430, 3261

Hubber, D. A. & Whitworth, A. P. 2005, *Astron. Astrophys.*, 437, 113

Hueso, R. & Guillot, T. 2005, *Astron. Astrophys.*, 442, 703

Hughes, A. M., Wilner, D. J., Qi, C., & Hogerheijde, M. R. 2008, *Astrophys. J.*, 678, 1119

Humphries, R. J. & Nayakshin, S. 2018, *Mon. Not. Roy. Astron. Soc.*, 477, 593

Ilee, J. D., Forgan, D. H., Evans, M. G., et al. 2017, *Mon. Not. Roy. Astron. Soc.*, 472, 189

Imara, N. & Blitz, L. 2011, *Astrophys. J.*, 732, 78

Ireland, M. J., Kraus, A. L., Martinache, F., Law, N., & Hillenbrand, L. A. 2011, *Astrophys. J.*, 726, 113

Isella, A., Carpenter, J. M., & Sargent, A. I. 2009, *Astrophys. J.*, 701, 260

Isella, A., Testi, L., Natta, A., et al. 2007, *Astron. Astrophys.*, 469, 213

Johansen, A., Blum, J., Tanaka, H., et al. 2014, Protostars and Planets VI, 547

Johansen, A., Oishi, J. S., Mac Low, M.-M., et al. 2007, *Nature*, 448, 1022

Johnson, B. M. & Gammie, C. F. 2003, *Astrophys. J.*, 597, 131, (c) 2003: The American Astronomical Society

Johnstone, D., Hollenbach, D., & Bally, J. 1998, *Astrophys. J.*, 499, 758

Jørgensen, J. K., van Dishoeck, E. F., Visser, R., et al. 2009, *Astron. Astrophys.*, 507, 861

Kalas, P., Graham, J. R., Chiang, E., et al. 2008, Science, 322, 1345, (c) 2008: Science

Kanagawa, K. D., Muto, T., Tanaka, H., et al. 2015a, *Astrophys. J. Letters*, 806, L15

Kanagawa, K. D., Tanaka, H., Muto, T., Tanigawa, T., & Takeuchi, T. 2015b, *Mon. Not. Roy. Astron. Soc.*, 448, 994

Kellogg, K., Metchev, S., Gagné, J., & Faherty, J. 2016, *Astrophys. J. Letters*, 821, L15

Kennedy, G. M. & Kenyon, S. J. 2008, *Astrophys. J.*, 673, 502

Kenyon, S. J. & Hartmann, L. 1987, *Astrophys. J.*, 323, 714

Kenyon, S. J., Hartmann, L. W., Strom, K. M., & Strom, S. E. 1990, *Astron. J.*, 99, 869

Kim, J. S., Clarke, C. J., Fang, M., & Facchini, S. 2016, *Astrophys. J. Letters*, 826, L15

King, A. R., Pringle, J. E., & Livio, M. 2007, *Mon. Not. Roy. Astron. Soc.*, 376, 1740

Kirk, J. M., Ward-Thompson, D., Palmeirim, P., et al. 2013, *Mon. Not. Roy. Astron. Soc.*, 432, 1424

Klessen, R. S. 2011, eprint arXiv, 1109, 467

Kley, W. & Nelson, R. P. 2012, *Ann. Rev. Astron, Astrophys.*, 50, 211

Koch, D. G., Borucki, W. J., Basri, G., et al. 2010, *Astrophys. J. Letters*, 713, L79

Koerner, D. W., Sargent, A. I., & Beckwith, S. V. W. 1993, , 106, 2

Kratter, K. M. & Lodato, G. 2016, ArXiv e-prints

Kratter, K. M. & Matzner, C. D. 2006, *Mon. Not. Roy. Astron. Soc.*, 373, 1563

Kratter, K. M., Matzner, C. D., & Krumholz, M. R. 2008, *Astrophys. J.*, 681, 375

Kratter, K. M., Matzner, C. D., Krumholz, M. R., & Klein, R. I. 2010, *Astrophys. J.*, 708, 1585

Kratter, K. M., Murray-Clay, R. A., & Youdin, A. N. 2010, *Astrophys. J.*, 710, 1375

Kraus, A. L., Ireland, M. J., Cieza, L. A., et al. 2014, *Astrophys. J.*, 781, 20

Kraus, A. L., Ireland, M. J., Martinache, F., & Lloyd, J. P. 2008, *Astrophys. J.*, 679, 762

Krumholz, M. R. 2006, *Astrophys. J.*, 641, L45

Krumholz, M. R. & Burkert, A. 2010, *Astrophys. J.*, 724, 895

Kuiper, G. P. 1951, Proceedings of the National Academy of Sciences of the United States of America, 37, 1

Kuzuhara, M., Tamura, M., Ishii, M., et al. 2011, *Astron. J.*, 141, 119

Kuzuhara, M., Tamura, M., Kudo, T., et al. 2013, *Astrophys. J.*, 774, 11

Kwon, J., Doi, Y., Tamura, M., et al. 2018, *Astrophys. J.*, 859, 4

Lada, C. J. 1987, in IAU Symposium, Vol. 115, Star Forming Regions, ed. M. Peimbert & J. Jugaku, 1–17

Laibe, G. 2014, *Mon. Not. Roy. Astron. Soc.*, 437, 3037

Laplace, P. S. 1796, Exposition du Systém du Monde (Imprimerie Cercle-Social)

Larson, R. B. 1969, *Mon. Not. Roy. Astron. Soc.*, 145, 271

Lee, C.-F. 2010, *Astrophys. J.*, 725, 712

Lee, C.-F. 2011, *Astrophys. J.*, 741, 62

Lee, C.-F., Hirano, N., Zhang, Q., et al. 2014, *Astrophys. J.*, 786, 114

Léger, A., Rouan, D., Schneider, J., et al. 2009, *Astron. Astrophys.*, 506, 287

Levison, H. F., Kretke, K. A., & Duncan, M. J. 2015, *Nature*, 524, 322

Li, Y., Kouwenhoven, M. B. N., Stamatellos, D., & Goodwin, S. P. 2015, *Astrophys. J.*, 805, 116

Li, Y., Kouwenhoven, M. B. N., Stamatellos, D., & Goodwin, S. P. 2016, ArXiv e-prints

Lin, D. N. C., Faulkner, J., & Papaloizou, J. 1985, *Mon. Not. Roy. Astron. Soc.*, 212, 105

Lin, D. N. C. & Papaloizou, J. C. B. 1993, in Protostars and Planets III, ed. E. H. Levy & J. I. Lunine, 749–835

Lin, D. N. C. & Pringle, J. E. 1990, *Astrophys. J.*, 358, 515

Lissauer, J. J. 1993, *Ann. Rev. Astron, Astrophys.*, 31, 129

Lissauer, J. J., Fabrycky, D. C., Ford, E. B., et al. 2011, *Nature*, 470, 53

Liu, H. B., Takami, M., Kudo, T., et al. 2016, Science Advances, 2, e1500875

Liu, Y., Herczeg, G. J., Gong, M., et al. 2015, *Astron. Astrophys.*, 573, A63

Lodato, G. & Clarke, C. J. 2011, *Mon. Not. Roy. Astron. Soc.*, 413, 2735

Lodato, G., Meru, F., Clarke, C. J., & Rice, W. K. M. 2007, *Mon. Not. Roy. Astron. Soc.*, 374, 590

Lodato, G. & Rice, W. K. M. 2004, *Mon. Not. Roy. Astron. Soc.*, 351, 630, (c) 2004 RAS

Lomax, O., Whitworth, A. P., Hubber, D. A., Stamatellos, D., & Walch, S. 2014, *Mon. Not. Roy. Astron. Soc.*, 439, 3039

Lomax, O., Whitworth, A. P., Hubber, D. A., Stamatellos, D., & Walch, S. 2015, *Mon. Not. Roy. Astron. Soc.*, 447, 1550

Lombardi, J. C., McInally, W. G., & Faber, J. A. 2015, *Mon. Not. Roy. Astron. Soc.*, 447, 25

Lommen, D., Jørgensen, J. K., van Dishoeck, E. F., & Crapsi, A. 2008, *Astron. Astrophys.*, 481, 141

Low, C. & Lynden-Bell, D. 1976, *Mon. Not. Roy. Astron. Soc.*, 176, 367

Lucy, L. B. 1977, *Astron. J.*, 82, 1013

Luhman, K. L. & Rieke, G. H. 1999, *Astrophys. J.*, 525, 440

Lynden-Bell, D. & Pringle, J. E. 1974, *Mon. Not. Roy. Astron. Soc.*., 168, 603

MacFarlane, B. A. & Stamatellos, D. 2017, *Mon. Not. Roy. Astron. Soc.*, 472, 3775

Machida, M. N., Inutsuka, S., & Matsumoto, T. 2011, *Astrophys. J.*, 729, 42

Machida, M. N., Inutsuka, S.-i., & Matsumoto, T. 2006, *Astrophys. J. Letters*, 649, L129

Macintosh, B., Graham, J. R., Barman, T., et al. 2015, Science, 350, 64

Makino, J. & Aarseth, S. J. 1992, *Pub. Astron. Soc. Japan*, 44, 141

Malik, M., Meru, F., Mayer, L., & Meyer, M. 2015, *Astrophys. J.*, 802, 56

Mannings, V., Koerner, D. W., & Sargent, A. I. 1997, *Nature*, 388, 555

Maret, S., Belloche, A., Maury, A. J., et al. 2014, *Astron. Astrophys.*, 563, L1

Marois, C., Macintosh, B., Barman, T., et al. 2008, Science, 322, 1348

Marois, C., Zuckerman, B., Konopacky, Q. M., Macintosh, B., & Barman, T. 2010, Nature, 468, 1080

Martin, R. G. & Livio, M. 2012, *Mon. Not. Roy. Astron. Soc.*, 425, L6

Martin, R. G. & Livio, M. 2013, *Mon. Not. Roy. Astron. Soc.*, 434, 633

Masunaga, H. & Inutsuka, S. 2000, *Astrophys. J.*, 531, 350

Matzner, C. D. & Levin, Y. 2005, *Astrophys. J.*, 628, 817

Mayer, L., Boss, A., & Nelson, A. F. 2010, in Astrophysics and Space Science Library, Vol. 366, Planets in Binary Star Systems, ed. N. Haghighipour, 195

McCaughrean, M. J. & O'Dell, C. R. 1996, *Astron. J.*, 111, 1977

Men'shchikov, A., André, P., Didelon, P., et al. 2012, *Astron. Astrophys.*, 542, A81

Meru, F. & Bate, M. R. 2010, *Mon. Not. Roy. Astron. Soc.*, 1504, (c) Journal compilation © 2010 RAS

Meru, F. & Bate, M. R. 2011, *Mon. Not. Roy. Astron. Soc.*: Letters, 411, L1

Meru, F., Juhász, A., Ilee, J. D., et al. 2017, *Astrophys. J. Letters*, 839, L24

Mesa-Delgado, A., Núñez-Díaz, M., Esteban, C., et al. 2012, *Mon. Not. Roy. Astron. Soc.*, 426, 614

Mihalas, D. 1970, Stellar atmospheres (Series of Books in Astronomy and Astrophysics, San Francisco: Freeman)

Monaghan, J. J. 1997, Journal of Computational Physics, 136, 298

Monaghan, J. J. & Gingold, R. A. 1983, Journal of Computational Physics, 52, 374

Morris, J. P. & Monaghan, J. J. 1997, Journal of Computational Physics, 136, 41

Morrison, P. J. 1998, Reviews of Modern Physics, 70, 467

Mróz, P., Ryu, Y.-H., Skowron, J., et al. 2018, *Astron. J.*, 155, 121

Murillo, N. M., Lai, S.-P., Bruderer, S., Harsono, D., & van Dishoeck, E. F. 2013, *Astron. Astrophys.*, 560, A103

Natta, A., Testi, L., & Randich, S. 2006, *Astron. Astrophys.*, 452, 245

Naud, M.-E., Artigau, É., Malo, L., et al. 2014, *Astrophys. J.*, 787, 5

Nayakshin, S. 2010, *Mon. Not. Roy. Astron. Soc.*: Letters, 408, L36

Nayakshin, S. 2011, *Mon. Not. Roy. Astron. Soc.*, 416, 2974

Nayakshin, S. 2015a, *Mon. Not. Roy. Astron. Soc.*, 446, 459

Nayakshin, S. 2015b, *Mon. Not. Roy. Astron. Soc.*, 454, 64

Nayakshin, S. 2016, *Mon. Not. Roy. Astron. Soc.*, 461, 3194

Nayakshin, S. 2017, *Mon. Not. Roy. Astron. Soc.*, 470, 2387

Nayakshin, S. & Cha, S.-H. 2013, *Mon. Not. Roy. Astron. Soc.*, 435, 2099

Nayakshin, S. & Fletcher, M. 2015, *Mon. Not. Roy. Astron. Soc.*, 452, 1654

Nelson, A. F. 2006, *Mon. Not. Roy. Astron. Soc.*, 373, 1039

Nelson, R. P. & Papaloizou, J. C. B. 1993, *Mon. Not. Roy. Astron. Soc.*, 265, 905

Nelson, R. P. & Papaloizou, J. C. B. 1994, *Mon. Not. Roy. Astron. Soc.*, 270, 1

O'Dell, C. R., Wen, Z., & Hu, X. 1993, *Astrophys. J.*, 410, 696

Offner, S. S. R., Klein, R. I., McKee, C. F., & Krumholz, M. R. 2009, *Astrophys. J.*, 703, 131

Offner, S. S. R., Kratter, K. M., Matzner, C. D., Krumholz, M. R., & Klein, R. I. 2010, *Astrophys. J.*, 725, 1485

Owen, J. E., Clarke, C. J., & Ercolano, B. 2012, *Mon. Not. Roy. Astron. Soc.*, 422, 1880

Oxley, S. & Woolfson, M. M. 2003, *Mon. Not. Roy. Astron. Soc.*, 343, 900

Paardekooper, S.-J., Baruteau, C., & Meru, F. 2011, *Mon. Not. Roy. Astron. Soc.*: Letters, 416, L65

Paardekooper, S.-J. & Mellema, G. 2006, *Astron. Astrophys.*, 459, L17

Palla, F. & Stahler, S. W. 1993, *Astrophys. J.*, 418, 414

Palmeirim, P., André, P., Kirk, J., et al. 2013, *Astron. Astrophys.*, 550, A38

Pattle, K., Ward-Thompson, D., Berry, D., et al. 2017, *Astrophys. J.*, 846, 122

Peneva, S. P., Semkov, E. H., Munari, U., & Birkle, K. 2010, *Astron. Astrophys.*, 515, 24

Peretto, N., Fuller, G. A., Duarte-Cabral, A., et al. 2013, *Astron. Astrophys.*, 555, A112

Pérez, L. M., Carpenter, J. M., Andrews, S. M., et al. 2016, Science, 353, 1519

Pérez, L. M., Chandler, C. J., Isella, A., et al. 2015, ArXiv e-prints

Piétu, V., Guilloteau, S., & Dutrey, A. 2005, *Astron. Astrophys.*, 443, 945

Pollack, J. B., Hubickyj, O., Bodenheimer, P., et al. 1996, Icarus, 124, 62

Price, D. J. 2004, PhD thesis, Institute of Astronomy, Madingley Rd, Cambridge, CB2 0HA, UK <EMAIL>dprice@cantab.net</EMAIL>

Price, D. J. 2012, Journal of Computational Physics, 231, 759

Price, D. J. & Monaghan, J. J. 2007, *Mon. Not. Roy. Astron. Soc.*, 374, 1347

Pringle, J. E. 1981, *Ann. Rev. Astron, Astrophys.*, 19, 137

Rafikov, R. R. 2005, *Astrophys. J.*, 621, L69

Rameau, J., Chauvin, G., Lagrange, A.-M., et al. 2013, *Astrophys. J. Letters*, 772, L15

Rees, M. J. 1976, *Mon. Not. Roy. Astron. Soc.*, 176, 483

Reiners, A., Ribas, I., Zechmeister, M., et al. 2018a, *Astron. Astrophys.*, 609, L5

Reiners, A., Zechmeister, M., Caballero, J. A., et al. 2018b, *Astron. Astrophys.*, 612, A49

Ricci, L., Testi, L., Natta, A., & Brooks, K. J. 2010, *Astron. Astrophys.*, 521, A66

Rice, W. K. M., Armitage, P. J., Bate, M. R., & Bonnell, I. A. 2003a, *Mon. Not. Roy. Astron. Soc.*, 339, 1025

Rice, W. K. M., Armitage, P. J., Bonnell, I. A., et al. 2003b, *Mon. Not. Roy. Astron. Soc.*, 346, L36

Rice, W. K. M., Forgan, D. H., & Armitage, P. J. 2012, *Mon. Not. Roy. Astron. Soc.*, 420, 1640

Rice, W. K. M., Lodato, G., & Armitage, P. J. 2005, *Mon. Not. Roy. Astron. Soc.*: Letters, 364, L56

Rogers, P. D. & Wadsley, J. 2012, *Mon. Not. Roy. Astron. Soc.*, 423, 1896

Rosotti, G. P., Ercolano, B., Owen, J. E., & Armitage, P. J. 2013, *Mon. Not. Roy. Astron. Soc.*, 430, 1392

Rosswog, S., Davies, M. B., Thielemann, F.-K., & Piran, T. 2000, *Astron. Astrophys.*, 360, 171

Safronov, V. S. 1969, Evoliutsiia doplanetnogo oblaka.

Safronov, V. S. & Zvjagina, E. V. 1969, Icarus, 10, 109

Sallum, S., Follette, K. B., Eisner, J. A., et al. 2015, *Nature*, 527, 342

Salmon, R. 1988, Annual Review of Fluid Mechanics, 20, 225

Scally, A. & Clarke, C. 2001, *Mon. Not. Roy. Astron. Soc.*, 325, 449

Schneider, J., Dedieu, C., Le Sidaner, P., Savalle, R., & Zolotukhin, I. 2011, *Astron. Astrophys.*, 532, A79

Schoenberg, I. J. 1946, Quarterly of Applied Mathematics, 4, 45

Scholz, A., Froebrich, D., & Wood, K. 2013, *Mon. Not. Roy. Astron. Soc.*, 430, 2910

Scholz, A., Jayawardhana, R., & Wood, K. 2006, *Astrophys. J.*, 645, 1498

Serna, A., Alimi, J.-M., & Chieze, J.-P. 1996, *Astrophys. J.*, 461, 884

Shakura, N. I. & Sunyaev, R. A. 1973, *Astron. Astrophys.*, 24, 337

Shvartzvald, Y., Yee, J. C., Skowron, J., et al. 2019, *Astron. J.*, 157, 106

Simon, M., Dutrey, A., & Guilloteau, S. 2000, *Astrophys. J.*, 545, 1034

Simon, M. & Prato, L. 1995, *Astrophys. J.*, 450, 824

Spiegel, D. S., Burrows, A., & Milsom, J. A. 2011, *Astrophys. J.*, 727, 57

Springel, V. 2005, *Mon. Not. Roy. Astron. Soc.*, 364, 1105

Springel, V. & Hernquist, L. 2002, *Mon. Not. Roy. Astron. Soc.*, 333, 649

Stamatellos, D. 2015, *Astrophys. J. Letters*, 810, L11

Stamatellos, D. & Herczeg, G. J. 2015, *Mon. Not. Roy. Astron. Soc.*, 449, 3432

Stamatellos, D., Hubber, D. A., & Whitworth, A. P. 2007a, *Mon. Not. Roy. Astron. Soc.*: Letters, 382, L30

Stamatellos, D. & Inutsuka, S.-i. 2018, *Mon. Not. Roy. Astron. Soc.*

Stamatellos, D., Maury, A., Whitworth, A., & André, P. 2011a, *Mon. Not. Roy. Astron. Soc.*, 413, 1787

Stamatellos, D. & Whitworth, A. 2011, Computational Star Formation, 270, 223

Stamatellos, D. & Whitworth, A. P. 2008, *Astron. Astrophys.*, 480, 879

Stamatellos, D. & Whitworth, A. P. 2009, *Mon. Not. Roy. Astron. Soc.*, 400, 1563

Stamatellos, D. & Whitworth, A. P. 2009a, in American Institute of Physics Conference Series, Vol. 1094, 15th Cambridge Workshop on Cool Stars, Stellar Systems, and the Sun, ed. E. Stempels, 557–560

Stamatellos, D. & Whitworth, A. P. 2009b, *Mon. Not. Roy. Astron. Soc.*, 392, 413

Stamatellos, D., Whitworth, A. P., Bisbas, T., & Goodwin, S. 2007b, *Astron. Astrophys.*, 475, 37

Stamatellos, D., Whitworth, A. P., & Hubber, D. A. 2011b, *Astrophys. J.*, 730, 32

Stamatellos, D., Whitworth, A. P., & Hubber, D. A. 2012, *Mon. Not. Roy. Astron. Soc.*, 427, 1182

Störzer, H. & Hollenbach, D. 1999, *Astrophys. J.*, 515, 669

Strom, K. M., Strom, S. E., Edwards, S., Cabrit, S., & Skrutskie, M. F. 1989, *Astron. J.*, 97, 1451

Takahashi, S. Z., Tsukamoto, Y., & Inutsuka, S. 2016, *Mon. Not. Roy. Astron. Soc.*, 458, 3597

Takakuwa, S., Saito, M., Lim, J., et al. 2012, *Astrophys. J.*, 754, 52

Tatematsu, K., Ohashi, S., Sanhueza, P., et al. 2016, *Pub. Astron. Soc. Japan*, 68, 24

Terebey, S., Shu, F. H., & Cassen, P. 1984, *Astrophys. J.*, 286, 529

Thi, W.-F., Mathews, G., Ménard, F., et al. 2010, *Astron. Astrophys.*, 518, L125

Throop, H. B. & Bally, J. 2005, *Astrophys. J. Letters*, 623, L149

Tobin, J. J., Chandler, C. J., Wilner, D. J., et al. 2013a, *Astrophys. J.*, 779, 93

Tobin, J. J., Hartmann, L., Chiang, H.-F., et al. 2013b, *Astrophys. J.*, 771, 48

Tobin, J. J., Looney, L. W., Li, Z.-Y., et al. 2016, *Astrophys. J.*, 818, 73

Tomida, K., Machida, M. N., Hosokawa, T., Sakurai, Y., & Lin, C. H. 2017, *Astrophys. J. Letters*, 835, L11

Tomida, K., Tomisaka, K., Matsumoto, T., et al. 2013, *Astrophys. J.*, 763, 6

Toomre, A. 1964, *Astrophys. J.*, 139, 1217

Tsukamoto, Y., Machida, M. N., & Inutsuka, S.-i. 2013, *Mon. Not. Roy. Astron. Soc.*, 436, 1667

Tsukamoto, Y., Takahashi, S. Z., Machida, M. N., & Inutsuka, S. 2015, *Mon. Not. Roy. Astron. Soc.*, 446, 1175

van der Marel, N., van Dishoeck, E. F., Bruderer, S., et al. 2013, Science, 340, 1199

van der Plas, G., Ménard, F., Ward-Duong, K., et al. 2016, *Astrophys. J.*, 819, 102

van Elteren, A., Portegies Zwart, S., Pelupessy, I., Cai, M., & McMillan, S. 2019, arXiv e-prints

Vaytet, N., Chabrier, G., Audit, E., et al. 2013, *Astron. Astrophys.*, 557, A90

Velikhov, E. 1959, J. Exptl. Theoret. Phys., 36, 1398

Vicente, S. M. & Alves, J. 2005, *Astron. Astrophys.*, 441, 195

Vorobyov, E. I. 2013, *Astron. Astrophys.*, 552, A129

Vorobyov, E. I. 2016, ArXiv e-prints

Vorobyov, E. I. & Basu, S. 2005, *Astrophys. J.*, 633, L137

Vorobyov, E. I. & Basu, S. 2015, *Astrophys. J.*, 805, 115

Wagner, K., Apai, D., Kasper, M., et al. 2016, Science, 353, 673

Ward, W. R. 1997, , 126, 261

Ward-Thompson, D., Pattle, K., Bastien, P., et al. 2017, *Astrophys. J.*, 842, 66

Weidenschilling, S. J. 1977, *Mon. Not. Roy. Astron. Soc.*, 180, 57, a&AA ID. AAA019.107.015

Wendland, H. 1995, Advances in Computational Mathematics, 4, 389

Whitehouse, S. C. & Bate, M. R. 2004, *Mon. Not. Roy. Astron. Soc.*, 353, 1078

Whitehouse, S. C. & Bate, M. R. 2006, *Mon. Not. Roy. Astron. Soc.*, 367, 32

Whitworth, A. 2018, arXiv e-prints

Whitworth, A. P. & Stamatellos, D. 2006, *Astron. Astrophys.*, 458, 817

Wilkins, D. R. & Clarke, C. J. 2012, *Mon. Not. Roy. Astron. Soc.*, 419, 3368

Wise, A. W. & Dodson-Robinson, S. E. 2018, *Astrophys. J.*, 855, 145

Wolk, S. J. & Walter, F. M. 1996, *Astron. J.*, 111, 2066

Wright, J. T. & Gaudi, B. S. 2013, Exoplanet Detection Methods, ed. T. D. Oswalt, L. M. French, & P. Kalas, 489

Wyatt, M. C. 2008, *Ann. Rev. Astron, Astrophys.*, 46, 339

Yen, H.-W., Koch, P. M., Takakuwa, S., et al. 2015a, *Astrophys. J.*, 799, 193

Yen, H.-W., Takakuwa, S., Koch, P. M., et al. 2015b, *Astrophys. J.*, 812, 129

Yen, H.-W., Takakuwa, S., Ohashi, N., & Ho, P. T. P. 2013, *Astrophys. J.*, 772, 22

Youdin, A. N. & Goodman, J. 2005, *Astrophys. J.*, 620, 459

Young, M. D., Bertram, E., Moeckel, N., & Clarke, C. J. 2012, *Mon. Not. Roy. Astron. Soc.*, 426, 1061

Zapatero-Osorio, M. R., Béjar, V. J. S., Martín, E. L., et al. 2000, Science, 290, 103

Zhu, Z., Hartmann, L., Calvet, N., et al. 2007, *Astrophys. J.*, 669, 483

Zhu, Z., Hartmann, L., & Gammie, C. 2009a, *Astrophys. J.*, 694, 1045

Zhu, Z., Hartmann, L., Gammie, C., & McKinney, J. C. 2009b, *Astrophys. J.*, 701, 620

Zhu, Z., Hartmann, L., Gammie, C. F., et al. 2010, *Astrophys. J.*, 713, 1134

Zhu, Z., Hartmann, L., Nelson, R. P., & Gammie, C. F. 2012, *Astrophys. J.*, 746, 110